



HAL
open science

Modelling of fluid structure interaction by potential flow theory in a pwr under seismic excitation

Roberto Capanna

► **To cite this version:**

Roberto Capanna. Modelling of fluid structure interaction by potential flow theory in a pwr under seismic excitation. Mechanics of materials [physics.class-ph]. Ecole Centrale Marseille, 2018. English. NNT : 2018ECDM0013 . tel-02103803

HAL Id: tel-02103803

<https://theses.hal.science/tel-02103803>

Submitted on 18 Apr 2019

HAL is a multi-disciplinary open access archive for the deposit and dissemination of scientific research documents, whether they are published or not. The documents may come from teaching and research institutions in France or abroad, or from public or private research centers.

L'archive ouverte pluridisciplinaire **HAL**, est destinée au dépôt et à la diffusion de documents scientifiques de niveau recherche, publiés ou non, émanant des établissements d'enseignement et de recherche français ou étrangers, des laboratoires publics ou privés.



**CENTRALE
MARSEILLE**



École Doctorale : Science pour l'ingénieur: mécanique, physique, micro et nanoélectronique
(ED353)

IRPHE - Institut de Recherche sur les Phénomènes Hors Equilibre
LMA - Laboratoire de Mécanique et d'Acoustique
CEA Cadarache - LTHC - Laboratoire de Thermohydraulique et d'Hydromécanique
analytique du Coeur et des circuits

THÈSE DE DOCTORAT

pour obtenir le grade de

DOCTEUR de l'ÉCOLE CENTRALE de MARSEILLE

Discipline : Mécanique

MODELLING OF FLUID STRUCTURE INTERACTION BY POTENTIAL FLOW THEORY IN A PWR UNDER SEISMIC EXCITATION

**Modélisation des interactions fluide structure par écoulement
potentiel dans un coeur de REP sous séisme**

par

CAPANNA Roberto

Directeur de thèse : ELOY Christophe

Soutenue le 07 Décembre 2018

devant le jury composé de :

P. BRANCHER	Professeur, Université Toulouse 3, Toulouse	Président
O. DOARE	ENSTA-Paris Tech, Paris	Rapporteur
A. CAMMI	Professeur Associé, Politecnico di Milano, Milan	Rapporteur
P. BARDET	Professeur Associé, GWU, Washington DC	Examinateur
C. ELOY	Professeur, ECM, Marseille	Directeur
E. SARROUY	Maitre de conférence, ECM, Marseille	Co-Directeur
G. RICCIARDI	Expert senior, HDR, CEA Cadarache	Invité (Superviseur)

Acknowledgement

I would like to take this opportunity to thank all of the committee members for the time they dedicated to my work and for the pertinent remarks they made on my thesis. I also want to acknowledge my supervisor Guillaume Ricciardi for his every day guidance and the support he gave me raising the motivation in difficult moments. I would also like to thank my thesis director and co-director Christophe Eloy and Emmanuelle Sarrouy for their precious help on theoretical work and for the work on the review of my manuscript. A special thanks also goes to professor Philippe Bardet who gave me the possibility to join the TFL lab at George Washington University.

A big thought also goes to all my colleagues of the LTHC and LETH labs at CEA CADARACHE. I want to thank all of you for your warm welcome and for the great time we spent together; I will never forget any of you! A special thanks to Jean Philippe and Fabienne who made possible to complete the experimental campaigns. for the help on the experiments. I also want to thank my internship student Lorenzo Longo for his hard work in data treatment of experimental results.

Furthermore, I want to thank all my friends I met during these three years and to the old ones as well for all the energy you gave me and for all the beautiful moments we shared together.

Finally, I want to express my heartfelt appreciation and love to my girlfriend Sara who I met at the beginning of these three years and has always been by my side especially in the tough moments. A special thanks also for the big effort she made in teaching french language making me fluent in French.

Infine, un ultimo ma non meno importante ringraziamento va ai miei genitori Felice e Paola e a mia sorella Ludovica per avermi supportato sia economicamente che emotivamente durante tutti i miei studi e per avermi dato l'opportunità di raggiungere questo importante obiettivo.

ACKNOWLEDGEMENT

Contents

Acknowledgement	3
Abstract	9
Résumé	11
Résumé Etendu	13
Nomenclature	45
List of Figures	49
List of Tables	55
General Introduction	57
1 Fluid Structure Interactions in Nuclear Reactors	61
1.1 PWR Nuclear Reactor	61
1.1.1 Reactor Vessel	62
1.1.2 Fuel Assembly	63
1.1.3 Dynamical Behaviour under Seismic Loading	64
1.2 Fluid Structure Interaction	65
1.2.1 Added Mass and Added Damping	66
1.2.2 Plate Structures	69
1.2.3 Cylindrical Structures	71
1.3 Fuel Assembly and Reactor Core Modelling	77
1.3.1 Linear Models	77
1.3.2 Non-Linear Models	78
1.3.3 Porous Media Model	78
1.4 Simplified Models	79
1.4.1 Euler Bernoulli Beam Theory	80
1.4.2 Potential Flow Theory	85
1.4.3 Bernoulli Equation	86

CONTENTS

2	Fuel Assembly Vibrational Experiments	89
2.1	Previous Experimental Works	89
2.1.1	EROS	89
2.1.2	ECHASSE	90
2.1.3	CADIX	90
2.1.4	COUPLAGE	90
2.1.5	HERMES	91
2.1.6	Summary on Previous Experimental Works	91
2.2	ICARE Experimental Facility	91
2.2.1	Hydraulic Jack Design	97
2.2.2	Test on the Force Perturbation for the New Sealing Design	100
2.2.3	Compensation Tank and Vortex Breaker Grid	101
2.3	Experimental Campaigns	103
2.3.1	Experimental Matrix	103
2.3.2	Data Analysis Tools	106
2.4	Experimental Results	108
2.4.1	Quasi Static Analysis	108
2.4.2	Dynamic Analysis	111
2.4.3	Parameters Estimation	117
2.4.4	Coupling Between Different Fuel Assemblies	120
2.4.5	Conclusions on Assembly Excitation Experimental Analysis	126
2.5	Laser Velocimetry	127
2.5.1	Laser Velocimetry Techniques on ICARE	127
2.5.2	LDV Experimental Matrix	131
2.5.3	Experimental Results with LDV	132
2.6	Concluding Remarks on Experimental Campaigns	141
3	Fluid Structure Interaction Model	143
3.1	Problem Statement	143
3.1.1	Structure Model	144
3.1.2	Fluid Model	145
3.1.3	Coupling Fluid and Structure Model	146
3.2	Single Cylinder Model	147
3.2.1	Problem in Fourier Space	147
3.2.2	Relation between Interaction Force and Structure Displacement	149
3.2.3	Main Analytical Results	153
3.3	Multi Cylinder Model	154
3.3.1	From one to Multiple Cylinders	154
3.3.2	ICARE Geometry Model	156

4	Numerical Calculations	159
4.1	FreeFem++	159
4.1.1	Main Characteristics	159
4.1.2	Weak Formulation	160
4.2	Single Cylinder Calculations	161
4.2.1	Slender Body Approximation	162
4.2.2	Empirical Formulation	163
4.2.3	Polynomial Interpolation	169
4.2.4	Confinement Effects	171
4.3	Multiple Cylinders Calculations and Comparison with Experimental Results	173
4.3.1	Two and Four Cylinders Calculations	173
4.3.2	Calculations for ICARE Geometry and Comparison with Experimental Results	178
4.3.3	Sum-Up on Numerical Calculations	186
5	GWU Experiments and Physical Analysis	189
5.1	Experimental Facility	189
5.1.1	Test Section	191
5.1.2	Measurement System	193
5.2	Experimental Data and Repeatability Problem	195
5.2.1	PIV Data Analysis	195
5.2.2	LVDT Data Analysis	198
5.3	POD and Projection on Theoretical Modes for GWU Dataset	199
5.3.1	Proper Orthogonal Decomposition	199
5.3.2	Application of POD Technique to GWU Experimental Data	200
5.4	Numerical Simulations	206
5.4.1	Single Cylinder 3D Geometry	206
5.4.2	Complete 3D Geometry	208
5.5	Analysis and Conclusions	215
	Conclusions & Perspectives	217
	Bibliography	221
	Appendix A Experimental Campaigns List	231
	Appendix B FreeFEM++ Script	247

CONTENTS

Abstract

Efficient modelling and accurate knowledge of the mechanical behaviour of the reactor core are needed to estimate the effects of seismic excitation on a nuclear power plant. The presence of cooling water flow (in PWRs) gives rise to fluid structure interaction phenomena. Modelling of fluid structure interactions on fuel assemblies is thus of fundamental importance in order to assure the safety of nuclear reactors. The main objective of the PhD project which is presented in this document is to investigate fluid structure interactions in order to have a better understanding of the involved phenomena. Both modelling and experimental approach are considered. A new simplified linear model for fluid structure interactions is developed by using the potential flow theory for fluid force modelling while the Euler-Bernoulli beam model is used for the structural part. The model, is first developed for a single cylinder and it is validated with reference works in literature. The effects of the confinement size and of the wavenumber are investigated. The potential flow model developed for a single cylinder, is thus extended to a multi cylinders geometry. The experimental approach is thus needed in order to validate the developed model. A new experimental facility, ICARE, is designed in order to investigate fluid structure interaction phenomena on half scale fuel assemblies. In this document, the results provided by displacement and LDV measurements are widely analysed. The dynamical behaviour of the fuel assembly and coupling effects are investigated. Calculations are compared to the experimental results in order to validate the model and to analyse its limits. The model is in agreement with experimental results regarding the added mass effect. In addition, the model qualitatively predicts couplings effects on different directions. As a drawback, the potential flow model cannot predict added damping effects, which are mainly due to viscous forces. Finally in this document another application of the developed model is described. The model is used in order to simulate experiments performed on a surrogate fuel assembly in the experimental facility installed at George Washington University (GWU). The model is able to predict and to provide a valid interpretation for the water flow perturbation due to the motion of the excited assembly. The thesis concludes with perspectives for further improvements of the model, by integrating viscous terms in the equations. Work needs to be carried out on the analysis of Particle Image Velocimetry (PIV) data collected during ICARE experimental campaigns.

ABSTRACT

Résumé

Une modélisation efficace et une connaissance précise du comportement mécanique du cœur du réacteur sont nécessaires pour estimer les effets de l'excitation sismique sur une centrale nucléaire. La présence d'un écoulement d'eau (dans les REP) engendre des phénomènes d'interaction fluide structure. La modélisation des interactions fluide structure sur les assemblages combustible revêt donc une importance fondamentale pour la sécurité des réacteurs nucléaires. L'objectif principal du projet de thèse présenté dans ce document est d'étudier les interactions fluide structure afin de mieux comprendre les phénomènes impliqués. La modélisation et l'approche expérimentale sont considérées. Un nouveau modèle linéaire simplifié pour les interactions fluide structure est développé en utilisant la théorie de l'écoulement potentiel pour la modélisation des forces fluide, tandis que le modèle de poutre d'Euler-Bernoulli est utilisé pour la partie structurelle. Le modèle est d'abord développé pour un seul cylindre et il est validé avec des ouvrages de référence dans la littérature. Les effets de la taille de confinement et du nombre d'onde sont examinés. Le modèle d'écoulement potentiel développé pour un seul cylindre est ainsi étendu à une géométrie multicylindre. La démarche expérimentale est donc nécessaire pour valider le modèle développé. Une nouvelle installation expérimentale, ICARE, a été conçue pour étudier les phénomènes d'interaction fluide structure sur des assemblages combustible à demi-échelle. Dans ce document, les résultats fournis par les mesures de déplacement et de LDV sont largement analysés. Le comportement dynamique de l'assemblage combustible et les effets de couplage sont étudiés. Les calculs sont comparés aux résultats expérimentaux afin de valider le modèle et d'en analyser ses limites. Le modèle est en accord avec les résultats expérimentaux concernant l'effet de masse ajouté. De plus, le modèle prédit qualitativement les effets des couplages dans différentes directions. Par contre, le modèle d'écoulement potentiel ne permet pas de prédire des effets d'amortissement ajouté, principalement dus aux forces visqueuses. Enfin, dans ce document, une autre application du modèle développé est décrite. Le modèle est utilisé afin de simuler des expériences réalisées sur une maquette d'assemblage combustible dans l'installation expérimentale installée à l'Université George Washington (GWU). Le modèle est capable de prédire et de fournir une interprétation valide de la perturbation du débit d'eau due au mouvement de l'ensemble excité. La thèse se termine par des perspectives d'amélioration du modèle, en intégrant des termes visqueux dans les équations. L'analyse des données de vélocimétrie par image de particules (PIV) recueillies au cours des campagnes expérimentales ICARE doit être poursuivie.

RESUME

Résumé Étendu

Cette section présente un résumé étendu en français du document suivant, rédigé en anglais.

Introduction

La sécurité des réacteurs nucléaires constitue aujourd'hui un défi industriel majeur. Les réacteurs nucléaires les plus répandus sont les réacteurs à eau sous pression (REP). Le combustible d'un REP est principalement constitué d'uranium enrichi, sous la forme de pellets qui sont assemblés pour former un crayon de combustible. Les barres de combustible sont regroupées dans un assemblage de combustible à 17×17 crayons. Chaque assemblage combustible comporte 10 grilles de support qui maintiennent ensemble les barres de combustible. Un noyau de REP est composé de plusieurs centaines d'assemblages combustibles. La chaleur produite par les assemblages combustibles est ensuite évacuée par un courant d'eau axial, ce qui garantit également une température superficielle des assemblages à un certain seuil. La température des assemblages combustibles doit être contrôlée afin d'éviter des contraintes excessives et d'éventuels dommages du revêtement extérieur. Le revêtement constituant la première barrière entre les produits nucléaires et l'environnement, son intégrité revêt une importance fondamentale pour garantir la sûreté des réacteurs nucléaires. Un cœur de réacteur nucléaire est donc un système très complexe constitué de plusieurs composants et de la présence de structures allongées et d'un fluide en écoulement.

Les tremblements de terre sont l'une des principales préoccupations concernant la sécurité des réacteurs nucléaires. En cas de séisme, tous les assemblages présents à l'intérieur du réacteur pourraient entrer en collision et provoquer des déformations permanentes des grilles de support. Des mesures de sécurité sont donc nécessaires pour assurer la chute des barres de commande, mais aussi pour assurer le refroidissement du noyau, même si les grilles d'entretoise de l'assemblage de combustible se heurtent. Ainsi, une modélisation appropriée du comportement mécanique des assemblages de combustible est inévitable. En raison de la présence d'un flux d'eau axial, des phénomènes complexes d'interactions entre le fluide et les structures se produisent. Afin de modéliser le comportement du cœur du réacteur sous des interactions de structure fluide-excitation sismique, il convient d'étudier attentivement ces interactions et de les prendre en compte pour une modélisation précise.

Au cours des années, de nombreux auteurs et entités industrielles ont étudié les interactions structure-fluide des assemblages de combustible nucléaire. Différents modèles ont été développés, chacun ayant pour objectif de modéliser certains aspects de leur compor-

RESUME ETENDU

tement mécanique. Parallèlement aux modèles, des travaux expérimentaux ont été menés afin d'observer les phénomènes d'interaction structure-fluide sur les grappes de combustible afin de valider ces-derniers.

Le comportement vibratoire des assemblages de combustible nucléaire est étudié depuis des décennies au CEA (Commissariat à l'Energie Atomique et aux Energies Alternatives). Dans le cadre d'une collaboration entre le CEA, EDF et FRAMATOME (ex-AREVA), plusieurs installations expérimentales ont été conçues et exploitées au CEA de Cadarache. Les premières expériences (EROS) ont été conçues avec des assemblages à l'échelle réduite afin d'étudier les forces d'impact sans écoulement axial. D'autres installations ont été construites afin de prendre en compte les assemblages combustibles à flux axial (ECHASSE) et à dimension réelle (CADIX). Plus tard, une nouvelle installation (COUPLAGE) a été construite afin d'étudier les couplages entre différents assemblages de combustible en raison de la présence d'eau. Quoiqu'il en soit, la conception des assemblages était à l'échelle très réduite et n'était pas considérée comme représentative des conditions réelles des assemblages combustibles. Enfin, une installation à grande échelle (HERMES) a été construite afin d'identifier les paramètres modaux d'un assemblage combustible réel à des fins de conception.

De plus, le laboratoire développe également des modèles numériques, en parallèle avec l'activité expérimentale. Le code COEUR3D a récemment été mis au point dans le but de simuler le comportement vibratoire d'assemblages de réacteurs REP dans des scénarios accidentels. Le modèle est basé sur une approche de milieu poreux, prenant en compte le débit d'eau, les grilles de support et les chocs entre les assemblages. Le code prend en compte des phénomènes très complexes et fournit des résultats numériques précis et validés par des expériences. Quoiqu'il en soit, ce code demande beaucoup de temps en termes de temps de calcul et ne peut pas être utilisé dans le cadre d'une analyse de sensibilité sur des paramètres géométriques.

La thèse qui sera présentée dans ce document s'inscrit dans le cadre de ce projet commun entre le CEA, EDF et FRAMATOME. Cette thèse a pour objectif de répondre à la nécessité d'un modèle simplifié qui permettrait de saisir les principales caractéristiques des interactions structure-fluide des assemblages de combustible et, grâce à un coût de calcul peu élevé mais aussi de réaliser une analyse de sensibilité sur différents paramètres afin de comprendre comment ils affectent les phénomènes d'interactions structure-fluide. Dans le but d'améliorer les connaissances phénoménologiques sur les phénomènes d'interaction structure-combustible sur des assemblages de combustible nucléaire, une approche de modélisation et une approche expérimentale sont mises en œuvre au cours de ces travaux. L'accent a été mis sur l'identification des limites de ce modèle simplifié afin d'identifier le champ d'application valide.

La première approche de la modélisation consistait à identifier les simplifications appropriées nécessaires pour développer un modèle simple permettant des calculs rapides. Les calculs d'interaction fluide-structure nécessitent beaucoup de temps, principalement en raison de la résolution des équations de Navier-Stokes pour les calculs de fluide. Ainsi, la

théorie du flux potentiel a été identifiée comme un bon outil pour réduire le temps de calcul. La théorie des écoulements potentiels introduit une quantité scalaire, ce qui permet d'éviter la solution des équations de Navier-Stokes pour le calcul des forces fluides. Le problème de fluide est ainsi réduit à un problème de Poisson, ce qui accélère considérablement les calculs. Des simplifications sont également introduites dans le modèle structurel, en considérant que l'assemblage combustible se comporte comme un faisceau d'Euler-Bernoulli. Pour réduire davantage le temps de calcul, le modèle est résolu dans l'espace de Fourier, ce qui permet de résoudre un problème 2D au lieu d'un problème 3D. La validité et les limites de ce modèle simplifié ont été testées avec des résultats expérimentaux.

Une nouvelle installation expérimentale a récemment été conçue au Laboratoire de thermohydraulique et d'hydromécanique analytique du cœur et des circuits (LTHC) dans le but d'étudier le couplage entre les assemblages de combustible. L'installation expérimentale ICARE comprend quatre assemblages de combustible (une demi-échelle) disposés en un réseau de 2×2 sous un écoulement axial. Les assemblages combustibles sont constitués de 64 crayons disposés dans un réseau 8×8 afin de garantir la bonne représentativité d'un assemblage combustible réel. Durant la thèse, plusieurs campagnes expérimentales ont été menées afin d'étudier les effets de différentes configurations sur les forces de couplage. Les campagnes expérimentales ont permis de valider le modèle développé et de définir ses limites.

Interactions fluide structure dans les réacteurs nucléaires

Dans ce premier chapitre, le contexte principal de cette thèse sera présenté. Un cœur de réacteur nucléaire PWR (textit Réacteurs à eau sous pression) sera présenté avec une attention particulière pour les composants principaux du cœur du réacteur : les assemblages de combustible.

Les REP représentent la grande majorité des centrales nucléaires dans le monde, notamment en France où ils constituent la totalité des centrales en exploitation pour la production d'électricité. Le composant principal (et le plus spécifique) du réacteur nucléaire est le cœur du réacteur, qui contient le combustible nucléaire et tous les autres composants nécessaires au maintien des réactions nucléaires et au processus de refroidissement. Les assemblages combustibles sont les personnages principaux de cette thèse. Pour plus de détails sur la conception générale des centrales nucléaires ou du cœur de réacteur, on peut se référer à [Glasston and Sesonske \(1994\)](#) et [Lamarsh \(2001\)](#).

La figure 1 donne une coupe intérieure d'une cuve de réacteur nucléaire. Il existe une buse d'entrée (ou à jambe froide) et une buse de sortie (ou à jambe chaude) pour chaque boucle du système de refroidissement du réacteur.

Un cœur de réacteur (REP) est constitué de plusieurs assemblages combustibles (entre 150 et 250 en fonction de la puissance du réacteur). Ces assemblages combustibles sont immergés dans un flux d'eau qui extrait la chaleur générée dans les assemblages combustibles. Le débit de liquide de refroidissement est caractérisé par une vitesse moyenne de

RESUME ETENDU

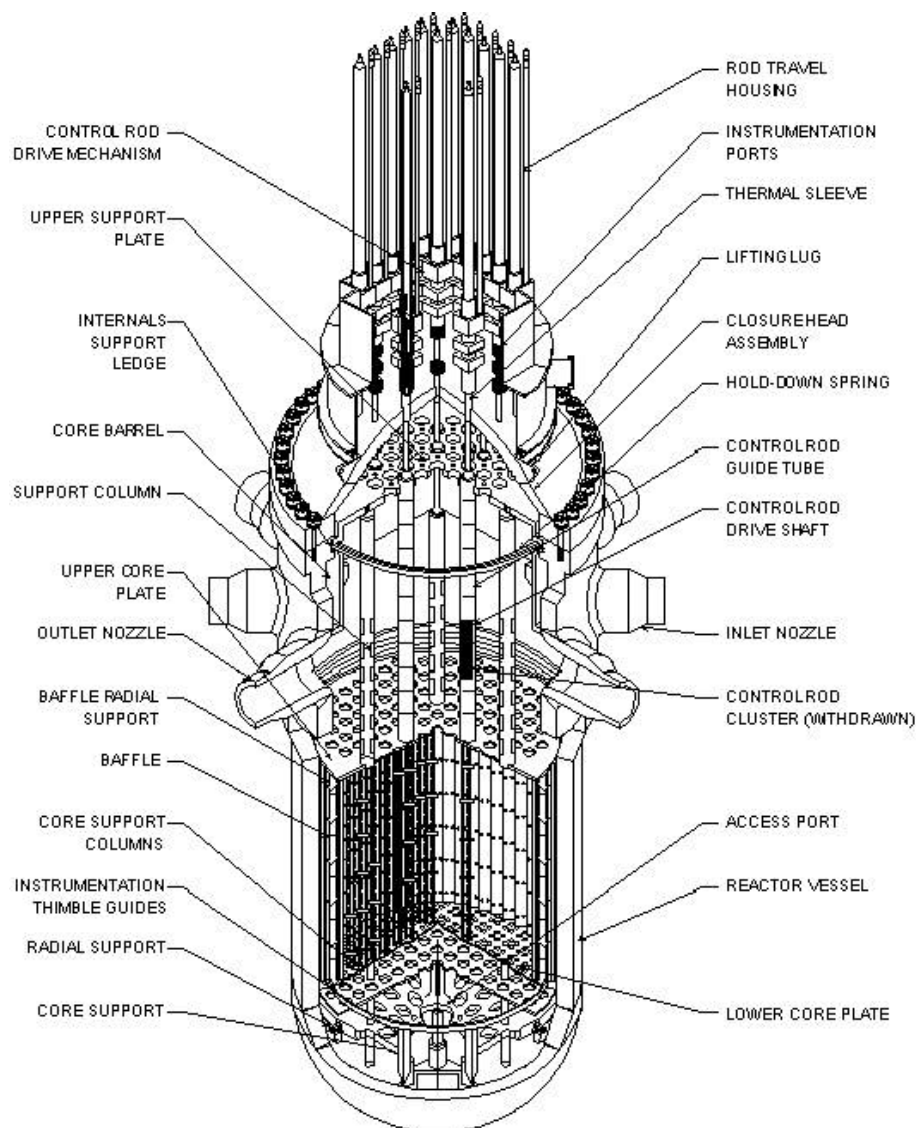


FIGURE 1 – Cuve du réacteur REP et composants internes

5 m/s, une température moyenne de 310 °C et une pression de 150 bar.

La voie d'écoulement du fluide de refroidissement du réacteur à travers la cuve du réacteur serait :

- Le liquide de refroidissement pénètre dans la cuve du réacteur par la buse d'admission et entre en contact avec le cylindre.
- Le carottier oblige l'eau à s'écouler dans l'espace situé entre la paroi de la cuve du réacteur et le carottier.
- Après avoir atteint le fond de la cuve du réacteur, le flux est dirigé vers le haut pour traverser les assemblages combustibles.
- Le liquide de refroidissement circule autour des assemblages combustibles et élimine la chaleur produite par le processus de fission.

- L'eau maintenant plus chaude pénètre dans la région des équipements internes supérieurs, où elle est acheminée par la buse de sortie et se dirige vers le générateur de vapeur.

Les travaux de cette thèse portent principalement sur la vibration des assemblages de combustible afin de modéliser le comportement du cœur du réacteur en cas de séisme. En cas de scénario accidentel, l'ensemble du cœur du réacteur bouge et des contacts entre les assemblages de combustible peuvent se produire. Des impacts violents pourraient provoquer des déformations importantes des assemblages de combustible, ce qui pourrait bloquer la chute des barres de commande. La sécurité de l'ensemble du cœur du réacteur serait alors compromise. Afin de garantir la sécurité du réacteur, une bonne modélisation du comportement dynamique des assemblages de combustible est requise. Le cœur d'un réacteur nucléaire est un système très complexe, c'est pourquoi plusieurs hypothèses doivent être retenues afin de fournir un modèle à la fois fiable et efficace (en ce qui concerne le temps de calcul).

Une première remarque importante à garder à l'esprit est que la modélisation du cœur d'un réacteur implique la présence de deux phases macroscopiques différentes : une phase solide (un assemblage combustible) et une phase liquide (eau de refroidissement). Il en résulte une brève description des phénomènes impliquant chacun d'eux.

D'un point de vue structurel, malgré sa structure allongée, l'assemblage combustible ne se comporte pas comme un simple faisceau, mais présente un comportement complexe (Pisapia, 2004). En fait, les barres de combustible sont maintenues ensemble par un système de un ressort et deux alvéoles, qui introduisent une relation de contact non linéaire. Les premières preuves expérimentales de non-linéarités sont observées au cours des tests de vibration et de relâchement (Brochard et al., 1993). D'autres expériences (comme la campagne expérimentale "MASSE" réalisée par Pisapia (2004)) ont souligné un phénomène d'hystérésis au cours du cycle de déplacement et des non-linéarités sont observées sur les coefficients de rigidité et d'amortissement.

En ce qui concerne la phase liquide dans le cœur d'un réacteur REP, comme décrit dans la section 1.1.1, l'eau se déplace sous un courant ascendant à environ 5 m/s à 150 bar et 310 °C. En prenant en compte les dimensions des canaux où le flux d'eau donne un nombre de Reynolds $Re \simeq 2 \cdot 10^5$, ce qui signifie que le flux est turbulent. Bien que le flux soit appelé "ascendant", il convient de noter la présence d'un flux transversal (environ 5 ÷ 15%) dû au mouvement des assemblages combustibles eux-mêmes. En première approximation, le flux transverse pourrait être négligé, mais certains modèles prennent en compte cet aspect, comme dans Ricciardi (2016) en utilisant une "modélisation de flux by-pass".

La présence de l'écoulement d'eau et de la structure donne lieu à des phénomènes complexes d'interaction entre le fluide et la structure. En fait, la présence de la structure influe sur le comportement du fluide, qui influe elle-même sur le comportement de la structure. Nous pourrions définir deux sources d'interactions différentes. Le premier est dû à la présence de l'eau elle-même, qui tend à opposer une résistance au mouvement de la structure.

RESUME ETENDU

La seconde est due à l'écoulement, ce qui ajoute une résistance supplémentaire à la structure pour qu'elle se déplace (en fonction de la vitesse). Dans les chapitres suivants, différents modèles d'interaction fluide-structure seront présentés. Nous discuterons ultérieurement de certains modèles prenant en compte l'assemblage de combustible et le comportement de l'ensemble du noyau. L'accent sera mis sur le "modèle de support poreux". L'un des objectifs principaux de cette thèse est de trouver, d'une manière ou d'une autre, une expression simplifiée des forces d'interaction, ce qui pourrait nous donner un modèle assez simple (et rapide du point de vue informatique), à utiliser de manière prédictive.

Comprendre et modéliser les forces d'interaction est d'une importance fondamentale pour disposer d'un modèle capable de décrire le comportement de l'ensemble du cœur du réacteur sous une charge sismique. Afin de bien comprendre les phénomènes physiques mis en jeu dans les problèmes généraux d'interaction structure-fluide, les principales études réalisées sur le sujet seront présentées ci-dessous. Les travaux scientifiques seront présentés dans le but de donner au lecteur une idée de l'évolution historique de la compréhension de ces phénomènes et des besoins industriels auxquels ils sont capables de répondre. La discussion portera sur les hypothèses impliquées par chaque modèle et sur la validation de leurs résultats.

Lorsqu'un composant structurel immergé dans un fluide vibre, le fluide environnant doit être déplacé pour permettre ces mouvements. En conséquence, des perturbations de pression sont générées. À son tour, l'effet intégré de ces perturbations de pression produit une force hydrodynamique agissant sur la structure. Le fluide en mouvement avec la structure a un effet important sur la dynamique de la structure vibrante ; en particulier sur ses fréquences propres et sur les caractéristiques d'amortissement. Idéalement, la force hydrodynamique devrait être calculée sur la base des équations tridimensionnelles de Navier-Stokes. Évidemment, la résolution de ces équations est difficile même dans des cas simples ; alors les scientifiques ont émis des hypothèses (en fonction de l'application spécifique) permettant de simplifier le problème.

Certains des travaux les plus importants de la littérature sur l'interaction fluide-structure de plaques immergées dans un fluide ont été analysés dans cette section. Le travail de [Guo and Païdoussis \(2000\)](#); [Eloy et al. \(2007, 2008\)](#); [Doaré et al. \(2011b\)](#) est considéré avec un intérêt particulier car certaines des méthodes présentées par ces auteurs (appliquées sur des structures en plaques) seront appliquées au cours de la thèse sur les structures cylindriques.

En conclusion, les paragraphes précédents ont fourni un résumé des travaux qui pourraient être trouvés dans la littérature sur les interactions de structures fluides. Différentes hypothèses et conditions ont été examinées en fonction des besoins spécifiques et des applications que les auteurs avaient l'intention de traiter. Plusieurs travaux sur la modélisation du comportement dynamique de structures cylindriques à la fois dans un fluide en repos ou sous un écoulement axial, ont été réalisés. Le cas de plusieurs cylindres a été pris en compte, d'une paire de cylindres à l'autre groupe de cylindres : seules les géométries symétriques axiales sont considérées et les cylindres de chaque groupe sont considérés comme libres de se déplacer indépendamment. Certaines études ont examiné la situation d'un écoulement

confiné, mais uniquement dans le cas d'un confinement annulaire. La plupart des travaux analysés ont utilisé la théorie des débits potentiels, une correction spécifique prenant en compte les différents phénomènes (typiquement la viscosité et les non-linéarités).

Par conséquent, il existe un manque de connaissances sur les effets de tout type de confinement (forme rectangulaire par exemple) sur le comportement dynamique d'un cylindre sous écoulement axial. En ce qui concerne les groupes de cylindres, il conviendrait de mieux étudier les géométries de réseau quadrillé, l'objectif principal étant de simplifier certains modèles existants complexes. Pour ces raisons, l'un des objectifs du projet de thèse décrit dans ce document est d'étudier un modèle simplifié d'interaction fluide-structure sur une structure cylindrique en confinement rectangulaire et disposée en réseau quadrillé. Certaines des approches utilisées dans la littérature pour la modélisation des interactions de structure fluide sur des plaques (transformée de Fourier) seront utilisées de manière analogue sur des structures cylindriques.

Deux modèles simplifiés sont utilisés pour dériver un modèle simplifié d'interaction structure de fluide : la théorie du faisceau d'Euler Bernoulli pour la structure et la théorie de l'écoulement potentiel pour le fluide.

La théorie des poutres d'Euler Bernoulli est une simplification de la théorie linéaire de l'élasticité qui permet de calculer les caractéristiques de portage et de déviation des poutres. Il couvre le cas des faibles déformations d'une poutre soumise uniquement à des efforts latéraux ([Bauchau and J.I., 2009](#)). Il s'agit donc d'un cas particulier de la théorie de faisceau de Timoshenko ([Timoshenko, 1953](#)). Les principales hypothèses de la théorie d'Euler Bernoulli sont les suivantes :

- Le rapport entre la longueur de la barre et son épaisseur est relativement grand (supérieur à 10) ;
- Les sections transversales restent planes et orthogonales à la ligne médiane ;
- Chaque section subit la même déflexion transversale ;
- La flexion due à son propre poids est négligée ;
- Le matériau se comporte linéairement.
- Les déflexions sont petites comparées à l'épaisseur du faisceau ;

Dans la dynamique des fluides, la théorie de l'écoulement potentiel décrit l'écoulement comme invisible et irrotationnel. Ces deux hypothèses simples mais fortes impliquent une énorme simplification des équations de la dynamique des fluides. Le principal résultat de la théorie de l'écoulement potentiel est que nous pouvons écrire un champ de vitesse de l'écoulement du fluide, qui est un champ de vecteur en fonction d'une fonction scalaire unique. Par conséquent, les problèmes d'écoulement potentiels se réduisent simplement aux solutions de l'équation de Laplace. Dans ces problèmes, toute la physique est régie par des conditions limites.

Ce résultat est l'une des conséquences les plus importantes de la théorie des écoulements potentiels, qui permet des grandes simplifications des équations de la mécanique des fluides.

Les flux externes peuvent être considérés comme non visqueux et irrotationnels car les effets visqueux se limitent à une couche mince située à proximité du corps, appelée couche limite, et peuvent dans de nombreux cas être négligés. Pour des modèles plus précis, la théorie de la couche limite doit être appliquée ([Ackroyd et al., 2001](#)).

À partir de l'équation générale de Navier-Stokes :

$$\rho \frac{D\mathbf{v}}{Dt} = -\nabla p + \rho \mathcal{F} + \mu \nabla^2 \mathbf{v} \quad , \quad (1)$$

en appliquant les hypothèses de la théorie des écoulements potentiels, nous obtenons l'équation linéarisée de Bernoulli décrivant le domaine fluide.

$$\frac{\partial \phi'}{\partial t} + \nabla \phi_\infty \cdot \nabla \phi' = -\frac{p'}{\rho} \quad . \quad (2)$$

Cette équation sera encore utilisée afin de trouver les équations permettant de résoudre le problème de fluide.

Expériences Vibratoires sur les Assemblages Combustible

Cette section est consacrée aux travaux expérimentaux sur l'interaction structure-fluide appliquée aux assemblages de combustible. Premièrement, les travaux expérimentaux précédents et leurs principaux résultats seront illustrés. Plus tard, l'installation expérimentale ICARE sera illustrée en détail et les campagnes expérimentales réalisées sur l'installation seront présentées. Les principaux résultats expérimentaux seront présentés et discutés. La dernière partie de ce chapitre est consacrée aux techniques de vélocimétrie au laser, mises en œuvre sur le site expérimental ICARE et certains résultats seront discutés.

Les résultats expérimentaux et l'analyse seront davantage utilisés dans le chapitre 4 afin d'être comparés aux calculs numériques effectués avec un modèle simple (hypothèse de flux potentiel) visant à reproduire les résultats expérimentaux. Ces derniers seront ensuite utilisés pour valider le modèle, en comprendre les limites et effectuer une analyse critique des phénomènes impliqués.

Au cours des dernières décennies, plusieurs installations expérimentales ont été réalisées en France au CEA (Commission des énergies alternatives et de l'énergie atomique) afin d'étudier les phénomènes d'interaction fluide-structure impliquant des assemblages de combustible nucléaire. Comme il serait compliqué et très coûteux de reproduire un noyau nucléaire à l'échelle 1, différentes installations ont été construites au cours des années, en ajustant certains des paramètres (nombre d'ensembles, taille des ensembles, pression, température, etc.). La dynamique des principaux travaux expérimentaux sur les assemblages de combustible est résumée dans le Tableau 1.

A partir de cette succincte représentation des précédents travaux expérimentaux sur l'étude des interactions fluide-structure sur les assemblages de combustible, nous pouvons conclure que la force de choc entre assemblages de combustible a été largement étudiée au cours des années à différentes échelles. D'autre part, les phénomènes de couplage impli-

Maquette	Objectifs	Limites
EROS	Évaluation des forces d'impact sur une ligne d'assemblages combustible	Assemblages à échelle réduite Pas de débit d'eau
ECHASSE	Évaluation des forces d'impact sous flux axial	Seulement deux assemblages Grand by-pass
CADIX	Évaluation des forces d'impact sur un assemblage réel	Pas de débit d'eau Assemblages sur une seule ligne
COUPLAGE	Évaluation du couplage entre les assemblages combustible	Assemblages à échelle fortement réduite : non représentatif Les assemblages ne sont pas libres de se déplacer
HERMES	Identification des paramètres modaux d'un assemblage combustible réel (campagnes DEDALE)	Un seul assemblage combustible

TABLE 1 – Résumé des installations expérimentales précédentes

quant différents assemblages de combustible n'ont été étudiés que sur une petite structure expérimentale (COUPLAGE) utilisant des grappes de combustible très simplifiées (3 grilles dans un réseau de 4×4) qui ne sont pas représentatives d'assemblages de combustible réels.

Pour ces raisons, une nouvelle installation expérimentale a été conçue et construite au CEA Cadarache : ICARE. L'objectif principal de cette installation expérimentale est d'étudier le couplage entre différents assemblages de combustible en fonction de la taille du confinement et de la vitesse d'écoulement. Les assemblages combustibles ne sont pas de taille réelle (demi-longueur), mais ils sont plus représentatifs d'assemblages combustibles réels (6 grilles dans un réseau de 8×8).

L'installation expérimentale ICARE a été réalisée au CEA pendant la thèse de S. Clement. Une description globale de l'installation suivra dans cette section afin de clarifier la compréhension des résultats expérimentaux. Pour plus de détails sur la conception de chaque composant de l'installation, le lecteur est appelé [Clement \(2012a,b, 2014\)](#).

L'installation expérimentale ICARE est constituée d'une boucle d'eau fermée composée d'une pompe centrifuge, d'une section de test, d'un réservoir de compensation et d'un

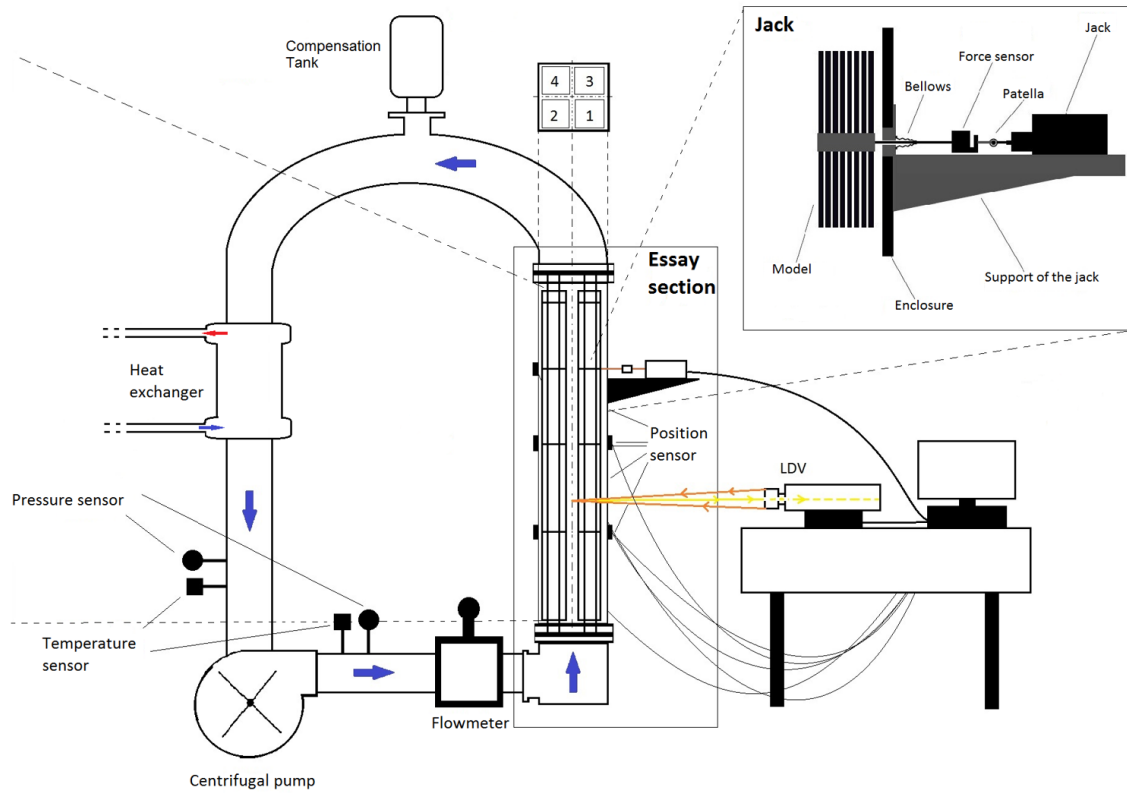


FIGURE 2 – Schéma du dispositif expérimental ICARE

échangeur de chaleur permettant de maintenir la température constante. La section d'essai est placée verticalement avec une section carrée de $22.5\text{ cm} \times 22.5\text{ cm}$ et accueille jusqu'à 4 assemblages combustibles disposés en un réseau de 2×2 . La longueur des assemblages combustibles est de $2,57\text{ m}$, soit environ la moitié des véritables assemblages combustibles. Chacune d'entre elles est constituée d'un réseau carré de barres de 8×8 , dans lesquelles se trouvent 60 barres simulant des barres de combustible (en acier inoxydable ou en polyméthacrylate de méthyle) et 4 tubes-guides en acier inoxydable. Les tubes de guidage sont vides à l'intérieur et ils sont soudés à 5 grilles d'espacement métalliques sur la longueur de l'ensemble. Les tubes-guides ont une fonction structurelle car ils donnent de la rigidité à l'ensemble et maintiennent ensemble les barres de combustible. Dans l'assemblage combustible réel, les barres de commande peuvent être insérées à l'intérieur des tubes guides. Chaque assemblage a une section de $10.1 \times 10.1\text{ cm}^2$ et les 64 crayons qui le constituent ont un diamètre de 9 mm . Le haut et le bas de l'assemblage sont fixés rigidement aux tubes-guides, ainsi qu'à la section de test par l'intermédiaire de la plaque de support inférieure et de la plaque de support supérieure. Un schéma de l'ensemble de l'installation expérimentale est représenté à la figure 2.

Un vérin hydraulique permet d'exciter l'un des quatre assemblages de combustible. Pour ces expériences, l'assemblage devant la porte est excité et le vérin hydraulique peut être placé à différents niveaux. Le vérin hydraulique est fixé à une des vis de la grille de

l'assemblage de combustible et un capteur de force est installé entre le vérin hydraulique et la tige. Le capteur de force varie de -500 N à 500 N avec une précision de 0.045% de la pleine échelle, ce qui correspond à une incertitude de $\pm 0.225\text{ N}$. L'actionneur hydraulique est également équipé d'un capteur de position (plage $\pm 10\text{ mm}$ et incertitude $\pm 0.03\text{ mm}$). Le capteur de force permettra de mesurer la force appliquée, cependant il n'est pas utilisé pour contrôler le vérin hydraulique. Le système de contrôle utilise le capteur de position car sa précision est bien supérieure à celle du capteur de force. Le vérin hydraulique peut être connecté à deux grilles différentes. La possibilité d'exciter l'assemblage sur la grille centrale et sur la grille supérieure permet d'exciter différents modes naturels. Lorsque le vérin hydraulique est fixé à la grille du milieu, seuls les modes pairs seront excités, tandis que lorsqu'il sera fixé à la grille supérieure, les modes pairs et impairs seront excités.

Quatre campagnes expérimentales différentes ont été menées sur le site ICARE. Toutes les campagnes expérimentales sont réalisées avec des assemblages combustibles en PMMA (poly-méthyl-méthacrylate). Les deux premières campagnes impliquent l'utilisation d'un confinement de grande taille (8 mm), tandis que deux autres campagnes utilisent un confinement de taille réduite (4 mm). La modification de la taille du confinement permet d'évaluer les effets de la dérivation de l'eau entre le mur et l'assemblage sur le comportement dynamique des assemblages combustibles.

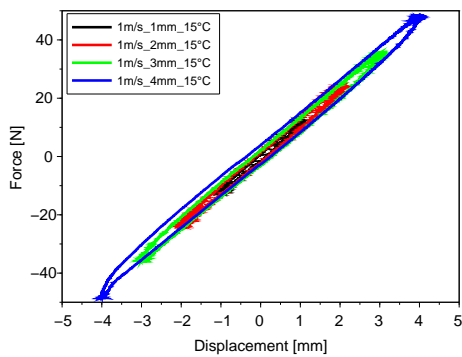
Confinement	Assemblies	Water Flow	Temperature	Excitation Amplitude	Frequency
Large: 8 mm	2	Air	15 °C	0,1 mm	Quasi-Static: 0,05 Hz
		0 m/s		0,3 mm	
		1 m/s		0,5 mm	
		2 m/s		0,8 mm	
		3 m/s		1 mm	
Small: 4 mm	4	4 m/s	30 °C	1,2 mm	Sweep: 0,05 ÷ 25 Hz
		5 m/s		1,7 mm	
				2 mm	

FIGURE 3 – Représentation schématique de la matrice expérimentale

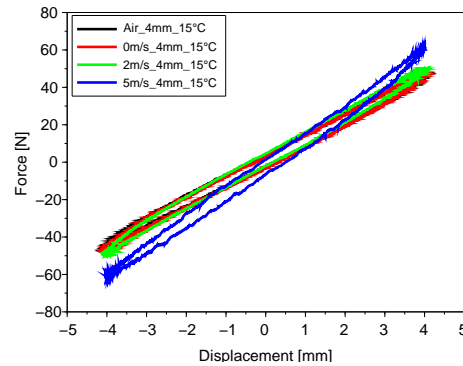
Pour les deux tailles de confinement, deux campagnes expérimentales sont exécutées, l'une avec les quatre assemblages et l'autre avec seulement deux assemblages combustibles. La présence de 4 assemblages de combustible (disposés en réseau carré) permet d'étudier les phénomènes hors-plan dans le couplage entre les assemblages de combustible. Les différentes campagnes expérimentales sont résumées dans une matrice expérimentale dans la figure 3.

RESUME ETENDU

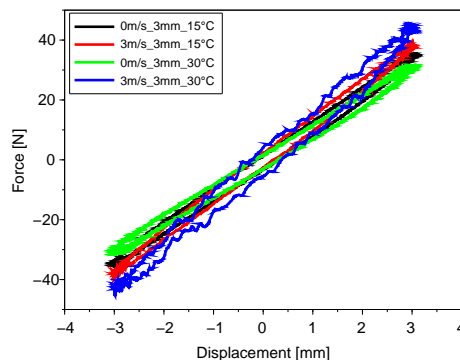
Des expériences quasi-statiques permettent de mettre en évidence la relation entre le déplacement de l'assemblage de combustible et l'effort nécessaire pour le déplacer sans prendre en compte les effets dynamiques (fréquence d'excitation 0.05 Hz). La figure 4 montre les relations force-déplacement pour différentes conditions expérimentales.



(a) Débit d'eau 1 m/s à 15 °C



(b) Amplitude d'excitation 4 mm à 15 °C



(c) Amplitude d'excitation 3 mm à 15 °C et 30 °C

FIGURE 4 – Relation force-déplacement pour des expériences d'excitation quasi statique

Les figures 4a, 4b et 4c représentent un modèle d'hystérésis typique. L'effort requis pour déplacer l'assemblage combustible dans une direction n'est pas le même lorsque le même assemblage combustible est déplacé dans la direction opposée. Cette hystérésis est principalement due à la présence des grilles de support, qui comportent plusieurs ressorts et alvéoles pour retenir les tiges en introduisant des forces de friction importantes. Le comportement d'hystérésis devient d'autant plus important que l'amplitude de l'excitation augmente (Figure 4a). L'hystérésis est en fait un comportement non linéaire qui est amplifié par des déplacements de grande amplitude.

La connaissance de la relation de déplacement de force permet également de connaître la rigidité de la structure. La raideur est en fait donnée par le rapport entre la force nécessaire pour déplacer le corps et le déplacement lui-même. La rigidité des assemblages combustibles, est affectée par le débit d'eau. Lorsque le débit augmente, la pente du tracé de déplacement de force augmente également, ce qui signifie que le débit induit une rigidité

supplémentaire sur l'assemblage de combustible. Ce phénomène de raideur est déjà connu dans la littérature et confirmé par les expériences (Ricciardi et al., 2009; Boccaccio, 2010). En revanche l'augmentation de la température de l'eau semble avoir un effet opposé.

L'analyse quasi statique a permis, grâce à des expériences simples et rapides, de cerner le comportement d'une des propriétés principales d'un assemblage combustible (la rigidité) et de souligner la présence de fortes non-linéarités sur la plateforme expérimentale ICARE, principalement en raison de la présence des grilles de support.

Les tests dynamiques sont effectués en excitant l'assemblage de combustible sur une plage de fréquences allant de 0 Hz à 25 Hz . La réponse de l'assemblage de combustible excité (capteurs de force et de position) et de ceux non excités (capteurs de position uniquement) est acquise à un taux d'échantillonnage de 2000 Hz (pour capturer les composants rapides). Les données collectées sont traitées au moyen de fonctions de transfert et analysées dans l'espace de Fourier. Les fonctions de transfert entre le déplacement et la force sur l'ensemble excité donnent des informations sur le comportement dynamique de la structure. Les pics représentent les fréquences de résonance, le départ de la courbe représente l'inverse de la rigidité et la largeur et l'intensité des pics de résonance représentent l'amortissement de la structure.

L'amortissement du système semble diminuer avec l'augmentation de l'amplitude d'excitation (les pics deviennent de plus en plus étroit) et la rigidité diminue (les pics se déplacent légèrement vers les basses fréquences). Les fréquences de résonance diminuent légèrement avec l'augmentation de l'amplitude d'excitation.

L'intensité du débit d'eau joue également un rôle très important dans la définition du comportement dynamique de l'assemblage de combustible. L'un des effets les plus importants et les plus évidents de la présence d'eau dans la section de test est un fort décalage des fréquences de résonance. La présence d'eau réduit fortement les fréquences auxquelles les résonances se produisent. La rigidité du système augmente également avec l'augmentation du débit d'eau. Plus l'eau coule rapidement autour de l'assemblage combustible, plus l'eau s'opposera au mouvement de l'assemblage proprement dit. Cette opposition au mouvement de l'assemblage combustible entraîne une augmentation de la rigidité de l'assemblage.

La taille de confinement détermine la quantité d'eau qui reste dans l'espace entre l'assemblage de combustible et les parois de la section d'essai. On suppose donc que cet intervalle joue un rôle dans le comportement dynamique de l'assemblage combustible immergé dans l'eau (eau stagnante ou courante). Bien entendu, la taille du confinement ne devrait jouer aucun rôle dans le comportement dynamique de l'assemblage de combustible "dans l'air".

La présence de 2 ou 4 assemblages de combustible n'affecte pas de manière sensible le comportement dynamique de l'assemblage de combustible excité, tant pour les petits confinements que pour les grands confinements. Quelques différences peuvent être observées sur le deuxième mode de vibration qui semble être atténué lorsque les 4 assemblages de combustible sont pris en compte. Néanmoins, il est utile de pouvoir comparer des essais expérimentaux avec 2 et 4 assemblages de combustible en ce qui concerne les effets de cou-

RESUME ETENDU

plage. On peut s'attendre, en effet, à ce que la configuration à 4 assemblages combustibles permette d'étudier les phénomènes de couplage existant dans le plan d'excitation et hors du plan d'excitation.

Les effets de la température de l'eau sont résolus en effectuant des expériences à deux températures différentes : $15\text{ }^{\circ}\text{C}$ et $30\text{ }^{\circ}\text{C}$. Les fonctions de transfert de l'assemblage de combustible excité semblent augmenter considérablement (environ 20%) en amplitude lorsque la température de l'eau augmente. Lorsque le débit d'eau augmente, les effets de la température deviennent de moins en moins importants.

Les paramètres de la fonction de transfert analytique (masse, rigidité, amortissement et fréquence de résonance) sont estimés à partir des courbes expérimentales.

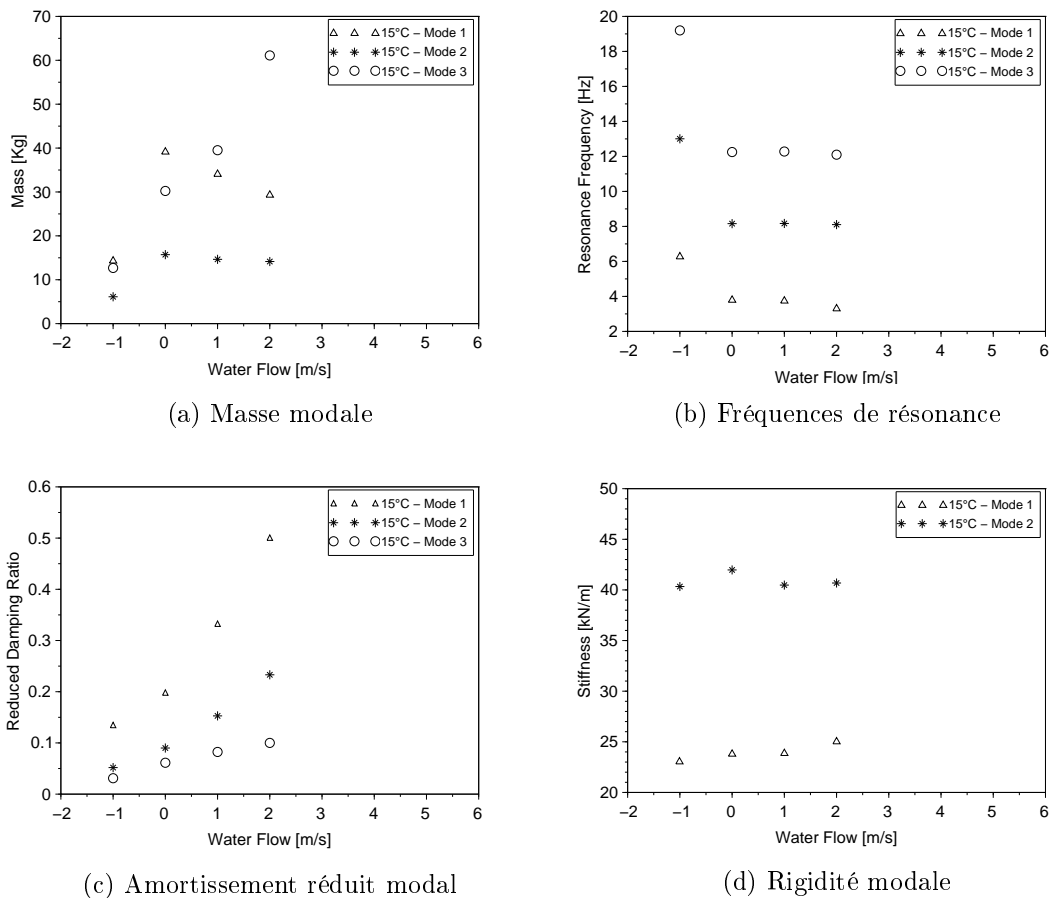


FIGURE 5 – Comportement des paramètres dynamiques estimés en fonction des débits d'eau pour les trois premiers modes avec amplitude d'excitation 0.5 mm à $15\text{ }^{\circ}\text{C}$ avec 2 assemblages en confinement grand. Débit -1 m/s veut dire "Dans l'air"

La figure 5 présente le comportement général des principaux paramètres dynamiques de l'assemblage de combustible excité. Les fréquences modales de masse, d'amortissement, de rigidité et de résonance sont identifiées pour les trois premiers modes naturels. Avec notre assemblage de carburant instrumenté qui a des capteurs dans trois emplacements verticaux différents, nous ne sommes pas en mesure d'identifier des modes plus élevés que

le troisième.

Les paramètres modaux de l'assemblage "In Air" sont identifiés et représentent les valeurs de référence. La première masse modale (Figure 5a) augmente de manière constante des conditions "en l'air" à l'eau stagnante (elle devient environ trois fois plus grande). Ensuite, lorsque le débit augmente, il diminue légèrement. Ce comportement décroissant est également identifié par Ricciardi (2016) et Boccaccio (2010) et semble avoir un comportement asymptotique. D'autre part, la deuxième masse modale semble augmenter continuellement lorsque le débit d'eau augmente. La différence entre la masse modale de l'assemblage combustible immergé dans l'eau et la masse modale de l'assemblage combustible dans l'air donne le coefficient de masse ajouté. Ainsi, le coefficient de masse ajouté pour le premier mode diminue avec le débit d'eau.

Les fréquences de résonance (Figure 5b) présentent le même comportement pour les trois modes : elles diminuent brusquement lorsque vous passez de l'état "Dans l'air" à l'eau stagnante, puis elles diminuent légèrement à mesure que le débit d'eau s'écoule augmente. L'important changement de fréquence de résonance est principalement dû aux changements de masse modale.

Le taux d'amortissement (Figure 5c) montre une tendance à la hausse continue et presque linéaire à mesure que le débit d'eau augmente. Le taux d'amortissement réduit change de manière très significative, il double en passant de l'état "En Air" à un débit d'eau de 2 m/s.

La rigidité (Figure 5d) augmente également avec l'augmentation du débit. L'effet du débit d'eau, augmentant la rigidité de l'assemblage, était déjà esquissé par une analyse quasi statique. Les coefficients de rigidité pour le troisième mode naturel ne sont pas représentés dans la figure 5d pour de meilleurs résultats visuels (hors échelle).

Enfin, les déplacements induits sur les assemblages combustibles non excités sont étudiés. La présence d'eau (stagnante ou ruisselante) induit une force sur les ensembles qui ne sont pas excités par le vérin hydraulique externe. La force induite provoque un mouvement induit des assemblages. La magnitude du mouvement induit est utilisée pour estimer la magnitude du couplage existant entre les différents assemblages et dans les différentes directions. Comme on pouvait s'y attendre, le couplage le plus efficace se produit entre l'ensemble excité et celui opposé (ensemble n° 2) dans le même sens de l'excitation. Le couplage dépend fortement des débits d'eau et augmente à mesure que le débit augmente. Le mouvement induit sur l'assemblage de combustible autrement au repos peut atteindre des valeurs supérieures à 40% du déplacement externe imposé.

Modèle d'Interaction Fluide Structure

Afin de mieux comprendre la nature profonde de l'interaction fluide-structure et l'influence de différents paramètres (c'est-à-dire la vitesse d'écoulement et la taille de confinement), il a été décidé de construire un modèle simplifié permettant des calculs rapides. Afin de simplifier la modélisation des forces du fluide, le modèle d'écoulement potentiel est consi-

RESUME ETENDU

déré, le cylindre est représenté par un faisceau d'Euler-Bernoulli et les effets de viscosité sont négligés.

Premièrement, le modèle est développé pour un seul cylindre sous écoulement axial dans la Section 3.1. Le modèle monocylindre est ensuite utilisé pour la comparaison avec les résultats de la littérature et des calculs sont effectués afin d'analyser les effets du confinement sur le comportement d'un cylindre sous flux axial (voir la section 4) dans la Section 3.2. Enfin, le modèle est étendu dans la Section 3.3 pour les géométries à plusieurs cylindres (2 et 4 cylindres) qui seront utilisées pour une analyse des effets des symétries. Dans cette section, le modèle est également mis à niveau afin de représenter l'installation expérimentale ICARE composée de 4 assemblages de combustible (réseau 8×8).

Un cylindre serré-serré de longueur L et de rayon R est considéré. Le cylindre est immergé dans un écoulement axial uniforme et constant avec la vitesse U et délimité dans les directions x et y par des parois rigides situées respectivement aux distances L_x et L_y . Le cylindre est considéré comme déviant dans la direction y et la déviation du cylindre est appelée $w(z, t)$. La théorie du faisceau d'Euler-Bernoulli est utilisée pour modéliser la déflexion des cylindres. La déviation du cylindre est donc régie par l'équation linéaire du faisceau d'Euler-Bernoulli :

$$m \frac{d^2 w(z, t)}{dt^2} + EI \frac{d^4 w(z, t)}{dz^4} = f^y(z, t) \quad , \quad (3)$$

où m est la masse par unité de longueur, E est le module de Young et $I = \frac{1}{4}\pi R^4$ est le deuxième moment d'aire du cylindre. f^y est la résultante des forces d'interaction entre le liquide et la structure dans la direction y .

La modélisation des fluides introduit une simplification : le flux est supposé être potentiel. Cette hypothèse semble raisonnable si nous considérons que le débit (dans des conditions types de REP) a un grand nombre de Reynolds. Dans la dynamique des fluides, la théorie des écoulements potentiels suppose que le débit du fluide est invisible et irrotationnel.

Le problème fluide se réduit à la résolution d'un problème de Laplace ($\Delta\phi = 0$). La dernière étape consiste à déterminer les conditions aux limites, qui sont données par la condition d'imperméabilité (le fluide a la même vitesse normale que la structure), aussi bien sur les parois que sur la surface du cylindre, en obtenant :

$$\Delta \hat{\phi} = 0, \quad (4)$$

$$\left[\frac{\partial \hat{\phi}}{\partial \hat{y}} \right]_{|\hat{y}|=\hat{l}_y} = 0, \quad (5)$$

$$\left[\frac{\partial \hat{\phi}}{\partial \hat{x}} \right]_{|\hat{x}|=\hat{l}_x} = 0, \quad (6)$$

$$\left[\frac{\partial \hat{\phi}}{\partial \hat{n}} \right]_{\hat{r}=\hat{R}} = (\partial_{\hat{t}} + \partial_{\hat{z}}) \hat{w}(\hat{z}, \hat{t}) \sin \theta \quad . \quad (7)$$

Afin d'étudier les interactions fluide-structure, le modèle de structure et le modèle de fluide doivent être couplés ensemble. Le couplage entre les deux modèles est dû à deux termes : le terme de forçage dans le modèle de structure ($\hat{f}^y(\hat{z}, \hat{t})$) et le terme de déplacement ($\hat{w}(\hat{z}, \hat{t})$). Les deux termes sont en fait présents à la fois dans l'équation de structure et dans les équations de fluide. Dans les équations du fluide, le terme de force n'apparaît pas directement, mais il existe la présence du terme de pression. Comme le terme de pression est directement lié au terme de forçage sur le cylindre, le terme de force apparaît indirectement dans les équations du fluide.

Afin de résoudre les équations précédentes, nous avons utilisé la même approche que celle proposée par [Doaré et al. \(2011b\)](#). La composante z du champ de pression est exprimée dans l'espace de Fourier. Cette approche nous permet de passer d'un problème 3D à un problème paramétrique 2D (le paramètre est le nombre d'onde sans dimension \hat{k}) : les calculs numériques sont plus rapides et plus simples.

La réalisation la plus importante de l'application de la théorie des écoulements potentiels est exprimée par l'équation suivante :

$$\frac{1}{2\pi} \int_0^1 \frac{\partial \hat{f}^y(\hat{\zeta}, \hat{t})}{\partial \hat{\zeta}} \hat{G}(\hat{z} - \hat{\zeta}; \hat{R}, \hat{l}_x, \hat{l}_y) d\hat{\zeta} = (\partial_{\hat{t}} + \partial_{\hat{z}})^2 \hat{w}(\hat{z}, \hat{t}) \quad . \quad (8)$$

En fait, la force d'interaction de la structure fluide peut être écrite en fonction du déplacement de la structure elle-même.

La fonction $\tilde{g}(\tilde{k}; \tilde{h}_x, \tilde{h}_y)$, qui peut être facilement calculée en résolvant un problème de Helmholtz, représente la solution élémentaire pour une frontière unitaire. Compte tenu de la linéarité du problème, la solution élémentaire revêt une extrême importance puisque toutes les solutions possibles peuvent être écrites en fonction d'elle grâce au principe de superposition.

Le modèle établi pour un seul cylindre est ensuite adapté pour être utilisé dans une configuration à plusieurs cylindres, qui représente la géométrie des assemblages de combustible de l'installation expérimentale ICARE et qui sera utilisée ultérieurement pour valider le modèle avec des données expérimentales.

Quatre géométries différentes sont construites, en tenant compte des quatre configura-

tions différentes utilisées lors des campagnes expérimentales (assemblages 2 et 4, confinement petit et grand). Certaines hypothèses sont faites dans la modélisation de ces géométries :

- les grilles d'espacement sont négligées ;
- tous les cylindres d'une même grappe de combustible sont supposés se déplacer ensemble et exactement de la même manière ;
- un seul des assemblages est excité à la fois ;
- la présence de quatre tubes guides dans chaque assemblage est négligée ;
- les conditions aux limites sont considérées comme des conditions aux limites parfaitement serrées ;
- les ensembles sont numérotés dans le sens des aiguilles d'une montre à partir de celui excité (celui représenté en rouge).

Calculs Numériques

Pour résoudre les équations aux dérivées partielles impliquées dans le problème des interactions structure-fluide, le logiciel FreeFem ++ a été utilisé. Pour plus de détails, le lecteur est adressé à [Hecht \(2012a,b\)](#).

Dans cette section, la résolution numérique du problème de Helmholtz sera présentée. L'objectif est de calculer la valeur de la fonction $\tilde{g}(\tilde{k}; \tilde{h}_x, \tilde{h}_y)$ pour différentes valeurs de \tilde{k} , \tilde{h}_x et \tilde{h}_y . Grâce aux symétries du problème, les équations ne sont résolues que sur un quart du domaine, ce qui permet des calculs plus rapides. Avant de commencer ces derniers, il convient de prendre en compte la discrétisation du domaine. Une étude de convergence a été réalisée afin de trouver le maillage optimal pour différentes combinaisons de taille de confinement et de nombre d'onde. Typiquement, la taille des mailles doit être diminuée si l'on veut augmenter le nombre d'onde \tilde{k} . De plus, le raffinement des mailles augmentera à mesure que la taille du confinement diminue.

Premièrement, une étude de validation du modèle et des calculs effectués a été réalisée. Dans la littérature ([Lighthill, 1960a,b](#)), il est connu que, dans le cas d'un corps mince soumis à un écoulement axial non confiné, il existe une formulation analytique pour la force d'interaction. Ainsi, des calculs sont effectués pour certaines configurations correspondant aux hypothèses du modèle formulé par [Lighthill \(1960a\)](#). L'hypothèse du flux non confiné est remplie en utilisant une taille de confinement dans les directions x et y plus grandes que 1 diamètre de la tige. L'hypothèse d'un corps élancé est réalisée à l'aide de nombres d'onde inférieurs à 1 ; cela signifie que nous ne considérons que les oscillations à faibles modes.

Les résultats obtenus avec le modèle pour les nombres d'ondes de petite taille et la grande taille de confinement pour la force d'interaction fluide-structure correspondent parfaitement à l'expression formulée par Lighthill sous les hypothèses de la théorie du corps

élancé. L'accord entre nos résultats numériques et les travaux de la littérature peut être considéré comme une preuve que la méthode mise en œuvre pour résoudre les équations de fluide est fondée et cohérente.

Des calculs numériques supplémentaires ont été effectués pour évaluer qualitativement les effets de la taille du confinement sur la fonction $\tilde{g}(\tilde{k}, \tilde{h}_x, \tilde{h}_y)$, donc sur le coefficient de masse ajouté. Deux cas extrêmes ont été analysés : le premier concernant les très faibles nombres d'ondes ($\tilde{k} \approx 10^{-2}$) et le second concernant les nombres d'ondes importants ($\tilde{k} \approx 10$). Pour les petits nombres d'onde, seule la taille de l'emprisonnement dans la direction x affecte la fonction \tilde{g} (l'isolement dans la direction y ne joue aucun rôle fondamental). Pour les nombres d'ondes importants, au contraire, nous arrivons à la conclusion opposée : la masse ajoutée dépend fortement du confinement y direction. Pour les nombres d'ondes situés entre les deux cas extrêmes, un comportement différent a été constaté : \tilde{g} dépend à la fois des confinements x et y direction. L'analyse du champ de vitesse a permis de comprendre un tel comportement. Pour les nombres d'ondes faibles (correspondant à un cylindre se déplaçant avec une grande longueur d'onde), un fort écoulement dans la direction y (opposé au déplacement du cylindre) a été observé le long de la ligne frontière $y = 0$. Cependant, pour les nombres d'ondes importants, aucun flux n'a été observé sur la limite $y = 0$. Comme le confinement dans la direction x modifie directement la dimension de la limite $y = 0$, nous pouvons maintenant comprendre la forte dépendance de la force d'interaction fluide-structure sur les confinements dans la direction x pour les nombres d'ondes faibles.

Enfin, pour tout nombre d'onde pris en compte et pour toute taille de confinement, la fonction \tilde{g} (donc le double du coefficient de masse ajouté) semble augmenter lorsque la taille de confinement diminue (dans les deux sens). Cette observation est en accord avec la littérature sur les flux de canaux réalisée par [Chen and Wamnganss \(1972\)](#); [Chen \(1985\)](#); [Païdoussis and Pettigrew \(1979\)](#).

Les calculs numériques pour les cylindres deux et quatre permettent de prendre en compte d'importantes considérations sur la nature des forces d'interaction. Lorsque plusieurs simulations sont prises en compte pour les simulations, il est en fait possible d'évaluer l'effet de l'excitation d'un cylindre sur les autres. La perturbation du champ de pression due au mouvement du cylindre excité dépend fortement du nombre d'onde. En fait, lorsque le nombre d'onde devient plus petit, cela signifie que la forme de déformation du cylindre devient sinusoïdale avec une grande longueur d'onde. Un autre effet qui peut être étudié lorsque deux cylindres différents sont simulés est l'effet de la disposition des cylindres. Les calculs pour trois arrangements différents sont effectués. On peut voir que tant qu'il existe une symétrie axiale entre les positions des deux cylindres, le champ de pression est symétrique par rapport aux axes y de chaque cylindre, ce qui signifie qu'aucun effort n'est induit sur la direction orthogonale à la direction d'excitation. (Pour rappel, le cylindre de gauche est excité dans la direction y). Lorsque les deux cylindres perdent leur positionnement symétrique, le champ de pression induit autour des deux cylindres perd toute sorte de symétrie. Un effort orthogonal apparaît sur le cylindre excité et un effort dans les deux sens

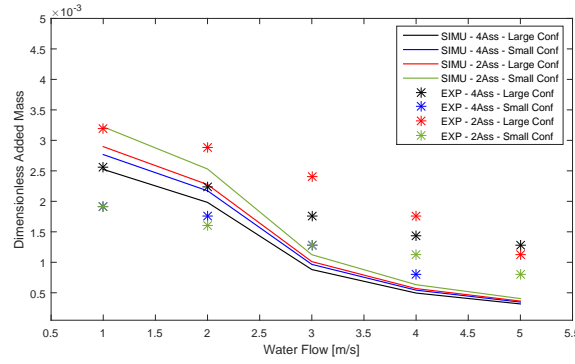
RESUME ETENDU

est induit dans le second cylindre. Plus en détail, l'effort induit sur le deuxième cylindre semble avoir le même ordre de grandeur dans les deux sens. Ce résultat est important pour les applications pratiques, car cela signifie que la perturbation appliquée à une structure peut se propager dans toutes les directions, et pas seulement dans la direction d'excitation. De plus, le phénomène décrit ci-dessus ne dépend ni du nombre d'onde ni de la taille du confinement, il se produit dans toutes les situations.

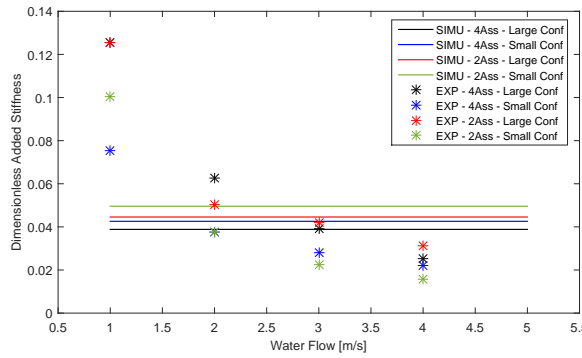
Des calculs sont également effectués pour un arrangement d'assemblages de combustible dans un réseau carré. Quatre assemblages combustibles sont considérés. L'excitation de l'un des quatre cylindres induit des efforts, donc du mouvement, sur les quatre cylindres présents dans la section, à la fois dans le sens de l'excitation et dans le sens orthogonal. Ce phénomène a déjà été observé expérimentalement par [Clement \(2014\)](#) et [Boccaccio \(2014\)](#). Différents calculs sont effectués pour augmenter le nombre d'ondes pour augmenter les modes naturels. Les tailles de cylindre considérées pour les calculs ont un rapport très élevé entre la longueur et les diamètres, ce qui donne aux premiers modes un très petit nombre d'onde. Le comportement de la fonction \tilde{g} , liée aux forces de couplage, est analysé. Pour les modes naturels faibles, \tilde{g} augmente avec l'augmentation des modes naturels, alors qu'il commence à diminuer lorsque les modes naturels dépassent un certain seuil. L'explication de ce comportement peut être trouvée en analysant deux facteurs différents : le champ de pression et la définition de la fonction \tilde{g} elle-même. On peut voir que le champ de pression de perturbation reste presque constant pour les premières modes naturels et qu'il montre une réduction importante lorsque des modes naturels supérieurs au centième sont pris en compte. Sur la taille opposée, le comportement de la fonction \tilde{g} tend à augmenter avec le nombre d'onde, car il est proportionnel au nombre d'onde \tilde{k} . Ainsi, deux tendances concurrentielles sont présentes. Pour les modes bas, les forces de couplage augmentent, alors qu'elles commencent à diminuer après un certain seuil qui dépend définitivement de la configuration géométrique. D'un point de vue physique, deux phénomènes différents sont impliqués. Les forces de couplage augmentent en raison des formes de mode croissantes car la pente de la déformation du cylindre devient plus importante lorsque les modes les plus élevés sont excités. Cependant, la propagation des perturbations sur les autres cylindres est plus efficace pour les formes de mode de petite taille (idéalement, le moyen le plus efficace de propager une perturbation consiste à déplacer la tige en tant que corps rigide). Les forces d'inertie sont responsables de la perturbation croissante due à l'augmentation du nombre d'onde, alors que les dissipations visqueuses sont responsables de la perte d'efficacité dans la propagation de perturbation pour les modes élevés. La force induite a toujours un comportement croissant. Ceci est raisonnable, car il n'y a pas de propagation de la perturbation. Le point de seuil où la force induite sur le cylindre non excité commence à diminuer, pour la configuration étudiée est $\tilde{k} \approx 0.8$, représentant approximativement le millièm mode du cylindre. Cela signifie que pour nos applications pratiques, on peut considérer que les forces de couplage augmentent avec les modes naturels excités.

Enfin, des calculs numériques sont effectués afin de simuler la même géométrie de la configuration expérimentale ICARE. Quatre configurations différentes sont ainsi mises en

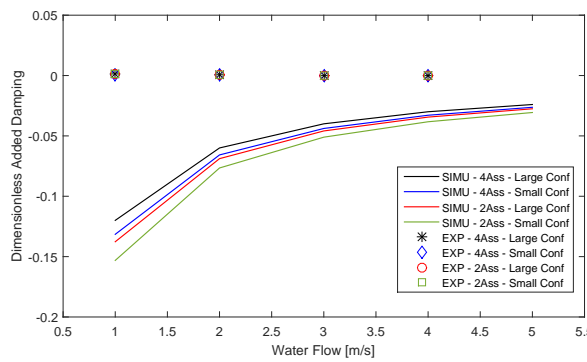
oeuvre dans le code : deux et quatre assemblages de combustible dans un confinement petit (4 mm) et grand (8 mm). Les excitations des trois premiers modes naturels sont simulées, correspondant aux nombres d'ondes sans dimension : $\tilde{k} = 0.0009$, $\tilde{k} = 0.0018$ et $\tilde{k} = 0.0027$. Des fonctions globales \tilde{G} sont calculées pour chaque assemblage à la fois dans x et y direction.



(a) Masse ajoutée adimensionnelle



(b) Raideur adimensionnelle



(c) Ammortissement adimensionnelle

FIGURE 6 – Paramètres de masse, de rigidité et d'amortissement ajoutées en fonction du débit d'eau, données expérimentales VS simulées

Le calcul effectué avec le modèle de flux de potentiel mis en œuvre permet également d'étudier l'effet du débit d'eau sur les paramètres dynamiques. L'effet du débit d'eau sur les paramètres dynamiques du système (masse ajoutée, amortissement ajouté, rigidité ajou-

RESUME ETENDU

tée) est analysé pour les quatre configurations implémentées. Les données simulées sont comparées aux données expérimentales. La figure 6a montre le comportement du coefficient de masse ajouté en fonction du débit d'eau. Les données simulées pour différentes tailles de confinement montrent un comportement très similaire. Le coefficient de masse ajouté semble diminuer avec l'augmentation du débit d'eau. Les données expérimentales et numériques montrent une tendance similaire en diminution par rapport au débit. Quoiqu'il en soit, pour des débits importants, les données numériques cherchent à sous-estimer le coefficient de masse ajouté. Cela pourrait être dû à un comportement non linéaire de l'assemblage combustible, mais il est également important de considérer que, pour les grands débits, les fonctions de transfert deviennent de plus en plus amorties, de sorte que l'estimation du paramètre devienne moins fiable. Le coefficient de rigidité ajoutée simulé sans dimension, ne montre aucune dépendance du débit (voir la Figure 6b). Puisque le processus de dimensionnalisation implique la division par le carré de la vitesse d'écoulement, le fait d'avoir une rigidité sans dimension constante signifie que la rigidité augmente proportionnellement au carré de la vitesse d'écoulement. Les données expérimentales et numériques ont le même ordre de grandeur, mais le modèle semble sous-estimer l'effet de raideur ajoutée pour les petits débits et surestimer celui-ci pour les grands. La surestimation du coefficient d'amortissement pourrait être due à la négligence des forces visqueuses, ce qui entraîne la diminution du coefficient de rigidité ajoutée pour des débits élevés. Enfin, les coefficients d'amortissement ajoutés y sont représentés dans la figure 6c. Comme prévu, les calculs ne correspondent pas à toutes les données expérimentales. En fait, la théorie de l'écoulement potentiel ne prend en compte aucune des forces visqueuses, qui sont les principales responsables de l'amortissement. Les effets de différentes tailles de confinement sur les données expérimentales ne concordent pas avec les données simulées. Cette incohérence n'est pas due au modèle, mais à certains biais expérimentaux. Comme indiqué au chapitre 2, en fait, lorsque la taille de confinement est modifiée dans le montage expérimental, le point d'excitation est modifié, ce qui entraîne une légère modification de la réponse mécanique de l'ensemble en raison de non-linéarités. L'amplitude d'excitation et la température de l'eau n'affectent en aucune manière les calculs. Toute considération à ce sujet est donc inutile.

Le couplage entre l'assemblage de combustible excité et non excité est également analysé. Les rapports entre la force induite sur l'ensemble 2 et la force induite sur l'ensemble 1 sont étudiés. Le couplage entre les deux assemblages est de l'ordre de 6% pour un petit confinement et il diminue à environ 1% lorsque la taille du confinement augmente. De petites différences peuvent être observées entre deux et quatre configurations d'assemblages. Ces résultats numériques sous-estiment considérablement le couplage expérimental mesuré entre l'assemblage 1 et l'assemblage 2. Les valeurs expérimentales pour le couplage sont d'environ 20% aux fréquences de résonance dans un confinement réduit et sont réduites à environ 10% quand la taille du confinement est augmentée. Ainsi, le modèle est capable de prédire qualitativement l'effet de la taille de confinement sur le couplage, mais n'est pas précis d'un point de vue quantitatif. Probablement que la force visqueuse joue un rôle très important sur le couplage dans la direction excitée, elle devrait donc expliquer les écarts

entre les résultats numériques et expérimentaux. Le couplage sur la direction orthogonale à l'excitation est également étudié. Aucun accouplement n'est visible entre les assemblages de combustible 1 et 2 dans la direction y . La même observation peut être faite pour les résultats expérimentaux. Enfin, l'analyse du couplage entre l'assemblage 1 et l'assemblage 4 est effectuée. Le couplage sur la direction excitée entre les assemblages 1 et 4 (l'assemblage 4 est situé dans le coin supérieur droit) s'avère être d'environ 20%. Deux remarques importantes doivent être faites sur cette observation : premièrement, le couplage entre les deux ensembles qui ne sont pas orientés dans le sens d'excitation est plus important que le couplage des ensembles 1 et 2 ; deuxièmement, la valeur numérique correspond parfaitement aux valeurs expérimentales pour le couplage entre les ensembles 1 et 4. Le modèle linéaire mis en œuvre et utilisé pour effectuer les calculs tenant principalement compte des forces d'inertie, ce résultat démontre que les forces d'inertie sont plus susceptibles d'agir sur des assemblages côte à côte et dont l'accouplement existant dans le sens de l'excitation peut ne pas être dû à des forces d'inertie. Un couplage moindre mais considérable est également observé entre les assemblages combustibles 1 et 4 dans la direction orthogonale à l'excitation (environ 5%).

En conclusion, le modèle simple développé prédit qualitativement les résultats expérimentaux et, pour certaines quantités (masse ajoutée et couplage), il est également capable de fournir des prédictions précises. Il échoue complètement, comme prévu sur le coefficient d'amortissement.

Expériences à GWU et Analyse Physique

Au cours de ma thèse, j'ai passé deux mois au laboratoire de thermo-fluides (TFL) de l'Université George Washington (GWU). Dans cette section, le travail effectué au cours de ces deux mois de collaboration sera présenté. Une installation expérimentale a été construite à cet endroit, à certains égards similaire et complémentaire à l'installation expérimentale ICARE. Il consiste en une assemblage combustible de substitution (6×6) sous flux axial déposée sur une table à secousses. Une fois que la table à secousses est en action, les déplacements du faisceau et le flux de fluide sont mesurés par des techniques de PIV (vélocimétrie par image de particules). Les principales différences avec l'installation ICARE consistent en la présence de la table à secousses (qui excite toute la structure) et en l'utilisation du fluide en écoulement, qui correspond aux grappes de combustible, donnant ainsi la possibilité d'accéder aux données de vélocimétrie sur l'ensemble du domaine fluide (même derrière et entre les tiges). La configuration expérimentale sera décrite plus en détail dans la section suivante. Les travaux menés dans le cadre de cette collaboration consistent en l'analyse de certains données mesurées lors des campagnes expérimentales de 2015 dans le but d'expliquer certains des phénomènes décrits à l'aide du modèle de flux potentiel développé précédemment. La nouvelle configuration expérimentale est implémentée dans le code FreeFem ++ et des simulations sont effectuées afin de comparer les résultats expérimentaux et numériques.

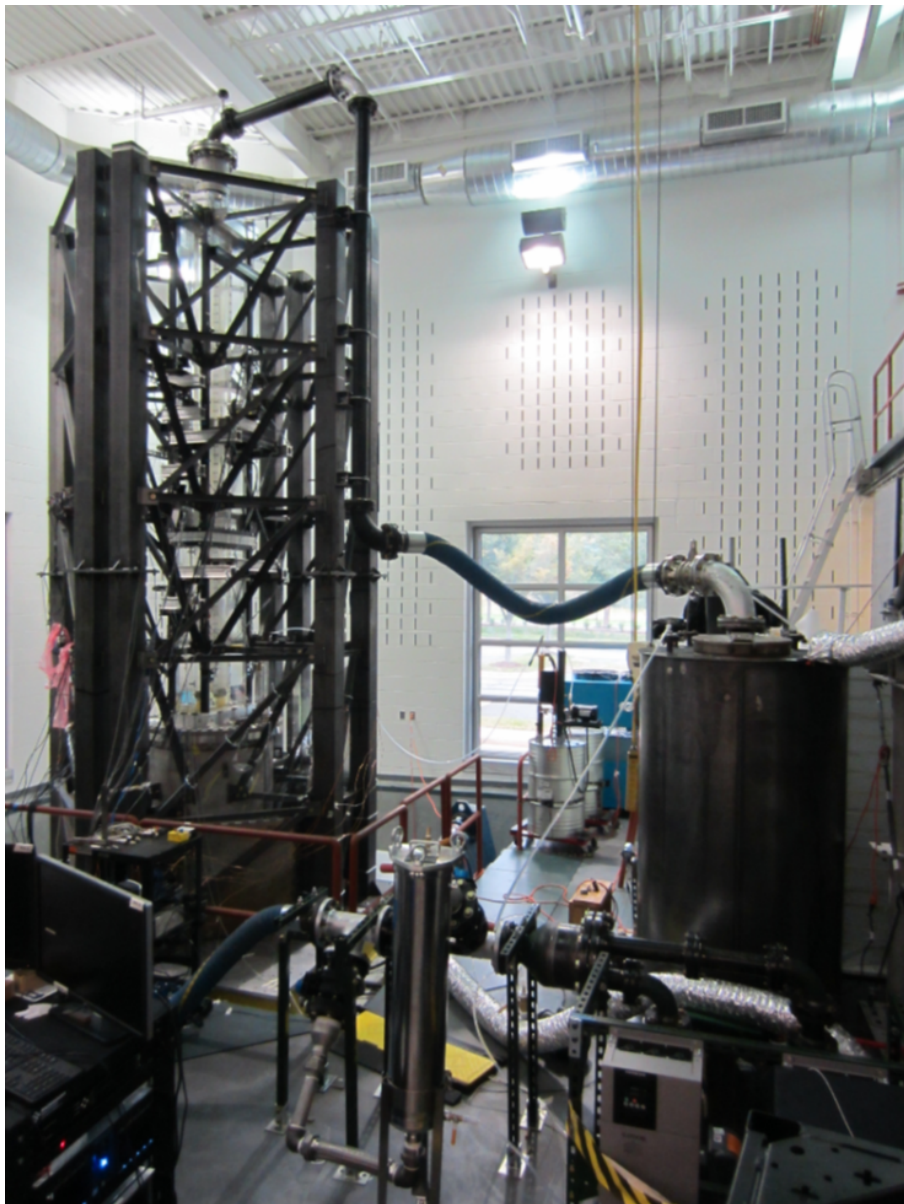


FIGURE 7 – Vue de l'installation expérimentale (Weichselbaum, 2015)

L'installation expérimentale installée à GWU consiste en un canal vertical monté sur une table à secousses et contenant un seul assemblage de combustible nucléaire à échelle réduite, comme représentée dans la figure 7. Elle est décrite en détail par Weichselbaum (2015); Weichselbaum et al. (2015) et Hussain (2017).

Après quelques essais sur l'installation expérimentale réalisés en 2014, plusieurs campagnes ont été réalisées en 2015 avec différents fluides (eau et para-cymène) et avec différents paramètres d'excitation. Une liste complète des campagnes expérimentales peut être trouvée dans Weichselbaum (2015). Quelques travaux préliminaires sur le post-traitement des données expérimentales sont discutés dans Weichselbaum (2015); Weichselbaum et al. (2015) et (Hussain, 2017). Il a été constaté que l'installation expérimentale fonctionne comme prévu et que toutes les techniques de mesure étaient cohérentes, donnant des ré-

sultats utiles pour les interprétations physiques.

En approfondissant l'analyse des données, nous avons étudié la répétabilité des expériences. Trois ensembles de données différents ont été analysés, tous ayant les mêmes paramètres d'entrée. La table à secousses est excitée à 1.3 Hz avec une amplitude de 3 mm . La fréquence de 1.3 Hz a été choisie car elle est supposée être assez importante, car elle est très proche de la première fréquence de résonance de la structure. Nous ferons référence à l'arborescence des différents ensembles de données en tant que "Case 1", "Case 2" et "Case 3"; les détails de chaque expérience sont résumés dans le Tableau 2.

Nome ensemble données	Date	Amplitude d'excitation	Fréquence d'excitation
Case 1	13/08/2015	3 mm	1.3 Hz
Case 2	13/08/2015	3 mm	1.3 Hz
Case 3	18/09/2015	3 mm	1.3 Hz

TABLE 2 – Paramètres d'entrée pour chaque ensemble de données

Dès le premier coup d'oeil aux organigrammes 2D, il a été constaté que les trois ensembles de données présentent des comportements très différents, en particulier dans la composante axiale de la vitesse d'écoulement. Plus précisément, les "Case 1" et "Case 2", qui sont exécutés le même jour (une demi-heure de différence) semblent être les plus différents, alors que "Case 1" et "Case 3" semblent très similaires. Le résultat important est la non-cohérence entre le profil de vitesse axiale de "Case 1" et "Case 2", même si les profils de vitesse transversale sont pratiquement les mêmes. La présence de différents comportements sur les profils d'écoulement axial, donnée par une excitation ayant les mêmes paramètres d'entrée, mérite d'être étudiée plus en profondeur. Une vérification des systèmes de mesure et des paramètres d'entrée a été effectuée. Il semble qu'aucune erreur systématique ne puisse expliquer de telles observations.

Une première étape pour approfondir les recherches sur les différences de flux induit commence par l'analyse de l'excitation elle-même. Les capteurs de position 6 LVDT qui sont placés dans la table à secousses sont analysés dans le domaine temporel et dans le domaine spectral. L'objectif de cette analyse est de comprendre si l'excitation sismique qui est donnée à la structure est la même du point de vue énergétique et du point de vue de la fréquence. Dorénavant, seuls les deux ensembles de données "Case 1" et "Case 2" sont considérés, car ils semblent être les plus significatifs.

L'analyse des composantes spectrales de l'excitation ne révèle aucune différence notable entre les deux cas de la composante principale de l'excitation (direction y). Afin d'étudier plus avant la réponse expérimentale des deux cas de test décrits précédemment, une meilleure compréhension de la déformation du faisceau de substitution est nécessaire. La décomposition orthogonale (POD) est un outil très puissant pour étudier le comportement dynamique des systèmes mécaniques. Elle permet d'extraire les principaux modes

RESUME ETENDU

du système et d'évaluer l'énergie capturée par chaque mode (Berkooz et al., 1993; Feeny, 1997).

La technique POD est utilisée pour effectuer une décomposition orthogonale des modes de vibration de la grappe de combustible dans les conditions expérimentales "Cas 1" et "Cas 2". Dans les deux cas, le premier mode correspond au premier mode du faisceau de Bernoulli à clampage serré, tandis que les modes supérieurs présentent des formes différentes, qui ne sont pas directement reconnaissables comme exemples connus dans la littérature. Les valeurs de POV indiquent que la contribution du premier mode est deux fois plus importante que celle du second, tandis que les troisième et quatrième modes ont une intensité négligeable par rapport au premier. Les deux ensembles de données, qui ont les mêmes paramètres d'entrée, devraient présenter les mêmes modes orthogonaux corrects, mais les modes supérieurs au premier sont significativement différents. Il n'est pas facile d'expliquer la raison de ces différences. Une première hypothèse pourrait être que la table à secousses insère des fréquences différentes dans le processus d'excitation, mais cette analyse est exclue des analyses précédentes. Une deuxième hypothèse serait que les conditions de température pourraient avoir changé entre les deux expériences différentes, affectant les résultats de la campagne expérimentale.

Quoi qu'il en soit, les différences remarquées entre les modes propres orthogonaux des deux jeux de données sont très faibles en amplitude, car, comme nous l'avons déjà dit, les deuxième, troisième et quatrième modes n'affectent que 1% du comportement de la grappe de combustible. Il est donc difficile de croire que les schémas d'écoulement, qui sont très différents entre "Case 1" et "Case 2", sont justifiés par une aussi petite différence dans la dynamique des grappes de combustible. Afin de vérifier si une si petite perturbation des modes hauts de la structure peut affecter de manière très significative l'écoulement axial induit, le modèle d'écoulement potentiel développé au cours de la thèse est utilisé pour simuler la structure expérimentale subissant différents modèles de déformation. Étant donné que la simulation est réalisée à l'aide d'un modèle simplifié, la structure doit être modélisée avec des conditions aux limites Euler-Bernoulli simples. Puisque la forme du POD du premier mode semble symétrique, une première hypothèse a été d'utiliser une poutre de Bernoulli serrée. Ainsi, les calculs sont effectués en utilisant les formes du mode naturel et l'évolution temporelle de chaque mode a été calculée avec une "projection" sur les formes du mode naturel. Les différences les plus importantes sur le comportement dynamique entre les deux cas sont dans le déphasage entre les différents modes et dans l'amplitude de forme du mode 4th.

Le code d'éléments finis implémenté dans FreeFem ++, basé sur le modèle d'écoulement potentiel, est maintenant utilisé afin de simuler le comportement de l'écoulement de fluide autour du faisceau de combustible sous l'excitation horizontale appliquée par la table vibrante.

Étant donné que la mise en œuvre de la géométrie complète de l'installation GWU aurait nécessité un effort important, un premier exercice a été effectué afin de comprendre si l'effort en valait la peine. Ainsi, une seule géométrie de cylindre a été mise en œuvre et des calculs

sont effectués pour la simulation d'un cylindre déviant sous la forme d'une poutre d'Euler Bernoulli serrée. Les amplitudes de chaque mode sont considérées comme identiques. Ces calculs ont permis de comprendre l'importance de la forme de la flèche sur la perturbation de l'écoulement de l'eau. Les résultats montrent que le champ de vitesse axiale du fluide est plus important pour les modes plus élevés que pour les modes plus bas (avec la même amplitude de déformation). Cette observation peut être expliquée par les gradients sur la surface du cylindre. En fait, les modes les plus élevés impliquent une flexion plus importante de la structure et, comme l'amplitude doit être identique, cela signifie que le gradient vertical de la déviation de la structure ($\partial_z w$) est plus important pour les modes les plus élevés. Le gradient vertical de la déformation entraîne la perturbation du domaine fluide, exprimée par la condition d'imperméabilité. Ces observations conduisent à la conclusion que les déformations ayant des contributions de modes élevées perturbent le champ de vitesse de fluide axial de manière plus importante que les déformations avec uniquement des contributions de modes faibles. Par conséquent, pour l'application expérimentale du jeu de données GWU, cela signifie que les différences observées pour les modes 3rd et 4th (même si elles sont relativement petites) peuvent contribuer de manière significative à la perturbation de pression, autour du paquet. Après ces considérations, nous pouvons affirmer que l'effort de simuler le comportement de la grappe de combustible en vaut la peine, afin de comprendre les raisons pour lesquelles le champ de vitesse du fluide dans "Case 1" et "Case 2" présente des différences importantes, même s'il semble se déplacer d'une manière assez similaire. Seuls les calculs de vitesse axiale seront traités, car les profils transversaux semblent être similaires entre "Case 1" et "Case 2".

Enfin, la géométrie 3D de toute la structure du réservoir interne est implémentée dans le code. Les grilles d'espacement sont également implémentées, mais leur géométrie a été fortement simplifiée : les ressorts et les fossettes ne sont pas pris en compte dans le modèle. Les supports qui maintiennent les grilles (supérieure et inférieure) au réservoir sont également négligés. Ces simplifications sont considérées comme légitimes, car nous ne nous intéressons qu'au comportement du fluide, qui est principalement influencé par les surfaces en mouvement. Le comportement dynamique de la grappe de combustible est considéré comme un paramètre d'entrée pour nos calculs.

Le flux axial global est ensuite reconstruit pour les deux cas en prenant en compte les valeurs pour les amplitudes et le déphasage. Pour chaque cas, le tir temporel correspondant à l'amplitude maximale de la vitesse axiale (0.45 pour "Case 1" et 0.6 pour "Case 2") a été tracé. On peut remarquer que même si les amplitudes de la vitesse axiale champ sont assez similaires pour les deux cas de test (pour les quatre modes), le comportement global est fortement différent pour les deux cas. L'amplitude de la vitesse axiale est environ dix fois plus petite pour le "Case 2" que pour le "Case 1". ne peut pas être expliqué par la différence d'amplitude pour chaque mode, mais seulement par les effets cumulés de différents modes avec des déphasages différents. Dans un cas ("Case 1"), le déphasage de chaque mode donne lieu à une interaction constructive, alors que dans l'autre cas ("Case 2"), cela donne lieu à une interaction destructive. Cette observation est en accord avec les résultats

RESUME ETENDU

expérimentaux. On peut remarquer que l'amplitude de vitesse axiale expérimentale pour "Case 2" est beaucoup plus petite que celle pour "Case 1". Le rapport entre les deux profils de vitesse expérimentaux est d'environ 8. Les résultats numériques correspondent donc avec une bonne approximation aux résultats expérimentaux.

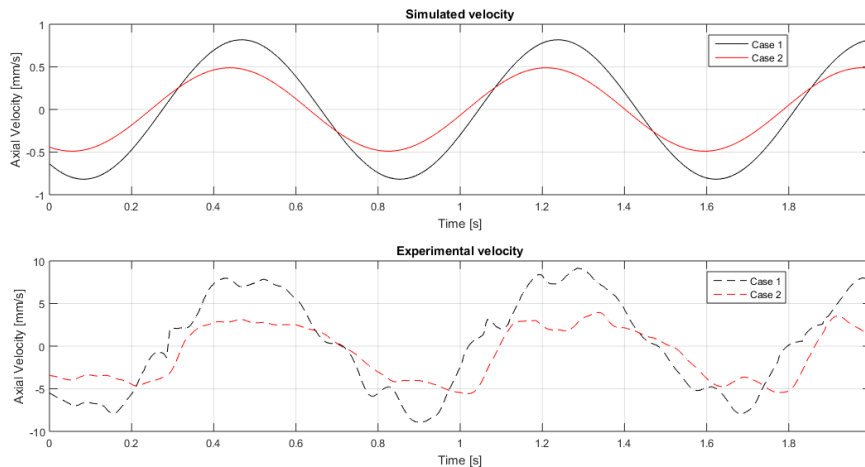


FIGURE 8 – Evolution temporelle des profils de vitesse axiale sur le point $x = 2200 \text{ mm}$, $y = 10 \text{ mm}$, $z = 33.5 \text{ mm}$ pour expérimental et numérique "Case 1" et "Case 2"

L'évolution temporelle des profils de vitesse axiale (numériques et expérimentaux) pour les deux cas est représentée dans la figure 8. Le rapport entre la vitesse axiale pour "Case 1" et "Case 2" est respecté, tandis que l'amplitude de la vitesse axiale est différente entre les données numériques et les données expérimentales. Ces calculs semblent indiquer la différence de débit axial mesurée qui n'était pas attendue. Les petites différences sur les formes de mode induisent des différences importantes dans le champ de vitesse axiale, et les différences sur le déphasage induisent des interactions très différentes entre les écoulements axiaux modaux, ce qui peut entraîner la complétion de différents champs de vitesse. Une enquête plus approfondie serait nécessaire pour comprendre les raisons de telles différences sur le déphasage. La sous-estimation des calculs numériques pour la vitesse axiale doit également être étudiée.

Une application du modèle d'interaction fluide-structure basée sur la théorie de l'écoulement potentiel a été présentée. Le modèle est utilisé pour simuler le comportement de l'installation expérimentale de GWU Thermo Fluid Lab. Les campagnes expérimentales sur cette maquette expérimentale ont donné des résultats inattendus sur la vitesse d'écoulement axiale mesurée pour deux expériences différentes avec les mêmes paramètres d'entrée. Le modèle est donc utilisé pour tenter d'expliquer les phénomènes observés. Une première analyse réalisée sur le POD de la grappe de combustible montre quelques différences sur le mode 4th, qui au début étaient considérées comme négligeables. Une fois les calculs effectués avec le modèle développé, les résultats montrent comment les modes les plus élevés sont ceux qui affectent le plus le champ de vitesse d'écoulement axial. Ce phénomène s'explique par une réflexion sur la forme des différents modes ; les modes les plus élevés ont

plus de flexion, ce qui signifie que la pente du déplacement dans la direction axiale est plus importante. Le gradient de déplacement induisant une perturbation de la pression autour de la structure, cela explique pourquoi les modes les plus élevés contribuent de manière plus significative au champ de vitesse axiale. Il reste à expliquer la raison pour laquelle la grappe de combustible se déplace de manière différente entre "Case 1" et "Case 2", étant donné que les paramètres d'entrée (excitation de la table à secousses) sont les mêmes. Un paramètre qui aurait pu affecter les mesures est la température. De plus, les hypothèses retenues pour la modélisation de la structure sont analysées. En première approximation, le faisceau est censé se comporter comme une poutre d'Euler Bernoulli serrée-serrée. Certaines analyses portant sur l'ensemble de la structure montrent que la structure externe affecte le comportement du faisceau et qu'il existe un décalage de phase entre le haut et le bas de la structure externe. Ainsi, il serait plus approprié de modéliser le faisceau en tant que structure sans pince (avec un déplacement imposé vers le haut). De plus, le déplacement relatif entre les parois du réservoir et le faisceau doit être pris en compte : même si le déplacement relatif est petit, les parois du réservoir sont solides et provoquent le déplacement de l'ensemble du fluide. Cela peut expliquer pourquoi le modèle sous-estime le flux axial. Des efforts devraient être déployés à l'avenir pour prendre en compte les considérations antérieures. D'autres simulations pourraient fournir de meilleures informations sur les phénomènes impliqués.

Conclusions et Perspectives

Les travaux présentés dans ce document représentent une contribution à l'étude du comportement vibratoire d'un assemblage de combustible REP. Deux approches principales ont été suivies au cours de cette thèse. Une approche de modélisation a conduit à l'élaboration d'un modèle simplifié pour les interactions de structure fluide dans l'assemblage de REP. Une approche expérimentale complémentaire a permis de réaliser plusieurs campagnes expérimentales sur l'installation expérimentale récemment conçue ICARE. Les deux approches sont considérées comme complémentaires puisque la modélisation nécessite des expériences pour les validations et que la démarche expérimentale nécessite une bonne modélisation afin de disposer d'une analyse solide des phénomènes observés.

La plupart des sujets traités dans ce travail de doctorat ont été introduits dans la revue bibliographique, y compris les modèles d'interaction de structure fluide pour des applications générales. Les modèles simplifiés ont été discutés en mettant l'accent sur leurs avantages de flexibilité et de temps de calcul réduit. De tels modèles simplifiés peuvent être utilisés pour des simulations paramétriques permettant d'effectuer une analyse de sensibilité sur différents paramètres, ce qui pourrait entraîner des calculs trop coûteux en utilisant des modèles complexes.

L'installation expérimentale ICARE pour l'étude des interactions entre la structure des fluides et les assemblages de combustible a été présentée après un bref examen des expériences antérieures dans ce domaine. Le système ICARE permet d'héberger jusqu'à

RESUME ETENDU

quatre assemblages de combustible (demi-échelle) et d'en exciter un. Le comportement dynamique de l'assemblage de combustible excité a été étudié et des paramètres modaux (masse, amortissement, rigidité) ont été identifiés. Des non linéarités ont été identifiées par la présence de grilles de support. La présence d'écoulement d'eau affecte principalement les paramètres de masse, tandis que la rigidité et l'amortissement présentent des changements plus petits, mais non négligeables. L'analyse du couplage entre l'ensemble excité et les autres a confirmé, comme on pouvait s'y attendre, que la présence d'un écoulement d'eau induit des forces de couplage entre différents assemblages de combustible. L'augmentation du débit d'eau induit un couplage statique et une augmentation des forces de couplage. Le couplage augmente également lorsque la taille du confinement est réduite. Des phénomènes de couplage sont observés, avec des magnitudes différentes, sur les trois assemblages non excités. L'analyse des mesures LDV a permis de comparer la force de couplage avec le flux axial oscillant induit. Le couplage et le flux axial oscillant ne montrent pas le même comportement vis-à-vis des fréquences excitées. Les données expérimentales ont ensuite été utilisées pour valider l'approche de modélisation.

Un autre aspect fondamental de ce travail de doctorat est lié au développement d'un modèle simplifié pour les interactions de structure fluide sur les assemblages de combustible. La théorie des écoulements potentiels a été présentée, mettant l'accent sur l'avantage que les forces d'interaction de la structure fluide peuvent être directement écrites en fonction du déplacement de la structure elle-même. Ce résultat est une réalisation importante car il permet de réduire considérablement le temps de calcul en évitant de résoudre des équations fluides.

Les calculs avec le modèle d'écoulement potentiel sont effectués pour des géométries à un cylindre et à plusieurs cylindres. La taille du confinement a des effets différents sur les forces d'interaction en fonction du nombre d'onde considéré. Les forces de couplage entre les cylindres dépendent des nombres d'ondes et un comportement de seuil a été défini. Le couplage augmente avec le nombre d'onde jusqu'à un certain seuil et, une fois ce seuil franchi, la force de couplage décroît par une propagation inefficace des perturbations de pression. L'importance des symétries pour la présence de couplage hors plan a également été identifiée. Lorsque les cylindres sont disposés sur un réseau bidimensionnel, des effets de couplage sur les directions non excitées apparaissent également.

Enfin, afin de valider le modèle, des calculs simulant la géométrie ICARE sont discutés et comparés aux résultats expérimentaux. Les paramètres modaux sont identifiés en fonction des débits et comparés à ceux expérimentaux. Le modèle correspond bien aux données expérimentales pour le coefficient de masse ajouté et reproduit qualitativement l'effet de rigidité ajouté (qui augmente avec le débit d'eau). L'effet de raideur ajouté est sur-estimé pour les débits importants. Les calculs pour le coefficient d'amortissement ajouté ne concordent pas du tout avec les résultats expérimentaux. Ce résultat était attendu car le modèle ne prend en compte aucune force visqueuse, source principale des effets d'amortissement. Les simulations permettent également d'estimer les forces de couplage entre différents assemblages. Le modèle sous-estime la force de couplage entre l'ensemble excité

et celui qui le précède, tout en reproduisant bien les forces de couplage hors du plan.

La comparaison entre les résultats numériques et les expériences permet de définir les limites d'un tel modèle d'écoulement potentiel : il peut reproduire l'effet de masse et de rigidité supplémentaires et ne permet de prédire qualitativement que les forces de couplage. Elle permet également de prévoir qualitativement les effets de la taille du confinement. De plus, comme prévu, le modèle ne peut prédire la présence de non-linéarités ni les effets de la température de l'eau.

Enfin, une application du modèle à d'autres résultats expérimentaux est discutée. Le modèle est utilisé afin de simuler les données expérimentales recueillies dans l'installation expérimentale installée à l'Université George Washington. Le modèle est capable de reproduire certains résultats observés liés à des effets de non reproductibilité. Il a démontré que de petites différences dans les déformations de modes élevés produisent des effets importants sur le flux axial induit. Cette application a prouvé que le modèle est non seulement utile pour prédire le comportement dynamique de la pièce structurelle, mais il peut également prédire les perturbations du flux d'eau dues au mouvement de la structure. Le modèle s'est avéré utile pour certaines applications pratiques et flexible grâce à son temps de calcul réduit.

À la suite de cette thèse de doctorat, de nombreuses perspectives s'ouvrent pour des approches de modélisation, numériques et expérimentales.

Comme indiqué au chapitre ref Chap4, le modèle mis en œuvre ne prend pas en compte les forces visqueuses. Une amélioration qui serait d'une importance fondamentale consiste à introduire avec un facteur empirique les forces visqueuses dans le modèle. Une façon d'introduire la viscosité dans le modèle consiste à considérer le flux d'eau axial comme la somme de deux flux : un flux potentiel en masse et un flux visqueux ayant une distribution empirique définie. De cette manière, les forces visqueuses sont prises en compte dans une formulation empirique et il serait extrêmement intéressant d'évaluer les effets de telles améliorations, en particulier sur l'estimation du coefficient d'amortissement ajouté.

D'autres améliorations pourraient être apportées à la mise en œuvre numérique du modèle. Le schéma d'itérations illustré dans le chapitre ref Chap3 pourrait être mis en œuvre afin d'avoir des solutions plus précises. De plus, les simulations effectuées ne prennent en compte que les formes en mode naturel pour le faisceau d'Euler-Bernoulli à clamping serré. Des efforts pourraient être déployés pour effectuer des calculs tridimensionnels prenant en compte des formes de mode plus complexes et également pour prendre en compte les effets des extrémités supérieure et inférieure du cylindre qui sont réellement négligés.

En ce qui concerne l'application des simulations à l'installation expérimentale GWU, certaines améliorations pourraient être apportées afin de prendre en compte une déviation relative entre les parois latérales et l'assemblage de combustible. Les parois du réservoir de confinement, qui sont soumises aux excitations de la table à secousses, présentent également une déviation qui induira une oscillation axiale dans le flux d'eau. Ce déplacement pourrait être pris en compte dans le modèle et les effets de cette amélioration pourraient être quantifiés afin de mieux comprendre les résultats expérimentaux.

RESUME ETENDU

Du point de vue expérimental, différentes possibilités restent ouvertes pour une exploration plus poussée. Tout d'abord, la grande quantité de données collectées au cours des campagnes expérimentales décrites pourrait être analysée de manière plus systématique et, par exemple, l'identification des paramètres pourrait être réalisée pour toutes les expériences. De plus, les formes de déviation des assemblages combustibles pourraient être étudiées avec l'application des méthodes POD.

Comme cela a déjà été présenté dans le chapitre ref Chap2, une campagne de mesures de PIV a été réalisée sur la base de données ICARE, cependant elles n'ont pas encore été analysées en raison de contraintes de temps. L'analyse des données PIV pourrait permettre de mieux comprendre les phénomènes de couplage. Les composantes axiales et horizontales de la vitesse d'écoulement de l'eau pourraient être comparées aux effets de couplage observés entre les différents assemblages de combustible. Les effets de la turbulence pourraient également être étudiés avec des mesures de PIV.

De plus, il serait d'un intérêt fondamental de déployer des efforts afin d'étudier expérimentalement l'effet de la viscosité. Nous avons déjà indiqué que des installations avaient été expérimentées à différentes températures sur l'installation ICARE afin d'obtenir différentes viscosités pour le débit d'eau. Malheureusement, la modification de la température de la boucle d'eau affecte également les propriétés des matériaux des assemblages. Ainsi, les effets de la viscosité ne peuvent être séparés des effets de la température sur la rigidité des matériaux de structure. Afin d'éviter ce problème et de mieux étudier les effets de viscosité, certaines expériences pourraient être conçues en utilisant différents fluides en écoulement ayant des densités similaires mais des viscosités différentes. De cette manière, la température serait maintenue constante et les seuls effets de la viscosité pourraient être étudiés.

Enfin, une nouvelle installation expérimentale (EUDORE) a été récemment conçue. L'installation EUDORE, qui remplacera la section ICARE, utilisera les mêmes assemblages que ceux utilisés dans ICARE. Trois ensembles sont disposés dans une rangée et une pré-déformation pourrait être imposée aux ensembles. La particularité de cette nouvelle installation est que toute la structure peut être excitée avec un système hydraulique. Pour les projets futurs, les résultats provenant de cette nouvelle installation expérimentale pourraient être comparés aux données collectées sur ICARE et le modèle de flux potentiel pourrait être utilisé pour effectuer des calculs sur cette nouvelle géométrie, en tenant compte des effets de viscosité (comme déjà discuté ci-dessus) et mouvement des murs.

Nomenclature

$\alpha_{acrylic}$	Linear thermal expansion coefficient for acrylic	$\hat{g}(\hat{k}; \hat{R}, \hat{l}_x, \hat{l}_y)$	Dimensionless solution for Helmholtz problem with unitary boundary conditions
α_{steel}	Linear thermal expansion coefficient for steel	$\hat{G}(\hat{z}; \hat{R}, \hat{l}_x, \hat{l}_y)$	Green function
β	Dimensionless flexural rigidity	\hat{k}	Wavenumber of the Fourier transformation (dimensionless)
$\chi(x)$	Mode shape function	\hat{l}_x	Dimensionless confinement size on the x direction
$\chi_n(x)$	n^{th} mode shape function	\hat{l}_y	Dimensionless confinement size on the y direction
$\Delta L_{acrylic}$	Acrylic tank elongation	\hat{m}	Dimensionless mass
ΔL_{diff}	Differential elongation	\hat{p}	Dimensionless pressure field
ΔL_{steel}	Steel structure elongation	\hat{R}	Dimensionless cylinder radius
$\eta_n(t)$	Generalized coordinates for the n^{th} mode	\hat{r}	Dimensionless radial coordinate
Γ	Domain's boundary	\hat{t}	Dimensionless time coordinate
$\hat{\phi}$	Dimensionless velocity potential	$\hat{v}(\hat{k}, \hat{t})$	Fourier transform of the impermeability boundary condition
$\hat{\Psi}$	Fourier transform of the dimensionless pressure field	$\hat{w}(\hat{z}, \hat{t})$	Dimensionless displacement along y direction
$\hat{f}^y(\hat{z}, \hat{t})$	Dimensionless interaction force on the y direction	\hat{x}	Dimensionless x coordinate
$\hat{F}^y(\hat{k}, \hat{t})$	Interaction force in Fourier space	\hat{y}	Dimensionless y coordinate
$\hat{F}^y(\hat{k}, \hat{t})^*$	Elementary solution of Helmholtz problem for unitary boundary conditions	\hat{z}	Dimensionless z coordinate
\hat{F}_A	Dimensionless inertial force	λ_0	Laser wavelength
		\mathcal{F}	External forces

NOMENCLATURE

$\mathbf{e}_r, \mathbf{e}_\theta, \mathbf{e}_z$	Unit vectors for cylindrical coordinates	$\tilde{\mathcal{G}}_{A_j}^y(\tilde{\mathbf{k}})$	Global proportionality function between global pressure field and assembly displacement relative to the j^{th} fuel assembly on the y direction
$\mathbf{e}_x, \mathbf{e}_y, \mathbf{e}_z$	Cartesian unit vectors		
\mathbf{v}	Fluid velocity	$\tilde{\varphi}$	Rescaled dimensionless velocity potential in Fourier space
\mathbf{v}'	Velocity perturbation		
$\mathbf{v}_r, \mathbf{v}_\theta, \mathbf{v}_z$	Velocity components on cylindrical coordinates	$\tilde{C}_m(\tilde{\mathbf{k}}; \tilde{h}_x, \tilde{h}_y)$	Virtual mass coefficient in Fourier space
\mathbf{v}_∞	Bulk velocity	$\tilde{C}_{m,i}(\tilde{\mathbf{k}}; \tilde{h}_x, \tilde{h}_y)$	Virtual mass coefficient in Fourier space relative to the i^{th} cylinder
\mathcal{M}	Bending moment		
μ	Dynamic viscosity	$\tilde{f}_i^y(\tilde{z}, \tilde{t})$	Dimensionless interaction force on the y direction relative to the i^{th} cylinder
ν	Poisson ration		
Ω	Integration domain	$\tilde{g}(\tilde{\mathbf{k}}; \tilde{h}_x, \tilde{h}_y)$	Rescaled solution for Helmholtz problem with unitary boundary conditions
ω	Harmonic angular frequency		
ω_i	Natural frequency	$\tilde{g}_i^x(\tilde{\mathbf{k}})$	Proportionality function between pressure field and structure displacement relative to the i^{th} cylinder on the x direction
ω_n	n^{th} natural frequency		
ω_{ri}	Resonance frequency	$\tilde{g}_i^y(\tilde{\mathbf{k}})$	Proportionality function between pressure field and structure displacement relative to the i^{th} cylinder on the y direction
\bar{p}	Pressure mean value		
\bar{T}	External tension	$\tilde{g}_i(\tilde{\mathbf{k}}; \tilde{h}_x, \tilde{h}_y)$	Proportionality function between pressure field and structure displacement relative to the i^{th} cylinder
ϕ'	Local perturbation potential		
$\phi(x, y, z)$	Velocity potential		
ϕ_∞	Free stream velocity potential		
ρ	Density of the fluid		
$\text{sgn } \tilde{z}$	Sign function of dimensionless reduced cylinder height		
$\mathbf{v}_i (i = 1, 2, 3)$	Spatial components of the fluid velocity	$\tilde{G}_i(\tilde{z}, \tilde{h}_x, \tilde{h}_y)$	Green function relative to the i^{th} cylinder
$\tilde{\mathcal{G}}_{A_j}^x(\tilde{\mathbf{k}})$	Global proportionality function between global pressure field and assembly displacement relative to the j^{th} fuel assembly on the x direction	\tilde{h}_x	Rescaled dimensionless x direction confinement size
		\tilde{h}_y	Rescaled dimensionless y direction confinement size

\tilde{k}	Rescaled dimensionless wavenumber	$f^y(z, t)$	Interaction forces on the y direction
$\vec{e}_{i1}, \vec{e}_{i2}$	Laser beam directions	f_d	Doppler frequency shift
\vec{u}_p	Particle velocity	F_I	Inertial Force
ξ_i	Reduced damping	F_L	Longitudinal viscous force
ξ_n	Modal damping ratio for the n^{th} mode	F_N	Normal viscous force
$A(x)$	Cross section area of a body	f_{max}	Maximum excitation frequency
$c(x)$	Viscous damping	f_{min}	Minimum excitation frequency
C_a	Added mass coefficient	F_{p_x}	x -direction hydrostatic force
C_B	Base shape drag coefficient	F_{p_y}	y -direction hydrostatic force
C_D	Drag coefficient	g	Gravitational constant
C_M	Inertial coefficient	H	Chord of a plate
C_N	Normal friction drag coefficient	h	Lateral displacement of a plate
C_T	Tangential drag coefficient	I	Inertial momentum
$Coh_{PF}(f)$	Coherence function between position and force	I	Invariant number
$Coh_{VP}(f)$	Coherence function between velocity and position	K_n	Modal stiffness of the n^{th} mode
D	Cylinder diameter	L	Cylinder length
D_{ch}	Confinement channel diameter	l	Span size of a plate
E	Young modulus	L_x	Confinement size on the x direction
E^*	Viscoelastic constant	L_y	Confinement size on the y direction
E_k	Kinetic energy of the fluid	m	Mass of the cylinder per unit length
EI	Flexural rigidity of the body	M_a	Added mass
$F(t)$	Interaction force acting on a body	$M_a^{cylinder}$	Added mass of a cylinder
$f(x, t)$	Transverse force per unit length	M_a^{plate}	Added mass of a plate
F^A	Inviscid force term	M_n	Modal mass of the n^{th} mode
F^L	Lift force per unit length	$m_{ij}(i, j = 1, 2, \dots, 6)$	Added mass components
		p	Pressure load
		p'	Pressure perturbation

NOMENCLATURE

$P(t) \star F(t)$	Cross spectral correlation function between position and force signals	$TF_{VP}(f)$	Transfer function between velocity and position
$P(t) \star P(t)$	Auto spectral correlation function of the position signal	U	Bulk flow velocity
p_∞	Bulk pressure	u	Translational velocity of a body
Q	Lateral shear force	V	Volume of the fluid element
q	Momentum per unit length	$V(t) \star P(t)$	Cross spectral correlation function between velocity and position signals
Q_n	Generalised force for the n^{th} mode	$V(t) \star V(t)$	Auto spectral correlation function of the velocity signal
R	Cylinder radius	$w(x, t)$	Transversal displacement along y direction
t	Time coordinate	x, y, z	Cartesian coordinates
T_s	Time of the swept sinus		
$TF_{PF}(f)$	Transfer function between position and force		

List of Figures

1	Cuve du réacteur REP et composants internes	16
2	Schéma du dispositif expérimental ICARE	22
3	Représentation schématique de la matrice expérimentale	23
4	Relation force-déplacement pour des expériences d'excitation quasi statique	24
5	Comportement des paramètres dynamiques estimés en fonction des débits d'eau pour les trois premiers modes avec amplitude d'excitation 0.5 mm à 15 °C avec 2 assemblages en confinement grand. Débit $-1 m/s$ veut dire "Dans l'air"	26
6	Paramètres de masse, de rigidité et d'amortissement ajoutées en fonction du débit d'eau, données expérimentales VS simulées	33
7	Vue de l'installation expérimentale (Weichselbaum, 2015)	36
8	Evolution temporelle des profils de vitesse axiale sur le point $x = 2200 mm$, $y = 10 mm$, $z = 33.5 mm$ pour expérimental et numérique "Case 1" et "Case 2"	40
1.1	PWR reactor vessel and internals	62
1.2	PWR Fuel Assembly	63
1.3	Scheme of a PWR core under seismic loading	64
1.4	Equivalence between flow near the body and near a cylinder of the same cross section	72
1.5	Displacement of a body in axial flow from its initial position	72
1.6	(a) An element δx of the cylinder showing forces and moments acting on it; (b) an equivalent rigid element surrounded by fluid. (Païdoussis, 1973) . . .	73
1.7	Porous media approach (Ricciardi et al., 2009)	79
1.8	Bending of an Euler Bernoulli Beam	80
2.1	Scheme of the ICARE Experimental Facility	93
2.2	Scheme of the ICARE assembly	94
2.3	Scheme of the displacement sensors on the ICARE test section	95
2.4	Picture of the ICARE test section and some details	96
2.5	Different possible configurations of the ICARE test section changing con- finement size and number of assemblies	96
2.6	First design of the hydraulic jack sealing system	98

LIST OF FIGURES

2.7	Comparison between bellow under normal conditions and under swelling conditions	98
2.8	New design for the sealing system	99
2.9	Force response of the membrane system to excitation	100
2.10	New design of the upper part of the ICARE facility with the compensation tank and the vortex breaker grid	102
2.11	Scheme of the assemblies in the test section with the respective identification numbers	103
2.12	Diagram of water viscosity and density as function of temperature	104
2.13	Schematic representation of experimental matrix	105
2.14	Schematic representation of data analysis work	106
2.15	Force-Displacement plot for quasi-static excitation experiments	110
2.16	Displacement-Force transfer function for assembly 1 in air in large confinement with two assemblies at 15 °C	111
2.17	Displacement-Force transfer functions for assembly 1 in large confinement with two assemblies with different flow rates at 15 °C: comparison between different excitation amplitudes	112
2.18	Displacement-Force transfer functions for assembly 1 with different excitation amplitudes in large confinement with two assemblies at 15 °C: comparison between different water flow rates	113
2.19	Displacement-Force transfer functions for different confinement sizes with an excitation amplitude of 0.8 mm and two fuel assemblies at 15 °C	114
2.20	Displacement-Force transfer functions for 2 VS 4 fuel assemblies with an excitation amplitude of 1.2 mm at 15 °C	115
2.21	Displacement-Force transfer functions for 15 °C VS 30 °C at 1 mm excitation amplitude with two fuel assemblies in small confinement	116
2.22	Comparison between experimental and estimated transfer functions for 0.5 mm excitation in 2 fuel assemblies large confinement configuration (15 °C)	117
2.23	Behaviour of the estimated dynamic parameters as function of the water flow rates for the first three modes with excitation amplitude 0.5 mm at 15 °C with 2 assemblies in large confinement configuration. Flow rate -1 m/s means "In Air"	118
2.24	Behaviour of the estimated dynamic parameters as function of the water flow rates and excitation amplitude for the first mode at 15 °C with 2 assemblies in large confinement configuration. Flow rate -1 m/s means "In Air"	119
2.25	Estimated modal stiffness and mass at 15 °C and 30 °C for the first mode with excitation amplitude of 0.8 mm with two assemblies in large confinement configuration.	120

2.26	Displacement time evolution of excited fuel assembly and assembly n° 2 in the excitation direction for 0.5 <i>mm</i> excitation with 1 <i>m/s</i> water flow in 2 fuel assemblies small confinement configuration at 15 °C. Measurements are showed for the three different levels	121
2.27	Coupling transfer functions between excited fuel assembly and assembly n° 2 in the excitation direction for 0.5 <i>mm</i> excitation with 1 <i>m/s</i> water flow in 2 fuel assemblies small confinement configuration at 15 °C. Measurements are showed for the three different levels	121
2.28	Coupling transfer functions between excited grid of assembly n°1 and grids of assembly n° 2 in the excitation direction for 0.5 <i>mm</i> excitation with 1 <i>m/s</i> water flow in 2 fuel assemblies small confinement configuration at 15 °C. Measurements are showed for the three different levels	121
2.29	Coupling transfer functions between central grids of excited fuel assembly and assembly n°2 in the excitation direction for 0.5 <i>mm</i> excitation with different water flows in 2 fuel assemblies small confinement configuration at 15 °C	122
2.30	Coupling transfer functions between bottom grids of excited fuel assembly and assembly n°2 in the excitation direction for 0.5 <i>mm</i> excitation with different water flows in 2 fuel assemblies small confinement configuration at 15 °C	123
2.31	Coupling transfer functions between central grids of excited fuel assembly and assembly n°2 in the excitation direction for different excitation amplitudes and different temperatures with 2 assemblies in small confinement configuration	123
2.32	Coupling transfer functions between excited fuel assembly and assembly n°2 in the excitation direction for 0.5 <i>mm</i> excitation at 2 <i>m/s</i> water flows in all configurations at 15 °C	124
2.33	Coupling transfer functions between excited fuel assembly and assembly n°2 in the direction orthogonal to the excitation for 0.5 <i>mm</i> excitation with 2 <i>m/s</i> water flow in 2 fuel assemblies small confinement configuration at 15 °C. Measurements are showed for the three different levels	125
2.34	Coherence functions between excited fuel assembly and assembly n°2 in the direction orthogonal to the excitation for 0.5 <i>mm</i> excitation with 2 <i>m/s</i> water flow in 2 fuel assemblies small confinement configuration at 15 °C. Measurements are showed for the three different levels	125
2.35	Coupling transfer functions between excited fuel assembly and assembly n°4 in the excitation direction for 0.5 <i>mm</i> excitation with 2 <i>m/s</i> water flow in 4 fuel assemblies small confinement configuration at 15 °C. Measurements are showed for the three different levels	126
2.36	Schematic representation of LDV experimental apparatus	128
2.37	Picture of LDV experimental apparatus on ICARE	129

LIST OF FIGURES

2.38	Schematic representation of a PIV experimental apparatus	130
2.39	Pictures of PIV experimental apparatus on ICARE	131
2.40	Schematic of LDV measurements points on ICARE	132
2.41	Schematic of LDV measurements matrix ICARE	132
2.42	Water velocity and hydraulic jack position for experiment at 1 <i>m/s</i> water flow, 1 <i>mm</i> excitation amplitude and LDV measurement point 1.C (see Figure 2.40)	133
2.43	Local water velocity evolution for experiments at different water flows, 1 <i>mm</i> excitation amplitude and LDV measurement point 2.C (see Figure 2.40)	133
2.44	Local water velocity evolution for experiments at different water flows without external excitation at LDV measurement point 2.C	134
2.45	Position and velocity PSDs for experiment at 2 <i>m/s</i> water flow, 1 <i>mm</i> excitation amplitude and LDV measurement point 1.C (see Figure 2.40)	135
2.46	Transfer function absolute value and coherence function for experiment at 2 <i>m/s</i> water flow, 1 <i>mm</i> excitation amplitude and LDV measurement point 1.C (see Figure 2.40)	136
2.47	Transfer functions V/P for experiments at different water flows at different LDV measurement points (see Figure 2.40) with 1 <i>mm</i> excitation amplitude	137
2.48	Transfer functions V/P for experiments at different excitation amplitudes with different water flows at different LDV measurement points (see Figure 2.40)	138
2.49	Transfer functions and power spectral densities for experiments at different temperatures (15 °C and 30 °C), with 1 <i>mm</i> excitation amplitude at LDV measurement point 2.B (see Figure 2.40)	138
2.50	Transfer functions V/P for different measurements points (see Figure 2.40) at 2 <i>m/s</i> water flow with 1 <i>mm</i> excitation amplitude	139
2.51	Power spectral density functions for different measurement points (see Figure 2.40) at 2 <i>m/s</i> water flow with 1 <i>mm</i> excitation amplitude	140
3.1	(a) Schematic view of clamped clamped cylinder deformed under axial flow in a finite confinement. (b) Coordinate systems.	144
3.2	Iteration scheme for the calculation of fluid structure interactions	147
3.3	Transformation of the 3D dimensional problem into multiples 2D dimensionless problems	148
3.4	Two and four cylinders configurations	154
3.5	Geometries implemented in the code representing ICARE configurations (red assembly is excited along horizontal direction)	157
4.1	Helmholtz problem represented in the FEM domain	161
4.2	Value of \tilde{g} as function of the wavenumber for several large confinements	162
4.3	Scheme of the parameters used to perform calculations	164

4.4	Differences in the behaviour of the \tilde{g} function depending on wavenumbers	165
4.5	Differences in the behaviour of the \tilde{g} function depending on confinement size	166
4.6	Numerical VS fitted values of the \tilde{g} function	170
4.7	Interpolation error with different polynomial degrees	170
4.8	Polynomial fitting coefficients for 11 th degree interpolation	171
4.9	Modal added mass coefficient as function of the confinement size for small wavenumbers	172
4.10	Modal added mass coefficient as function of the confinement size for large wavenumbers	172
4.11	Velocity fields calculations in Fourier space for both small and large wavenumbers	173
4.12	Pressure fields for 2 cylinders configuration with different wavenumbers	174
4.13	Pressure fields for 2 cylinders configurations with different symmetries for medium wavenumbers ($\tilde{k} = 0.1$)	175
4.14	Pressure field calculation for first natural mode ($\tilde{k} = 9 \cdot 10^{-4}$) excitation with four cylinders in 4 mm confinement	176
4.15	Behaviour of the \tilde{g} functions in both directions as function of wavenumbers for different cylinders and directions with confinement of 4 mm with excitation given on the y direction on cylinder 1	177
4.16	Pressure field distribution and coupling coefficients for large confinement configuration (8 mm)	177
4.17	Calculation meshing for the four configurations simulating the ICARE set-up	179
4.18	Pressure field calculations for four fuel assemblies in large confinement	180
4.19	Resultant of global forces (in Fourier Space) for excited assembly in x direction for the four different configurations	181
4.20	Added mass, stiffness and damping parameters as function of the water flow rate, simulated VS experimental data	183
4.21	Simulated coupling forces between the assembly 1 (excited) and assembly 2 on the excitation direction (x direction)	185
4.22	Simulated coupling forces between the assembly 1 (excited) and assembly 4 both on the excited direction and on orthogonal direction	186
5.1	View of the experimental facility (Weichselbaum, 2015)	190
5.2	View of primary and secondary tanks (Weichselbaum, 2015)	191
5.3	Primary channel profile (Weichselbaum, 2015)	192
5.4	Experimental facility scheme with rigid connections, accelerometers locations and PIV planes location	193
5.5	Positioning of cameras in non inertial reference frame for PIV measurements (Weichselbaum, 2015)	194
5.6	Location of PIV planes, cameras and FOVs for experimental campaigns	196
5.7	Transversal velocity profiles for three test cases at different phases	197

LIST OF FIGURES

5.8	Axial velocity profiles for three test cases at different phases	197
5.9	Time plot and FFT plot of the 6 LVDT sensors of the shaking table	198
5.10	POMs and POVs for dataset "Case 1"	201
5.11	POMs and POVs for dataset "Case 2"	201
5.12	Mode Shapes for Clamped-Clamped Beam	202
5.13	Time history on natural modes projection	205
5.14	Axial velocity for a single cylinder undergoing 4 different modes displacement ($t = 0$)	206
5.15	Transversal velocity for a single cylinder undergoing 4 different modes displacement ($t = 0$)	207
5.16	Section of the 3D geometry of the fuel bundle implemented in FreeFEM++	209
5.17	Meshing section of the fuel bundle in FreeFEM++	209
5.18	Axial velocity field due to 4 modes on section $z = 33.5 \text{ mm}$, $2150 \text{ mm} < x < 2250 \text{ mm}$ for "Case 1" ($t = 0$)	210
5.19	Axial velocity field due to 4 modes on section $z = 33.5 \text{ mm}$, $2150 \text{ mm} < x < 2250 \text{ mm}$ for "Case 2" ($t = 0$)	211
5.20	Global axial velocity field on section $z = 33.5 \text{ mm}$, $2150 \text{ mm} < x < 2250 \text{ mm}$ for "Case 1" ($t = 0.45 \text{ s}$)	211
5.21	Global axial velocity field on section $z = 33.5 \text{ mm}$, $2150 \text{ mm} < x < 2250 \text{ mm}$ for "Case 2" ($t = 0.45 \text{ s}$)	212
5.22	Axial velocity profiles on section $z = 33.5 \text{ mm}$, $x = 2200 \text{ mm}$ for "Case 1" and "Case 2"	213
5.23	Temporal evolution of axial velocity profiles on point $x = 2200 \text{ mm}$, $y = 10 \text{ mm}$, $z = 33.5 \text{ mm}$ for experimental and numerical "Case 1" and "Case 2"	214

List of Tables

1	Résumé des installations expérimentales précédentes	21
2	Paramètres d'entrée pour chaque ensemble de données	37
1.1	Mode Shape Solutions for Fixed-Fixed Beam	83
2.1	Summary of previous experimental facilities	92
4.1	Fitting parameters for Slender Body Approximation	167
4.2	Fitting parameters for Large Span Approximation	168
5.1	Input parameters for each data set	195
5.2	A_n values for Clamped-Clamped beam	203
5.3	Natural mode shapes for Clamped Clamped Beam with four measurement points	203
5.4	Time history amplitudes for two test cases	204
5.5	Time history phase shift respect to the first mode for two test cases	204
5.6	Amplitude ratios for displacement and axial velocity - "Case 1"	212
5.7	Amplitude ratios for displacement and axial velocity - "Case 2"	213

LIST OF TABLES

General Introduction

"A theory is something nobody believes, except the person who made it. An experiment is something everybody believes, except the person who made it."

Albert Einstein

Safety of nuclear reactors is a main industrial challenge nowadays. Most diffused nuclear reactors are Pressurised Water Reactors (PWRs). The fuel of a PWR is mainly made by enriched uranium, under the shape of pellets which are assembled together creating a fuel rod. Fuel rods are grouped together on a 17×17 fuel assembly. Each fuel assembly has 10 supporting grids which hold together the fuel rods. A PWR core is made of more than hundreds of fuel assemblies. The heat produced by the fuel assemblies is then removed by an axial water flow, which also guarantees that the superficial temperature of the assemblies does not overcome a certain threshold. The temperature of the fuel assemblies must be controlled in order to avoid excessive stress, and eventual damage of the external cladding. Since the cladding represents the first barrier between the nuclear products and the environment, its integrity is of fundamental importance in order to guarantee the safety on nuclear reactors. A nuclear reactor core is thus a very complex system made of several components and with the presence of elongated structures and of a flowing fluid.

One of the main concerns for the safety of nuclear reactors is represented by earthquake events. In case of an earthquake, all the assemblies which are present inside the reactor could collide and provoke permanent deformations of supporting grids. Safety measures are required to ensure the drop of control rods and to assure that the core is cooled even if the fuel assembly spacer grids strike each other. Thus, proper modelling of the mechanical behaviour of fuel assemblies is needed. Due to the presence of an axial water flow, complex phenomena of interactions between the fluid and the structures arise. In order to model the behaviour of a reactor core under seismic excitation fluid structure interactions should be carefully investigated, and they must be taken into account for accurate modelling.

GENERAL INTRODUCTION

During the years many different authors and industrial entities have investigated fluid structure interactions on nuclear fuel assemblies. Different models have been developed, each with the objective of modelling some aspects of their mechanical behaviour. In parallel with models, experimental works have been carried out in order to observe fluid structure interaction phenomena on fuel bundles and to validate the models.

The vibrational behaviour of nuclear fuel assemblies has been studied for decades at CEA (French Atomic Energy Agency). In the framework of a collaboration between the CEA, EDF and FRAMATOME (ex AREVA) several experimental facilities have been designed and operated at CEA in Cadarache. First experiments (EROS) have been designed with assemblies in reduced scale in order to study the impact forces without axial flow. Other facilities have been constructed in order to take into account axial flow (ECHASSE) and full size fuel assemblies (CADIX). Later a new facility (COUPLAGE) has been constructed in order to investigate the couplings between different fuel assemblies due to the presence of the water. Anyway the design of the assemblies was in highly reduced scale, and was considered not representative of real conditions of fuel assemblies. Finally a full scale facility (HERMES) has been built in order to identify modal parameters of a real fuel assembly for design purposes.

Moreover, the laboratory also develops numerical models in parallel with the experimental activity. The code COEUR3D has been recently developed with the objective of simulating the vibrational behaviour of PWR fuel assemblies in accidental scenarios. The model is based on a porous media approach, taking into account the water flow, supporting grids and shocks between assemblies. The code takes into account very complex phenomena, and provides numerical results which are accurate and have been experimentally validated. Anyway, this code is time demanding in terms of computational time, and it could not be used in the frame of sensitivity analysis on geometrical parameters.

The PhD work that will be presented in this document is set in the framework of this joint project between CEA, EDF and FRAMATOME. This PhD aims to respond to the need for a simplified model which could allow to catch the main features of the fluid structure interactions of fuel assemblies, and thanks to a low computational cost, could allow to perform sensitivity analysis on different parameters in order to understand how they affect fluid structure interactions phenomena. With the objective of improving the phenomenological knowledge of fuel structure interactions phenomena on nuclear fuel assemblies both a modelling and experimental approach are implemented during this work. Stress has been put on the identification of the limits of this simplified model in order to identify the valid field of application.

The first approach to the modelling consisted in the identification of appropriate simplifications necessary in order to develop a simple model which allows fast calculations. Fluid structure interaction calculations are time demanding mainly due to the resolution of Navier-Stokes equations for fluid computations. Thus, the potential flow theory has been identified as a good tool for reducing the computational time. Potential flow theory introduces a scalar quantity, which allows to avoid the solution of Navier-Stokes equations

for fluid forces calculations. The fluid problem is thus reduced to a Poisson' problem, making the calculations much faster. Simplifications are also introduced in the structural model, by considering the fuel assembly to behave as a Euler-Bernoulli beam. For further reduction of computational time, the model is solved in the Fourier space, thus allowing to solve a 2D problem instead of a 3D problem. The validity and the limits of this simplified model have been tested with experimental results.

A new experimental facility has been recently designed at the LTHC (Laboratoire de Thermo Hydraulique et d'Hydromécanique Analytique du Coeur et des Circuits) with the objectives of investigating the coupling between fuel assemblies. ICARE experimental facility involves four fuel assemblies (half scale) arranged in a 2×2 lattice under axial water flow. The fuel assemblies are made of 64 rods arranged in a 8×8 lattice in order to ensure a good representativeness of a real fuel assembly. Several experimental campaigns have been performed during the PhD in order to investigate the effects of different configurations on coupling forces. The experimental campaigns allowed to validate the developed model and to define its limits.

This PhD Thesis is organised in five Chapters. The first Chapter consists in a bibliographic review of the different subjects which are involved in this work. A nuclear reactor is first presented and a description of the main components is provided. Then the fluid structure interactions are introduced in the context of nuclear reactors. Different models developed during the years for modelling the mechanical behaviour of fuel assemblies are presented. The linear theories of Euler-Bernoulli beam and potential flow are presented since they will be widely used for the PhD work. The second Chapter is devoted to the experimental works. The Chapter first presents a brief review of past experimental facilities realised at CEA for simulating fuel assemblies and to measure important dynamical characteristics. Then, the ICARE experimental facility is presented. Some improvements to the existing facility are illustrated and the experimental campaigns are presented. The experimental data are treated and analysed. Three main axes of analysis are used: the first axis involves the analysis of the dynamic behaviour of one fuel assembly, the second axis aims at investigating coupling forces between different assemblies and the third one focuses on laser velocimetry measurements. In the third Chapter, the fluid structure model developed during the PhD project is discussed. The equations are illustrated, and the method implemented in order to solve the equations is presented. The model is first developed for a single cylinder configuration and then extended to multiples cylinders. The fourth Chapter is dedicated to the analysis of numerical results obtained with the developed potential flow model. First results for one single cylinder are presented. A validation process with literature works is then carried out. Furthermore a parametric study for one single cylinder configuration is presented. Numerical results relative to multiple cylinders calculations are then illustrated. Finally numerical results relative to the geometry which represents the ICARE set-up are discussed. Numerical results are compared to experimental ones, with the objective of both validating the model and interpreting physical phenomena. The fifth Chapter presents a different application for the developed model. In the framework of a

GENERAL INTRODUCTION

collaboration between LTHC and George Washington University (GWU) the developed model has been used for practical application. The potential flow model has been used to simulate an experimental facility involving a fuel assembly surrogate bundle under axial flow put on a shaking table. Finally a conclusive section will end the document with a summary of the main outcomes of this PhD work and some space is left to perspectives.

Chapter 1

Fluid Structure Interactions in Nuclear Reactors

In this first chapter the main context of this PhD work will be presented. A PWR (*Pressurized Water Reactors*) nuclear reactor core will be presented with a special focus on the main components of the reactor core: the fuel assemblies. An analysis of the different models representing the dynamical behaviour of a fuel assembly will be carried out. First, phenomena occurring in a fuel assembly will be reviewed. Then, the presence of a water flow will be considered and a bibliographic overview of the fluid structure interaction models applied to nuclear reactors will be given, including models accounting for a single fuel rod, the fuel assembly and the whole reactor core. Finally two simplified models for the structure (Euler Bernoulli theory) and the fluid (potential flow theory) will be discussed. Those two theories will be used in the next sections to develop a simplified model for fluid structure interactions.

1.1 PWR Nuclear Reactor

PWRs constitute the large majority of the world's nuclear power plants, especially in France where they constitute the totality of operational power plants for electrical production. The main (and the most specific) component of nuclear reactor is the reactor core, which contains the nuclear fuel and all the other components necessary for the maintain of nuclear reactions and for the cooling process. The reactor vessel of a nuclear reactor will be briefly described hereafter, with a special focus on the fuel assemblies which constitute the reactor core. Fuel assemblies are, in fact, the main characters of this PhD work. For further details on the general design of nuclear power plants or reactor core one can refer to [Glasston and Sesonske \(1994\)](#) and [Lamarsh \(2001\)](#).

1.1.1 Reactor Vessel

The major components in the reactor vessel are the core barrel, the reactor core, and the upper internals package. An inside cut of a nuclear reactor vessel is given in Figure 1.1. There are one inlet (or cold leg) nozzle and one outlet (or hot leg) nozzle for each reactor coolant system loop. The upper internals package sits on top of the fuel. It contains the guide columns which guide the control rods when they are pulled from the fuel.

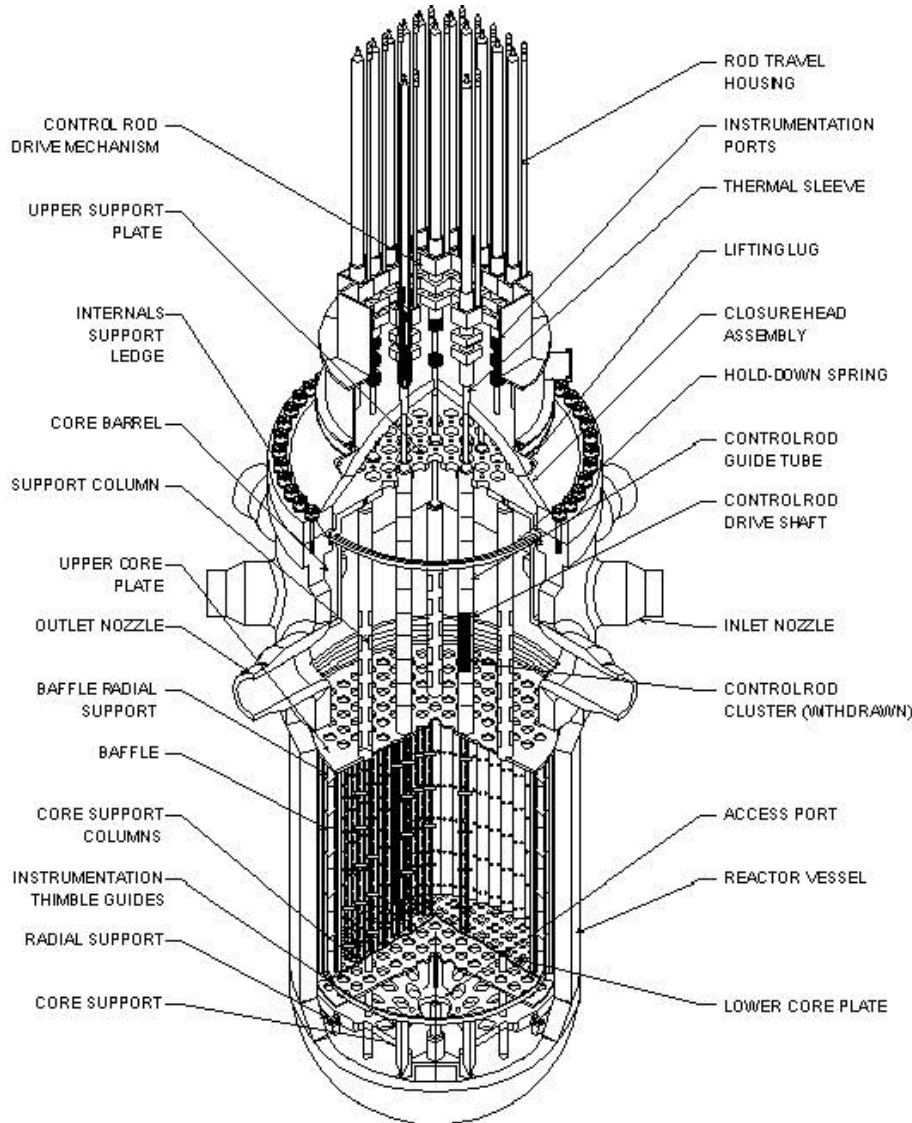


Figure 1.1 – PWR reactor vessel and internals

The core barrel slides down inside the reactor vessel and houses the fuel. A reactor core (PWR) is made of several fuel assemblies (between 150 and 250 depending on the power of the reactor).

These fuel assemblies are submerged in a water flow which extracts the heat generated in the fuel assemblies. The coolant flow is characterized by an average speed of 5 m/s , an average temperature of $310 \text{ }^\circ\text{C}$ ($290 \text{ }^\circ\text{C}$ at the inlet and $330 \text{ }^\circ\text{C}$ at the outlet) and a

pressure of 150 *bar*.

The flow path for the reactor coolant through the reactor vessel would be :

- The coolant enters the reactor vessel at the inlet nozzle and hits against the core barrel.
- The core barrel forces the water to flow downward in the space between the reactor vessel wall and the core barrel.
- After reaching the bottom of the reactor vessel, the flow is turned upward to pass through the fuel assemblies.
- The coolant flows all around and through the fuel assemblies, removing the heat produced by the fission process.
- The now hotter water enters the upper internals region, where it is routed out the outlet nozzle and goes on to the steam generator.

1.1.2 Fuel Assembly

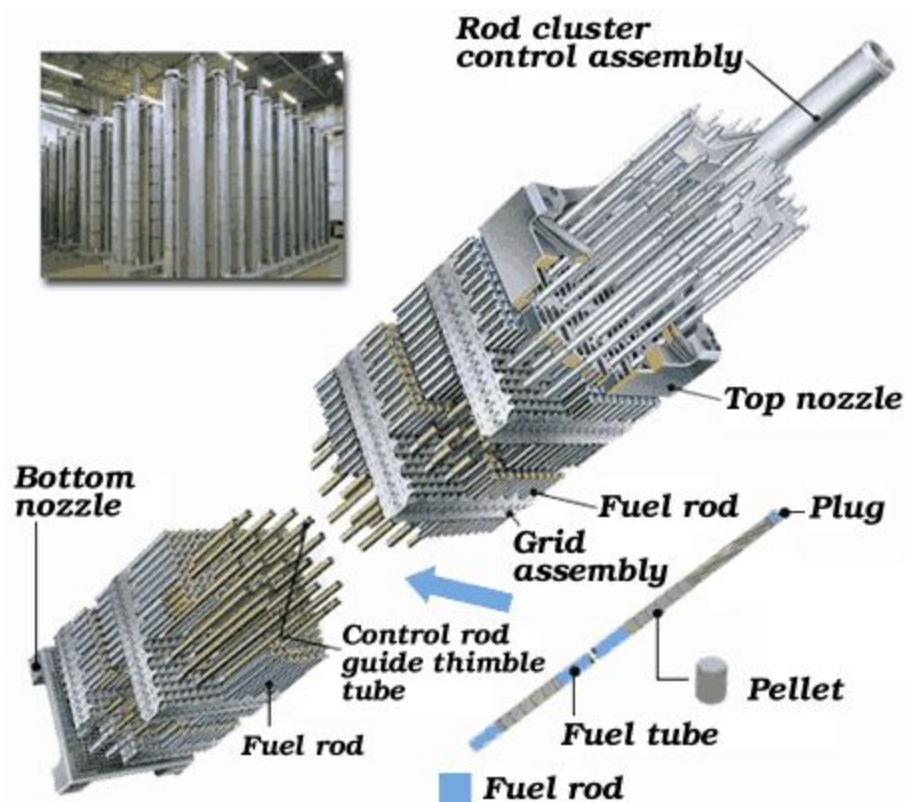


Figure 1.2 – PWR Fuel Assembly

As shown in Figure 1.2 a PWR fuel assemblies is made of 264 fuel rods (disposed in a squared pattern of $17 * 17$). A PWR fuel assembly stands between four and five meters high, is about 20 *cm* across and weights about 800 *kg*. Each fuel rod has a diameter of about 1 *cm* for 4 *m* high; the space between each others in the assembly is about 3 *mm*.

The fuel rods are made of uranium oxide fuel pellets, which are the elements where nuclear reactions happen, and so where the thermal power is produced. Fuel rods are held together by grids (between 8 and 10 depending on the power of the reactor) distributed along the fuel assembly. Springs and dimples are used in between the grid and the rods in order to avoid any drop of the fuel rods.

The assembly has vacant rod positions (about 25), replaced by "guide thimbles" in order to allow the vertical insertion of a control rod and to give more rigidity to the structure (guide thimbles are directly welded on the assembly grids). Some of the guide tubes are likely to be dedicated to instrumentation. A PWR fuel assembly comprises a bottom nozzle into which rods are fixed through the lattice and it is crowned by a top nozzle. The bottom and top nozzles are heavily constructed as they provide much of the mechanical support for the fuel assembly structure.

1.1.3 Dynamical Behaviour under Seismic Loading

The work of this PhD mainly focuses on the vibration of fuel assemblies in order to model the behaviour of the reactor core in case of earthquakes. In case of an accidental scenario, in fact the whole reactor core moves and contacts between fuel assemblies could happen, as shown in Figure 1.3. Strong impacts could induce important deformations of the fuel assemblies, which could block the drop of the control rods; the safety of the whole reactor core would then be compromised.

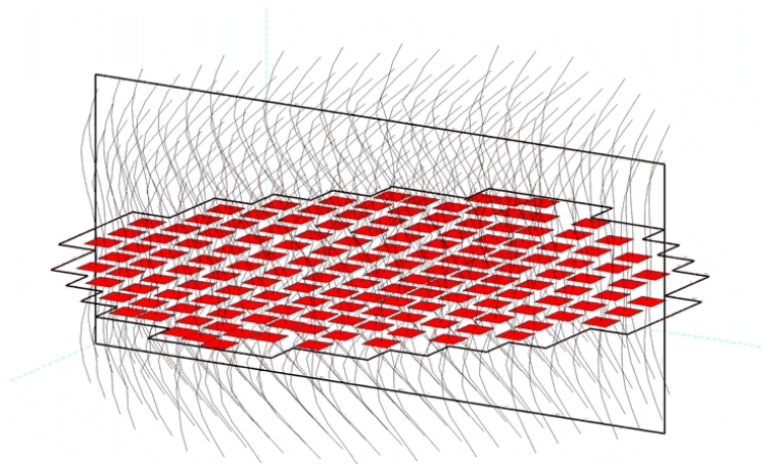


Figure 1.3 – Scheme of a PWR core under seismic loading

In order to guarantee the safety of the reactor, a good modelling of the dynamical behaviour of fuel assemblies is required. The core of a nuclear reactor is a very complex system, therefore several assumptions need to be done in order to provide a model which is at the same time reliable and efficient (regarding the computational time). In the following pages we will describe at first the different physical phenomena involved in the problem, and later a bibliographic analysis of the previous studies and models will be carried out.

Physical Context

One first important remark that we have to keep in mind is that the modelling of a reactor core involves the presence of two different macroscopic phases: a solid one (fuel assemblies) and a liquid one (water coolant). It follows a brief description of the phenomena involving each of them.

From a structural point of view, despite its elongated structure, the fuel assembly does not behave as a simple beam, but has a complex behaviour (Pisapia, 2004). In fact the fuel rods are held together by a system of 1 spring and 2 dimples, which introduce a non-linear contact relation. First experimental evidences of non-linearities are observed during vibration and snap back test (Brochard et al., 1993). Further experiments (like the experimental campaign "MASSE" done by Pisapia (2004)) underlined an hysteresis phenomenon during displacement cycle and non-linearities are observed on the stiffness and damping coefficients.

Regarding the liquid phase in a PWR reactor core, as already described in Section 1.1.1, the water moves under an ascendant flow at about 5 *m/s* at 150 *bar* and 310 °C. Taking into account the dimensions of the channels where the water flow gives a Reynolds number $Re \simeq 2 \cdot 10^5$, meaning that the flow is turbulent. Despite the flow is called "ascendant", it should be noted that there is the presence of a transverse flow (about 5 ÷ 15%) due to the motion of the fuel assemblies themselves. In a first approximation the transverse flow could be neglected, but there are some models which take into account this aspect, like in Ricciardi (2016) by using a "by-pass flow modelling".

The presence of the water flow and the structure give rise to complex phenomena of interaction between the fluid and the structure. The presence of the structure, in fact, influences the behaviour of the fluid, which itself influences the behaviour of the structure. We could outline two different sources of interactions. The first one is due to the presence of the water itself, which tends to oppose resistance to the movement of the structure. The second one due to flow, which adds further resistance for the structure to move (depending on the velocity). In the following chapters different models of fluid-structure interaction will be presented. Later on, some models accounting for the fuel assembly and for the whole core behaviour will be discussed. A focus will be put on the "porous media model". One of the main goal of this PhD thesis is to find, in some way, a simplified expression for the interaction forces, which could give us a model simple enough (and fast from a computational point of view), to be used in a predictive analysis.

1.2 Fluid Structure Interaction

Understanding and modelling the interaction forces is of fundamental importance in order to have a model capable of describing the behaviour of the whole reactor core under seismic loading. In order to have a good understanding of the physical phenomena involved in general fluid structure interaction problems, the main studies carried out on the subject

will be presented hereafter. The scientific works will be presented with the intent to give the reader an idea of the historical evolution in the comprehension of these phenomena and the industrial needs they are able to respond to. The discussion will focus on the assumptions implied by each model and on the validation of their results.

When a structural component which is submerged in a fluid vibrates, the surrounding fluid must be displaced to accommodate these motions. As a result, pressure perturbations are generated. In turn, the integrated effect of these pressure perturbations produces a hydrodynamic force acting on the structure. The fluid moving with the structure has an important effect on the dynamics of the vibrating structure; particularly on its natural frequencies and on damping characteristics. Ideally, the hydrodynamic force should be calculated based on the three-dimensional Navier-Stokes equations. Obviously, this is difficult, even in simple cases, so scientists made assumptions (depending on the specific application) allowing to simplify the problem.

1.2.1 Added Mass and Added Damping

In fluid mechanics, added mass or virtual mass is the inertia added to a system because an accelerating or decelerating body must move (or deflect) some volume of surrounding fluid as it moves through it. For simplicity this can be modelled as some volume of fluid moving with the object, though in reality all the fluid will be accelerated to various degrees. In the same way, the presence of the water induces changes in the slowing down of the free vibration of an object immersed in a fluid, due to the viscous resistance applied by the fluid on the body. Many authors, tried to describe the behaviour of a body in a fluid using only the concept of added mass, and eventually of added damping, thus reducing a very complex problem to a much simpler problem, governed by at most two coefficients: the added mass coefficient and the added damping coefficient.

The notion of added mass, also referred to as hydrodynamic mass or virtual mass in the literature, can be found in textbooks of classical hydrodynamics ([Lamb, 1895](#)), but it was first introduced by [Du Buat \(1786\)](#) in order to explain discrepancies between theory and experiments on the pendulum oscillations. One of the most common way to derive an added mass formulation is to analyse the kinetic energy associated with the motion of the fluid, but it is not the only way: for instance, momentum conservation relations could be used. Below, a possible formulation of added mass is shown, adapted from ([Brennen, 1982](#)). The added mass is seen has the parameters determining the necessary work done to change the kinetic energy associated with the motion of the fluid. In fact, any motion of a fluid, such as the one which occurs when a body moves through it, implies a certain amount of kinetic energy associated with the fluid motion. The kinetic energy of the fluid, E_k , can be expressed by:

$$E_k = \frac{\rho}{2} \int_V (\mathbf{v}_1^2 + \mathbf{v}_2^2 + \mathbf{v}_3^2) dV = \frac{\rho}{2} \int_V (\mathbf{v}_i \mathbf{v}_i) dV \quad , \quad (1.1)$$

where V is the entire volume of fluid, \mathbf{v}_i ($i = 1, 2, 3$) represents the spatial components of the fluid velocity in this volume, and repeated indexes imply a summation. It is assumed throughout that the fluid is incompressible with density ρ . Any increase in the kinetic energy of the fluid implies that additional work must be done on the fluid to supply the extra energy, and vice versa.

Considering that the motion of a non-deformable body through an unbounded fluid otherwise at rest is a rectilinear translation at velocity, u , the kinetic energy can be expressed as:

$$E_k = \frac{1}{2}\rho I u^2 \quad , \quad \text{where} \quad I = \int_V \left(\frac{\mathbf{v}_i \mathbf{v}_i}{u \ u} \right) dV \quad , \quad (1.2)$$

and the integral I would be a simple invariant number.

If the velocity of the body is steady, the kinetic energy of the fluid remains constant in time even for unsteady and/or turbulent flows (in a statistical sense). If the body is accelerated the velocity at each point in the fluid relative to the body varies in direct proportion to the change in u : clearly the kinetic energy of the fluid also begins to increase. This means that additional work must be done on the fluid by the body in order to increase the kinetic energy of the fluid. The rate of additional work required is equal to the rate of change of the kinetic energy with time. This comes from the effect that an additional inertial force, F_I , is experienced by the body such that the work done by the body in the unit time $-F_I u$ is equal to dE_k/dt ; thus we can write the additional inertial term as:

$$F_I = -\rho I \frac{du}{dt} \quad . \quad (1.3)$$

The inertial force has the same form and sign as that required to accelerate the mass m of the body itself, namely $m(du/dt)$. Consequently, it is rational to consider the mass of fluid given by ρI as an added mass, denoted M_A , of fluid being accelerated ‘by’ the body, but not ‘with’ the body. The added mass, in fact, is not a concentrated mass attached to the centroid of the body, but it is distributed throughout the fluid set in motion by the body. Thus, its magnitude and centroid changes with time as the intensity and distribution of the kinetic energy of the fluid changes with time (Sarpkaya, 2004). In literature some authors speak about the added mass coefficient, which is defined as the ratio between the added mass and the mass of the fluid contained in the same volume of the moving body:

$$C_a = \frac{M_a}{\rho V} \quad . \quad (1.4)$$

Much has been written on the subject of added mass and a lot of work (both theoretically and experimentally) has been carried out to find the added mass for many different specific applications. Wendel (1956) made a review of the added mass found in literature and experimental verification for bodies with circular and elliptical cross sections, spheres and plates translating in an unconfined still fluid. He also found expressions for the added mass of bodies with a rectangular cross section and studied the apparent moment of inertia

occurring in rotational motions. A complete collection of added mass for many different geometry shapes and flow conditions can be found in (Brennen, 1982).

It came out that, for a single cylinder (radius R and length L), translating in an inviscid, unconfined and otherwise still fluid, the added mass is the mass of the fluid occupied by the cylinder:

$$M_a^{cylinder} = \rho\pi R^2 L \quad . \quad (1.5)$$

From the previous definition, it follows that the theoretical value (with unconfined potential flow hypothesis) of the added mass coefficient should be equal to unity ($C_a^{cylinder} = 1$).

For completeness, Imlay (1961) generalized the definition of the added mass considering, for a body of arbitrary shape, three translational accelerations $\partial u_j / \partial t (j = 1, 2, 3)$ and three rotational accelerations $\partial u_j / \partial t (j = 4, 5, 6)$. Thus the added mass expresses in a unified way the linear forces and moments F_i :

$$F_i = m_{ij} \frac{\partial u_j}{\partial t} \quad , \quad (1.6)$$

imposed on the body due to all six possible components of acceleration. Therefore, for the general case, there are 36 different added mass components, $m_{ij} (i, j = 1, 2, \dots, 6)$, which could be arranged in a squared matrix.

Imlay (1961) found that for ideal fluid, the added mass matrix is symmetric, so that only 21 added mass derivatives are necessary and sufficient to define completely the added mass properties of any body moving in any manner in an ideal fluid. Further simplifications arise from the existence of symmetries in the body shape; for instance for a body of revolution with symmetric fins, the added mass matrix reduces to only 6 different components: one for each kind of motion.

Konstantinidis (2013) revised the concept of added mass, by remarking that the added mass concept is usually misinterpreted by thinking that inertia force is:

$$\text{inertia force} = \text{added mass} \times \text{body acceleration}.$$

The above expression is incorrect unless the fluid far from the body is at rest. He made a new derivation of the added mass force in the frame of reference of the oscillating cylinder. He found that, even for a simple case of potential flow around a circular cylinder undergoing sinusoidal oscillation, the added mass gives rise to a complex non-harmonic inertial force in the same direction that the movement. On the light of these new outcomes, he stated that a better way to conceptualize the inertia force due to added mass is:

$$\text{inertia force} = \text{added mass} \times \text{added-mass acceleration}.$$

So, the physical meaning of the added mass could be revised as follows: as a body moves through a fluid, it displaces the fluid particles permanently in the direction of its motion; if the body accelerates, parts of the fluid close to the body will also accelerate

while being pushed aside by the body. Hence, an additional inertial force is required to accelerate this part of the fluid.

In an analogous way to the added mass, the presence of fluid around a body oscillating leads to an added damping effect on the structure dynamics. Even if the damping force acting on a submerged body is usually relatively small, it should be taken into account if detailed model of the fluid structure interactions is sought for. The damping has not a great influence on the resonance frequencies of the system, while it strongly affects the amplitude of the oscillations of the structure. The contributions to added damping are:

- Fluid viscosity
- Component impact
- Wave generation
- Acoustic generation.

The last two terms are forms of radiation damping: for instance, wave or acoustic energy generated radiate away from the submerged body. We do not expect a significant amount of acoustic energy generation for the structures and excitations of our concern. Wave generation is generally not important for fully submerged structures under seismic excitation. Component impact may be a significant source of damping for multiple structures situated in close patterns (typical of a fuel assembly), but for simplicity in a first approximation the impact between structures will be neglected. Therefore, in most of the cases of interest, fluid viscosity is the only source of damping.

[Taylor \(1952\)](#) proposed a model for the damping force which has been used as a reference by many authors ([Gosselin and De Langre, 2011](#); [Triantafyllou and Cheryssostomidis, 1985](#); [Païdoussis, 1966a](#); [Singh et al., 2012](#)). The model assumes that the damping force is the sum of two terms, a normal force plus a friction force depending on the inclination angles of the body with respect to the fluid flow.

1.2.2 Plate Structures

Fluid structure interaction of plates and flags (the plate has a finite density and bending stiffness) is a problem of practical importance in aerospace and nuclear engineering. In particular, the major concern is represented by the stability of plates (and flags) in axial flows. Already back in the 19th century, [Rayleigh \(1879\)](#), in a paper on the instabilities of jets, suggested that an infinite plate immersed in an axial flow is always unstable. After this first theoretical study, many different authors investigated the stability of plate structures (considering finite size) both theoretically and experimentally. ([Kornecki et al., 1976](#)) showed that a plate of infinite span, but finite chord is stable for some velocities smaller than a critical velocity.

It has been showed, that the behaviour of plate structures strongly depend on the aspect ratio (ratio between span and chord) of the plate itself. In particular, two models

have been developed for limit cases of small and big aspect ratio: lifting-surface theory, or slender body theory (Lighthill, 1971) and lifting line theory, or two dimensional theory (Wu, 2001).

Some authors tried to find the expression for the pressure jump across the plate coming to different expression which were showing similar results in term of the stability analysis. In particular, Lucey and Carpenter (1993) used a 3D wing theory in order to obtain an expression for the generalized fluid loading on a flexible plate (infinite span and finite chord); he identified 3 contributions to the fluid loading: aerodynamic inertia contribution, damping contribution and stiffness contribution.

Stability analysis of plates has also been dealt by using the concept of added mass (Yadykin et al., 2000; Liang et al., 2001; Jaiman et al., 2014). Yadykin et al. (2000) used energy conservation laws to calculate the added mass considering 1 single mode of vibration of the plate. He assumed that the variation of kinetic energy (dE_k/dt) could be written in two different ways, by using either the pressure load or the plate displacement:

$$\frac{dE_k}{dt} = - \int_0^H \int_0^l \frac{\partial h}{\partial t} \nabla p \, ds \, dy \quad , \quad \text{and} \quad \frac{dE_k}{dt} = M_a^{plate} \int_0^H \int_0^l \frac{\partial h}{\partial t} \frac{\partial^2 h}{\partial t^2} \, ds \, dy \quad , \quad (1.7)$$

where M_a^{plate} is the added mass of the plate, h is the lateral displacement, H and l are respectively is the chord and the span size. Equation 1.7 leads to the following expression for the added mass:

$$M_a^{plate} = - \frac{\int_0^H \int_0^l \frac{\partial h}{\partial t} \nabla p \, ds \, dy}{\int_0^H \int_0^l \frac{\partial h}{\partial t} \frac{\partial^2 h}{\partial t^2} \, ds \, dy} \quad . \quad (1.8)$$

Yadykin et al. (2000) demonstrated coherence with previous works in literature and showed the dependence of the non-dimensional added mass to the aspect ratio: decrease of the aspect ratio leads to a decrease of the added mass. It has been demonstrated as well that the higher the mode of vibration is, the smaller will be the added mass.

Later, Liang et al. (2001) extended the analysis to the first 6 modes of natural vibration for submerged cantilevered plates, validating the structural models of the simple beam theory and Euler-Bernoulli Beam to model the dynamic behavior of plates. Jaiman et al. (2014) extend the added mass model for plates by considering confinement effects.

A different approach has been used by Guo and Païdoussis (2000) which consists in using the Fourier space to solve the pressure distribution (which has been assumed to be continue everywhere except across the plate) along the plate. Later, Eloy et al. (2007, 2008); Doaré et al. (2011a); Eloy et al. (2010) extended the work of Guo and Païdoussis (2000) applying the same method to rectangular plates of variable aspect ratio with different boundary conditions. In particular, Doaré et al. (2011b) solved the pressure distribution in the Fourier space for plates in confined channel flow and they found a simple empirical expression for the pressure jump over the plate depending directly on the confinement size

and on the aspect ratio. The two limit cases of slender body approximation and large span approximation has been recovered, and it was established that for all aspect ratios, the pressure jump could be expressed as a linear combination of the two limit cases.

In conclusion, some of the most significant works in literature about fluid structure interaction of plates submerged in fluid were analysed in this section. The work of [Guo and Païdoussis \(2000\)](#); [Eloy et al. \(2007, 2008\)](#); [Doaré et al. \(2011b\)](#) is regarded with particular interest, since some of the methods presented by these authors (applied on plate structures), will be applied during the PhD work on cylindrical structures.

1.2.3 Cylindrical Structures

First studies on fluid structure interactions on cylinders date back to the 19th century. [Stokes \(1851\)](#), in fact, wrote down the solutions for simple bodies (sphere and cylinder) oscillating in an otherwise quiescent fluid. For the cylinder case, solutions are presented for an infinite cylinder oscillating with velocity $u = -A\omega \cos \omega t$ (with A a small amplitude) in an unlimited mass of fluid, in a direction perpendicular to its axis. Stoke's solution cannot be decomposed into an inviscid inertia force and a viscous force; both are affected by the diffusion of vorticity in which resides the memory of viscous fluids.

It took many years until [Morison et al. \(1950\)](#) proposed a force decomposition for the determination of wave force (meaning that the body is subjected to lateral flow) on a cylindrical object. The force is made up of two terms as follows:

$$F(t) = \frac{1}{2}\rho C_D |u| u + \rho C_M \frac{\pi D^2}{4} \frac{du}{dt} \quad , \quad (1.9)$$

where $F(t)$ is the inline force acting on the whole cylinder, represented as a velocity squared dependent drag force (first term) and an acceleration-dependent inertial force (second term). C_D and C_M are respectively the shape drag and inertial coefficients determined experimentally. Morison equation found its main applications in off-shore engineering.

Later on, [Lighthill \(1960a,b\)](#) also considered the problem of a body in an axial flow. Using the slender body theory, he wrote a simple expression for the forces acting on a cylinder vibrating in an axial flow (unconfined flow). The main idea behind the whole slender body theory is that when a body moving through a fluid satisfies the slenderness condition (the surface makes everywhere a small angle with its direction of motion) then the flow in any small region near the body approximates to a two-dimensional flow around a cylinder whose cross-section is the same as the local cross section of the body (see schematics in [Figure 1.4](#)). Now considering the above theory, this local two dimensional flow due to the displacements of cross sections is the irrotational flow which would result from the motion of a cylinder of constant cross section through the fluid, which has a local velocity $\mathbf{v}(x, t)$:

$$\mathbf{v}(x, t) = \frac{\partial w}{\partial t} + U \frac{\partial w}{\partial x} \quad , \quad (1.10)$$

where w is the displacement of the structure from the straight arrangement (see Figure 1.5), and U is the bulk flow velocity. The fluid momentum is commonly regarded as an effective added momentum to that of the cylinder itself, and therefore as a product of its velocity ($v = dw/dt$) and an added (or virtual) mass associated with the fluid, which corresponds to the mass of the fluid displaced by the presence of the body itself. The virtual mass per unit length of the body could thus be written as $\rho A(x)$ where $A(x)$ represents the cross section area of the body. Thus, the fluid momentum per unit length (q) is:

$$q = \rho A(x)v(x,t) \quad , \quad (1.11)$$

and the lift force per unit length (which is equal and opposite to the change rate of momentum) is:

$$F^L(x,t) = - \left(\frac{\partial q}{\partial t} + U \frac{\partial q}{\partial x} \right) \quad . \quad (1.12)$$

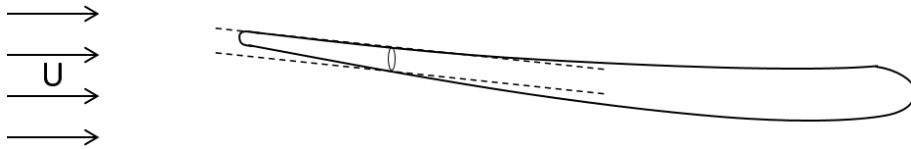


Figure 1.4 – Equivalence between flow near the body and near a cylinder of the same cross section

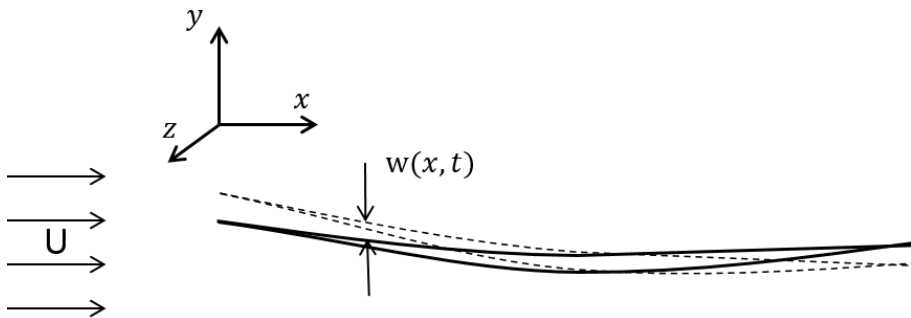


Figure 1.5 – Displacement of a body in axial flow from its initial position

Based on the work of [Lighthill \(1960b\)](#), [Païdoussis \(1966a,b\)](#) studied the dynamics of a flexible slender cylinder immersed in axially flowing fluid both theoretically and experimentally. The cylinder was considered isolated in a fairly large flow channel (confinement effects are not considered), thus the pressure drop due to the flow itself could be considered negligible. The flow velocity was assumed to be perfectly axial, uniform and steady. The potential flow theory is applied regarding the fluid modelling, while for the cylinder the Euler-Bernoulli beam theory is applied and the displacement of the cylinder is considered to be small (in comparison with the cylinder length). A simple summary of the Païdoussis model is given below, focusing on the force balance which leads to write the equation of

motion for a cylinder in axial flow.

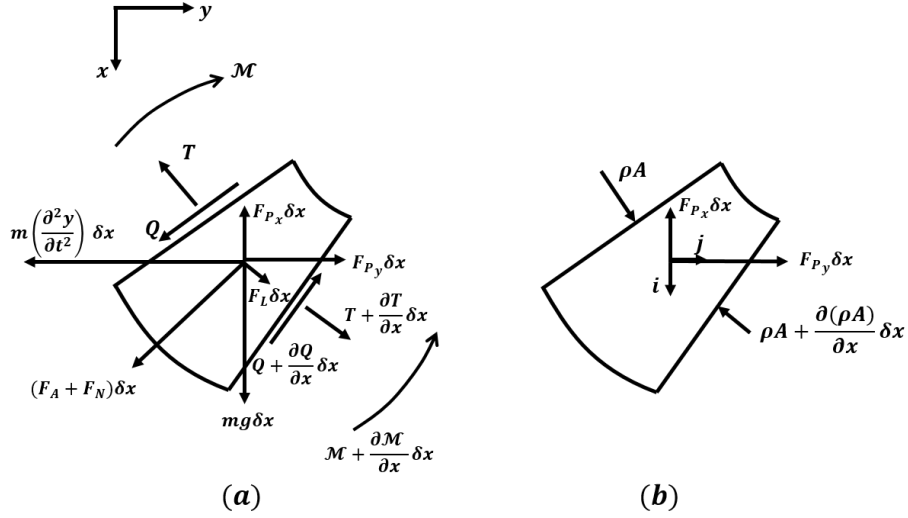


Figure 1.6 – (a) An element δx of the cylinder showing forces and moments acting on it; (b) an equivalent rigid element surrounded by fluid. (Païdoussis, 1973)

The forces and moments acting on an element δx of the cylinder undergoing small oscillations, $w(x, t)$ are shown in Figure 1.6(a), where F_A represents the inviscid hydrodynamic force, F_N and F_L are the viscous forces per unit length in the normal and longitudinal direction respectively, and F_{p_x} and F_{p_y} are the hydrostatic forces in the x and y direction respectively; Q is the lateral shear force, \mathcal{M} the bending moment, T the axial tension, and m the mass of the cylinder per unit length.

The inviscid force term is taken from Lighthill theory (Lighthill, 1960b) by putting together Equations 1.10, 1.11 and 1.12 leading to:

$$F_A = \left(\frac{\partial}{\partial t} + U \frac{\partial}{\partial x} \right) \left[M_a \left(\frac{\partial w}{\partial t} + U \frac{\partial w}{\partial x} \right) \right] , \quad (1.13)$$

where the M_a stands for the virtual or added mass of the cylinder and U is the bulk flow velocity. The virtual mass is equal to ρA for unconfined flow (A is the cross section area of the cylinder), while for a confined flow it increases as the diameter of the flow channel decreases (Chen and Wamnganss, 1972; Chen, 1985; Païdoussis and Pettigrew, 1979).

The frictional forces are taken essentially as proposed by Taylor (1952), which could be approximated, for small displacements (small $\partial w/\partial x$ and $(\partial w/\partial t)/U$) by:

$$F_N = \frac{1}{2} \rho D U C_N \left(\frac{\partial w}{\partial t} + U \frac{\partial w}{\partial x} \right) + \frac{1}{2} \rho D U C_D \frac{\partial w}{\partial t} ,$$

$$F_L = \frac{1}{2} \rho D U^2 C_T , \quad (1.14)$$

where C_N and C_T are the friction drag coefficients for normal and tangential frictions respectively, C_D is the shape drag coefficient and D is the cylinder diameter.

In order to determine the forces F_{p_x} and F_{p_y} (resultants of the mean pressure p acting on the external surface of the element), we can consider Figure 1.6(b) which represents the element of the cylinder momentarily frozen and immersed in fluid on all sides. The resultant of all the forces is known to be the buoyancy force and, by assuming that the pressure is a linear function of x , we can write:

$$-F_{p_x} = -\frac{\partial p}{\partial x}A + \frac{\partial(pA)}{\partial x} \quad , \quad F_{p_y} = \frac{\partial}{\partial x} \left(pA \frac{\partial w}{\partial x} \right) \quad . \quad (1.15)$$

After a balance of forces on both x and y directions, and considering Euler-Bernoulli theory for relating the lateral shear force and the bending moment ($Q = -\delta \mathcal{M} / \delta x$), Païdoussis got one of the most important results of his work: the equation of small lateral motion for a cylinder in unconfined flow, which writes as follows:

$$\begin{aligned} & \left(E^* \frac{\partial}{\partial t} + E \right) I \frac{\partial^4 w}{\partial x^4} + \rho A \left(\frac{\partial}{\partial t} + U \frac{\partial}{\partial x} \right)^2 w - \left\{ \delta [\bar{T} + (1 - 2\nu)(\bar{p}A)] \right. \\ & \quad \left. + \left[\frac{1}{2} \rho D U^2 C_T + (m - \rho A)g \right] \left[\left(1 - \frac{1}{2} \delta \right) L - x \right] + \frac{1}{2} \rho D^2 U^2 (1 - \delta) C_B \right\} \frac{\partial^2 w}{\partial x^2} \\ & + \frac{1}{2} \rho D U C_N \left(\frac{\partial w}{\partial t} + U \frac{\partial w}{\partial x} \right) + \frac{1}{2} \rho D U C_D \frac{\partial w}{\partial t} + (m - \rho A)g \frac{\partial w}{\partial x} + m \frac{\partial^2 w}{\partial t^2} = 0 \quad , \quad (1.16) \end{aligned}$$

where E and E^* are respectively the Young's modulus and the viscoelastic constant, I is the inertial momentum, \bar{p} is the mean value of the pressure at half height of the cylinder, \bar{T} is a general external imposed uniform tension, ν is the Poisson ratio, g is the gravitational constant (for most of the applications it could be neglected) and C_b is a form drag coefficient referred to the base of the cylinder. The δ takes into account the boundary condition, $\delta = 0$ if the downstream end is free to slide axially and $\delta = 1$ if the supports do not allow axial extension.

Equation 1.16 is a general formulation since it accounts also for gravity, and pressurization effects. If gravity, tensioning pressurization and dissipative effects are absent, the simple form of Equation 1.16 becomes:

$$EI \frac{\partial^4 w}{\partial x^4} + MU^2 \frac{\partial^2 w}{\partial x^2} + 2MU \frac{\partial^2 w}{\partial x \partial t} + F_v + (M + m) \frac{\partial^2 w}{\partial t^2} = 0 \quad , \quad (1.17)$$

Thanks to this equation, Païdoussis (1987) showed the similarity between the motion of a cylinder in external flow and the motion of a pipe conveying fluid.

Païdoussis used the general equation of lateral motion for a flexible cylinder in an axial flow in order to study its dynamics and its stability (Païdoussis, 1966a, 1973). It was demonstrated that small flow velocities damp the free motions of the cylinder and generally diminish its natural frequencies as compared to those in still fluid. For sufficiently high flow velocities, however, fluid-elastic instabilities may occur; both buckling (divergence) and oscillatory instabilities (flutter) are possible, the former generally occurring at lower

flow velocities than the latter. The effects of different boundary conditions (pinned-pinned, cantilevered, pinned-free cylinder) and of different system parameters has been studied, analysing the behaviour of the critical velocity (minimum flow velocity for the instability to occur). It was also shown that the oscillatory instabilities of inherently conservative systems are specifically caused by frictional forces.

Later this work was generalized to the case of towed quasi-cylindrical bodies (Païdoussis, 1968, 1970). It was found that similar behaviours are obtained in this case also, except that this system may also be subject to instabilities even at very low flow velocities, in its rigid-body modes of motion.

Païdoussis (1973); Païdoussis and Pettigrew (1979) extended the study to cylinders in axisymmetrically confined axial flow based on the work of Clasen (1972); Chen and Wamngans (1972). The main idea is that Equation 1.13 holds true also for a confined flow, but changing the added mass term to $M_a = \chi\rho A$ where $\chi = [(D_{ch}^2 + D^2)/(D_{ch}^2 - D^2)]$ and D_{ch} is the diameter of the confinement channel. Thus meaning that the added mass for a confined cylinder tends to increase as the confinement get smaller, and natural frequencies for confined cylinders are smaller than that for unconfined cylinders (maintaining the same parameters). In all these studies it was assumed that the flow velocity is perfectly axial, uniform and steady. Of course, this is never the case in practice, and it was observed that small amplitude vibration occurs at flow velocities well below those required to cause instability.

Païdoussis (1973); Païdoussis et al. (1977); Païdoussis and Suss (1977); Païdoussis (1979) further generalized its theory considering a cluster of N cylinders under axial flow. It has been shown that free motions are coupled, so that the different modes of the system are characterized not only by the axial modal shapes of each cylinder, but also by the cross-sectional patterns of motion involving all cylinders in the cluster. At low flow velocities, the eigenfrequencies of the system are in groups of $2N$, each group lying in the neighbourhood of one of the eigenfrequencies of an equivalent solitary cylinder. At higher flow velocities, the grouping of the eigenfrequencies becomes less well ordered. In terms of stability, although small flow velocities damp free motions of the system, at sufficiently high flows clusters with cylinders supported at both ends lose stability by buckling in one of the modes of the first-mode group. At any given flow velocity beyond the critical velocity for the onset of the first instability (u_{cb}), the system may be subjected to several buckling and flutter instabilities simultaneously. The further the cylinders are positioned from one another, the more closely spaced are the eigenfrequencies within the same group, and the smaller is the interval between the onset of, let us say, buckling in one mode and buckling in the next one. Furthermore, the more closely the cylinders are positioned, the lower the value of u_{cb} . The theoretical model, and the phenomena described above are strongly supported by experimental observations.

Later, Païdoussis (1975) made a first attempt to apply the theoretical models describing the behaviour of cylindrical a structure for modelling a string-like structure. In many design on nuclear industry, in fact, a number of fuel elements are assembled in bundles, and

bundles could be held together, forming a fuel string (it is the case of CANDU reactors). It is important to remark that the flexibility of a fuel string could be high, despite the high rigidity of its individual components. Starting from a kinetic energy balance (on the structure and on the fluid), he got an elementary modelling capable to catch the main features of a fuel string behaviour. It was found, as expected, that even at flow velocities much lower than those causing instabilities of fuel elements, the whole fuel string may be unstable, either in buckling or flutter. Thus, this model represented a first tool, for the designer, to improve the stability of the structure. For a complete description of Païdoussis' fluid structure interaction models of slender structures, the reader is referred to Païdoussis (1998, 2008).

Wamsganss et al. (1974) calculated a closed form solution for added mass and damping of a cylindrical rod vibrating in a viscous fluid enclosed by a rigid, concentric cylindrical shell. Comprehensive study has been done by Chen (1985) on fluid structure interactions applied on a single cylinder, a couple of cylinders and on a group of cylinders (axial-symmetric lattice). Both quiescent fluid or axial fluid flow has been considered, and viscous effects have also been considered. As other authors, most of the attention has been given to the stability analysis and to the determination of instability causes. In the same years, Dong (1978) made similar studies on added mass and damping coefficients landing to similar conclusion. There exists several similar works to the cited ones, but they will not be reported in this review.

Furthermore, Van Brummelen (2009) investigated the effects of a compressible flow on the added mass. The study outlined the big differences between compressible and incompressible flows, especially regarding computational aspects.

Later on, Divaret (2014); Divaret et al. (2011, 2013, 2014) studied the damping effects created by the fluid on rigid cylinders (both single or clusters). Since the structure is moving in a rigid manner, the oscillation of the cylinder in an axial flow could be seen as the cylinder fixed in his central position, and changing the inclination angle (α) with respect to the flow direction. The experimental work led to empirical correlations relating the damping forces to the angle of the cylinder with respect to the horizontal direction; a linear dependence on α has been found for small angles ($\alpha < 5^\circ$), while a quadratic dependence was observed for bigger angles. The application fields and limits of this should work should still be analysed.

In most recent years Païdoussis force model has been used to theoretically address fluid elastic instabilities of cylindrical structures subjected to axial flow (De Langre et al., 2007). Furthermore, modal characteristics and elastic instabilities of cylindrical structures are studied with numerical simulations by De Ridder et al. (2013, 2015). The model is than extended for clusters of cylinders under axial flow (De Ridder et al., 2017).

In conclusion, the previous paragraphs reported a summary of works which could be found in literature on fluid structures interaction. Different hypothesis and conditions have been considered depending on the specific needs and applications the authors intended to address. Several works on modelling the dynamical behaviour of cylinder structures both in

quiescent fluid or under axial flow were carried out. The case of multiple cylinders has been considered, starting from a couple of cylinders until considering a cluster of cylinders: only axial symmetrical geometries are considered and cylinders in each cluster are considered to be free to move independently. Some studies considered the situation of a confined flow, but only in the case of annular confinement. Most of the analysed works used the potential flow theory, with specific correction accounting for the different phenomena (typically viscosity and non-linearities).

Therefore, there is a lack of knowledge on the effects of any kind of confinement (rectangular shape for instance) on the dynamic behaviour of a cylinder under axial flow. Regarding groups of cylinders, squared lattice geometries should be better investigated, with the main objective of simplifying some complex existing models. For these reasons, one of the objectives of the PhD project described in this document is to study a simplified model for fluid structure interaction on cylindrical structure in rectangular confinement and arranged in squared lattice. Some of the approaches applied in literature for modelling fluid structure interactions on plates (Fourier transform) will be used in an analogous way on cylindrical structures.

1.3 Fuel Assembly and Reactor Core Modelling

There exists many fuel assembly models in literature. One can distinguish between linear and non-linear models. A brief bibliographic review on these models is carried out hereafter.

1.3.1 Linear Models

Linear models have been the first approach used to model the mechanical behaviour of fuel assemblies due to its simplicity. Some linear models consider the whole fuel assembly like a single beam representing both fuel rods, fuel grids and guide thimbles (Nuno et al., 1973; Kim et al., 1981). All the contacts between fuel grids and fuel rods are neglected by these models, and boundary conditions could be clamped (0 degrees of freedom) or simply supported conditions (2 degrees of freedom). The section of the equivalent beam is the sum of the sections of control rods and guide thimbles; the mass of the beam is the real mass of the fuel assembly.

Some other models represent the fuel assembly with two different beams : one modelling the fuel rods and the other one accounting for the structural elements (grids and guide thimbles). The two beams are held together by linear links (linear and rotational springs). The different kinds of links between the two beams give rise to many different models; some of them are described by Preumont et al. (1982), Preumont (1981), Johnson (1983) and Leroux et al. (1983). One of the models which better fits experimental results (even if it does not represent the physical reality of the problem) is the QUEVAL model (Queval, 1988) (Queval et al., 1991). The QUEVAL model uses a rotational spring to represent the grid constrain and its feature is to apply a modulation coefficient on the value of the elastic

constant of the spring which depends on the excitation amplitude.

In all cases, linear models cannot represent the variation of damping and frequency observed during vibration and snap back tests (Brochard et al., 1993). The model parameters have to be adjusted a priori for each loading. In the case of seismic excitation, which is not stationary, it is not easy to find the good adjustment of parameters able to represent the behaviour of an actual assembly.

1.3.2 Non-Linear Models

In order to have a better understanding of the real physical behaviour of fuel assemblies, non-linear models have been developed during the years. Brochard et al. (1993) developed a triple beam model, using two different kinds of beam: one beam is accounting for the structural components (grids and guide thimbles) and two beams, symmetrically disposed are accounting for the fuel rods. This non-linear model confirms the predictions of linear models for low frequency vibrations and well predicts the first resonance frequency depending on the excitation amplitude of the system. Nevertheless it does not catch dependencies of stiffness and damping coefficients on the excitation amplitude. Helen (1993) took into account the possibility of loss of contact between the fuel rods and the dimples of the grid using three different kinds of beams: 1 beam for the guide thimbles, 1 beam for the fuel grids and 2 beams for the fuel rods. Later, Fontaine (1999), developed a model of two beams taking into account the loss of contact between rods and grids by changing the rigidity and the forces holding the rods in the assembly grid. This model showed good agreement with experimental results for a single fuel assembly. Multi-beam models are not suitable for a description of the whole reactor. The huge amount of friction problems arising from these models, result in very difficult problems (and time consuming) to solve numerically. Broc et al. (2003) proposed a model with two degrees of freedom for each fuel assembly, accounting for the coupling between them, and then developed a linear model for the whole reactor core. Pisapia (2004) presented a single degree of freedom non-linear model based on the maximum likelihood principle for the empirical identification of the model parameters. This model qualitatively reproduces the main phenomena observed by experimental campaigns.

1.3.3 Porous Media Model

The state of the art model was proposed by Ricciardi (2008) and Ricciardi et al. (2009) using a porous media approach based on the Païdoussis theory (Païdoussis, 1966a). For the formulation of this model, the following assumptions are made: the fluid is assumed to be viscous, incompressible and Newtonian; gravity effects are considered to be negligible compared to viscous and inertial forces, thus they are neglected; the distance between fuel rods (inside fuel assembly) is assumed constant and the section of the fuel rods does not deform; the turbulent kinetic energy is considered negligible with respect to the turbulent diffusion. The model proceeds with the space averaging of the equations regarding the

fluid equations and a space averaging regarding the structure equations, thus obtaining an equivalent fluid model and an equivalent structure model which are then coupled together (as shown in Figure 1.7). Equations are written using an ALE approach (Duarte et al., 2004): the fluid is observed through a moving window which follows the motion of the structure. The structure is described by a Timoshenko beam model (Timoshenko, 1921).

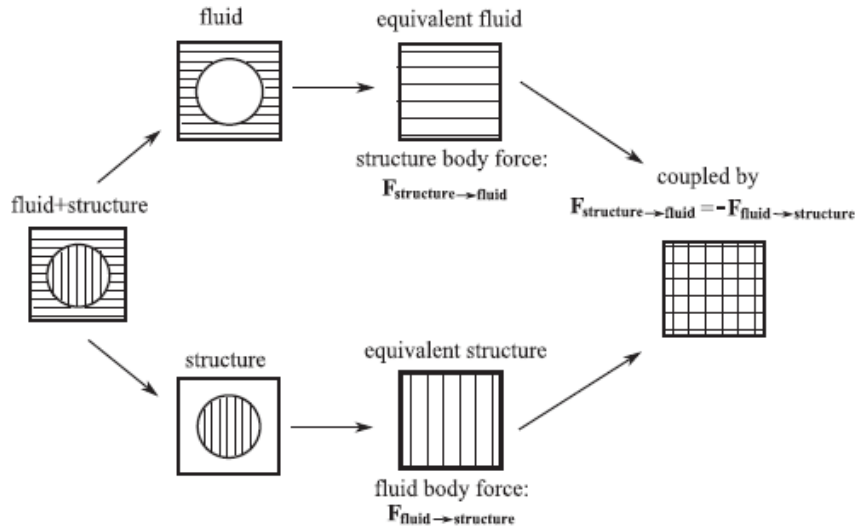


Figure 1.7 – Porous media approach (Ricciardi et al., 2009)

The model allows to avoid the large number of degrees of freedom necessary to make a direct numerical simulation of the fluid and structure dynamics. A fluid structure problem with a complex geometry (large number of rods linked by numerous contact friction points) has been transformed into a problem with a simpler geometry (equivalent beam for each fuel assembly). It then becomes possible to simulate both the fluid and the structure dynamics of a whole core. Some local informations are lost compared to a direct numerical simulation, such as vibrations of rods into grids, but interactions between fuel assemblies, via fluid or contacts, are conserved. Effects on the whole core of an external excitation can be simulated. The model showed good agreement with the experimental data. The effect of the fluid velocity on the damping of the structure is well reproduced, whereas the coupling between fuel assemblies is qualitatively reproduced.

1.4 Simplified Models

In the previous sections different models for the fluid structure interaction have been discussed. This section is devoted to the description of two simplified models: Euler Bernoulli beam theory for the structure and the potential flow theory for the fluid. Those theories will be used in next chapter for the derivation of the fluid structure interaction model developed during the PhD.

1.4.1 Euler Bernoulli Beam Theory

Euler Bernoulli beam theory is a simplification of the linear theory of elasticity which provides a means to calculate the load-carrying and deflection characteristics of beams. It covers the case for small deflections of a beam that is subjected to lateral loads only (Bauchau and J.I., 2009). It is thus a special case of Timoshenko beam theory (Timoshenko, 1953). The main assumption made in the Euler Bernoulli theory are:

- Ratio between the length of the bar and its thickness is relatively large (greater than 10);
- The cross-sections remain plane and orthogonal to the centreline;
- Each cross-section undergoes the same transverse deflection;
- The bending due to its own weight is neglected;
- The material behaves linearly;
- The deflections are small compared to the beam thickness;

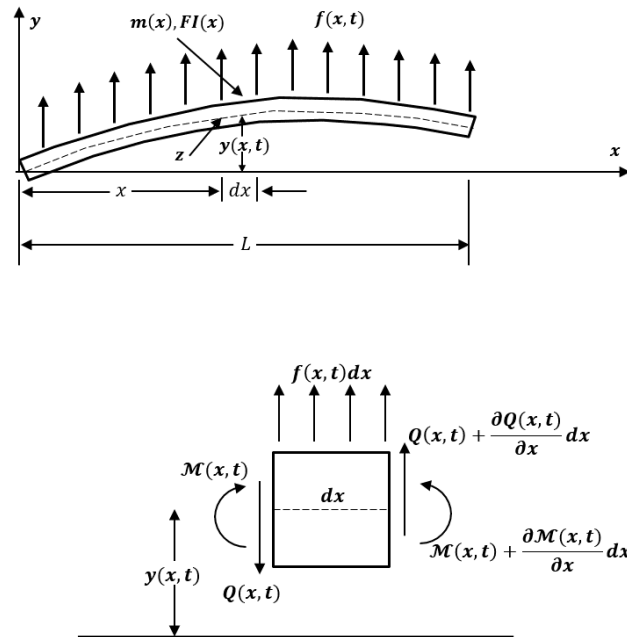


Figure 1.8 – Bending of an Euler Bernoulli Beam

Euler Bernoulli Beam Equations

We consider a generic beam in flexure and we note $w(x, t)$ the transverse displacement (along y direction) at any point x and time t and $f(x, t)$ the transverse force per unit length. The system parameters are the mass per unit length $m(x)$ and flexural rigidity

$EI(x)$. Consideration of the equilibrium of the forces and moments (see Fig. 1.8) yields to the following governing differential equation of motion:

$$m(x)\frac{\partial^2 w(x,t)}{\partial t^2} + \frac{\partial^2}{\partial x^2} \left\{ EI(x)\frac{\partial^2 w(x,t)}{\partial x^2} \right\} = f(x,t) \quad . \quad (1.18)$$

By considering the flexural rigidity and the section uniform along the whole length of the beam, Equation 1.18 reduces to:

$$m\frac{\partial^2 w(x,t)}{\partial t^2} + EI\frac{\partial^4 w(x,t)}{\partial x^4} = f(x,t) \quad . \quad (1.19)$$

Viscous damping $c(x)$ could be included in the equation, thus giving a complete equation on the form of:

$$m(x)\frac{\partial^2 w(x,t)}{\partial t^2} + c(x)\frac{\partial w(x,t)}{\partial t} + \frac{\partial^2}{\partial x^2} \left\{ EI(x)\frac{\partial^2 w(x,t)}{\partial x^2} \right\} = f(x,t) \quad . \quad (1.20)$$

Euler Bernoulli Beam Solutions

Since the problem involves a continuous system with linear behaviour, the Euler Bernoulli Beam equations can be solved using the mode superposition technique. In order to apply the superposition technique, it is necessary first to know the natural frequencies and corresponding mode shapes. The natural frequencies and mode shapes are obtained considering the homogeneous solution of the beam vibration equation (Equation 1.19) when no external load is applied, thus $f(x,t) = 0$. We obtain the free (undamped) vibration equation:

$$m\frac{\partial^2 w(x,t)}{\partial t^2} + EI\frac{\partial^4 w(x,t)}{\partial x^4} = 0 \quad . \quad (1.21)$$

Equation 1.21 can be solved with the assumption of the displacement being an harmonic vibrations of the form:

$$w(x,t) = \chi(x)e^{i\omega t} \quad , \quad (1.22)$$

where $\chi(x)$ is called the mode shape function and ω is the vibration circular frequency.

By substituting Equation 1.22 in Equation 1.21, we obtain a parametric differential equation:

$$\frac{d^4 \chi(x)}{dx^4} - \alpha^4 \chi(x) = 0 \quad , \quad (1.23)$$

where $\alpha = \left(\frac{m\omega^2}{EI}\right)^{\frac{1}{4}}$.

The general solution of Equation 1.23 can be written in the form of:

$$\chi(x) = A \sin(\alpha x) + B \cos(\alpha x) + C \sinh(\alpha x) + D \cosh(\alpha x) \quad , \quad (1.24)$$

where A, B, C, D are integration constants to be evaluated from boundary conditions. For a clamped clamped beam, boundary conditions are:

$$\chi(0) = 0; \quad \chi'(0) = 0; \quad \chi(L) = 0; \quad \chi'(L) = 0 \quad . \quad (1.25)$$

By substituting boundary conditions in Equation 1.24, we can represent in a matrix form the linear system given by boundary conditions as follows:

$$\begin{bmatrix} 0 & 0 & 1 & 1 \\ 1 & 0 & 1 & 0 \\ \sin(\alpha L) & \cos(\alpha L) & \sinh(\alpha L) & \cosh(\alpha L) \\ \cos(\alpha L) & -\sin(\alpha L) & \cosh(\alpha L) & \sinh(\alpha L) \end{bmatrix} \begin{bmatrix} A \\ B \\ C \\ D \end{bmatrix} = \begin{bmatrix} 0 \\ 0 \\ 0 \\ 0 \end{bmatrix} \quad . \quad (1.26)$$

In order to have non trivial solutions, the determinant of the boundary condition matrix is set to zero, thus giving the following characteristic equation:

$$\cos(\alpha x) \cosh(\alpha x) = 1 \quad . \quad (1.27)$$

The previous transcendental equation has infinite solutions which can be calculated numerically. The solutions of the Equation 1.27 are represented by α_n where n indicates the n^{th} mode. In Table 1.1 are shown computations of the first 5 solutions of the characteristic equation for a fixed fixed beam. Once the solutions of the characteristic equation are known, we can calculate the solutions for the displacement, which are also called Mode Shape Functions:

$$\chi_n(x) = A_1 \{ \cosh(\alpha_n x) - \cos(\alpha_n x) - \beta_n [\sinh(\alpha_n x) - \sin(\alpha_n x)] \} \quad , \quad (1.28)$$

where $\beta_n = \frac{\cos(\alpha_n L) - \cosh(\alpha_n L)}{\sin(\alpha_n L) - \sinh(\alpha_n L)}$ and A_1 is a parameter depending on initial conditions. A_1 is usually set to the unity, thus a multiplication constant will appear in the time dependent function, which will be determined by using boundary conditions.

From the definition of α , we can now calculate the natural circular frequencies of vibrations, which are defined as follows:

$$\omega_n = \alpha_n^2 \sqrt{\frac{EI}{m}} \quad . \quad (1.29)$$

The natural frequencies of the beam correspond to the frequencies around which resonance can occur. The most important property of the normal modes is that of orthogonality. This property makes possible the uncoupling of the equations of motion for different modes. Normal modes satisfy the following equations:

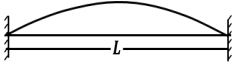
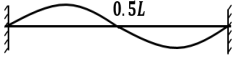
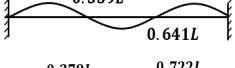
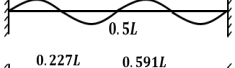

n	$\alpha_n L$	β_n	Shape
1	4,730042	0.98250221	
2	7,853203	1.00077731	
3	10,99561	0.99996645	
4	14,13716	1.00000145	
5	17,27876	0.99999994	

Table 1.1 – Mode Shape Solutions for Fixed-Fixed Beam

$$\int_L m(x)\chi_n(x)\chi_m(x) dx = \begin{cases} 0 & \text{for } n \neq m \\ M_n & \text{for } n = m \end{cases} \quad (1.30)$$

$$\int_L \frac{d^2}{dx^2} \left[EI(x) \frac{d^2 \chi_n(x)}{dx^2} \right] \chi_m(x) dx = \begin{cases} 0 & \text{for } n \neq m \\ K_n & \text{for } n = m \end{cases} \quad (1.31)$$

$$(1.32)$$

where M_n is called modal mass and K_n is called the modal stiffness of the n_{th} mode.

Finally, we can affirm that the solution for the free vibration of an Euler-Bernoulli beam is given by the sum:

$$w(x, t) = \sum_{n=1}^{\infty} \Re (K_n \chi_n(x) e^{-i\omega_n t}), \quad K_n \in \mathbb{C} \quad (1.33)$$

Now, having obtained natural frequencies and mode shapes, we can solve the problem for vibrations of an Euler-Bernoulli beam under an external load (Equation 1.18) by using the mode superposition technique. The solution for the transverse displacement of a beam under a general external load can be written as:

$$w(x, t) = \sum_{n=1}^{\infty} \chi_n(x) \eta_n(t) \quad , \quad (1.34)$$

where $\eta_n(t)$ are the generalized time-dependent coordinates.

Assuming the beam is under a time-varying distributed external load $f(x, t)$, which can be expressed as function of the mode shapes by:

$$f(x, t) = \sum_{n=1}^{\infty} \chi_n(x) f_n(t) \quad , \quad (1.35)$$

we can write the general equations of motions for an Euler Bernoulli beam (expressed by

Equation 1.20) as follows:

$$\sum_{n=1}^{\infty} \left\{ \frac{d^2}{dx^2} \left[EI(x) \frac{d^2 \chi_n(x)}{dx^2} \right] \eta_n(t) + c(x) \chi_n(x) \dot{\eta}_n(t) + m(x) \chi_n(x) \ddot{\eta}_n(t) \right\} = \sum_{n=1}^{\infty} \chi_n(x) f_n(t) \quad , \quad (1.36)$$

where $\dot{\eta}_n(t)$ and $\ddot{\eta}_n$ are respectively the first and second time derivative of the generalized coordinates. Multiplying both sides of Equation 1.36 by the k^{th} mode shape, integrating in the domain of the beam and applying orthogonality condition of normal modes – assuming that orthogonality Equation 1.31 holds for viscous damping too, that is when $m(x)$ is replaced by $c(x)$ –, the partial differential equation of motion can be turned into a collection of uncoupled ordinary differential equations of motion:

$$\ddot{\eta}_k(t) + 2\xi_k \omega_k \dot{\eta}_k(t) + \omega_k^2 \eta_k(t) = Q_k(t) \quad , \quad (1.37)$$

where ξ_k is the modal damping ratio expressed by:

$$\xi_k = \frac{1}{2\omega_k} \frac{\int_L c(x) \chi_k^2(x) dx}{\int_L m(x) \chi_k^2(x) dx} \quad , \quad (1.38)$$

and Q_k is the generalised force for the k^{th} mode whose expression is given by:

$$Q_k(t) = \sum_{n=1}^{\infty} \frac{\int_L \chi_k(x) \chi_n(x) dx}{\int_L m(x) \chi_k^2(x) dx} f_n(t) \quad . \quad (1.39)$$

In most cases, mass per unit length m , flexural rigidity EI and viscous damping c do not vary along the beam. Orthogonality of modes can then be expressed as follows

$$\int_L \chi_n(x) \chi_m(x) dx = 0 \quad \text{for } n \neq m \quad (1.40)$$

$$\int_L \frac{d^2}{dx^2} \left[\frac{d^2 \chi_n(x)}{dx^2} \right] \chi_m(x) dx = 0 \quad \text{for } n \neq m \quad (1.41)$$

and above equations can be simplified as follows:

$$\xi_k = \frac{1}{2\omega_k} \frac{c}{m} \quad , \quad (1.42)$$

$$Q_k(t) = \frac{1}{m} f_n(t) \quad . \quad (1.43)$$

Theoretically, infinite number of modes for the continuous systems are possible. However, contribution of higher modes towards the response is negligible; hence in computations only first few modes are considered.

1.4.2 Potential Flow Theory

In previous discussions the concept of potential flow theory has been introduced. In fluid dynamics, potential flow theory describes the fluid flow as inviscid and irrotational. These two simple but strong hypotheses imply huge simplification in the fluid dynamics equations, has one could catch by the statement of [White \(1998\)](#):

"When a flow is both frictionless and irrotational, pleasant things happen".

The main outcome of the potential flow theory is that we can write velocity field of the fluid flow, which is a vector field as function of a single scalar function.

By definition for irrotational flow:

$$\nabla \times \mathbf{v} = 0 \quad . \quad (1.44)$$

Therefore, we can relate the velocity vector to a potential function $\phi(x, y, z)$ as follows:

$$\mathbf{v} = \nabla\phi \quad . \quad (1.45)$$

The potential function $\phi(x, y, z)$ is called velocity potential and components of the velocity in Cartesian coordinates are:

$$\mathbf{v}_1 = \frac{\partial\phi}{\partial x}\mathbf{e}_x \quad , \quad \mathbf{v}_2 = \frac{\partial\phi}{\partial y}\mathbf{e}_y \quad , \quad \mathbf{v}_3 = \frac{\partial\phi}{\partial z}\mathbf{e}_z \quad . \quad (1.46)$$

Since the velocity must satisfy the conservation of mass equation, we can write (for incompressible fluid):

$$\frac{\partial v_1}{\partial x} + \frac{\partial v_2}{\partial y} + \frac{\partial v_3}{\partial z} = 0 \quad , \quad (1.47)$$

and by replacing the velocities with the velocity potential one can write:

$$\frac{\partial^2\phi}{\partial x^2} + \frac{\partial^2\phi}{\partial y^2} + \frac{\partial^2\phi}{\partial z^2} = 0 \quad \Rightarrow \quad \nabla^2\phi = 0 \quad . \quad (1.48)$$

Therefore, potential flow problems simply reduce to the solutions of Laplace equation. In these problems all the physics is governed by boundary conditions. Since our concern are cylindrical structures, here after is reported the Laplace equation for cylindrical coordinates:

$$\mathbf{v} = v_r\mathbf{e}_r + v_\theta\mathbf{e}_\theta + v_z\mathbf{e}_z = \frac{\partial\phi}{\partial r}\mathbf{e}_r + \frac{1}{r}\frac{\partial\phi}{\partial\theta}\mathbf{e}_\theta + \frac{\partial\phi}{\partial z}\mathbf{e}_z = \nabla\phi \quad , \quad (1.49)$$

$$\nabla^2\phi = \frac{1}{r}\frac{\partial}{\partial r}\left(r\frac{\partial\phi}{\partial r}\right) + \frac{1}{r^2}\frac{\partial^2\phi}{\partial\theta^2} + \frac{\partial^2\phi}{\partial z^2} = 0 \quad . \quad (1.50)$$

This outcome is one of the most important consequences of the potential flow theory, which allows huge simplifications of the fluid mechanics equations. External flows can be

treated as inviscid and irrotational because viscous effects are limited to a thin layer next to the body called the boundary layer and in many cases could be neglected. For more accurate models, boundary layer theory should be applied (Ackroyd et al., 2001).

Since Laplace equation is linear, the superposition of different potential flows is still a potential flow. Thus, in literature, potential flows have been solved for very simple flow structures like uniform stream, sink source, vortex sources, line sources, etc... (Houghton et al., 2012). The potential for the flow around a cylinder, for instance, could be seen as the superposition of a uniform stream in the x direction, a doublet located at the origin pointing in the $-x$ direction, and a vortex located at the origin. Thus, the potential for such a system will be the sum of the potentials of each simple problem (indirect method).

First applications of potential flow theory concern spatial application and aerodynamic flows. Taylor (1894); Fuhrmann (1911); Von Karman (1930) solved the problem of potential flow about a body of revolution using two different methods, an indirect method (used by Taylor and Fuhrmann) who computed the pressure distribution by the method of sources and sinks and a direct method (used by Von Karman) which directly calculated pressure distribution over a given streamline shape. Munk (1924) demonstrated that all aerodynamic flows are potential flows since they could be seen as the superposition of many infinitely small impulsive pressures (which give rise to potential flows). It has also been shown that for each body immersed in a fluid, there exists only one potential flow.

Later, Hess and Smith (1967); Nakayama and Patel (1978) used potential flow theory for representing bodies of revolution in an axial water flow and they showed that for a large class of bodies, the pressure distribution obtained from the potential flow velocity distribution is in good agreement with the real flow. This study spread out the use of potential flow theory in many fields of industry concerned by fluid structure interactions (space industry, naval industry, energy and nuclear industry). Also biology used potential flow theory in order to describe for example the locomotion of fishes and birds or even the blood flow in veins.

1.4.3 Bernoulli Equation

In order to solve Laplace equation for potential flow, boundary conditions are needed. The boundary condition are also known in terms of pressure distribution on the boundaries of the problem. Thus, fluid mechanics equations relating the pressure distribution to the velocity potential are needed.

Starting from the general Navier-Stokes equation:

$$\rho \frac{D\mathbf{v}}{Dt} = -\nabla p + \rho \mathcal{F} + \mu \nabla^2 \mathbf{v} \quad , \quad (1.51)$$

and applying the hypotheses of no frictional forces ($\mu = 0$), incompressible flow ($\rho = \text{const}$) and neglecting external forces ($\mathcal{F} = 0$) one obtains the Bernoulli equation:

$$\frac{D\mathbf{v}}{Dt} = -\frac{\nabla p}{\rho} \quad , \quad (1.52)$$

where $D\mathbf{v}/Dt$ stays for the substantial derivatives which is equal to the local derivative $(\partial/\partial t)$ plus the convective derivative $(\mathbf{v} \cdot \nabla)$.

Since from linear algebra:

$$\mathbf{v} \cdot \nabla \mathbf{v} = \frac{1}{2} \nabla(\mathbf{v} \cdot \mathbf{v}) - \mathbf{v} \times (\nabla \times \mathbf{v}) = \frac{1}{2} \nabla \|\mathbf{v}\|^2 - \mathbf{v} \times (\nabla \times \mathbf{v}) \quad , \quad (1.53)$$

and from irrotational hypothesis $(\nabla \times \mathbf{v} = 0)$, Bernoulli equation could be reformulated as:

$$\frac{\partial \mathbf{v}}{\partial t} + \frac{1}{2} \nabla \|\mathbf{v}\|^2 = -\frac{\nabla p}{\rho} \quad . \quad (1.54)$$

Velocity potential could be at this moment put in Equation 1.54 obtaining thus the Bernoulli equation for velocity potential flow:

$$\nabla \left(\frac{\partial \phi}{\partial t} + \frac{1}{2} |\nabla \phi|^2 \right) = -\frac{\nabla p}{\rho} \quad . \quad (1.55)$$

Linearised Bernoulli Equation

Since, for construction, potential flow theory assumes linearity of the equations, we could assume that a small disturbance \mathbf{v}' is superposed to the uniform flow \mathbf{v}_∞ , giving rise to a perturbation pressure field p' which itself superposes to a bulk pressure term p_∞ . In an analogous way, the velocity potential is given by a free stream term ϕ_∞ and a local perturbation term ϕ' . In these conditions, the quadratic term in Equation 1.55 could be linearised to the first order as follows:

$$|\nabla \phi|^2 = |\nabla(\phi_\infty + \phi')|^2 \approx |\nabla \phi_\infty|^2 + 2\nabla \phi_\infty \cdot \nabla \phi' \quad , \quad (1.56)$$

thus, by making an integration on the whole domain and considering that bulk terms cancel out for the steady state Bernoulli equation, we get to the linearised Bernoulli expression:

$$\frac{\partial \phi'}{\partial t} + \nabla \phi_\infty \cdot \nabla \phi' = -\frac{p'}{\rho} \quad . \quad (1.57)$$

Equation 1.57 will be used in Chapter 3 in order to find the equations allowing to solve the fluid problem.

Chapter 2

Fuel Assembly Vibrational Experiments

This chapter is devoted to experimental works on fluid structure interaction applied to fuel assemblies. First, previous experimental works and their main results will be illustrated. Later the ICARE experimental facility will be illustrated in details and the experimental campaigns performed on the facility will be presented. Main experimental results will be presented and discussed. The last part of the chapter is dedicated to the laser velocimetry techniques implemented on the ICARE experimental facility, and some results will be discussed.

Experimental results and analysis will be further used in Chapter 4 in order to be compared with the numerical calculations performed with a simple model (potential flow assumption) aiming to reproduce the experimental results. The experimental results will be then used to validate the model, to understand its limits and to perform a critical analysis of the involved phenomena.

2.1 Previous Experimental Works

During the last decades several experimental facilities have been realised in France at CEA (Alternative Energies and Atomic Energy Commission) in order to study the fluid structure interaction phenomena involving nuclear fuel assemblies. Since it would be complicated and very expensive to reproduce a scale one nuclear core, different facilities have been constructed during the years scaling some of the parameters (number of assemblies, size of assemblies, pressure, temperature, etc.). Hereafter a brief review of the previous experimental works is presented.

2.1.1 EROS

The first experimental tests were realised in 1990 on the EROS experimental facility ([Brochard, 1993](#)). The main objectives of this experimental campaign were to under-

CHAPTER 2. FUEL ASSEMBLY VIBRATIONAL EXPERIMENTS

stand the main phenomena involved when fuel assemblies are excited. The facility is made of 5 reduced scale (6×6 lattice) fuel assemblies mock ups placed on a shaking table. These preliminary tests showed that the assembly can be modelled as non-linear beams (Queval et al., 1990a,b).

2.1.2 ECHASSE

Later, the test section ECHASSE was built in 1999 (Pont, 1998). Two reduced scale fuel assemblies (8×8) are put under a water axial flow. The experimental facility was built in order to study impact forces between the assemblies and between assemblies and test section walls. The shocks were induced by the displacement of an assembly from its equilibrium position and a consequent fast release. The assembly going back to its equilibrium position was impacting either the other assembly or the wall of the structure. Different experimental campaigns were realised, allowing to develop a model for the impact forces depending on the water flow rate (Collard, 2000; Vallory, 2000, 1999).

2.1.3 CADIX

Few year later, a new experimental facility called CADIX was realised. For the first time the experimental facility was involving full scale fuel assemblies. The test section consisted in a row of six fuel assemblies in stagnant water (or air) put on a shaking table. CADIX has been used in order to study impact forces (Queval, 2002). The experimental results were used in order to validate numerical codes. Effect of confinement size were also investigated (Broc, 2001).

2.1.4 COUPLAGE

The next step in the experimental research on fluid structure interactions of fuel assemblies, passes through the realization of COUPLAGE, an experimental facility involving a three-dimensional arrangement of the fuel assemblies. COUPLAGE was made of 9 fuel assemblies (3×3) in a highly reduced scale (4×4 lattice). The assemblies were held together by only one spacer grid, placed in the middle. Only one of the 9 assemblies is excited by an hydraulic jack with a sinusoidal input. Even though the geometry of the experimental facility is not representative of a nuclear reactor core, and the assemblies scale is too small to be able to well represent a real nuclear fuel assembly, the COUPLAGE experiments allowed to study coupling force between the fuel assemblies and to outline the presence of non negligible interaction forces between assemblies placed on different rows (Ricciardi, 2008). Since the facility is not well representative of reactor conditions, further experimental structure are required in order to better understand the involved phenomena.

2.1.5 HERMES

In order to study the dynamical behaviour of real fuel assemblies two experimental facilities using scale one fuel assemblies (made of depleted uranium) were constructed: HERMES P and HERMES T. The first test section HERMES P can host only one fuel assembly in reactor operational conditions (155 *bar* and 330 °C). It was designed in order to analyse the pressure drops along real fuel assemblies and to be able to validate new designs for fuel assemblies and to ensure the compatibility between fuel assemblies with different designs. On the other side, HERMES T has loop conditions lower than real operative conditions (55 *bar* and 50 °C) but can host 2 scale one fuel assemblies. Furthermore, one of the two assemblies can be excited by an hydraulic jack, and the walls of the structure have transparent portholes allowing to perform laser velocimetry measurements. The displacement of the assemblies and the applied force are measured. Experimental campaigns on this facility allowed to measure the stiffness and the damping coefficients in order to quantify the effect of the water flow on the added mass, added stiffness and added damping and to analyse the frequency response of a real nuclear fuel assembly (Boccaccio, 2010, 2011, 2012a,b). Some laser measurements of the fluid velocity field were performed.

2.1.6 Summary on Previous Experimental Works

All the previous experimental works are summarised in Table 2.1.

From this quick overview of the previous experimental works performed on the study of fluid structure interactions on fuel assemblies, we can conclude that the impact force between fuel assemblies have been widely investigated during the years on different scales. On the other hand, the coupling phenomena involving different fuel assemblies have only been investigated on a small experimental structure (COUPLAGE) using very simplified fuel bundles (3 grids, 4 × 4 lattice) which are not representative of real fuel assemblies.

For these reasons a new experimental facility has been designed and constructed at CEA Cadarache: ICARE. The main objective of this experimental facility is to study the coupling between different fuel assemblies depending on the confinement size and on the flow velocity. The fuel assemblies are not on real size (half length), but they are more representative of real fuel assemblies (6 grids and 8 × 8 lattice rods). The ICARE experimental facility will be illustrated in the next section. Finally the experimental results will be discussed.

2.2 ICARE Experimental Facility

The ICARE experimental facility has been realised in CEA during the PhD of S. Clement. A global description of the facility will follow in this section as a matter of clarity for the understanding of experimental results. For details on the design of each components of the facility the reader is referred to Clement (2012a,b, 2014).

Facility	Objectives	Limitations
EROS	Evaluating impact forces on a line of fuel assemblies	Reduced scale assemblies No water flow
ECHASSE	Evaluating impact forces under axial flow	Only 2 assemblies Large By-pass
CADIX	Evaluating impact forces on a real fuel assembly	No water flow Assemblies on a single line
COUPLAGE	Evaluating coupling between fuel assemblies	Highly reduced scale assemblies: not representative Assemblies are not free to move
HERMES	Identification of modal parameters of a real fuel assembly (DEDALE campaigns)	Only one fuel assembly

Table 2.1 – Summary of previous experimental facilities

The ICARE experimental facility is constituted of a closed water loop made of a centrifugal pump, the test section, a compensation tank and an heat exchanger to keep the temperature constant. The test section is placed in vertical position with a square section of $22.5\text{ cm} \times 22.5\text{ cm}$ and hosts up to 4 fuel assemblies arranged in a 2×2 lattice. The fuel assemblies length is 2.57 m , about half of the real fuel assemblies. Each of them is constituted of a squared lattice of 8×8 rods, in which there are 60 rods simulating fuel rods (made of stainless steel or poly-methyl-methacrylate) and 4 stainless steel guide tubes. The guide tubes are empty inside, and they are welded to 5 metallic spacer grids along the length of the assembly. The guide tubes have a structural function since they give rigidity to the assembly and they hold together fuel rods. In the real fuel assembly, the control rods can be inserted inside the guide tubes. Each assembly has a section of $10.1 \times 10.1\text{ cm}^2$, and the 64 rods constituting it have a diameter of 9 mm (see Figure 2.2). The top and bottom of the assembly are rigidly fixed to the guide tubes, and they are fixed to the test section through the LSP (Lower Support Plate) and the USP (Upper Support Plate). A scheme of the whole experimental facility is represented in Figure 2.1.

An hydraulic jack allows to excite one of the four fuel assemblies. For these experiments

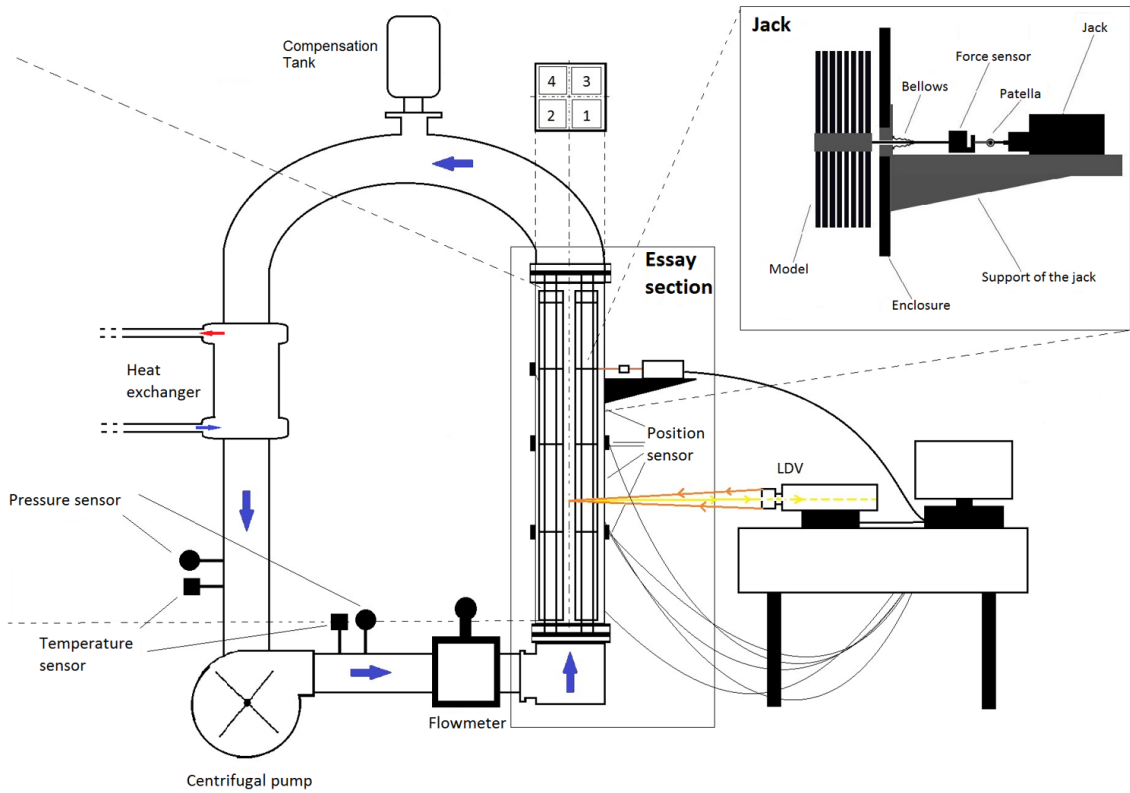


Figure 2.1 – Scheme of the ICARE Experimental Facility

the right assembly in front of the door is excited, but the hydraulic jack can be placed on every position. The hydraulic jack is attached to one of the grid of the fuel assembly through a screw, and a force sensor is installed in between the hydraulic jack and the stem. The force sensor (SM-S by PM Instrumentation) has a range from -500 N up to 500 N with an accuracy of 0.045% of the full scale, meaning an uncertainty of $\pm 0.225\text{ N}$. The hydraulic actuator is also equipped of a position sensor ($\pm 10\text{ mm}$ range and $\pm 0.03\text{ mm}$ uncertainty). The force sensor will allow to measure the applied force, but it is not used in order to control the hydraulic jack. The control system uses the position sensor since its precision is much higher than the one of the force sensor. The hydraulic jack can be attached to two different grids, grid number 3 and grid number 4 (see Figure 2.2). The possibility to excite the assembly on the middle grid and on the upper grid allows to excite different natural modes. When the hydraulic jack is attached to the middle grid, only the even modes will be excited, while when it is attached to the upper grid both even and odd modes will be excited.

The test section is equipped with 24 LVDT (Linear Variable Differential Transformer) position sensors. The LVDT sensors (model D5/300AW by PHIMESURE) have a working range of $\pm 7.5\text{ mm}$ and an uncertainty of $\pm 0.0225\text{ mm}$ (0.3% of full scale). The position sensors are installed at the level of the 2^{nd} , 3^{rd} and 4^{th} grid. The first and the last grids are not instrumented since they are close to the support plate and they are supposed not to

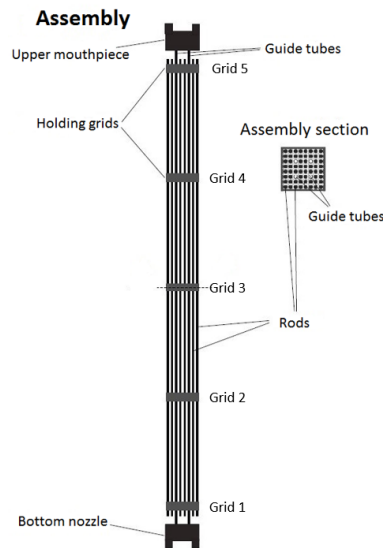


Figure 2.2 – Scheme of the ICARE assembly

move. For each spacer grid there are two position sensors, one monitoring the displacement on the x-direction and the other one on the y-direction, as represented in Figure 2.3. The sensor called CDDV is the LVDT which is placed inside the hydraulic actuator. Finally the test section is also equipped with some pressure sensors in order to control the pressure drops along the section and the uniformity of the flow along the different assemblies. One pressure sensor aiming to measure the pressure drops all along the test section has a range of $0 - 620 \text{ hPa}$ with $\pm 150 \text{ Pa}$ uncertainty. Four pressure sensors for measuring the asymmetries of the flow have a range of $0 - 60 \text{ hPa}$ with 4 Pa uncertainty. Finally one pressure sensor has the objective of measuring very small pressure asymmetries and has a range of $0 - 750 \text{ Pa}$ with $\pm 0.81 \text{ Pa}$ uncertainty. Furthermore, in order to know the loop parameters, a temperature sensor and a static pressure sensor are installed at the inlet and outlet of the pump. In addition, a flow meter is installed on the loop, allowing to know the water flow rate circulating in the test section. The displacement sensors and the force sensor are collected with a sampling frequency of 2 kHz , while loop parameters are sampled at about 1 Hz . Data are collected with the software TRIDENT. In Figure 2.4 pictures of the whole test section, the displacement sensor sealing system and the hydraulic jack connection system are presented.

A specific characteristic of the ICARE experimental facility is the modular design which allows to choose between two different confinement sizes. The large confinement configuration leaves a 8 mm gap between the fuel assemblies and the walls and between each fuel assembly; the small confinement, instead, leaves only a 4 mm gap. Furthermore, plastic slabs are available in order to substitute fuel assemblies and to create configurations with one, two or four fuel assemblies. This modular design gives rise to six different possible configurations of the test section, which are represented in Figure 2.5. The configuration

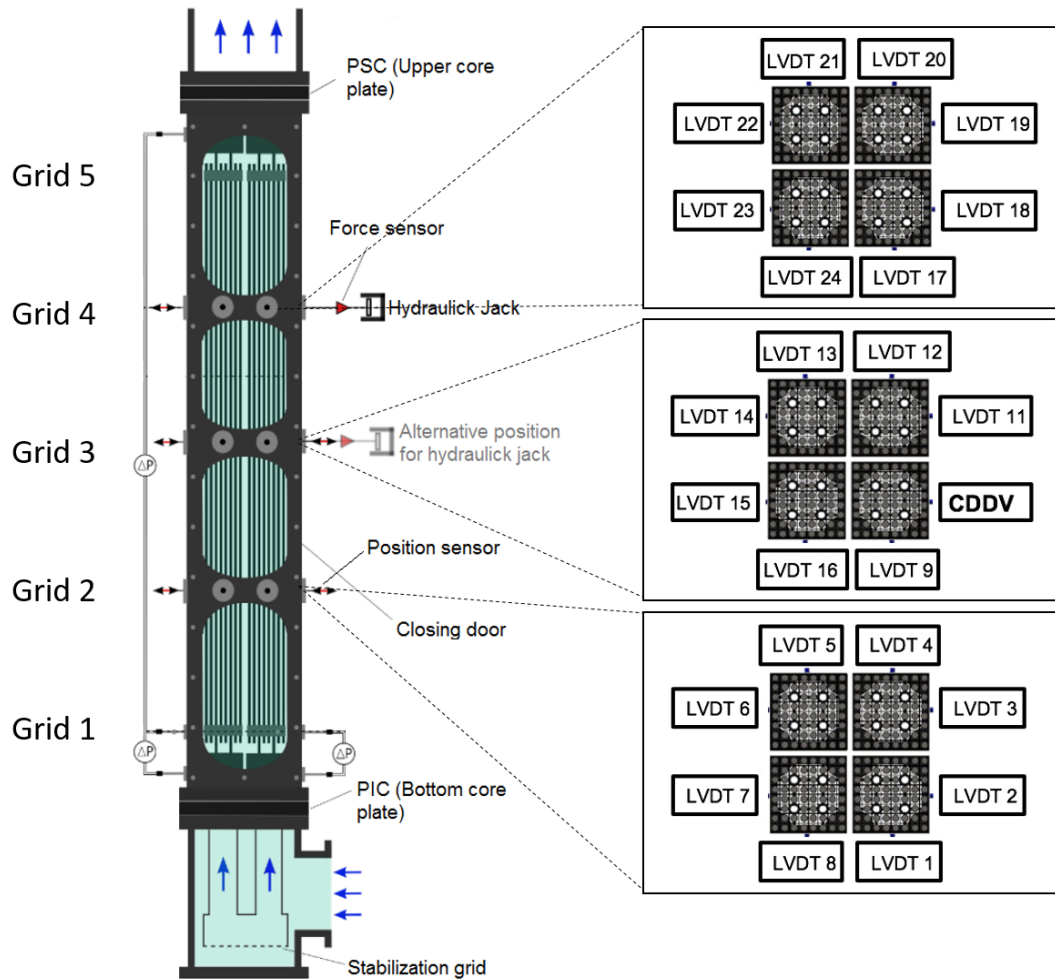


Figure 2.3 – Scheme of the displacement sensors on the ICARE test section

with a single assembly will not be used for our experimental campaigns.

Another parameter that can be changed on the test section is the material of the fuel assemblies. In fact, two different set of assemblies exist: one with stainless steel rods and the other one with PMMA (Poly-Methyl-MethAcrylate) rods. Since the physical properties of the two materials are very different each other, the mechanical and dynamical behaviour of the two assemblies will be very different. The steel assemblies will have the rigidity and the weight which is comparable (taking into account scaling factors) to the real fuel assemblies. However, the length of the structure and the grids are quite different. Since one of the main objectives of the experimental campaigns run on the ICARE facility is to characterize and measure fluid forces induced by the movement of the structure the use of PMMA assemblies results to be fundamental. The rigidity of the PMMA is much smaller than that of the steel, allowing thus to maximize the ratio between the fluid forces and the structural forces (fluid forces become easier to measure). Furthermore, PMMA

CHAPTER 2. FUEL ASSEMBLY VIBRATIONAL EXPERIMENTS

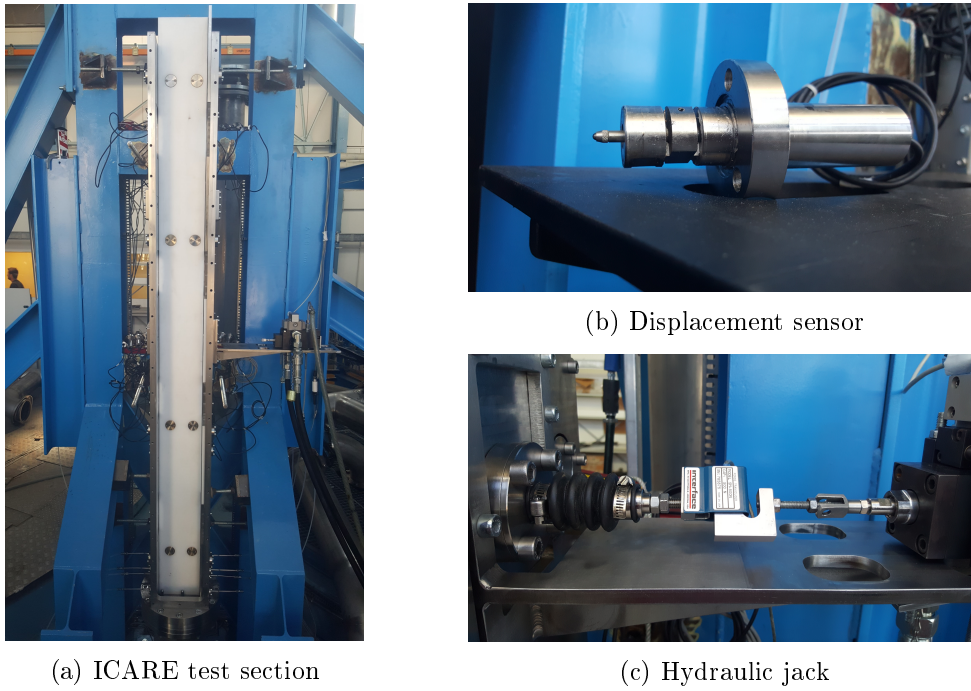


Figure 2.4 – Picture of the ICARE test section and some details

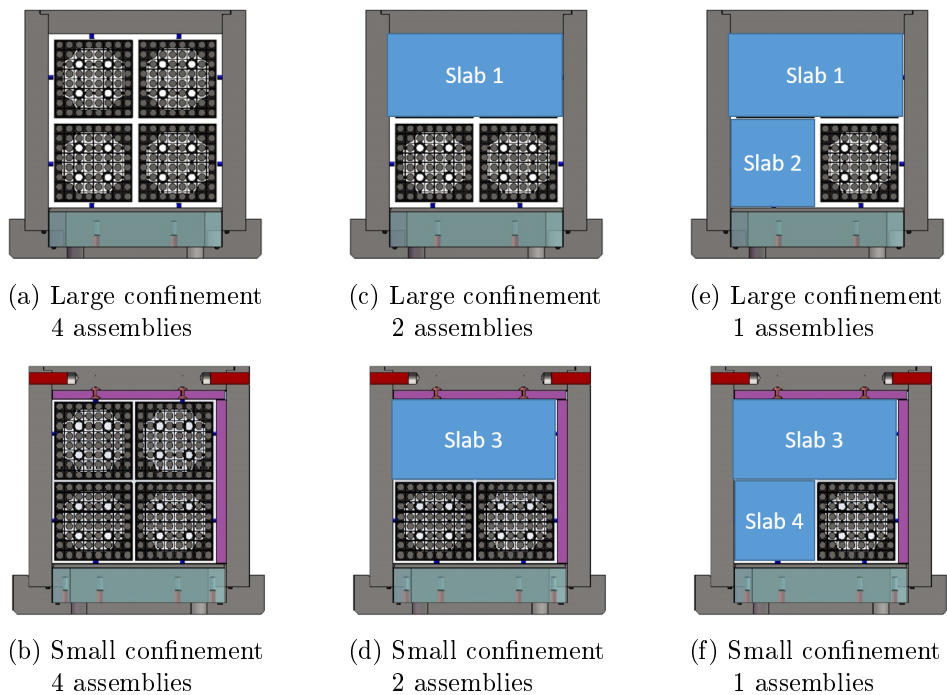


Figure 2.5 – Different possible configurations of the ICARE test section changing confinement size and number of assemblies

fuel assemblies have a natural frequency which fits the resonance frequency of real fuel assemblies ($\simeq 2 - 4 \text{ Hz}$) in water. For these reasons, all the experimental campaigns which are treated in the following chapters will be performed using PMMA fuel assemblies.

In addition to that, the water flowing along each assembly can be controlled by placing some small plates with different hole sections at the inlet channels. In this way an asymmetry on the water distribution can be imposed and the effects of the water redistribution along the fuel assemblies could be measured. Furthermore, a pre-stress on the fuel assemblies could be imposed by using a toolbox which allows to impose a flexure or a torsion on one or more fuel assemblies. The force applied by the water flow on such pre-stressed assemblies can be measured with high accuracy.

Finally, the walls of the test section have some transparent portholes on the front face and on the lateral faces allowing to perform local fluid velocity measurements using laser velocimetry techniques. The laser velocimetry techniques implemented on the ICARE facility are the LDV (Laser Doppler Velocimetry) and PIV (Particle Image Velocimetry). The LDV experimental results will be illustrated at the end of this chapter, while the PIV measurements will be not discussed in this document and will be the object of further publications.

Before starting the experimental campaigns, some improvements are made on the experimental facility in order to avoid some of the problems outlined from previous experiments. The main improvements will be briefly described in the next paragraphs.

2.2.1 Hydraulic Jack Design

The hydraulic jack attached to one of the fuel assemblies represents one of the most important components of the facility, since it allows to introduce a perturbation (lateral excitation) on the system. Thus the response to such excitation can be measured. Particular attention must be paid to the realisation of a perfect sealing between the hole on the wall of the structure and the metallic body which links the hydraulic jack to the fuel assembly. The criticality resides in the need for this rod to move freely in the horizontal direction in order to transmit the motion to the assembly. In addition, there is the need that the sealing system opposes the smallest effort possible to the motion of the metallic rod, since the force sensor is placed in between the sealing system and the hydraulic actuator. In order words, there is the need to seal the hole which allows the hydraulic jack to pass through the structure, but this sealing system must not influence the displacement of the rod itself.

The first adopted solution implied the use of a rubber bellow, as showed in Figure 2.6. The bellow is required to elongate few millimetres in order to accommodate the displacement of the hydraulic jack. Since the bellow is very flexible, it opposes a very small effort to the translation of the metallic rod, thus a very small perturbation is induced on effort measurements.

After the first experimental campaign, problems arose with the sealing system, in par-

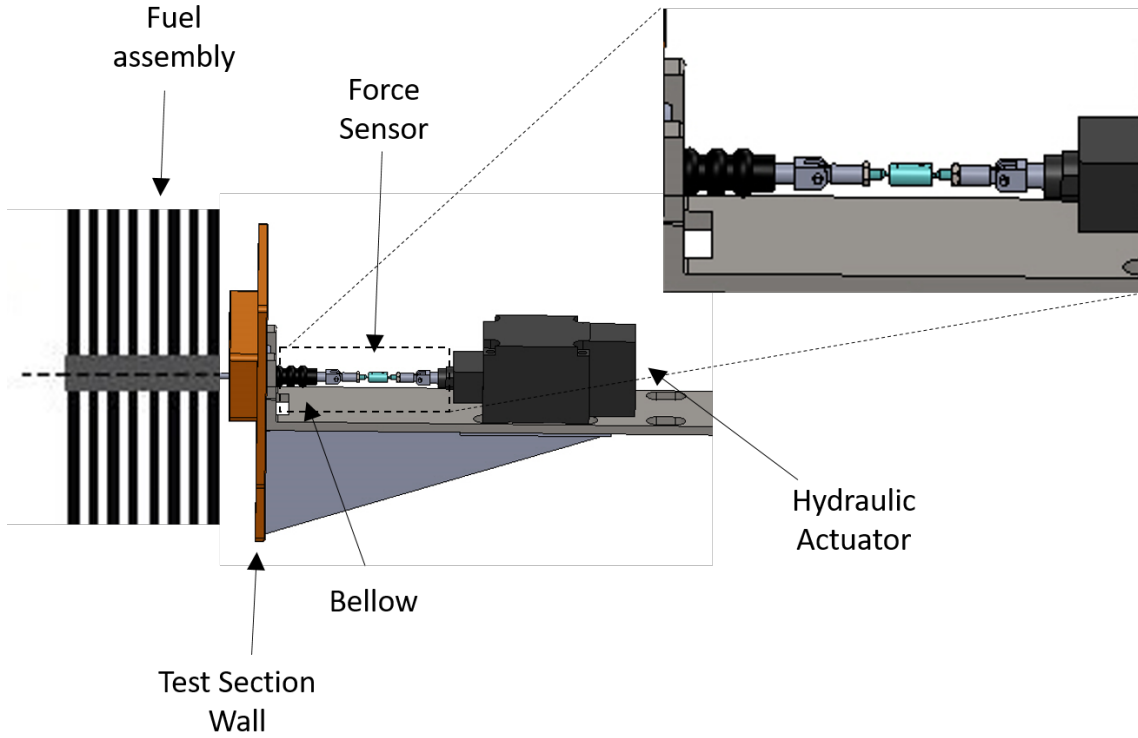
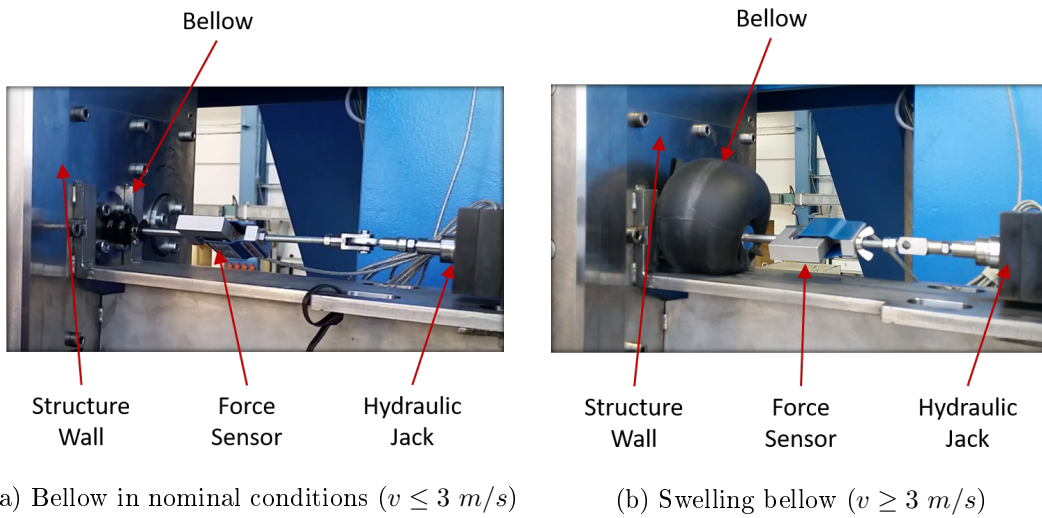


Figure 2.6 – First design of the hydraulic jack sealing system



(a) Bellow in nominal conditions ($v \leq 3 \text{ m/s}$)

(b) Swelling bellow ($v \geq 3 \text{ m/s}$)

Figure 2.7 – Comparison between bellow under normal conditions and under swelling conditions

ticular with the rubber bellow. In fact, since the bellow walls are very thin, as soon as the water flow velocity reaches the value of 3 m/s (as displayed in Figure 2.7) the bellow starts to swell and quickly explodes. The swelling of the bellow is due to the static pressure (driven by the pressure drop) which distributes on the thin lateral walls of the bellow. This effect was underestimated during the design process. Thus, in order to be able to perform

experimental campaigns with a water flow velocity larger than 2 m/s the sealing system of the hydraulic jack needed to be modified.

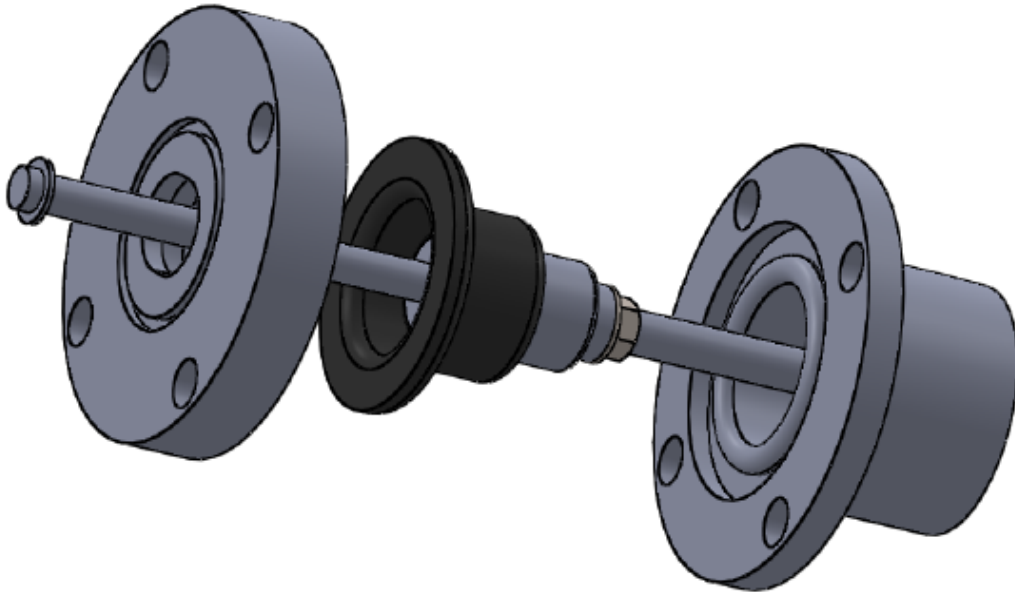


Figure 2.8 – New design for the sealing system

In order to avoid these problems on the bellow, a new sealing system was conceived. The new design consists in a piston and cylinder system, with a rubber membrane which guarantees the confinement of the water inside the experimental test section. The rod linking the hydraulic jack and the excited assembly is larger than the old one and works as a piston. A membrane is inserted in the middle of the cylinder; this membrane is then held in between two flanges. The rod (piston) can then move inside the flanges (cylinder) and the membrane ensures the confinement of the water. A scheme of the new design is represented in Figure 2.8. The membrane, installed with such a design, can resist important pressures ($\geq 20 \text{ bar}$) and then guarantees the sealing even when the water flow reaches high velocities. This system has one limitation regarding the displacement amplitude the rod can undergo. In fact, the motion of the rod is limited to a few millimetres from the rest position ($-5 \text{ mm} \leq x \leq 5 \text{ mm}$). This limitation does not affect our experimental conditions since the maximum displacement we want to apply is of the order of 2 mm for dynamic tests and 4 mm for quasi static tests.

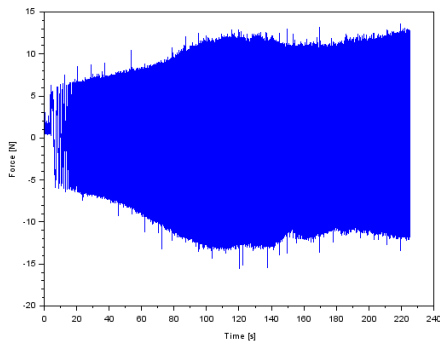
The first tests showed, as expected, that the system can resist without any deformation to high water flow rates.

The last issue we need to address with such a new configuration is the parasite efforts that the membrane can introduce. The bellow used in the previous design was very thin and

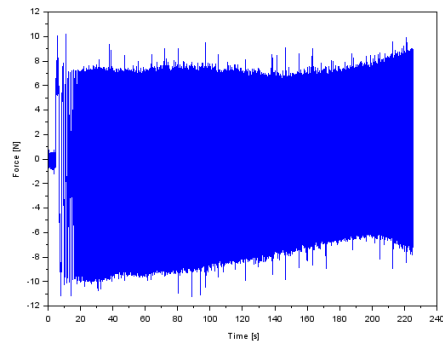
it was not opposing any resistance to the motion of the hydraulic jack (the effort coming from the bellow was measured to be smaller than 1 N). However, the membrane realised for the new sealing system results to be much stiffer than the bellow. Thus, the membrane can introduce important resistance to the motion of the hydraulic jack. The resistance introduced by the membrane will be translated in an error on the force measurement, since the force sensor is placed in between the hydraulic actuator and the sealing membrane. In the next section some dynamic tests on the new system will be discussed in order to estimate the effect of the membrane on the force measurements.

2.2.2 Test on the Force Perturbation for the New Sealing Design

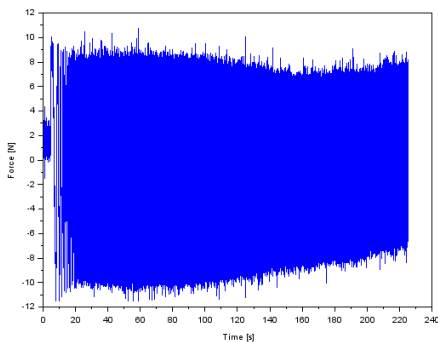
In order to evaluate the magnitude of the force perturbation introduced into the measurements from the membrane, some test were performed with the hydraulic jack not connected to the fuel assembly. In this way, the measured force response is only due to the resistance of the membrane.



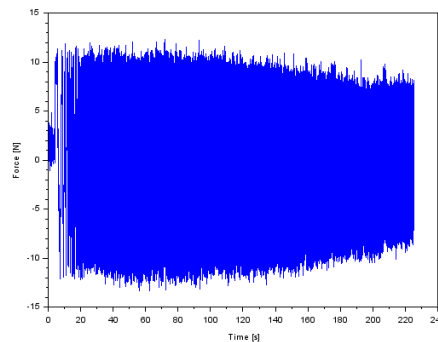
(a) Force evolution for test at 1.5 mm amplitude in air



(b) Force evolution for test at 1.5 mm amplitude in stagnant water



(c) Force evolution for test at 1.5 mm amplitude in 2 m/s axial water flow



(d) Force evolution for test at 1.5 mm amplitude in 4 m/s axial water flow

Figure 2.9 – Force response of the membrane system to excitation

Tests were run with an oscillation amplitude of the hydraulic jack of 1.5 mm repre-

senting one of the maximum excitation amplitudes used during the dynamic experimental campaigns. The tests are run for different values of the water flow, going from 0 m/s to 5 m/s . Tests on air are performed as well. The results show that the resistance opposed by the membrane to the motion of the hydraulic jack slightly depends on the water flow velocity. In Figure 2.9 are reported the force sensor measurements for an imposed excitation of 1.5 mm with a frequency sweep from 0 Hz to 25 Hz . Different plots represent different water flow conditions.

Figures 2.9b, 2.9c, 2.9d result to be very similar. We can thus affirm that the perturbation introduced by the membrane does not depend on the water flow conditions. Some differences can be seen when the test is performed in air. At low frequency the membrane exerts a smaller force. Since the importance of experimental campaigns performed in air is less significant than the one performed in water, we can neglect this difference and we can assume that the force exerted by the membrane on the force sensor is about 10 N for an excitement of 1.5 mm . The test on the membrane shows that we can assume the effort of the membrane to be independent on the water flow rate and on the excitation frequency. This means that the contribution of the membrane can be considered as an added stiffness ($\frac{10 N}{1.5 mm} \simeq 0.67 N/mm$) in parallel to the stiffness of the whole assembly. All the measurements done with the membrane sealing system will be thus filtered by assuming this artificial added stiffness due to the sealing system. Such added stiffness does not affect the natural frequency of the measured system.

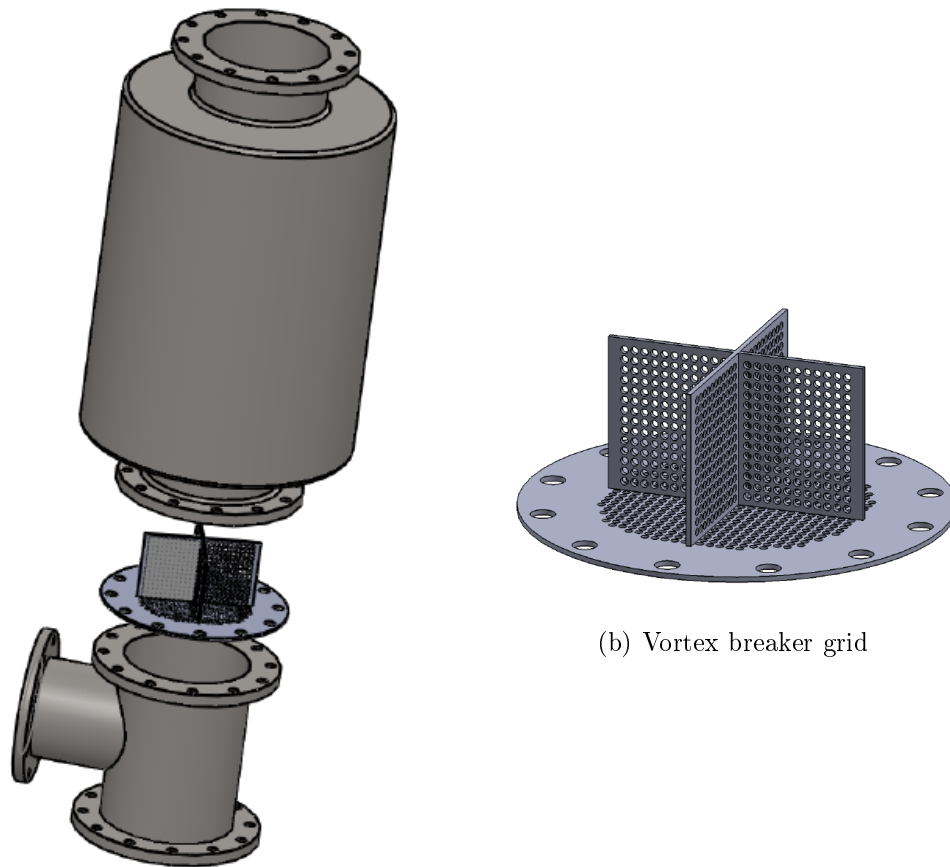
The error done with this assumption is of the order of 2 N . Since the precision of the force sensor (with all the electronics) is of the same order of magnitude, we can consider this error negligible. Furthermore, the error is more important for high frequencies ($\geq 10 Hz$). In this range of frequencies, the typical measured effort is of the order of hundred Newton. Thus, the membrane will introduce a global error of the order of a few percent, which is acceptable for our purposes.

2.2.3 Compensation Tank and Vortex Breaker Grid

After the first tests on the experimental facility another problem arose: a system allowing to evacuate the bubbles present inside the water loop was missing. In order to allow the bubbles to escape from the system, a compensation tank with a free open surface was added to the loop (see Figure 2.10a).

Even if the design of the compensation tank is not the optimal one, it was able to evacuate the gas present inside the loop with the pump running at low power for a few minutes. The optimal design for a compensation tank, in order to be more efficient, should have the inlet on one side of the tank, and the outlet in the bottom of the tank. In this way the bubble coming from the side of the tank can evacuate towards the free surface and the water without bubbles will be injected back in the loop. Due to limitation from the existing design of the loop the tank is realised as explained before.

The new compensation tank showed a good efficiency in evacuating the bubbles present



(a) Compensation tank on the upper part of the facility

(b) Vortex breaker grid

Figure 2.10 – New design of the upper part of the ICARE facility with the compensation tank and the vortex breaker grid

in the system due to the filling up of the loop. Anyway, when the water flow velocity was increased to large values some bubbles started to enter the system from the free surface of the tank. Since the distance from the free surface to the inlet (which also corresponds to the outlet) of the compensation tank was not big enough, the water flow creates big vortices inside the tank and it starts to pump air into the system. In order to keep a one phase flow, it is fundamental to avoid the presence of important quantities of air in the loop. In order to prevent the injection of air in the water loop a new countermeasure was taken.

A vortex breaker grid was designed and placed between the two flanges of the bottom part of the compensation tank. The vortex breaker grid, which is represented in Figure 2.10b is a perforated plate with an empty surface of about 50%. Four vertical perforated plates were welded on the horizontal plate in order to break eventual big vortices. This grid introduces localised pressure drop into the system, forcing the flow at the inlet of the compensation tank to be as uniform as possible. After the preliminary tests, the compensation tank with the perforated plate allowed to remove gas inside the loop and to

run the system with an axial water flow up to 6 m/s without bubbles being pumped into the loop.

2.3 Experimental Campaigns

The ICARE facility has been used to run several experimental campaigns. In this section the experimental matrix is presented and all the parameters that can be changed during different experimental campaigns are explained. Later on, the tools used to analyse the huge amount of data collected during the experiments are illustrated.

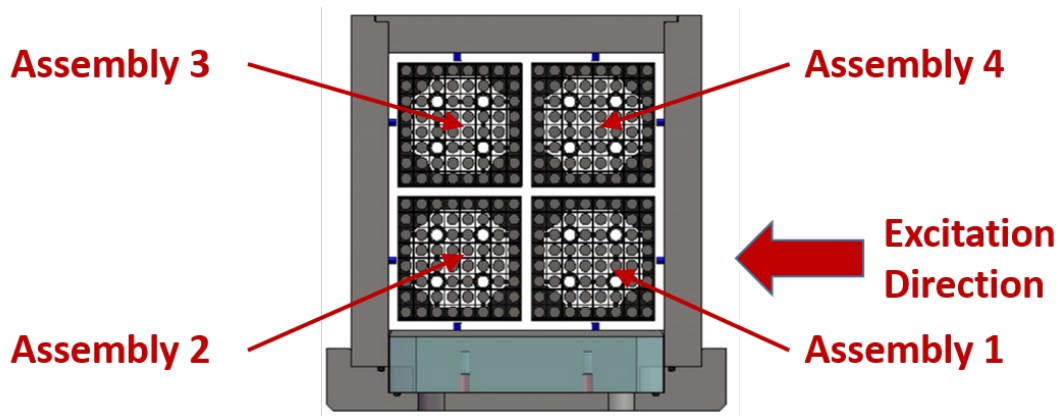


Figure 2.11 – Scheme of the assemblies in the test section with the respective identification numbers

For the sake of clarity, a scheme of the four fuel assemblies present in the experimental test section is reported in Figure 2.11 with the numbers corresponding to each assembly. As a reminder, during all the experiments the excited fuel assembly is always the assembly 1, and the excitation direction is always the x-direction.

2.3.1 Experimental Matrix

Four different experimental campaigns were conducted on the ICARE facility. All the experimental campaigns are performed using the PMMA (poly-methyl-methacrylat) fuel assemblies. First two campaigns involve the use of a large confinement (8 mm), while two further campaigns use a reduced size confinement (4 mm). The change of the confinement size allows to evaluate the effects of the water bypass in between the wall and the assembly on the dynamic behaviour of the fuel assemblies.

For both confinement sizes, two experimental campaigns are run, one with the four assemblies and one with only two fuel assemblies. The presence of 4 fuel assemblies (arranged in square lattice) gives the possibility to investigate the out of plane phenomena in the coupling between fuel assemblies.

During all the four campaigns several experiments are run changing three different parameters: the water flow velocity, the water temperature and the excitation amplitude.

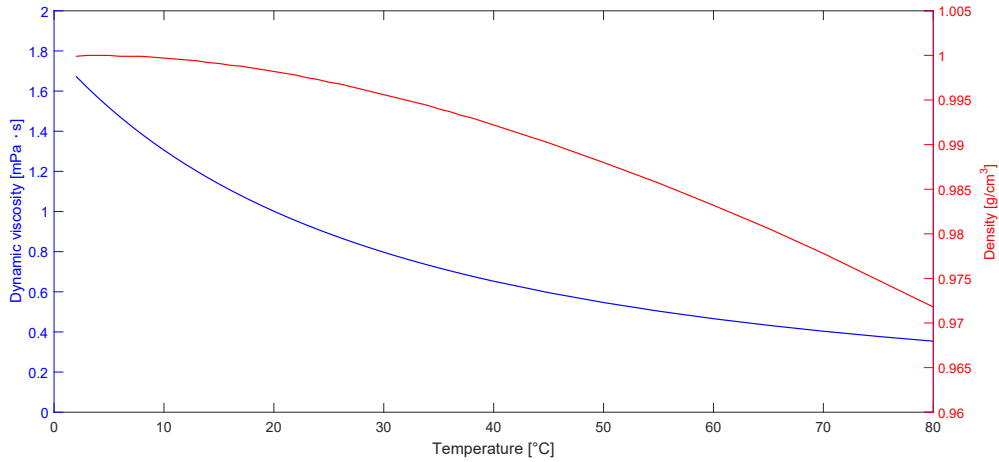


Figure 2.12 – Diagram of water viscosity and density as function of temperature

The changes in the water flow velocity will allow to study the effect of the water flow on the dynamics of the fuel assembly (added mass, added stiffness, added damping) and the effects on the coupling between different fuel assemblies. The range of water flow velocity goes from 0 m/s (stagnant water) up to 5 m/s . Experiments in air are also performed in order to know the nominal dynamical behaviour of the fuel assemblies. Experiments are repeated with two different water temperatures: 15 °C and 30 °C. These two temperatures are set in order to investigate the effect of the viscosity. In fact, even if the temperature difference seems to be quite small, the viscosity changes more than 30% as it can be seen in Figure 2.12, while all the other properties stay constant. The water temperature is not increased more than 30 °C due to limitation on the PMMA of the fuel assemblies. The last parameter that was varied during the experiments is the excitation amplitude in a range from 0.1 mm to 2 mm . The change of the excitation amplitude can outline the presence of nonlinearities in the system.

Finally, two different kinds of excitation are given to the fuel assembly number 1. A first kind of excitation is a quasi-static excitation, consisting in a sinusoidal excitation with very low frequency: 0.05 Hz . With this excitation the dynamic behaviour does not play any role, but the hysteresis pattern of the fuel assembly is visible. The stiffness of the fuel assembly can also be calculated from the hysteresis plot, and the effects of the water flow and confinement can be investigated.

The second type of excitation applied to the assembly aims to study the dynamics of the fuel assemblies. Thus higher frequencies are needed. The fuel assembly is excited from a frequency of 0.05 Hz to a frequency of 25 Hz with a swept sinus excitation. The excitation amplitude follows the Equation below:

$$a(t) = A \sin \left(\frac{\pi(f_{max} - f_{min})}{T_s} t^2 + 2\pi f_{min} t + \psi_0 \right) \quad , \quad (2.1)$$

2.3. EXPERIMENTAL CAMPAIGNS

where A is the excitation amplitude (from 0.1 mm to 2 mm), $f_{min} = 0.05 \text{ Hz}$ and $f_{max} = 25 \text{ Hz}$ are respectively the minimum excitation frequency and the maximum one and ψ_0 indicate the phase at the origin (which is assumed to be 0 in all the experiments). The quantity T_s represents the time needed to sweep from initial frequency to the final one. For our experiments the sweep time used is $T_s = 500 \text{ s}$ thus giving a sweep velocity of 0.05 Hz/s .

Dealing with a swept sinus, the sweep velocity is an extremely important parameter. In fact, in order to catch the transfer function of a system, we need to excite each of the frequencies in an harmonic way. This is possible if the sweep velocity is small enough in order to avoid transient phenomena. For more details on such problems the reader is referred to [Gloth and Sinapius \(2004\)](#); [Martert and Seidler \(2001\)](#). The international standard *ISO-7626* defines the rules to respect for determining the transfer function with a swept sinus excitation. For our experimental conditions, the sweep velocity of 0.05 Hz/s respects the rules defined in that document. An experimental verification of the sweep velocity has been performed by checking different sweep velocities.

Confinement	Assemblies	Water Flow	Temperature	Excitation Amplitude	Frequency
Large: 8 mm	2	Air 0 m/s 1 m/s 2 m/s	15 °C	0,1 mm 0,3 mm 0,5 mm 0,8 mm	Quasi-Static: 0,05 Hz
Small: 4 mm	4	3 m/s 4 m/s 5 m/s	30 °C	1 mm 1,2 mm 1,7 mm 2 mm	Sweep: 0,05 ÷ 25 Hz

Figure 2.13 – Schematic representation of experimental matrix

Finally, the parameters which can be controlled in the different experimental campaigns are summed up in an experimental matrix in [Figure 2.13](#).

In addition to the experimental campaigns mentioned before, some further measurements were carried out for the configuration with small confinement size. LDV (Laser Doppler Velocimetry) technique was implemented on the configuration with four fuel assemblies in order to measure the local velocity of the water flow in different locations between the fuel assemblies. Furthermore, the PIV (Particle Image Velocimetry) has been implemented for the configuration with small confinement size and two fuel assemblies.

The PIV measurements allow to have the information on the local velocity on a 2D plane and not only on one point as in the case of the LDV technique. PIV measurement data are not analysed in this document but they will be object of further publications. For more details on the experimental matrix the reader is referred to Appendix A.

2.3.2 Data Analysis Tools

This paragraph is devoted to the description of the data analysis performed on the collected data during experimental campaigns.

As a preliminary work, all the data collected with a CEA software called TRIDENT are transformed in text files easily readable by any other engineering software for data manipulation.

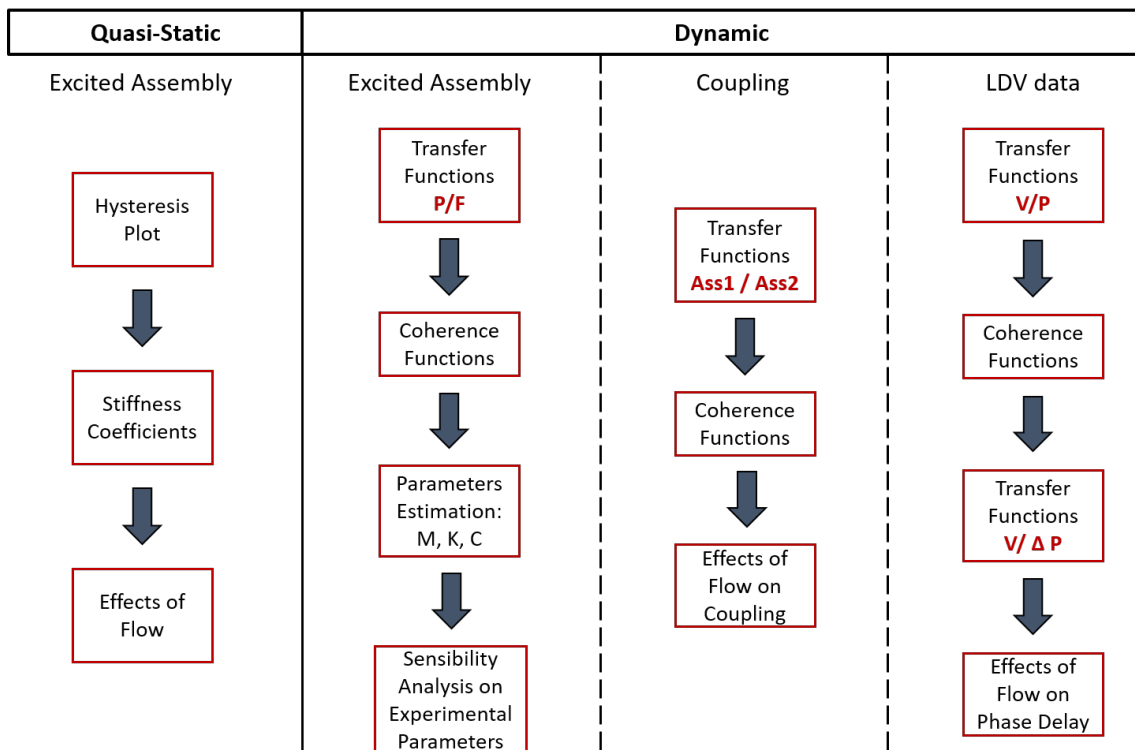


Figure 2.14 – Schematic representation of data analysis work

In order to simplify the reading of the next pages, Figure 2.14 shows a simplified scheme of the analyses performed on the collected experimental data. This scheme is commented in detail in the next paragraphs.

Quasi Static Analysis

The first analyses are performed on the quasi-static data. The quasi static data are represented in a Force (exerted on the fuel assembly) VS Position (of the excited grid) plot where the hysteretic behaviour is outlined. The stiffness of the fuel assembly can be cal-

culated from the slope of the curve. Plot for different amplitudes and different water flow velocities are compared.

Dynamic Analysis on the Excited Assembly

Later on, the data related to dynamic experiments are treated. First, the dynamic response of the excited assembly is analysed. Thus, the force data and position data of the excited grid are used. The transfer functions between the position and the force are calculated in order to outline the dynamical behaviour of the system (resonance frequencies, amplitude, damping, stiffness, etc.). Since the data are related to a swept sinus excitation, the transfer functions are calculated using the cross correlation product, and are defined as follows:

$$TF_{PF}(f) = \frac{P(t) \star P(t)}{P(t) \star F(t)} \quad , \quad (2.2)$$

where $TF_{PF}(f)$ is the transfer function in the frequency domain between position and force of the fuel assembly, $P(t) \star P(t)$ is the spectral autocorrelation of the position signal and $P(t) \star F(t)$ is the spectral cross correlation between the position signal and the force signal. In addition, the coherence function is also analysed in order to understand if the transfer function calculated before is really due to external excitation imposed to the fuel assembly and is not due to noise or other phenomena. The coherence function is thus calculated as follows:

$$Coh_{PF}(f) = \frac{|P(t) \star F(t)| \cdot |P(t) \star F(t)|}{|P(t) \star P(t)| \cdot |F(t) \star F(t)|} \quad . \quad (2.3)$$

Cross correlation functions are calculated using a windowing filter of Hamming type in order to clean up the noise from the signal. The transfer function are now used in order to evaluate the effect of the different experimental parameters (as the flow velocity, temperature etc.) on the dynamic behaviour of the fuel assembly.

Furthermore, the transfer functions are used to perform an estimation of the dynamical parameters of the fuel assembly as the modal mass (m_i), the modal stiffness (k_i) and the modal damping (c_i). The system is supposed to behave as a linear system, thus the module of its transfer function can be written as:

$$TF_{PF}(\omega) = \frac{1}{k_i - m_i \omega^2 + j c_i \omega} = \frac{1}{m_i (j 2 \xi_i \omega_i \omega - (\omega^2 - \omega_i^2))} \quad , \quad (2.4)$$

where ω represents the pulsation, $\xi_i = \frac{c_i}{2\sqrt{m_i k_i}}$ represents the reduced damping, $\omega_i = \sqrt{k_i/m_i}$ is the natural pulsation. One can note that such a transfer function has its maximum at the resonance pulsation $\omega_{ri} = \omega_i \sqrt{1 - 2 \xi_i^2}$. The theoretical transfer function defined above is used to estimate the mass, stiffness and damping parameters of the fuel assembly with the use of the LSM (Least Square Method). Such a regression method for the estimation of the parameters is simple to implement but does not ensures the convergence to the good set of parameters for any initial guess. A trial and error routine is thus used

in order to choose the proper initial guess allowing the LSM method to converge to the right values. Once the parameters estimated, the effect of the water flow velocity and of the excitation amplitude is analysed.

Dynamic Analysis on the Coupling between Assemblies

The next step of the data analysis focuses on the study of the coupling between the excited assembly and the ones which are not excited. For experiments run with a water flow we expect that once the first fuel assembly is excited, an excitation is also induced on the other fuel assemblies due to the presence of the fluid. First, the coupling effects on the Assembly 2 are analysed. Since the Assembly 2 is the one in the same direction as the excitation we expect to have the most important effect of the coupling on this fuel assembly. Later, the couplings existing between Assembly 1 and other assemblies are also investigated.

The coupling phenomena are investigated by using the mathematical tools already described in the previous sections. Transfer and coherence functions are calculated and the effect of the different experimental parameters are investigated by comparison.

LDV Data Analysis

Finally, some analysis have been performed on the Laser Doppler Velocimetry data. First, the temporal evolution of the local water velocity is analysed. It can be easily seen that as soon as the assembly starts to move, the water velocity starts to oscillate. Thus meaning that it is worth the effort to further analyse the velocity signals as a function of the displacement of the fuel assembly.

Transfer functions between the water velocity and the position of the excited fuel assembly are calculated. Different measurement points for the local water velocity are compared. The effect of different mean water flow rates and different excitation amplitude are investigated.

2.4 Experimental Results

In this section the experimental results obtained from the 4 different campaigns on the experimental facility ICARE will be discussed.

After a brief quasi static analysis, data related to the dynamic behaviour of the excited fuel assembly are analysed first. Later, the coupling effects between the excited fuel assembly and the other ones will be addressed.

2.4.1 Quasi Static Analysis

This paragraph aims to study the impact of different parameters (as water flow rate, excitation amplitude, etc.) on the quasi static measurements. Since the main features of such a study are similar when changing the number of fuel assemblies and the confinement

size, the most general condition with 2 fuel assemblies and large confinement is studied unless otherwise specified.

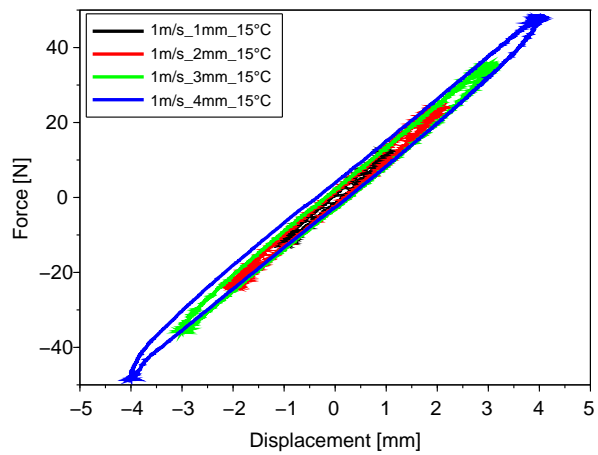
Quasi-static experiments allow to put in evidence the relation between the displacement of the fuel assembly and the effort which is needed in order to move it without taking into account the dynamic effects (excitation frequency 0.05 Hz). Figure 2.15 shows the force-displacement relationships for different experimental conditions.

Figures 2.15a, 2.15b and 2.15c show a typical hysteresis pattern. The effort required to move the fuel assembly in one direction is not the same when the same fuel assembly is moved in the opposite direction. This hysteresis is mainly due to the presence of the support grids, which have several springs and dimples to hold the rods introducing important friction forces. The hysteresis behaviour becomes more important as the excitation amplitude becomes larger (Figure 2.15a). Hysteresis is in fact a non linear behaviour which is amplified by large amplitude displacements.

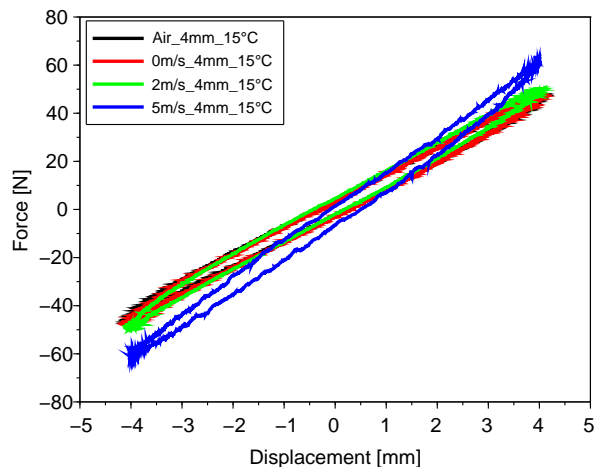
The knowledge of the force displacement relationship allows to also know the stiffness of the structure. The stiffness is in fact given by the ratio between the force necessary to move the body and the displacement itself. Thus the stiffness of the fuel assembly results to be the slope of the curves in Figures 2.15a, 2.15b and 2.15c. The slope of these curves, thus the stiffness of the fuel assemblies, is affected by the water flow rate. When the flow rate increases, the slope of the force displacement plot also increases, meaning that the flow induces an added stiffness on the fuel assembly (see Figure 2.15b). This added stiffness phenomenon is already known in literature and confirmed by experiments (Ricciardi et al., 2009; Boccaccio, 2010). The increasing of the temperature water seems, on the other hand, to have an opposite effect (see Figure 2.15b).

In conclusion, the quasi static analysis allowed with some simple and fast experiments to catch the behaviour of one of the main properties of a fuel assembly (the stiffness) and to outline the presence of strong non linearities on the experimental facility ICARE mainly due to the presence of the support grids.

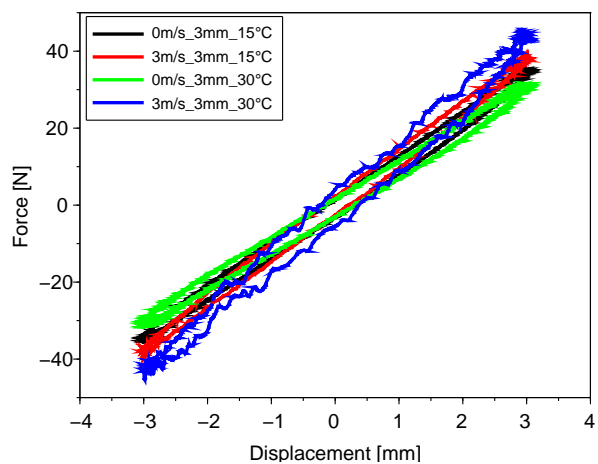
CHAPTER 2. FUEL ASSEMBLY VIBRATIONAL EXPERIMENTS



(a) Water flow rate 1 m/s at 15 °C



(b) Excitation amplitude 4 mm at 15 °C



(c) Excitation amplitude 3 mm at 15 °C and 30 °C

Figure 2.15 – Force-Displacement plot for quasi-static excitation experiments

2.4.2 Dynamic Analysis

This paragraph is devoted to the analysis of the behaviour of the experimental data of dynamic experiments. Dynamic tests are performed by exciting the fuel assembly over a frequency range from 0 Hz up to 25 Hz . Response of the excited fuel assembly (force and position sensors) and of the not excited ones (only position sensors) are acquired at a sampling rate of 2000 Hz (to catch fast components). Collected data are treated by means of transfer functions and analysed in the Fourier space, as already illustrated in Section 2.3.2.

The transfer functions between displacement and force on the excited assembly give information about the dynamical behaviour of the structure. The peaks represent the resonance frequencies, the departure of the curve represents the inverse of the stiffness and the width and intensity of the resonance peaks represent the damping of the structure.

Excitation Amplitude Effects

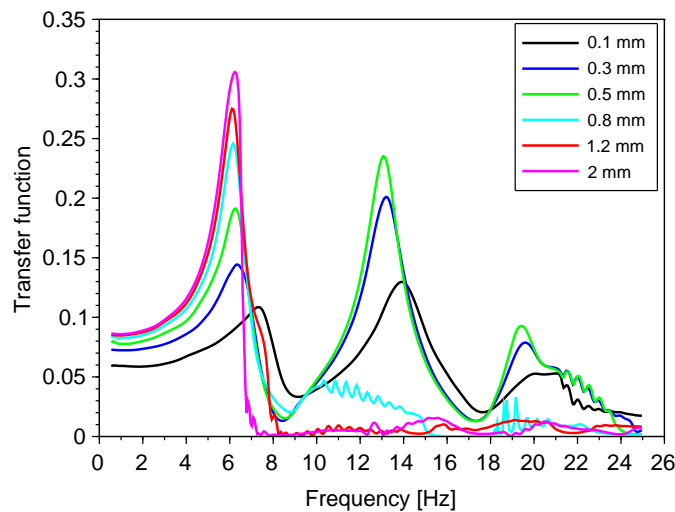


Figure 2.16 – Displacement-Force transfer function for assembly 1 in air in large confinement with two assemblies at 15 °C

A first analysis on the dynamic behaviour of the excited fuel assembly is performed in air. The behaviour of the fuel assembly without any interaction with the fluid can be observed. Figure 2.16 shows the dynamic behaviour of the excited fuel assembly when the excitation amplitude changes (from 0.1 mm up to 2 mm). Three peaks are visible in the frequency range from 0 Hz to 25 Hz . Each peak indicates respectively the first, second and third natural mode. The second and third modes are only excited for small amplitude excitations in order to avoid the fuel assembly to strike with the walls of the structure.

If the system was linear, one would expect the transfer functions to be perfectly identical. The transfer function appears to be considerably different with one another, especially

when considering the peaks amplitudes. These differences are other proofs of the non linearities present in the system. The damping of the system appears to decrease with the increase of the excitation amplitude (peaks become narrower and higher) and the stiffness decreases (peaks slightly move to lower frequencies). The resonance frequencies slightly decrease with the increasing of the excitation amplitude.

The most important parameters that should be noted from the "In Air" dynamical analysis of the fuel assembly are resonance frequencies. Even if they depend on the excitation amplitude, the average value can be considered to be a reference value for resonance frequencies. The first resonance mode in air appears at about 7 Hz , while the second and third resonances appear respectively at about 13.5 Hz and 20 Hz .

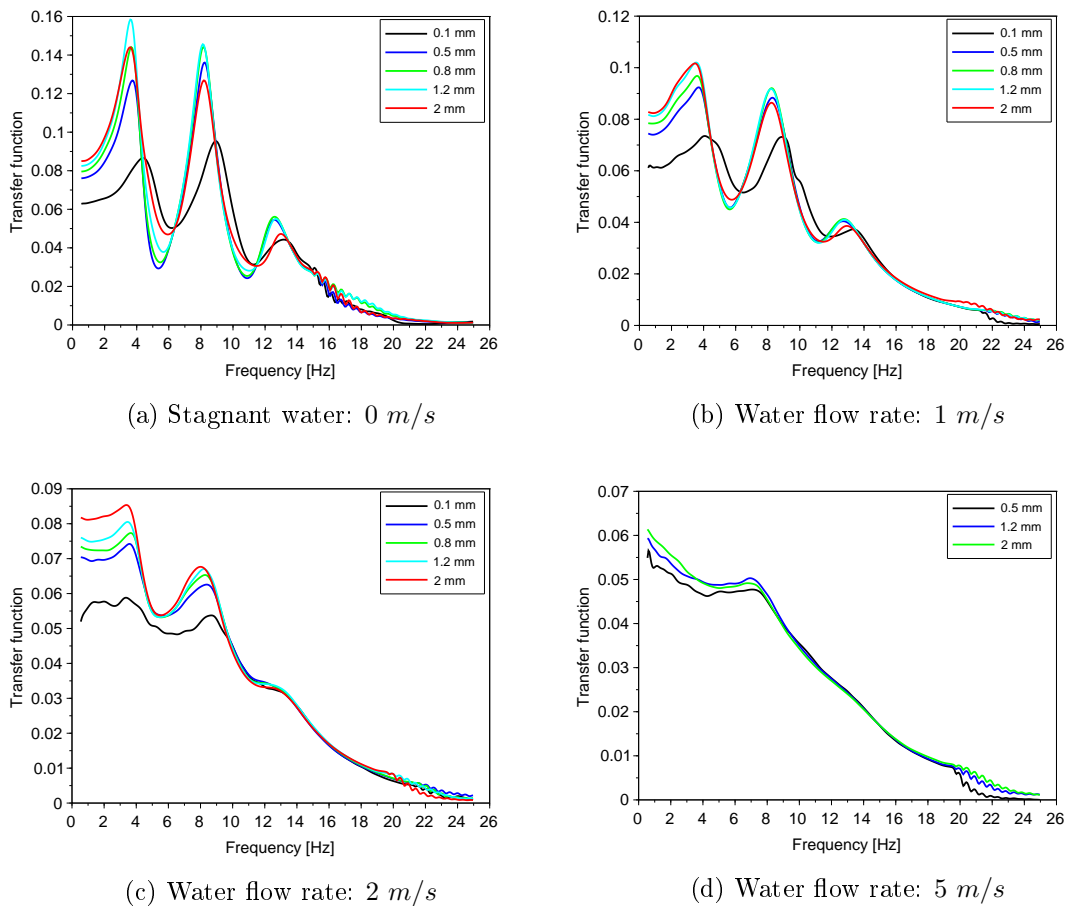


Figure 2.17 – Displacement-Force transfer functions for assembly 1 in large confinement with two assemblies with different flow rates at $15\text{ }^{\circ}\text{C}$: comparison between different excitation amplitudes

Later on, the dynamical behaviour of the fuel assembly under water (stagnant and flowing water) is analysed. Even when the fuel assemblies are subject to an axial water flow, non linearity plays an important role in shifting the resonance frequencies, damping and stiffness values (see Figure 2.17). The presence of the water flow attenuates the effect of non linearities and when the water flow increases up to 5 m/s the differences almost

disappear (see Figure 2.17d).

Water Flow Effects

The intensity of the water flow rate does play a very important role on the definition of the dynamical behaviour of the fuel assembly. This result was expected, since the interaction between the fluid and structure strongly changes when the water flow velocity changes.

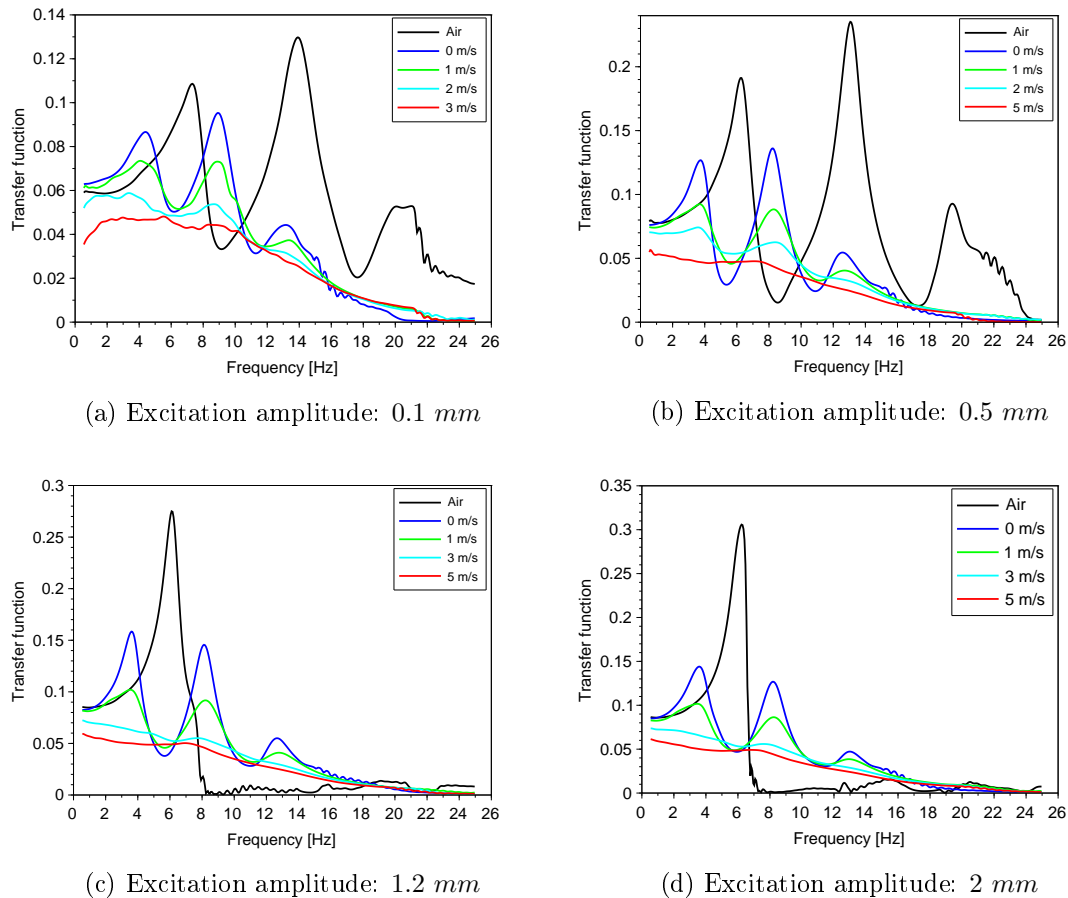


Figure 2.18 – Displacement-Force transfer functions for assembly 1 with different excitation amplitudes in large confinement with two assemblies at 15 °C: comparison between different water flow rates

One of the most important and most evident effects of the presence of the water in the test section is a strong shift of the resonance frequencies. The presence of water strongly reduces the frequencies at which resonances occur (see Figure 2.18). The first resonance frequency decreases from about 7 Hz to about 4 Hz, the second one goes from 13.5 Hz to 8.5 Hz and the third one decreases from 20 Hz to 13 Hz. The increase of the water flow rate causes a further decrease of the resonance frequencies and a strong increase of the damping. When the water flow velocity is larger than 3 m/s (red and purple curves in Figures 2.18a, 2.18b, 2.18c and 2.18d) the system appears to be overdamped and resonances are not even visible.

The stiffness of the system also increases with the increasing of the water flow rate. The faster the water flows around the fuel assembly the stronger the water will oppose to the movement of the assembly itself. This opposition to the motion of the fuel assembly results in the increasing of the stiffness of the assembly.

Recalling the definition of natural frequency:

$$f_i = \frac{1}{2\pi} \sqrt{\frac{k_i}{m_i}} \quad , \quad (2.5)$$

one can affirm that since the stiffness slightly increases, the mass of the system needs to increase in order to make the resonance frequency decrease. Since the resonance frequency decrease on the order of 50%, while the stiffness only increases of few percent, we can affirm that the mass needs to increase much more than the stiffness and damping. The added mass effect is thus the most important one for the considered experimental conditions. This result is already known in literature ([Brennen, 1982](#); [Wendel, 1956](#)).

Confinement Effects

The confinement size determines the amount of water lying in the gap between the fuel assembly and the walls of the test section. It is thus supposed that this gap plays a role in the dynamic behaviour of the fuel assembly immersed in water (either stagnant or flowing water). Of course, the confinement size should not play any role in the dynamic behaviour of fuel assembly "In Air".

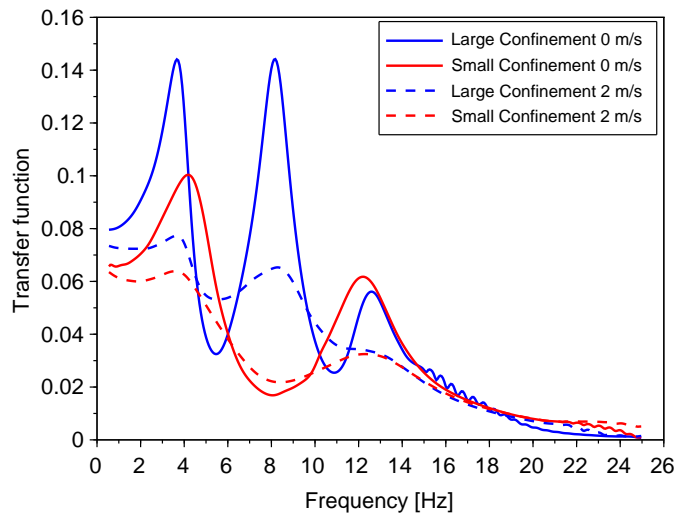


Figure 2.19 – Displacement-Force transfer functions for different confinement sizes with an excitation amplitude of 0.8 *mm* and two fuel assemblies at 15 °C

Due to technical problems, when the confinement size of the test section was changed, the link between the hydraulic jack and the fuel assembly grid broke. The reparation of

the same grid was not possible, thus the hydraulic jack was attached to the middle grid for experiments with small confinement instead of being attached to the top grid (as in the case of large confinement experiments). If the system was linear, the dynamical behaviour of the system should not change when changing excitation location. The main difference that one can expect is that when the fuel assembly is excited in the middle grid the even modes are not excited. Thus one expects to have similar transfer functions for the two cases, without even resonance peaks. Since the system is already proven to be non linear, some effect when changing excitation position are expected.

The effect of the confinement size changes are visible in Figure 2.19: the second resonance frequency is not visible for small confinements as expected. On the other hand, a remarkable shift on the resonance frequencies and on the departure amplitude of the transfer function (which corresponds to the inverse of the stiffness) is visible. The stiffness of the fuel assembly decreases and resonance frequencies are shifted when the confinement size changes. Anyway, this behaviour cannot be related exclusively to the confinement size changes, since the excitation point is changed.

2 VS 4 Fuel Assemblies

Experimental measurements with two and four fuel assemblies in the test section are performed. The presence of 4 fuel assemblies arranged in a squared lattice of 2×2 is closer to the real arrangement in a nuclear reactor core. For this reason it is interesting to investigate the effects of the presence of two or four fuel assemblies.

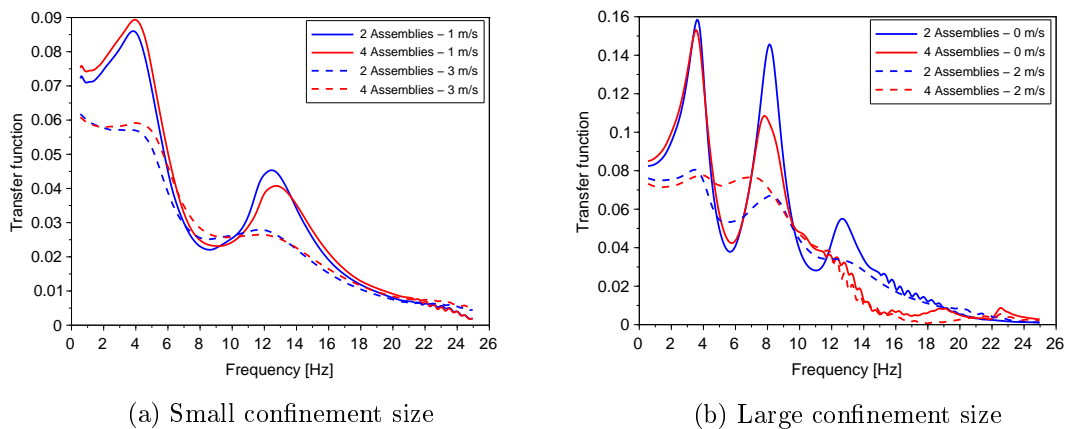


Figure 2.20 – Displacement-Force transfer functions for 2 VS 4 fuel assemblies with an excitation amplitude of 1.2 mm at $15 \text{ }^\circ\text{C}$

The presence of 2 or 4 fuel assemblies does not affect in a sensible way the dynamic behaviour of the excited fuel assembly both for small (see Figure 2.20a) and large confinement (see Figure 2.20b). Some differences can be seen on the second vibration mode which seems to be attenuated when the 4 fuel assemblies are considered. This attenuation could be due to the flexibility of the fuel assemblies which are close to the excited one, which

thus represent a moving boundary around the excited fuel assembly.

Nevertheless it is useful to have the possibility to compare experimental tests with 2 and 4 fuel assemblies regarding the coupling effects. One can expect, in fact, that the configuration with 4 fuel assemblies allows to study the coupling phenomena existing in the excitation plane and out of the excitation plane. This subject will be treated in the next paragraphs.

Temperature Effects

The effects of the water temperature are addressed by performing experiments at two different temperatures: 15 °C and 30 °C. The effect of the viscosity changes can be thus analysed by comparing measurements at different temperatures.

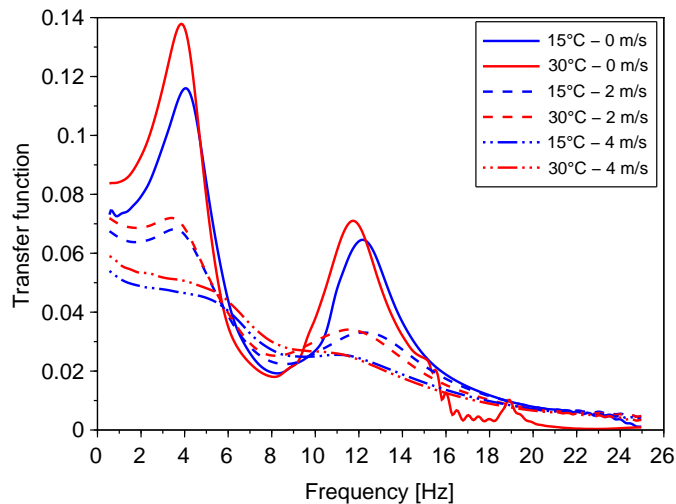


Figure 2.21 – Displacement-Force transfer functions for 15 °C VS 30 °C at 1 mm excitation amplitude with two fuel assemblies in small confinement

The transfer functions of the excited fuel assembly appears to considerably increase (about 20%) in amplitude when the water temperature increases (see Figure 2.21). Furthermore, the departure of the transfer function curve also increases of about 20%. In addition to that, the peaks translate to lower frequencies. When the water flow rate increases, the temperature effects become less and less important.

These effects are due to a decrease of the fuel assembly stiffness. For sure, the observed phenomenon is a proof that the water temperature affects the dynamic behaviour of a fuel assembly. As the temperature increases, in fact, the water viscosity decreases (as already seen in Figure 2.12). The decrease of the water viscosity can change the added stiffness effect.

Anyway, it was not expected that such a slight difference in the water temperature can affect the behaviour of the fuel assembly in such an important way. In addition, the

parameter that was expected to be affected the most was the apparent mass of the assembly, and not its stiffness. From a more detailed reflection, the causes of such big differences reside in the changes of the constituting material properties. The PMMA, in fact, suddenly changes its Young's modulus when the temperatures increases of few degrees. The Young's modulus rapidly decreases, inducing the whole stiffness of the assembly to decrease.

Experimental results thus prove that temperature effects do affect the dynamics of an excited fuel assembly due to a combined effect of the viscosity (and eventually density) reduction and to the changes of material properties which reduce the stiffness of the structure. It is thus evident that from an experimental point of view it is important to control and stabilize the temperature of the water flow. ICARE facility is equipped with a refrigerated system which is capable of controlling the water flow temperature in a very efficient way (~ 0.5 °C accuracy).

2.4.3 Parameters Estimation

Previous discussion was based on the analysis of the transfer functions of the excited structure and some inference was done on the dynamic behaviour of the fuel assembly depending on the parameters. In particular, mass, stiffness, damping and resonance frequency have been cited. This paragraph aims to mathematically determine from the experimental data these dynamic properties of fuel assembly, which will allow us to completely describe the dynamics of the structure.

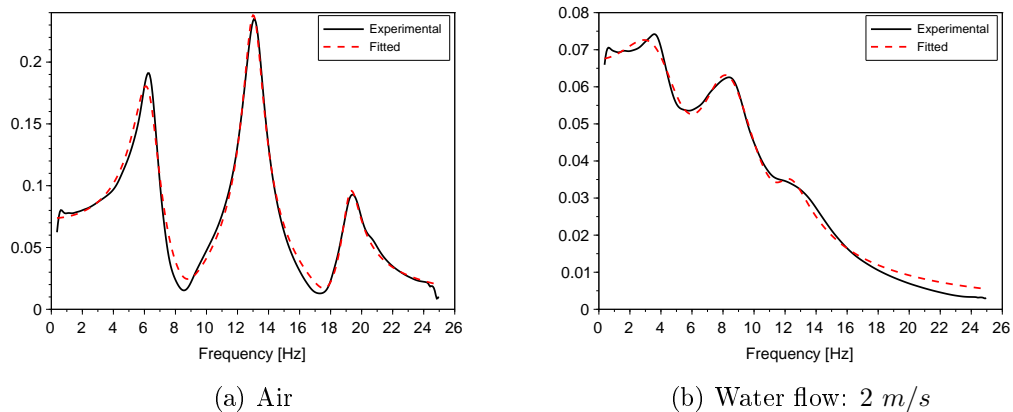


Figure 2.22 – Comparison between experimental and estimated transfer functions for 0.5 mm excitation in 2 fuel assemblies large confinement configuration (15 °C)

As described in Section 2.3.2 the analytical transfer function parameters are estimated from the experimental curves. As a first step for validating the parameters estimation method some comparison between estimated and experimental transfer functions are showed in Figure 2.22. For any situation the estimation method is pertinent and the estimated transfer function follows exactly the experimental curve with an error smaller than 2%. The implemented method is thus proved to be stable and to converge to the true

solution (when using the right initial guess).

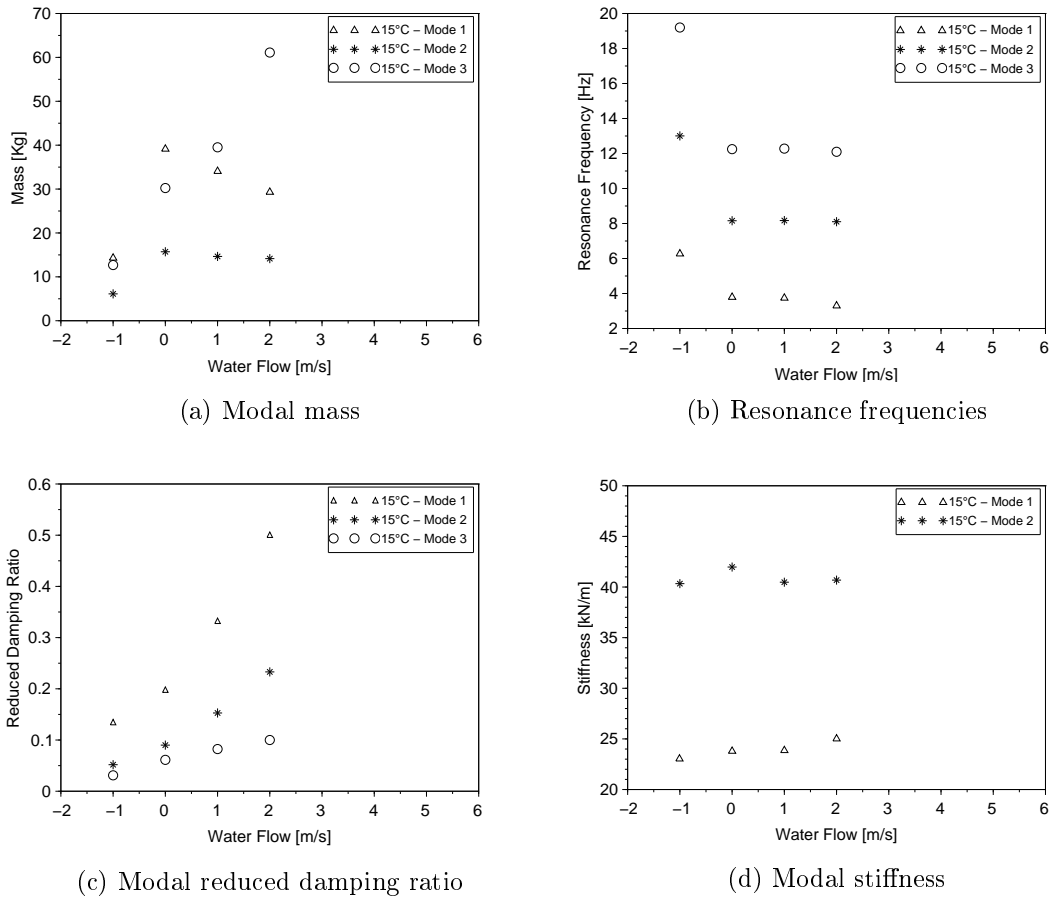


Figure 2.23 – Behaviour of the estimated dynamic parameters as function of the water flow rates for the first three modes with excitation amplitude 0.5 mm at $15 \text{ }^\circ\text{C}$ with 2 assemblies in large confinement configuration. Flow rate -1 m/s means "In Air"

In Figure 2.23 the general behaviour of the main dynamic parameters of the excited fuel assembly are presented. Modal mass, damping, stiffness and resonance frequencies are identified for the first three natural modes. With our instrumented fuel assembly which has sensors in three different vertical locations we are not able to identify higher modes than the third one.

The modal parameters of the assembly "In Air" are identified and they represent the reference values. First modal mass (Figure 2.23a) increases in a consistent way from "In Air" conditions to stagnant water (it becomes about three times larger). Then, when the flow rate increases it slightly decreases. This decreasing behaviour is also identified by Ricciardi (2016) and Boccaccio (2010) and seems to have an asymptotic behaviour. On the other hand, the second modal mass appears to continuously increase when the water flow rate increases. The difference between the modal mass of the fuel assembly immersed in water and the modal mass of the fuel assembly in air gives the added mass coefficient. Thus, the added mass coefficient for the first mode decreases with the water flow rate.

2.4. EXPERIMENTAL RESULTS

Resonance frequencies (Figure 2.23b) show the same behaviour for all the three modes: it suddenly decreases when passing from "In Air" condition to stagnant water, and then it continues to slightly decrease as the water flow rate increases. The huge change of the resonance frequency is mainly due to the modal mass changes.

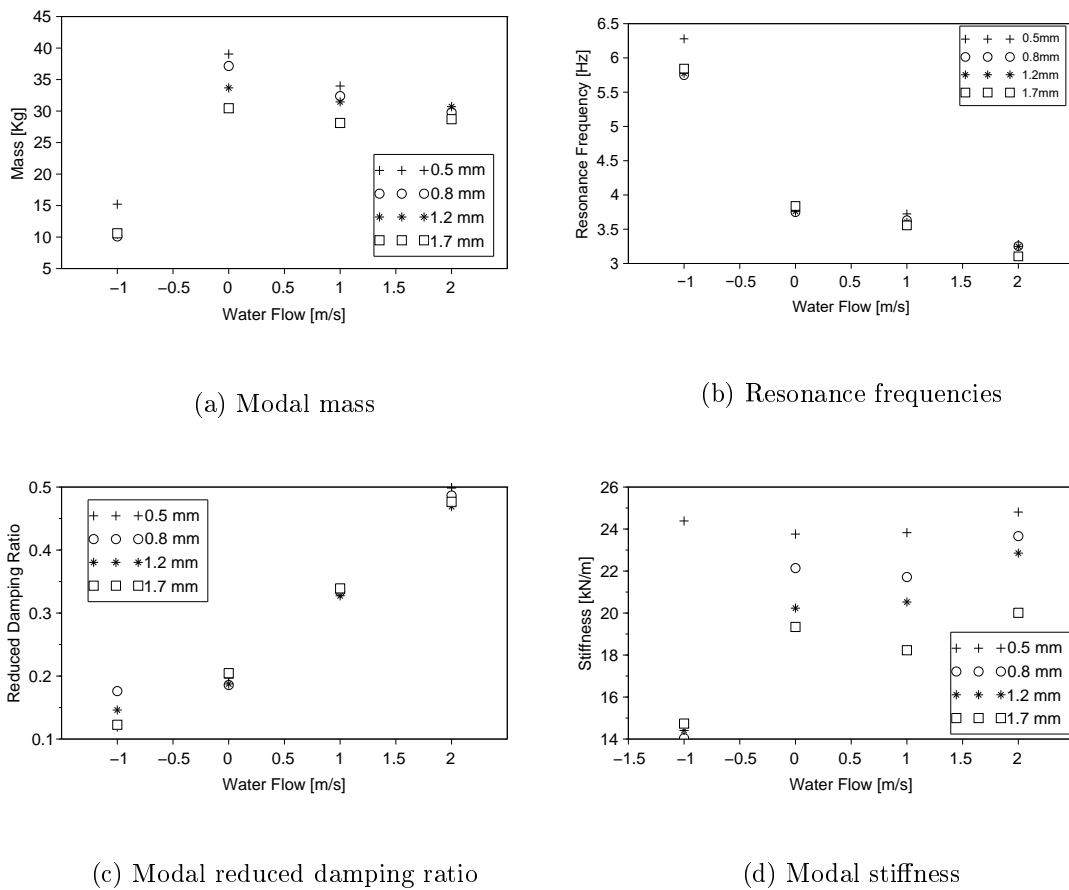


Figure 2.24 – Behaviour of the estimated dynamic parameters as function of the water flow rates and excitation amplitude for the first mode at 15 °C with 2 assemblies in large confinement configuration. Flow rate -1 m/s means "In Air"

The damping ratio (Figure 2.23c) shows a continuous and almost linear increasing trend as the water flow increases. The reduced damping ratio changes in a very significant way, it doubles when passing from "In Air" condition to 2 m/s water flow.

The stiffness (Figure 2.23d) also increases with the increase of the flow rate. The effect of the water flow, increasing the stiffness of the assembly, was already outline by quasi-static analysis. Stiffness coefficients for the third natural mode are not represented in Figure 2.23d for better visual results (out of scale).

Finally the effects of non linearities appearing when changing the excitation amplitude can be quantified (see Figure 2.24). The modal parameters relative to the first mode are analysed and compared when the fuel assembly is excited with different amplitudes under different flow conditions. Either the modal mass, resonance frequency and modal damping

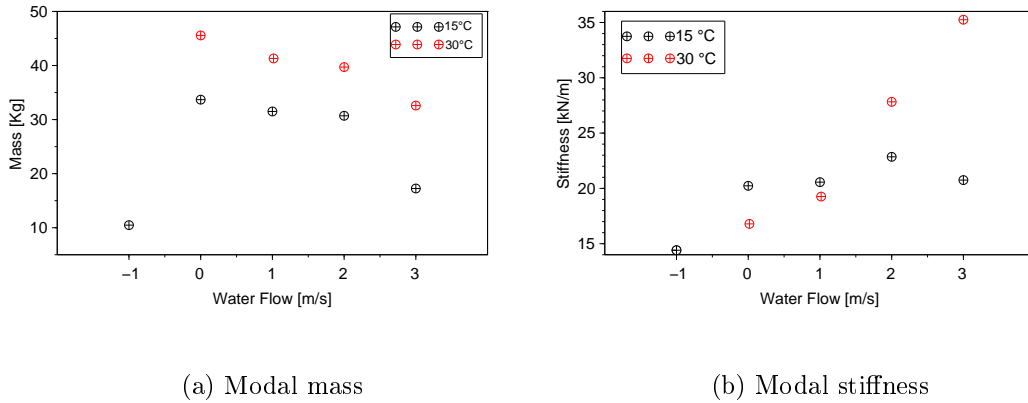


Figure 2.25 – Estimated modal stiffness and mass at 15 °C and 30 °C for the first mode with excitation amplitude of 0.8 mm with two assemblies in large confinement configuration.

appear to be affected in a marginal way by the changes of the excitation amplitude. On the other hand, the modal stiffness is strongly affected by the changes in the excitation amplitude (see Figure 2.24d). The stiffness coefficient appears to change more than 40% when the excitation amplitude changes from 0.5 mm to 1.7 mm. This important change is justified by the presence of the spring and dimples in the five support grids which hold the fuel rods.

The effects of temperature are visible both on the mass and stiffness coefficient plots in Figure 2.25. More in the specific, the mass coefficient (Figure 2.25a) increases when the temperature increases from 15 °C to 30 °C, but the trend for the two temperatures appears to be similar. On the other side, the stiffness coefficient shows a behaviour which changes in a consistent way when the temperature increases. The stiffness parameter, in fact has an asymptotic trend respect to the water flow rate at 15 °C, while it continues to increase (almost) linearly with the flow rate when the temperature is 30 °C. The asymptotic behaviour of the stiffness coefficient is due to an equilibrium between inertial and viscous forces. When the temperature changes, the viscosity changes considerably, thus the equilibrium between viscous and inertial forces also changes.

2.4.4 Coupling Between Different Fuel Assemblies

From the literature it is known that when a network of structures subject to an excitation is immersed in a liquid, the interaction between the fluid and the structure creates a coupling between the different structures which would otherwise behave independently (Païdoussis, 1998, 2008).

In this section the coupling existing between the four different fuel assemblies of the ICARE experimental set up will be analysed.

As a first approach, one can expect that the main coupling phenomenon will involve the excited fuel assembly (assembly n°1) and the one which is in front of him (assembly

2.4. EXPERIMENTAL RESULTS

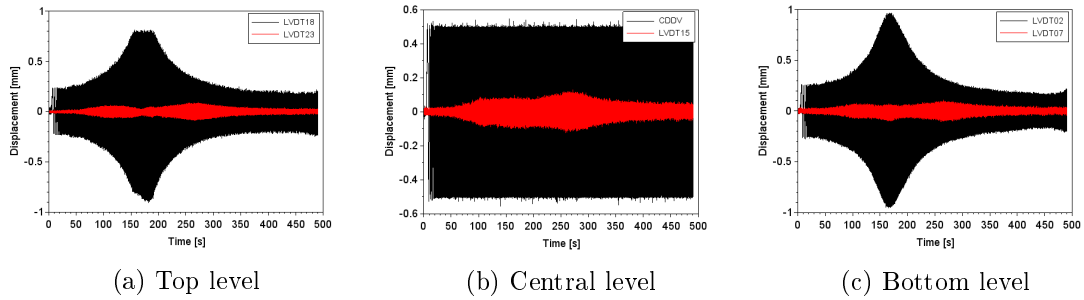


Figure 2.26 – Displacement time evolution of excited fuel assembly and assembly n° 2 in the excitation direction for 0.5 mm excitation with 1 m/s water flow in 2 fuel assemblies small confinement configuration at $15 \text{ }^\circ\text{C}$. Measurements are showed for the three different levels

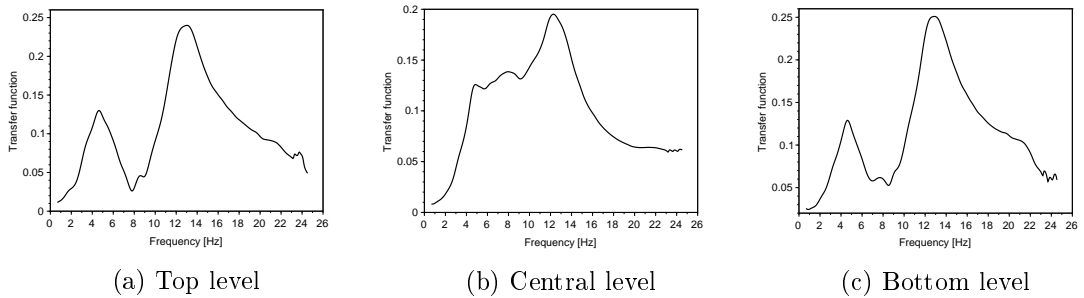


Figure 2.27 – Coupling transfer functions between excited fuel assembly and assembly n° 2 in the excitation direction for 0.5 mm excitation with 1 m/s water flow in 2 fuel assemblies small confinement configuration at $15 \text{ }^\circ\text{C}$. Measurements are showed for the three different levels

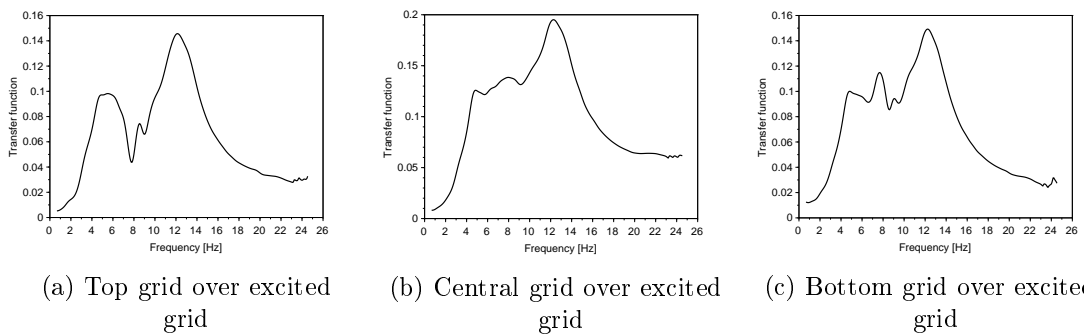


Figure 2.28 – Coupling transfer functions between excited grid of assembly n°1 and grids of assembly n° 2 in the excitation direction for 0.5 mm excitation with 1 m/s water flow in 2 fuel assemblies small confinement configuration at $15 \text{ }^\circ\text{C}$. Measurements are showed for the three different levels

n°2) in the excitation direction (x direction). For this reason, the analysis of the coupling between fuel assemblies 1 and 2 (see Figure 2.11) is investigated first. Figure 2.26 shows the temporal evolution of the displacement sensors for these two fuel assemblies in the

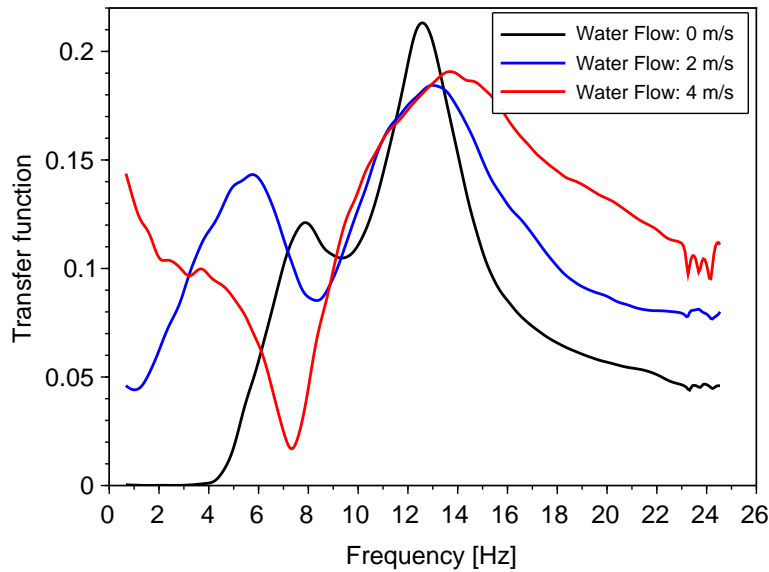


Figure 2.29 – Coupling transfer functions between central grids of excited fuel assembly and assembly n°2 in the excitation direction for 0.5 mm excitation with different water flows in 2 fuel assemblies small confinement configuration at 15 °C

excitation direction. The three different sensor locations are analysed (for sensor position see Figure 2.3). It is obvious that the fuel assembly is mostly excited in the top and bottom locations at the resonance frequency, while for frequencies far from the resonance the most excited position is the central one (where the hydraulic jack is attached). The coupling intensity between the grids over the three different levels are similar.

In Figure 2.27 the ratios between the displacement of the assembly n°2 and the excited assembly are presented in the frequency domain. The displayed curves can be read as a transfer function between the displacements of the two assemblies. It can be noticed that in the top and bottom locations the coupling is more intense at the first and third resonance frequencies (Figures 2.27a and 2.27c), while in the central location (Figure 2.27b) the coupling spectrum is much wider. A peak appears at about 8 Hz which corresponds to the second mode resonance frequency; even if this mode is not excited on the first assembly, it is excited on the second one due to the coupling. The intensity of the coupling is stronger between the excited grid and middle grid of assembly n°2 (Figure 2.28b), while it is about half of the intensity between the excited grid and top and bottom grids of assembly n°2 (Figures 2.28a, 2.28c).

In Figure 2.29 the coupling transfer functions are represented for different water flow conditions. It is obvious how the increasing of the water flow induces an increasing coupling between the two fuel assemblies. The maximum induced displacement is about 25% of the displacement of the excited assembly for the stagnant water (third mode at the top and bottom levels) while it increases to 40% when the axial water flow rate is 4 m/s. This

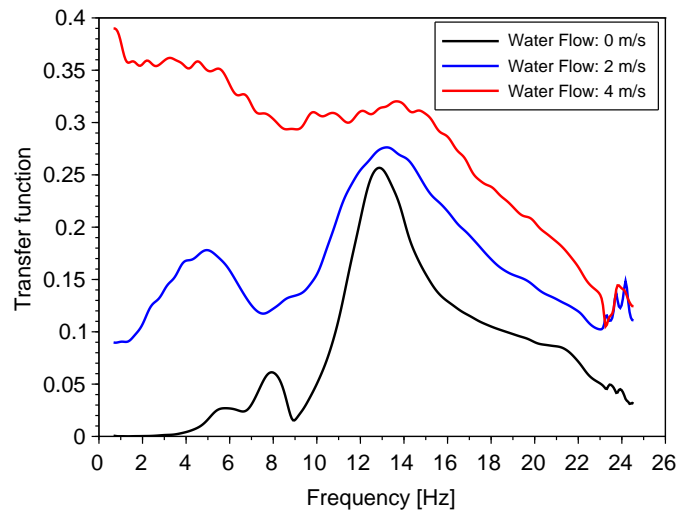


Figure 2.30 – Coupling transfer functions between bottom grids of excited fuel assembly and assembly n°2 in the excitation direction for 0.5 mm excitation with different water flows in 2 fuel assemblies small confinement configuration at $15\text{ }^{\circ}\text{C}$

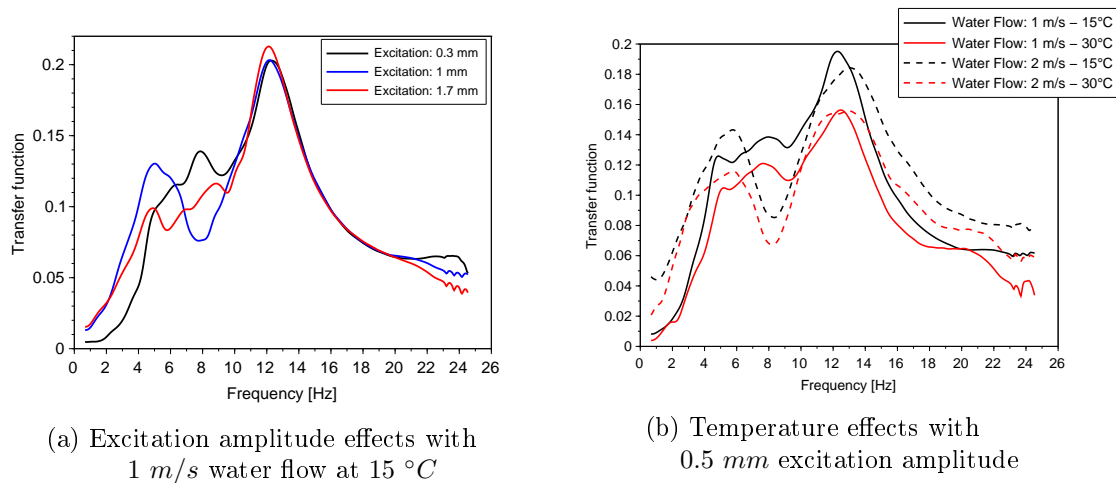


Figure 2.31 – Coupling transfer functions between central grids of excited fuel assembly and assembly n°2 in the excitation direction for different excitation amplitudes and different temperatures with 2 assemblies in small confinement configuration

demonstrates that an increase of the flow rate induce an increase of the coupling forces and that fluid structure interactions can induce the motion of a structure which is not in contact with the excited one. The high flexibility of the PMMA assemblies makes this phenomenon more accentuated that really is in full scale fuel assemblies. As the water flow increases, a static coupling appears and the coupling becomes effective on a wide range of frequencies. In addition an anti resonance peak appears at the frequency of 8.5 Hz which corresponds to the second natural frequency. When the flow increases, the coupling

between bottom grids becomes more important, up to 40% (see Figure 2.30).

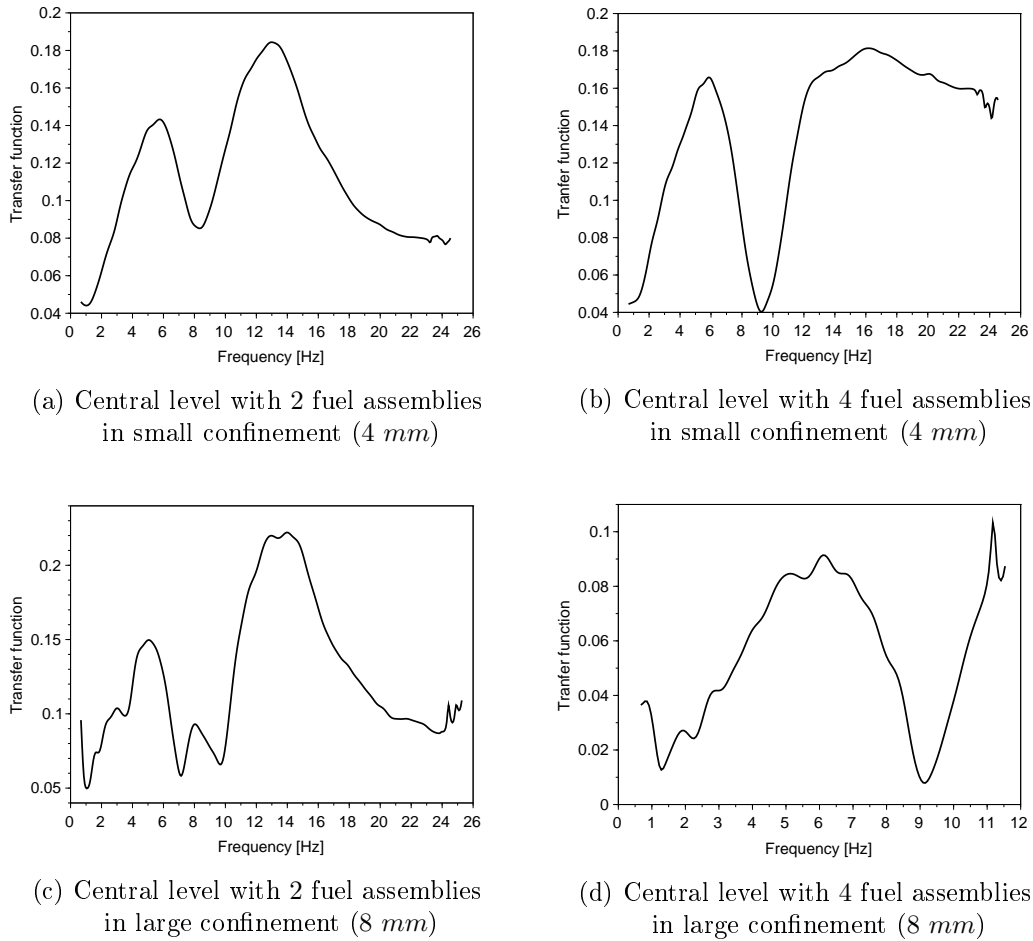


Figure 2.32 – Coupling transfer functions between excited fuel assembly and assembly n^2 in the excitation direction for 0.5 mm excitation at 2 m/s water flows in all configurations at 15 °C

The effects of excitation amplitude and water temperature can be investigated by comparing different experiments, as shown in Figure 2.31. The excitation amplitude does not affect in a considerable way the intensity of coupling between the two fuel assemblies (Figure 2.31a). Some small differences are visible for low frequencies, but a clear trend cannot be identified. The effects of the temperature, on the other hand, are clearly visible (Figure 2.31b). The intensity of the coupling strongly decreases (about 25%) when the water temperature increases from 15 °C to 30 °C. The decrease of the coupling forces due to an increase of temperature is mainly due to the changes in the water viscosity. Viscous forces, in fact, plays an important role in the fluid structure interaction, and are also responsible for the propagations of the efforts in the water domain.

The coupling between the two fuel assemblies can be affected by the number of fuel assemblies in the test section and by the confinement size. In order to analyse the influence of these parameters on the coupling effects Figure 2.32 shows the coupling transfer functions

for 2 and 4 assemblies, both in small and large confinement configurations.

It is demonstrated that the confinement size has a fundamental importance in the magnitude of the coupling phenomena. When the confinement size is large (8 mm) the presence of two or four fuel assemblies does not seem to perturb in a consistent way the coupling phenomena. In addition the coupling between the two fuel assemblies appears all along the length of the fuel assemblies (top, central and bottom levels) with the same order of magnitude. This is due to the central position of the hydraulic jack for experiments with small confinement size.

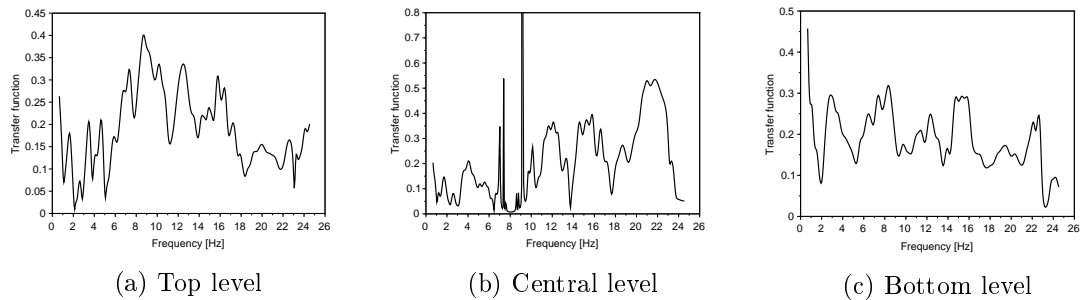


Figure 2.33 – Coupling transfer functions between excited fuel assembly and assembly n°2 in the direction orthogonal to the excitation for 0.5 mm excitation with 2 m/s water flow in 2 fuel assemblies small confinement configuration at 15 °C. Measurements are showed for the three different levels

On the opposite side, when the confinement size is reduced to 4 mm, the coupling between the two assemblies strongly changes when the configuration changes from two to four fuel assemblies. The magnitude of the coupling is reduced from about 30% to 20%. More generally, when the confinement size is increased, the coupling is reduced. The changes in the confinement size, in fact, implicate a change in the distance between the two assemblies (as specified in Figure 2.5). Thus, the larger the confinement size is, the more distant the two assemblies are, implying a decrease in the coupling effects.

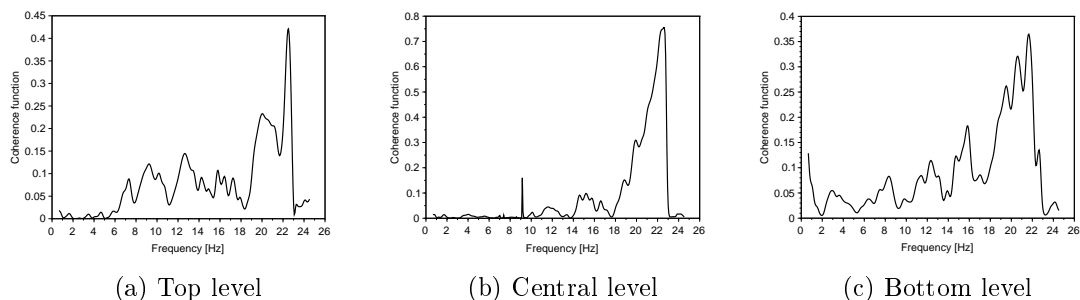


Figure 2.34 – Coherence functions between excited fuel assembly and assembly n°2 in the direction orthogonal to the excitation for 0.5 mm excitation with 2 m/s water flow in 2 fuel assemblies small confinement configuration at 15 °C. Measurements are showed for the three different levels

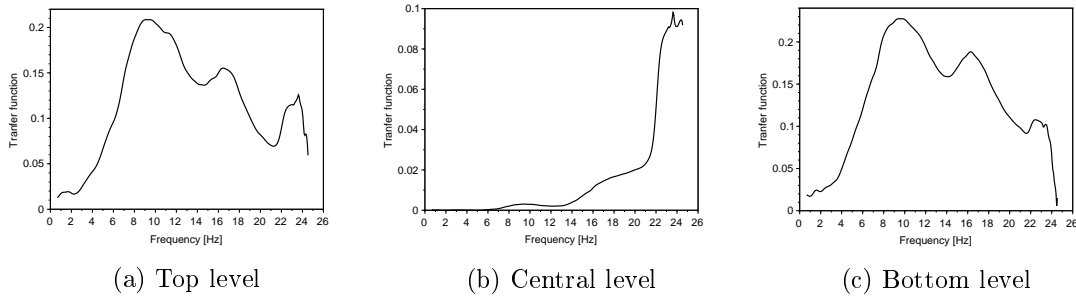


Figure 2.35 – Coupling transfer functions between excited fuel assembly and assembly n°4 in the excitation direction for 0.5 mm excitation with 2 m/s water flow in 4 fuel assemblies small confinement configuration at 15 °C. Measurements are showed for the three different levels

The coupling between the two fuel assemblies can also happen on the direction orthogonal to the excitation direction. Figure 2.33 represents the coupling transfer functions between the fuel assemblies n°1 and n°2 in the direction orthogonal to the excitation (y direction). From Figure 2.33 at a first sight one can conclude that there is a kind of coupling on the orthogonal direction all over the excitation spectrum of the same order of magnitude than in the excitation direction. Contrariwise, looking at the coherence function between the signals of the two fuel assemblies (see Figure 2.34) one discovers that there is no coherence between the two signals. Thus the relation outlined by the transfer function is mainly noise, and no founded conclusions can be drawn. We can thus affirm that the out of plane coupling between assembly n°1 and assembly n°2 is negligible. There is, instead, evidence of an existing coupling on the excitation direction between the fuel assemblies n°1 and n°4 (see Figure 2.11). The coupling happens only in the locations which are not excited, while there is no coupling at the level of the excited grid (see Figure 2.35).

2.4.5 Conclusions on Assembly Excitation Experimental Analysis

In the previous paragraphs the large amount of experimental data collected on the experimental facility ICARE have been analysed. In this section the conclusions are summed up.

The quasi static analysis of the fuel assembly allowed to analyse the non linearities of the system and to describe their effects on the behaviour of the fuel assembly. The stiffness of the assembly can also be estimated from the slope of the quasi static force-displacement relationship.

Later on the dynamic analysis of the excited fuel assembly has been performed. The effects of different experimental parameters have been investigated. The presence of the water flow induces a dramatic decrease of the resonance frequencies due to an increase of the modal masses and damping. As the water temperature increases, a reduction of the stiffness of the assembly is manifested. This phenomenon is not due to the changes in the water properties but it is assumed to be mainly due to the changes of the properties of the

plastic materials the assembly is made of.

Furthermore, the quantities which characterise the dynamical behaviour of the fuel assemblies (modal mass, modal damping, modal stiffness and resonance frequencies) are estimated from the experimental transfer functions. The estimation has been proven to be accurate, and quantitative consideration on the added mass, added damping and added stiffness effect can be performed. The added mass effect appear to be the most important one for our operative conditions; anyway, added damping and added stiffness effects cannot be neglected.

Finally, the displacement induced on the non excited fuel assemblies are investigated. The presence of the water (either stagnant or flowing) induces a force on the assemblies which are not excited by the external hydraulic jack. The induced force causes an induced motion of the assemblies. The magnitude of the induced motion is used to estimated the magnitude of the coupling existing between the different assemblies and in the different directions. As expected, the most effective coupling happens between the excited assembly and the opposite one (assembly n°2) in the same direction of the excitation. The coupling strongly depends on the water flow rates, and it increases as the water flow rate increases. The induced motion on the otherwise at rest fuel assembly can reach values of above 40% of the external imposed displacement.

2.5 Laser Velocimetry

Laser velocimetry is a branch of the optical technique for velocity measurements; it is based on light scattering by tiny particles assumed to follow the flow, which allows the local fluid flow velocity and its fluctuations to be determined. It is a widely used non-intrusive technique to measure velocities in fluid flows, either locally or in a map. During the years, different techniques and technologies have been developed in order to improve the quality, the efficiency, the accuracy and to extend the domain of application of such techniques. For general information on laser velocimetry techniques the reader is referred to [Boutier \(2013\)](#).

This section is devoted to the presentation of laser velocimetry techniques implemented on the ICARE experimental facility. Some of the experimental results will be discussed.

2.5.1 Laser Velocimetry Techniques on ICARE

Two different techniques were implemented and thus discussed: Laser Doppler Velocimetry (LDV) and Particle Image Velocimetry (PIV).

Laser Doppler Velocimetry

Laser Doppler Velocimetry (LDV), also known as Laser Doppler Anemometry (LDA), is a technique using the Doppler shift in a laser beam to measure the velocity in transparent or semi-transparent fluid flows, or the linear or vibratory motion of opaque, reflecting,

surfaces. The measurement with LDV is absolute, linear with velocity and requires no pre-calibration. LDV is one of the simplest and most used techniques for non intrusive measurements of velocity in fluids.

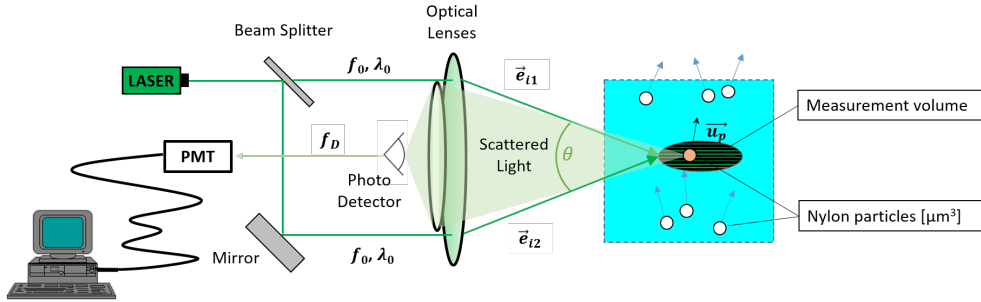


Figure 2.36 – Schematic representation of LDV experimental apparatus

Doppler velocimetry works on the principle of Optical Heterodyne Detection (De Lange, 1968). In its simplest and most presently used form, LDV crosses two beams of collimated, monochromatic and coherent laser light in the flow of the fluid being measured. The two beams are usually obtained by splitting a single beam, thus ensuring coherence between them. Lasers with wavelengths in the visible spectrum (390 – 750 nm) are commonly used. A transmitting optic focuses the beams to intersect at their waists (the focal point of a laser beam), where they interfere and generate a set of straight fringes. As particles (either naturally occurring or induced) entrained in the fluid pass through the fringes, they reflect light that is then collected by a receiving optic and focused on a photo detector (typically an avalanche photo diode). This chain is summed up in Figure 2.36.

The reflected light fluctuates in intensity, the frequency of which is equivalent to the Doppler shift between the incident and scattered light. The Doppler shift frequency is proportional to the component of particle velocity which lies in the plane of two laser beams. If the sensor is aligned with the flow such that the fringes are perpendicular to the flow direction, the electrical signal from the photo detector will then be proportional to the particle velocity.

From optical physics, the relation which allows to relate the frequency shift due to the Doppler effect to the velocity of the particles is given by:

$$f_d = \frac{\vec{u}_p}{\lambda_0} \cdot (\vec{e}_{i1} - \vec{e}_{i2}) \quad , \quad (2.6)$$

where f_d is the phase shift between incident and scattered light, \vec{u}_p is the velocity of the measured particle, λ_0 is the wavelength of the laser beam, \vec{e}_{i1} and \vec{e}_{i2} are respectively the direction of the first and of the second laser beam. With some geometrical consideration, Equation 2.6 can be simplified in:

$$f_d = \frac{2 \cdot \sin\left(\frac{\theta}{2}\right)}{\lambda_0} \cdot |u_{py}| \quad , \quad (2.7)$$

where θ is the angle between the two laser beams and $|u_{py}|$ is the module of the axial particle velocity. For further informations on LDV techniques the reader is referred to [Albrecht et al. \(2002\)](#); [Drain \(1980\)](#); [Durst et al. \(1976\)](#).

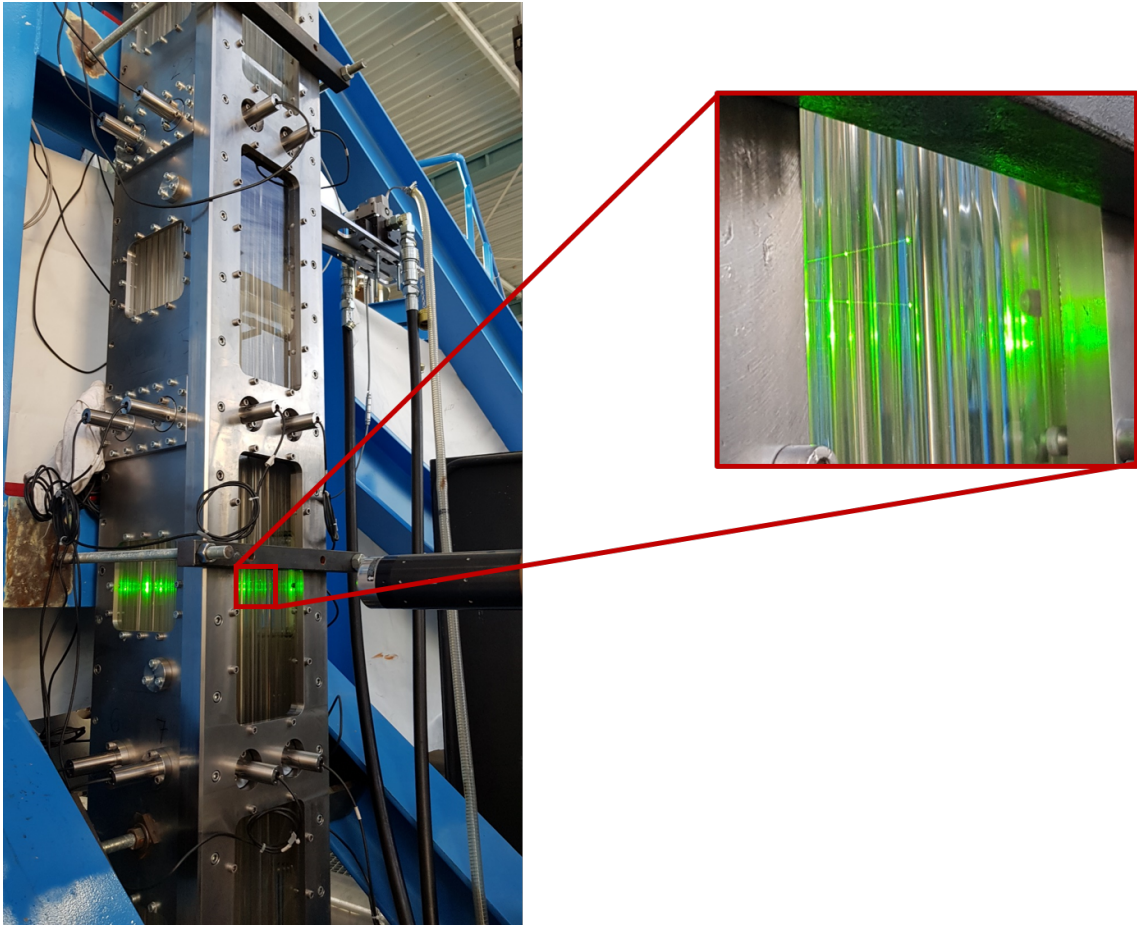


Figure 2.37 – Picture of LDV experimental apparatus on ICARE

Since the ICARE test section is equipped with transparent portholes, LDV techniques can be implemented in order to obtain local information on the flow velocity. The laser used for LDV measurements on ICARE is a solid state green continuous laser with a wavelength of 561 nm and power of 0.3 mW . Nylon particles (diameter size about 40 nm) are injected in the water loop to perform the measurements. Figure 2.37 shows a picture of the LDV laser beams facing the test section. The geometrical path of the two laser beam can be seen looking at the width of the transparent porthole (zoom on the right side of Figure 2.37).

Particle Image Velocimetry

Particle Image Velocimetry (PIV) is an optical method of flow visualization mainly used for research purposes. It is used to obtain instantaneous velocity measurements and related properties in fluids. The fluid is seeded with tracer particles which, for sufficiently small

particles, are assumed to faithfully follow the flow dynamics (the degree to which the particles faithfully follow the flow is represented by the Stokes number). The fluid with entrained particles is illuminated so that particles are visible. The motion of the seeding particles is used to calculate speed and direction (the velocity field) of the flow being studied.

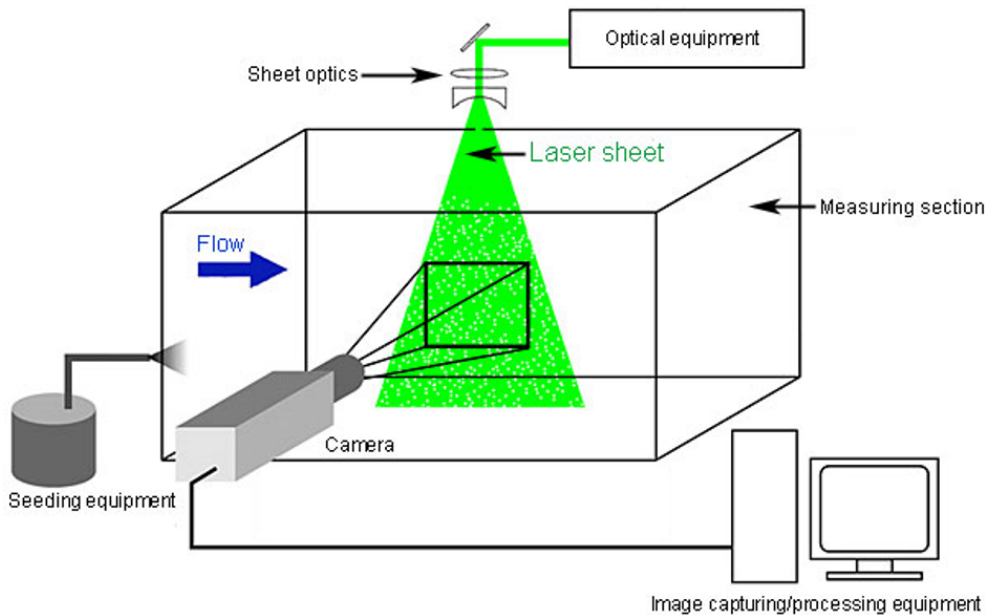


Figure 2.38 – Schematic representation of a PIV experimental apparatus

Typical PIV apparatus consists of a camera (normally a digital camera with a CCD chip in modern systems), a laser with an optical arrangement to create a laser sheet, a synchronizer to act as an external trigger for control of the camera and laser, the seeding particles and the fluid under investigation as shown in the scheme in Figure 2.38.

PIV software is used to post-process the optical images. Two different images are compared. If the time lag between the two images is small enough, the particles position slightly changes from one picture to the other one. With a correlation algorithm, the software is thus able to reconstruct the path of the particles and to extract their instantaneous velocity.

Standard PIV systems can obtain two dimensional velocity fields. With some more sophisticated systems one can also obtain informations on the three-dimensional velocity of the particles. For more information on PIV the reader is referred to [Adrian \(1991\)](#); [Raffel et al. \(2007\)](#).

The PIV technique, allowing to measure the velocity field of an extended 2D region is considered to contain much more information than the LDV technique. For this reason, in recent time (June 2018) a PIV system has been installed on the ICARE facility and an experimental campaign has been run. The laser used for PIV measurements on ICARE is a solid state green continuous laser with a wavelength of $532 \mu m$ and power of $10 W$. A

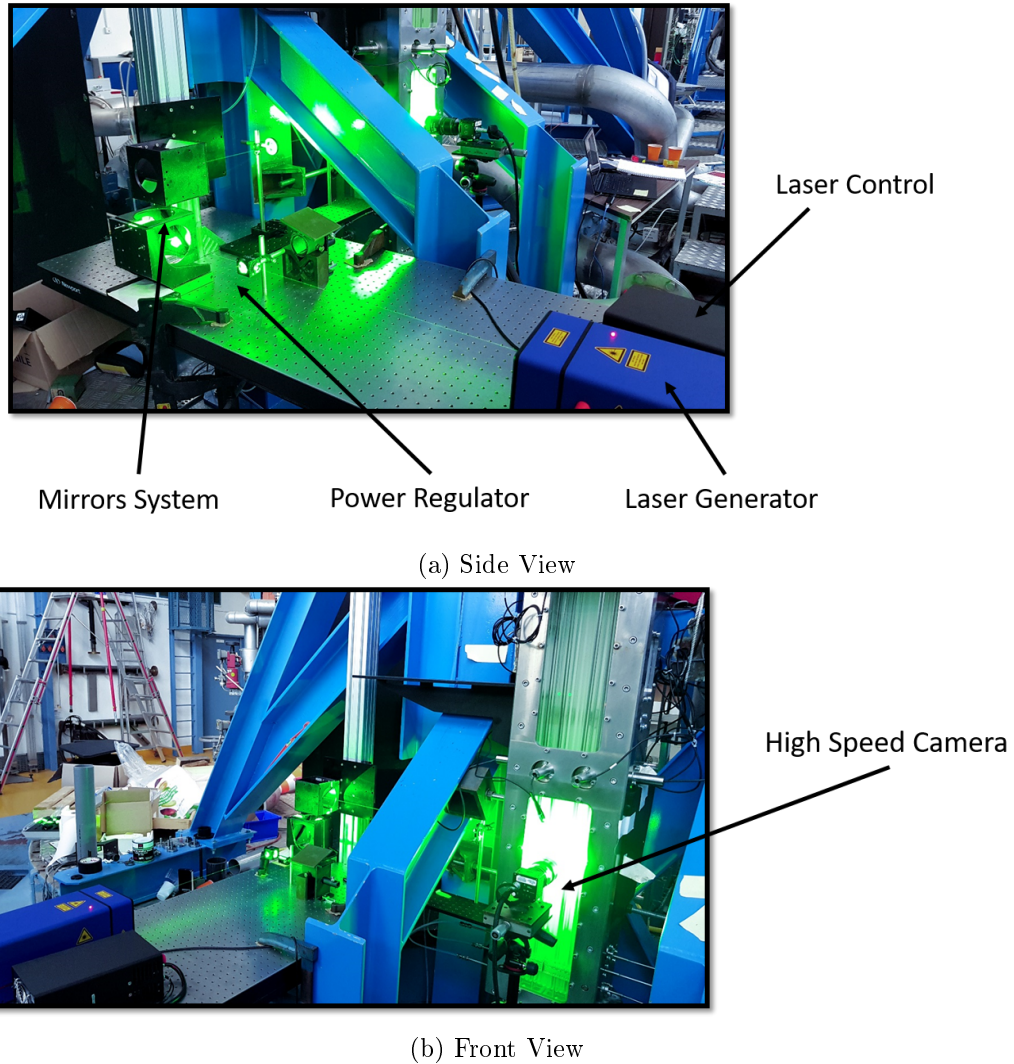


Figure 2.39 – Pictures of PIV experimental apparatus on ICARE

system of mirrors and lenses has been used to bring the laser on the measurement point. The high speed camera has a an acquisition rate high enough to allow to be time resolved for the typical velocities we want to measure ($\sim 1 \text{ m/s}$). Silver coated nylon particles (diameter size about $10 \mu\text{m}$) are injected in the water loop to perform the measurements. Some pictures of the PIV experimental set-up are showed in Figure 2.39.

2.5.2 LDV Experimental Matrix

In this paragraph the LDV measurement matrix is described.

LDV measurements are performed on the water flow in between the two frontal fuel assemblies (Assembly 1 and Assembly 2 in Figure 2.11). Measurements are repeated at five different depth locations (from 2.5 mm to 105 mm). Deeper measurements were not possible due to limitation on the optics. Two different positions in the vertical direction are used to perform the measurements. In this way the axial evolution of the flow can be

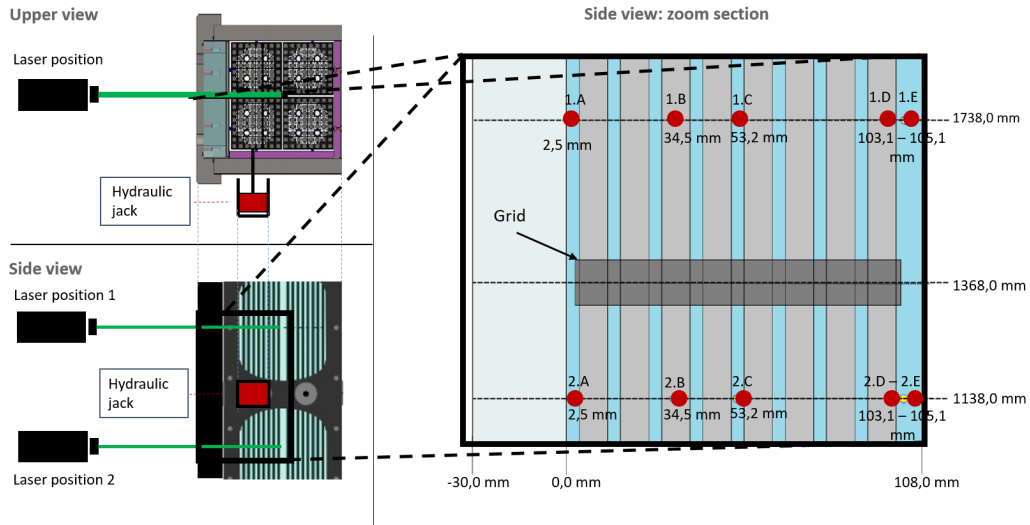


Figure 2.40 – Schematic of LDV measurements points on ICARE

investigated. A schematic representation of the ten different measurement points where LDV is applied is presented in Figure 2.40.

LDV Depth	LDV Height	Confinement	Assemblies	Water Flow	Temperature	Excitation Amplitude	Frequency
A: 2.5 mm	1: 1738 mm 2: 1138 mm	Small: 4 mm	4	1 m/s	15 °C 30 °C	0 mm	Sweep: 0,05 ÷ 25 Hz
B: 34.5 mm				2 m/s		0,5 mm	
C: 53.2 mm				3 m/s		1 mm	
D: 103.1 mm				4 m/s		1,7 mm	
E: 105.1 mm							

Figure 2.41 – Schematic of LDV measurements matrix ICARE

The LDV measurement is run for 500 s while the fuel assembly 1 is excited within a frequency range going from 0.05 Hz up to 25 Hz. For each measurement point, several LDV measurements are repeated for different conditions of excitation amplitude, water flow rate and water temperature. A scheme with the LDV measurement matrix is presented in Figure 2.41.

2.5.3 Experimental Results with LDV

In this section experimental results obtained with LDV technique will be discussed. All the data and curves refer to temperature condition of 15 °C unless otherwise specified.

Raw Signal Analysis

First of all, the raw data coming from the LDV acquisition system need to be analysed. Since the LDV measurements are performed while the fuel assembly is moving, one expects the water flow to have an induced axial oscillation. The noise of LDV measurements could be very high either due to electrical noise or to turbulence in the water flow which make particles to have different velocities. It is thus important to understand if the LDV technique can detect oscillations in the water flow, whether they can be easily distinguished from the noise or not.

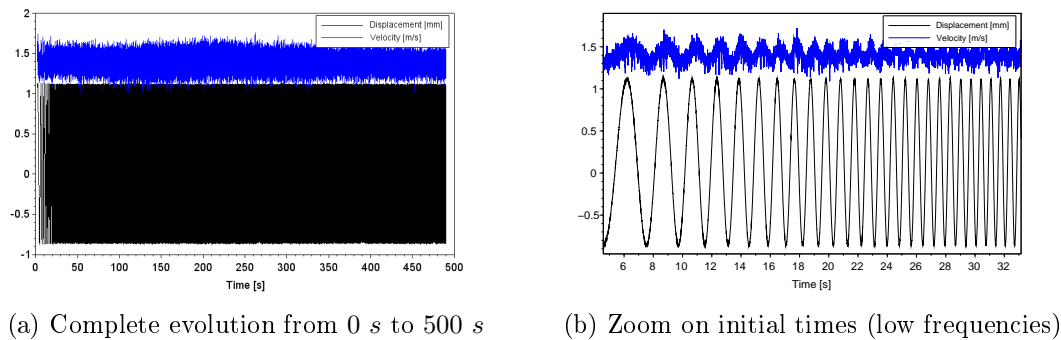


Figure 2.42 – Water velocity and hydraulic jack position for experiment at 1 m/s water flow, 1 mm excitation amplitude and LDV measurement point 1.C (see Figure 2.40)

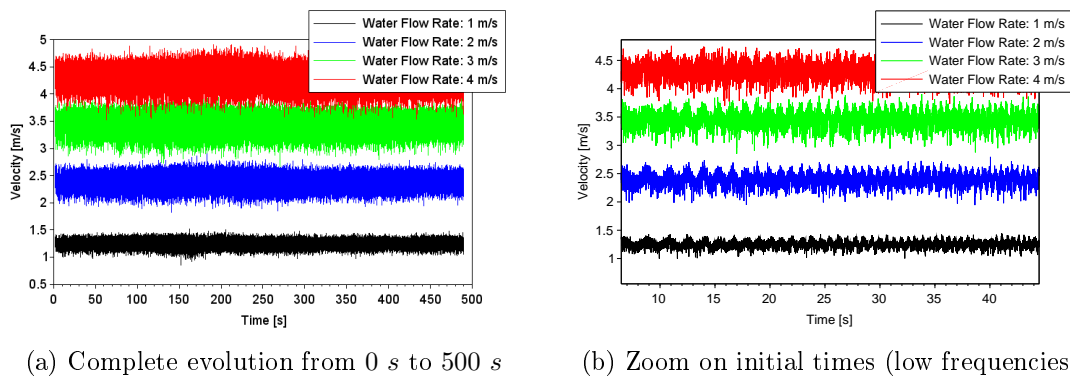


Figure 2.43 – Local water velocity evolution for experiments at different water flows, 1 mm excitation amplitude and LDV measurement point 2.C (see Figure 2.40)

Figure 2.42 shows the raw data of the time evolution of the local fluid velocity compared to the position of the excitation hydraulic jack system. The plot is related to an experiment performed with an excitation amplitude of 1 mm and a water flow of 1 m/s and the LDV measurements are taken in the position above the excitation system and in the middle position (position 1.C in Figure 2.40). Figure 2.42a representing the whole signal during the 500 s acquisition time is not resolved enough in order to appreciate the oscillations of both the position and the velocity. In Figure 2.42b, instead, it can be remarked that the velocity signal appears to oscillate with the same frequency of the position signal. It means

that the displacement of the fuel assembly induces oscillations in the axial velocity of the fluid which can be measured with the LDV technique. Even if the noise on the velocity signal is quite important, oscillations can be measured. This observation confirmed that it is worth the effort to perform an experimental campaign for LDV measurements.

It is also interesting to investigate how the velocity oscillations change when the average velocity of the water flow changes. In Figure 2.43 the LDV measures with average water flows going from 1 m/s up to 4 m/s are showed (2.C position in Figure 2.40). The oscillations of the velocity appear to be proportional to the average velocity of the flow (Figure 2.43b). That is reasonable, since the perturbation in the flow will be amplified when the average flow rate increases. Furthermore, it can also be remarked that the noise on the velocity signal increases as the average velocity increases (Figure 2.43a). This noise is mainly due to the turbulence in the flow, thus it is reasonable that it increases with the increase of the flow rate. The nature of the noise in the LDV measurement is also confirmed by Figure 2.44 where the same behaviour on the noise is found without any external excitation of the fuel assembly. Thus it is confirmed, that the increasing spread of the velocity profile is only due to the increasing turbulences in the fluid.

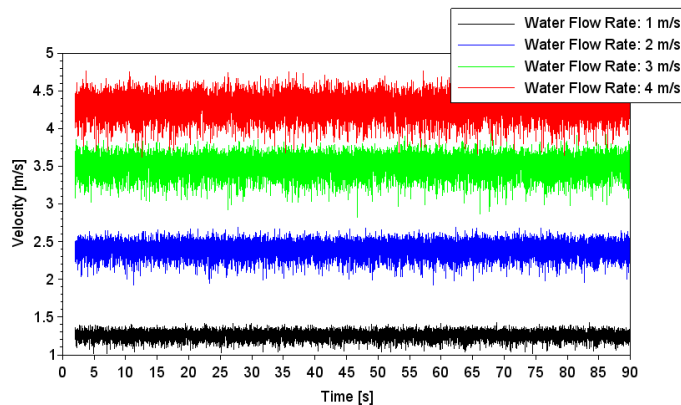


Figure 2.44 – Local water velocity evolution for experiments at different water flows without external excitation at LDV measurement point 2.C

It can also be noted that the measured average velocity is always about 50% bigger than the imposed average velocity. This happens because the average velocity is calculated on the whole fluid domain both inside the fuel assemblies and in between them. Since the measurements are taken in the space in between two fuel assemblies, the velocity is bigger than in the middle of the assembly because the hydraulic diameter is larger.

Power Spectral Density and Transfer Function Analysis

Once understood that the excitation of the fuel assembly produces measurable effects on the LDV velocity profiles, experimental data from LDV campaigns are analysed by means of Power Spectral Density (PSD) and Transfer Functions (TF).

Both PSDs of water velocity and excited grid position are plotted. In Figure 2.45 a

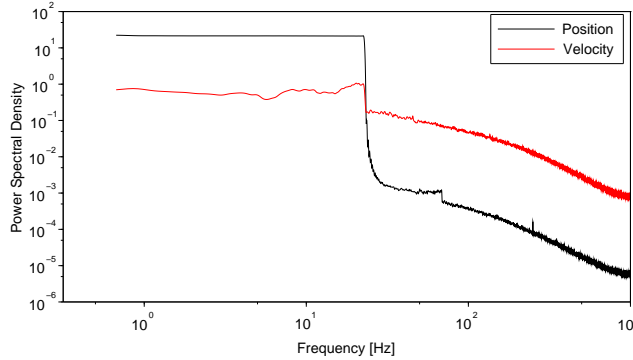


Figure 2.45 – Position and velocity PSDs for experiment at 2 m/s water flow, 1 mm excitation amplitude and LDV measurement point 1.C (see Figure 2.40)

typical PSD profile for the position and the velocity are presented in order to discuss the main features which are common to all the experimental data. The position Power Spectral Density is constant from 0 Hz up to 25 Hz since a constant amplitude excitation is imposed on that frequency range. At the frequency of 25 Hz the modulus of the PSD suddenly goes down of several order of magnitudes. At about 70 Hz the PSD presents a peak which is due to electronic noise in the command line of the hydraulic jack (also present in previous experiments with the same electronics). The velocity power spectral density also presents a sharp edge (about one order of magnitude) at the frequency of 25 Hz demonstrating that the oscillations showed in Figures 2.42-2.44 are effectively due to the excitation of the fuel assembly. The PSD from 0 Hz to 25 Hz is quite stable but is not constant showing that the excitation frequency affects the water flow oscillations. The tail of the velocity PSD shows a change in the slope (at about 100 – 200 Hz) which is due to the turbulence and depends on the water velocity.

The PSDs spectra can be useful in order to extract some common general behaviour. Anyway, in order to perform further investigations on the parameters which could affect the oscillating flow, the transfer functions and coherence functions between the velocity and position are pertinent. Transfer function between velocity and position is defined, in analogy with Section 2.3.2, by:

$$TF_{VP}(f) = \frac{V(t) \star V(t)}{V(t) \star P(t)} \quad , \quad (2.8)$$

while the coherence function is given by:

$$Coh_{VP}(f) = \frac{|V(t) \star P(t)| \cdot |V(t) \star P(t)|}{|V(t) \star V(t)| \cdot |P(t) \star P(t)|} \quad , \quad (2.9)$$

where $TF_{VP}(f)$ is the transfer function in the frequency domain between flow velocity and fuel assembly position, $V(t) \star V(t)$ is the spectral autocorrelation of the water velocity signal, $V(t) \star P(t)$ is the spectral cross correlation between the water velocity signal and

the excited grid position signal, $P(t) \star P(t)$ is the spectral autocorrelation of position signal and $Coh_{VP}(f)$ is the coherence function between water velocity and excited grid position.

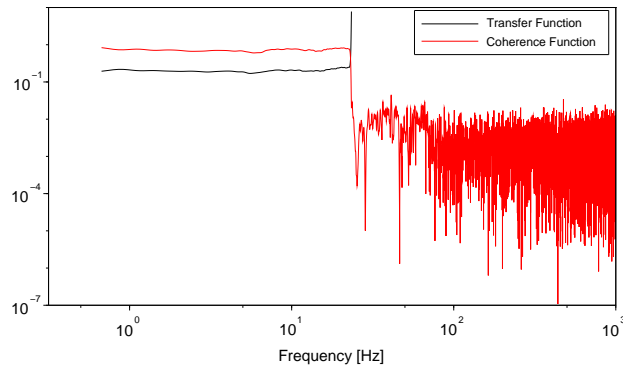


Figure 2.46 – Transfer function absolute value and coherence function for experiment at 2 m/s water flow, 1 mm excitation amplitude and LDV measurement point 1.C (see Figure 2.40)

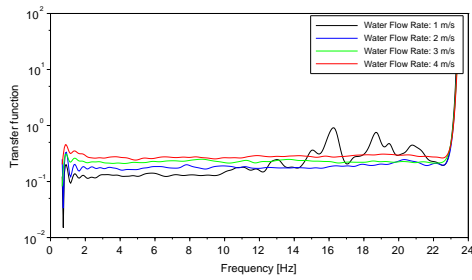
The transfer function between the velocity and position signals presents once again a first zone up to about 25 Hz which is quite constant and is of the order of magnitude of 10^{-1} (depending on the experimental parameters). For higher frequencies, which are not directly excited by the hydraulic jack, the transfer function goes to infinity since the position signal goes to zero. The coherence function shows that the oscillation signal which is detected either by the time evolution plots and by the PSD plots are effectively due to the excitation of the assembly since its value in the frequency range of $0 - 25\text{ Hz}$ is close to unity. This can be seen in Figure 2.46 which shows a typical sample of transfer function and coherence function for LDV data sets.

Water Flow Effects

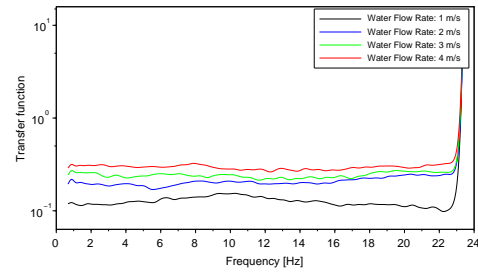
In this paragraph the effects of changing the water flow inside the ICARE test section will be investigated.

As already seen in Section 2.5.3 we expect the oscillations of the fluid velocity to increase with the increase of the average flow velocity. Figure 2.47 shows the transfer functions absolute value to increase with the increasing of the bulk flow velocity. There is not a perfect direct proportionality between the increase of the transfer function magnitude and the water flow velocities probably due to the addition of some dissipation related to non linearities.

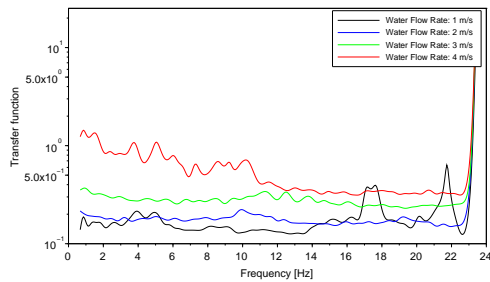
It can be seen that the behaviour of the transfer functions depending on the flow rate generally repeats in different measurement points with change in the absolute value of the transfer function. The water flow, in fact, is not the same in all the locations along the gap between the two fuel assemblies. Measurements taken closer to walls have a larger perturbation of the local flow velocity (Figures 2.47a and 2.47c) than the ones taken at



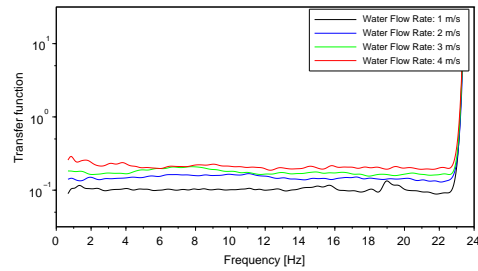
(a) LDV measurement point 1.A



(b) LDV measurement point 1.C



(c) LDV measurement point 2.A



(d) LDV measurement point 2.C

Figure 2.47 – Transfer functions V/P for experiments at different water flows at different LDV measurement points (see Figure 2.40) with 1 mm excitation amplitude

middle depth of the fuel assemblies (Figures 2.47b and 2.47d).

Excitation Amplitude Effects

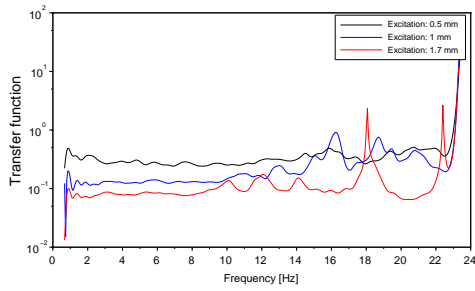
As already discussed in previous sections, the structure response is not proportional to the excitation amplitude due to the presence of non-linearities. Thus, we expect a similar behaviour on the induced flow.

Even if the amplitude of the induced oscillating flow increases with the increase of the excitation amplitude, there is not a direct proportionality relationship. The transfer function between the local velocity and assembly positions are not superimposed (Figure 2.48); the ratio between the flow oscillations and the excitation amplitude is not constant. The ratio is higher for smaller amplitude excitations, and it decreases as the excitation amplitude increases. This means that the energy introduced in the system by small amplitude oscillations is transferred to the fluid in a more efficient way than the energy introduced by large amplitude excitation.

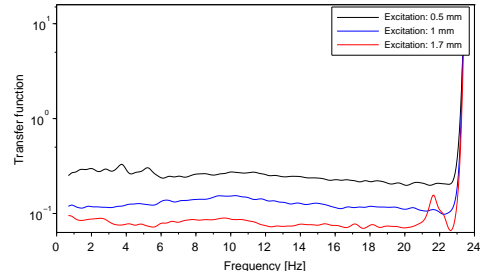
Water Temperature Effects

This paragraph aims to analyse the effects of water temperature changes on the induced axial flow. While most of the experiments are performed with the water at the temperature of 15°C some of them are run with the water at the temperature of 30°C. As already mentioned in the Section 2.3.1 such a slight difference on the water temperature implies

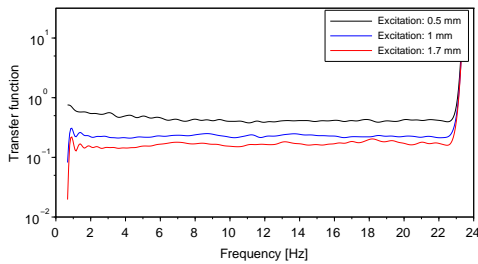
CHAPTER 2. FUEL ASSEMBLY VIBRATIONAL EXPERIMENTS



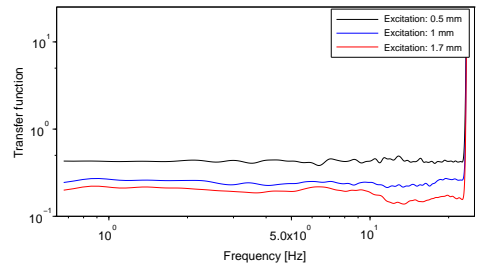
(a) LDV measurement point 1.A
at 1 m/s water flow



(b) LDV measurement point 1.C
at 1 m/s water flow

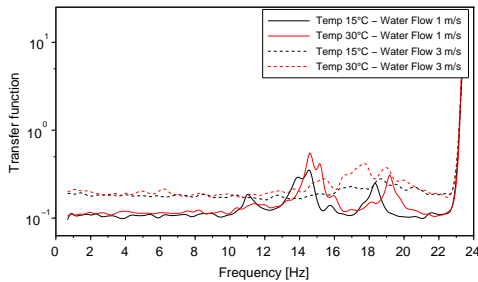


(c) LDV measurement point 1.A
at 3 m/s water flow

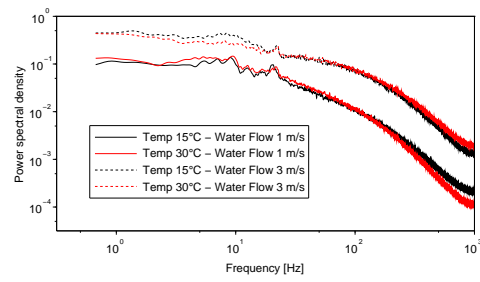


(d) LDV measurement point 1.C
at 3 m/s water flow

Figure 2.48 – Transfer functions V/P for experiments at different excitation amplitudes with different water flows at different LDV measurement points (see Figure 2.40)



(a) Transfer functions V/P



(b) Velocity power spectral density

Figure 2.49 – Transfer functions and power spectral densities for experiments at different temperatures ($15^\circ C$ and $30^\circ C$), with 1 mm excitation amplitude at LDV measurement point 2.B (see Figure 2.40)

an important difference on the water viscosity (see Figure 2.12).

Figure 2.49a shows that the amplitude of the induced axial flow does not change when the water temperature changes from $15^\circ C$ to $30^\circ C$. On the other hand, it needs to be considered that the experiments with the two different temperatures are performed at the same water flow velocity, while the viscosity was changing. This means that the Reynolds conditions changes from one experiment to another one. As the viscosity decreases, the Reynolds number ($Re = \frac{\rho v D_h}{\mu}$) increases. The changes in the Reynolds number can be

recovered in the tails of the power spectral densities, which show some differences (see Figure 2.49b).

In order to have perfect equivalent conditions from a fluid dynamics point of view, experiments with two different temperatures should be performed by maintaining the same Reynolds number. Anyway, it is estimated that on such a range of temperatures the changes in the induced axial flow due to excitation of a fuel assembly is not relevant.

For future works, some extended experimental analysis on the temperature effects on fluid structure interactions could be of extreme interest.

LDV Measurement Location Effects

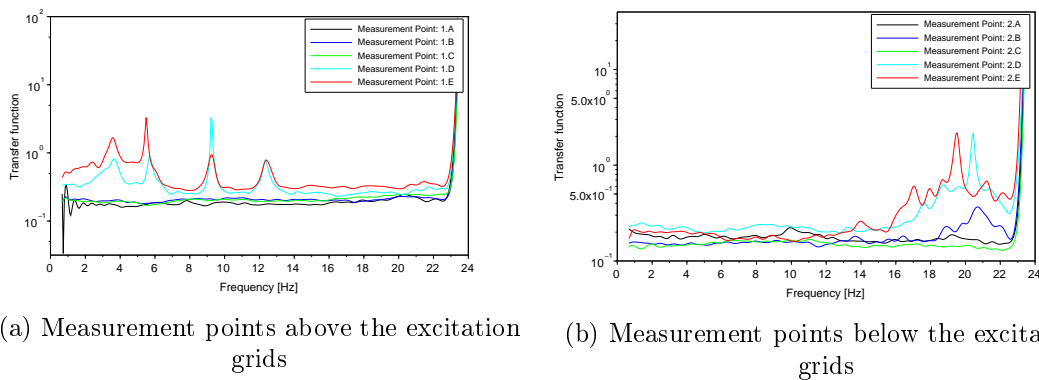


Figure 2.50 – Transfer functions V/P for different measurements points (see Figure 2.40) at 2 *m/s* water flow with 1 *mm* excitation amplitude

Finally, in this section, LDV measurements performed in different locations are compared. Transfer functions are not affected in a significant way from the measurement locations. This is more specifically true for the measurement point located below the excitation grid (Figure 2.50b), while transfer functions related to the measurements taken above the grid are more spread out. This effect is probably due to the presence of the grid itself, which perturbs the flow introducing turbulence and edge effects. Furthermore, the errors in the alignment of the laser parallel to the assembly can introduce some variations on the measured values of the velocity oscillations since the distance between the measurement point and the fuel assemblies can change.

In addition, it is also useful to observe the power spectral density for measurements in different locations (Figure 2.51). By comparing the two Figures 2.51b and 2.51a one can remark that the water velocity is always larger (about 20%) for the measurement points located below the grid than for the ones located above the grid. Since the two measurement points are distant of each other of about 50 *cm* and the distance from the inlet of the test section is around 1 *m*, such a velocity profile can be due to the redistribution of the water flow inside the test section. The inlet of the test section, in fact, is made of 4 small nozzles which inject the water in the whole structure which has a section much larger than the total

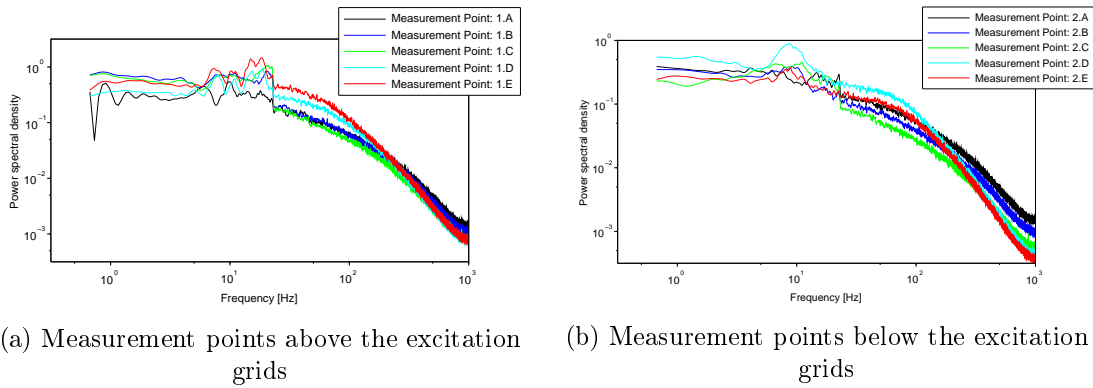


Figure 2.51 – Power spectral density functions for different measurement points (see Figure 2.40) at 2 m/s water flow with 1 mm excitation amplitude

section of the nozzles. Thus the water needs to be redistributed inside the test section.

Moreover, the velocity profile is not uniform along the depth. Velocity profile has a maximum for the measurement points located next to the walls, while it decreases for the points located in the middle of the fuel assemblies. The gap between the fuel assemblies and the wall has an hydraulic diameter which is larger than the one in between the assemblies, thus it justifies the water velocity to be larger in the gap between the walls and the assemblies. This assumption is valid if the measurements are performed within a distance large enough to avoid the boundary layer, where the velocity profile rapidly decreases.

Conclusions on LDV Experimental Campaigns

Laser Doppler Velocimetry experimental campaigns have been illustrated and some experimental results have been discussed in the previous paragraphs. One of the fuel assemblies is excited over a frequency range from 0 Hz to 25 Hz . Measurements show that an induced oscillating axial flow appears over the same excited frequency range.

The amplitude of such oscillations strongly depends on the intensity of the average fluid velocity with a non linear behaviour. In fact the higher the mean velocity of the water flow is, the higher is the relative oscillation of the fluid velocity. This result also explains the coupling between fuel assemblies becoming stronger for large water flow velocities. On the other hand the amplitude of the fuel assembly excitations affects the induced axial flow in an opposite way. As the excitation amplitude increases, the induced velocity oscillations are smaller in intensity (relatively to the excitation amplitude). Such a behaviour is probably due to dissipation forces (viscosity for instance) which have a stronger effect on larger amplitude oscillations.

One other parameter which could affect the induced flow is the water temperature. Since the temperature can sensibly modify the density and viscosity of the fluid, one can expect the induced flow to depend on this parameter. In order to investigate the temperature effects, experiments are performed with two different water temperatures: $15\text{ }^\circ\text{C}$ and $30\text{ }^\circ\text{C}$. The temperature range is limited by the acrylic material used in the

2.6. CONCLUDING REMARKS ON EXPERIMENTAL CAMPAIGNS

test section for the fuel assemblies. No important effects are visible on the induced axial flow as the temperature changes, but a difference on the turbulence intensity is outlined (Reynolds number changes). Thus, in order to better investigate temperature effects, new experiments should be designed over a larger temperature range, and the experiments should be compared by keeping the Reynolds number constant.

Finally, the comparison between measurements taken in different points of the water domain confirms that the flow is not uniform over the test section. In particular an axial redistribution occurs due to the inlet nozzle system, causing the flow to considerably change in intensity as we move along the axial direction on the test section. Moreover the water flow is measured to be stronger in the bypasses next to the walls than in between fuel assemblies, as expected.

In conclusion, LDV measurements allowed to catch some phenomena involving the induced axial flow due to fluid structure interactions. A large data set has been collected and some analyses performed. Data can still be used in the future to perform more detailed analyses by using for instance a spectrogram analysis method. The induced flow can be also related not only to the fuel assembly position but to the size of the gap in between them. Moreover such data can be used for comparison with PIV data which will allow to double check these results and will provide a more complete data set with the two dimensional velocity field of the water flow.

2.6 Concluding Remarks on Experimental Campaigns

In conclusion, in this section the experimental test section ICARE has been presented. Experimental results related to dynamical response of one excited assembly are presented and the coupling effects between different fuel assemblies are analysed. Finally experimental results relative to the LDV measurements relative to the axial induced flow are discussed. LDV measurements could not be performed "in Air" and in stagnant water due to the nature of the technique itself.

Both dynamical analysis and LDV measurements showed the non linearities of the system mainly due to the presence of support grids, which with their springs and dimples induce the assembly to deviate from the linear behaviour.

Added mass, stiffness and damping effects due to the presence of water in the test section are evident once the dynamical parameters are estimated. The added mass appears to decrease when the water flow rate increases, while added stiffness and added damping increase. The natural frequencies of the assembly have a continuous decreasing behaviour. Added mass and added stiffness effects will be compared with numerical results in Chapter 4 in order to validate the potential flow model and to understand its limits.

The analysis on the coupling between the excited assembly and non excited ones can be related to LDV measurements. The coupling forces, in fact, are induced by the perturbation of the water flow. Thus, the measurement on the water local velocity (Section 2.5.3) should be related to the coupling phenomena observed in Section 2.4.4. One important difference

between the two kind of measurement is the dependencies on the excitation frequencies. While the coupling is more intense when the excitation frequency is close to the natural frequencies of the assembly, the oscillation of the axial flow does not depend in significant way on the excitation frequency. This is a first hint that the fluctuations of the axial water flow may not affect directly the coupling between the two assemblies.

Another important remark can be done by comparing the excitation amplitude, flow rate, and temperature effects on the coupling and on the oscillating flow. All three parameters affect the coupling in an opposite way as they affect the axial velocity oscillations. The increase of temperature, for instance, causes a decrease of the coupling intensity between the fuel assemblies, while it causes an increase in the axial flow oscillations. This phenomenon, can be thus explained by considering not only the axial velocity perturbation. When the assembly is excited, in fact, not only an oscillation of the axial velocity is induced, but also oscillation of the horizontal velocity (mainly in the excitation direction) is induced. Probably, the behaviour of the horizontal velocity oscillation is different respect to the axial one, and it should be consistent with the observation on the coupling phenomena.

For future works, in order to better understand the relationship between the water velocity perturbation and the coupling existing between the two fuel assemblies, further measurements on the velocity field could be used. For instance, PIV measurement campaigns could bring important results on this subject.

Chapter 3

Fluid Structure Interaction Model

As already mentioned in Chapter 1, the main goal of this PhD work is to study and model fluid structure interaction on fuel assemblies. Thus slender cylinders subjected to an axial flow are studied. In order to better understand the deep nature of fluid-structure interaction and the influence of different parameters (i.e. flow velocity and confinement size), it has been decided to build a simplified model allowing fast calculations. In order to simplify the modelling of fluid forces the potential flow model is considered, the cylinder is represented by an Euler-Bernoulli beam and viscosity effects are neglected.

In this chapter, the fluid structure interaction model will be discussed in detail, with emphasis on the main assumptions behind the model and the mathematical methods used to solve the resulting problem. First, the model is developed for a single cylinder under axial flow in Section 3.1. The single cylinder model is then used for comparison with literature results and calculations are performed in order to analyse the confinements effects on the behaviour of a single cylinder under axial flow (further discussed in Chapter 4) in Section 3.2. Finally, the model is extended in Section 3.3 for multiple cylinder geometries (2 and 4 cylinders) that will be used for some analysis on the effects of symmetries. In this section, the model is also upgraded in order to represent the experimental facility ICARE made of 4 different fuel assemblies (8×8 squared lattice).

3.1 Problem Statement

In order to better understand the deep nature of fluid-structure interaction and the influence of different parameters (i.e. flow velocity and confinement size), a simple linear model is proposed with the objective of evaluating its representativeness and its limits. In order to achieve this objective the fluid is treated as being potential, the cylinder is modelled as an Euler-Bernoulli beam and viscosity effects are neglected. As first step, the problem of a single cylinder has been treated.

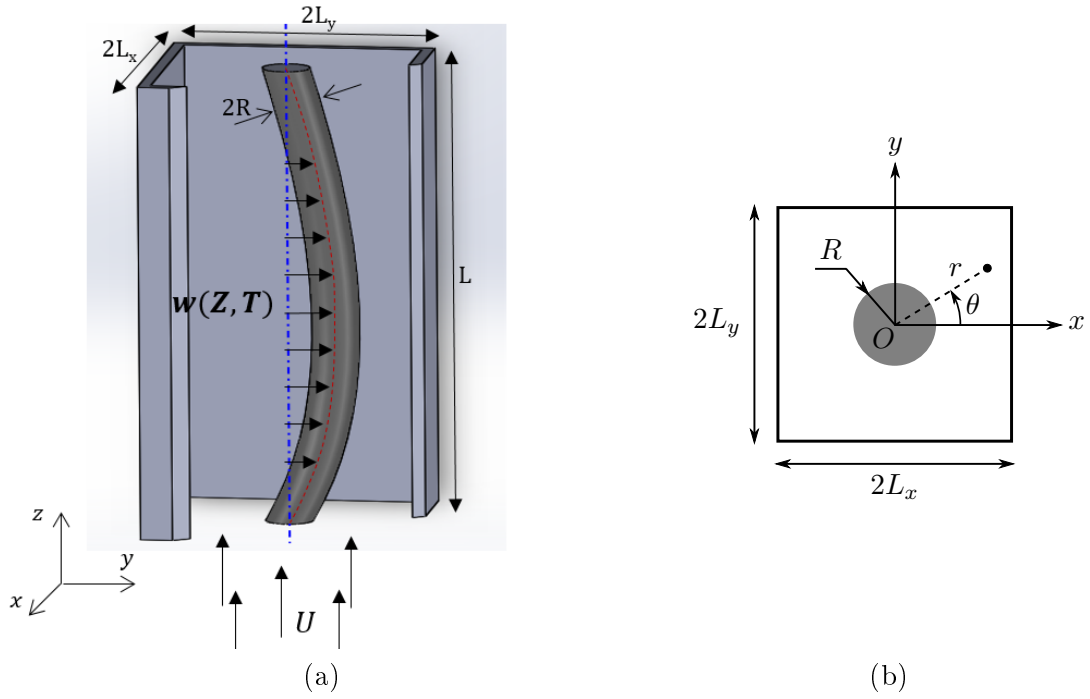


Figure 3.1 – (a) Schematic view of clamped clamped cylinder deformed under axial flow in a finite confinement. (b) Coordinate systems.

3.1.1 Structure Model

As sketched in Figure 3.1, a clamped-clamped cylinder of length L and radius R is considered. Two coordinate systems will be used: a Cartesian one based on x , y and z axis represented in Figure 3.1 with origin at the bottom of the cylinder and centred on its neutral axis at rest, and a cylindrical one with same origin and z axis.

The cylinder is submerged in a uniform and constant axial flow with velocity U and bounded in the x and y directions by rigid walls at distances L_x and L_y respectively. The cylinder is considered to deflect in the y direction and the cylinder deflection is called $w(z, t)$. Euler-Bernoulli beam theory (presented in Section 1.4.1) is used to model the cylinder deflection. Thus, the deflection of the cylinder is governed by the linear Euler-Bernoulli beam equation:

$$m \frac{d^2 w(z, t)}{dt^2} + EI \frac{d^4 w(z, t)}{dz^4} = f^y(z, t) \quad , \quad (3.1)$$

where m is the mass per unit length, E is the Young's modulus and $I = \frac{1}{4} \pi R^4$ is the second moment of area of the cylinder. f^y is the resultant of the interaction forces between the liquid and the structure on the y direction that can be expressed as function of the pressure field p as:

$$f^y(z, t) = \int_0^{2\pi} p(R, \theta, z, t) \sin(\theta) R d\theta \quad , \quad (3.2)$$

where $p(\theta, R, t)$ stands for the pressure field per unit length on the cylinder surface.

In order to have a general formulation, all the physical quantities are made dimensionless using the cylinder length L as typical length and the flow velocity U as typical speed. The following dimensionless quantities are introduced (as general rule for the following pages, dimensionless quantities are designated with a hat):

$$\hat{R} = \frac{R}{L}, \quad \hat{r} = \frac{r}{L}, \quad \hat{x} = \frac{x}{L}, \quad \hat{y} = \frac{y}{L}, \quad \hat{z} = \frac{z}{L}, \quad \hat{t} = \frac{Ut}{L}$$

and

$$\hat{l}_x = \frac{L_x}{L}, \quad \hat{l}_y = \frac{L_y}{L}, \quad \hat{w}(\hat{z}, \hat{t}) = \frac{w(z, t)}{L}, \quad \hat{p}(\hat{x}, \hat{y}, \hat{z}, \hat{t}) = \frac{p(x, y, z, t)}{\rho U^2},$$

thus Equation 3.1 becomes:

$$\hat{m} \frac{d^2 \hat{w}(\hat{z}, \hat{t})}{d\hat{t}^2} + \beta \frac{d^4 \hat{w}(\hat{z}, \hat{t})}{d\hat{z}^4} = \hat{f}^y(\hat{z}, \hat{t}) \quad , \quad (3.3)$$

where $\hat{m} = \frac{m}{\rho L^3}$, $\beta = \frac{EI}{\rho U^2 L^4}$ and $\hat{f}^y(\hat{z}, \hat{t}) = \frac{f^y(z, t)}{\rho U^2 L}$.

3.1.2 Fluid Model

Simplification is introduced in the fluid modelling: the flow is supposed to be potential. This assumption sounds reasonable if we consider that the flow (in PWR typical conditions) has a large Reynolds number. In fluid dynamics, Potential Flow Theory assumes the fluid flow to be inviscid and irrotational. These two simple but strong hypotheses lead to the linearised unsteady Bernoulli equation as demonstrated in Sections 1.4.2 and 1.4.3. The bulk flow \mathbf{v}_∞ in our case is equal to U in z direction. Hence, $\nabla \phi_\infty \cdot \nabla = U \partial_z$ in our case. Equation 1.57 then becomes:

$$\frac{p(x, y, z, t)}{\rho} = -(\partial_t + U \partial_z) \phi \quad , \quad (3.4)$$

which, for dimensionless quantities writes:

$$\hat{p}(\hat{x}, \hat{y}, \hat{z}, \hat{t}) = -(\partial_{\hat{t}} + \partial_{\hat{z}}) \hat{\phi} \quad , \quad (3.5)$$

where $\hat{\phi}$ is the dimensionless velocity potential defined as follows:

$$\hat{\phi} = \frac{\phi}{UL} \quad . \quad (3.6)$$

The fluid problem reduces to the resolution of a Laplace problem ($\Delta \phi = 0$). The last step is to determine boundary conditions, which are given by the impermeability condition (the fluid has the same normal velocity as the structure), both on the walls and on the cylinder surface obtaining:

$$\Delta \hat{\phi} = 0, \quad (3.7)$$

$$\left[\frac{\partial \hat{\phi}}{\partial \hat{y}} \right]_{|\hat{y}|=\hat{l}_y} = 0, \quad (3.8)$$

$$\left[\frac{\partial \hat{\phi}}{\partial \hat{x}} \right]_{|\hat{x}|=\hat{l}_x} = 0, \quad (3.9)$$

$$\left[\frac{\partial \hat{\phi}}{\partial \hat{n}} \right]_{\hat{r}=\hat{R}} = (\partial_{\hat{t}} + \partial_{\hat{z}}) \hat{w}(\hat{z}, \hat{t}) \sin \theta \quad . \quad (3.10)$$

A remark should be made on the presence of the sinus factor on the last boundary condition (Equation 3.10) in order to take into account the angle between the normal derivative ($\partial/\partial n$) and the displacement (which is in the y direction).

Applying $(\partial_{\hat{t}} + \partial_{\hat{z}})$ to each equation and using Equation 3.5, a Laplace problem with Neumann boundary conditions describing the pressure field is finally obtained:

$$\Delta \hat{p} = 0, \quad (3.11)$$

$$\left[\frac{\partial \hat{p}}{\partial \hat{y}} \right]_{|\hat{y}|=\hat{l}_y} = 0, \quad (3.12)$$

$$\left[\frac{\partial \hat{p}}{\partial \hat{x}} \right]_{|\hat{x}|=\hat{l}_x} = 0, \quad (3.13)$$

$$\left[\frac{\partial \hat{p}}{\partial \hat{n}} \right]_{\hat{r}=\hat{R}} = -(\partial_{\hat{t}} + \partial_{\hat{z}})^2 \hat{w}(\hat{z}, \hat{t}) \sin \theta \quad . \quad (3.14)$$

3.1.3 Coupling Fluid and Structure Model

In order to study fluid structure interactions, structure model and fluid model need to be coupled together. The coupling between the two models happens due to two terms: the forcing term in the structure model ($\hat{f}^y(\hat{z}, \hat{t})$) and the displacement term ($\hat{w}(\hat{z}, \hat{t})$). Both terms are in fact present both in the structure equation (Equation 3.3) and in the fluid equations (Equations 3.11 - 3.14). In the fluid equations the force term does not appear directly, but there is the presence of the pressure term. Since the pressure term is directly related to the forcing term on the cylinder (as expressed by Equation 3.2), the force term indirectly appears in the fluid equations.

The presence of interactions between fluid forces and structure forces means that the behaviour of the structure is going to influence the behaviour of the fluid and vice versa. Thus the two set of equations should be solved in an iterative way following the scheme represented in Figure 3.2.

In a first approximation, since the deflection of the structure is assumed to be small, we can avoid to perform the iteration process and assume that the structure deflects following the first natural mode shape of a clamped clamped Euler-Bernoulli beam. Thus

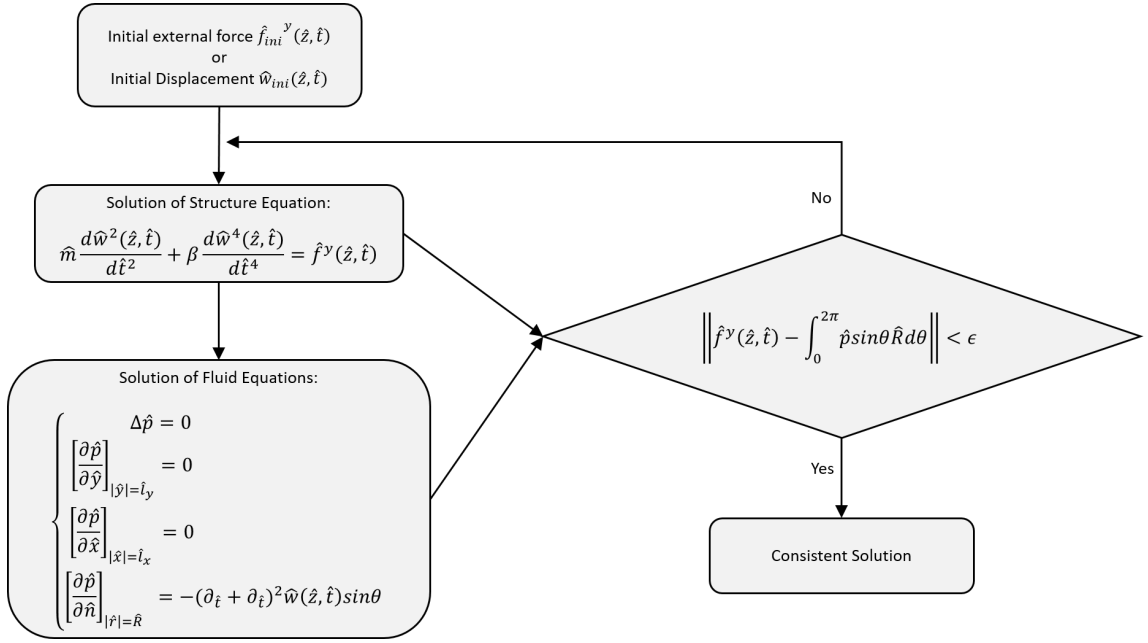


Figure 3.2 – Iteration scheme for the calculation of fluid structure interactions

the resulting pressure field gives the information about the perturbation of the fluid due to the deflection of the structure. Once the pressure field is known, the force applied on the structure can be calculated.

The negligence of such iteration system will insert some errors in the calculations, but since we have already done a big assumption about the perfect behaviour of the structure which follows the ideal deformation of a clamped-clamped Euler Bernoulli beam, this approximation is consistent. In the following calculations the iteration method won't be used.

3.2 Single Cylinder Model

In this section the model applied to a single cylinder (represented in Figure 3.1) undergoing small oscillations (in the y direction) is discussed. The mathematical formalism used to solve the problem is presented.

3.2.1 Problem in Fourier Space

In order to solve the previous set of equations (Equations 3.11-3.14), we used the same approach as the one proposed by Doaré et al. (2011b). The z component of the pressure field is expressed in the Fourier space such that:

$$\hat{p}(\hat{x}, \hat{y}, \hat{z}, \hat{t}) = \int_{-\infty}^{\infty} \hat{\Psi}(\hat{x}, \hat{y}, \hat{k}, \hat{t}) e^{ik\hat{z}} d\hat{k} \quad , \quad (3.15)$$

where $\hat{\Psi}$ is the Fourier transform of the dimensionless pressure field.

CHAPTER 3. FLUID STRUCTURE INTERACTION MODEL

This approach allows us to switch from a 3D problem to a 2D parametric problem (the parameter is the dimensionless wavenumber \hat{k}): numerical calculations are faster and simpler. The problem thus becomes:

$$(\partial_{\hat{x}}^2 + \partial_{\hat{y}}^2)\hat{\Psi} = -\hat{k}^2\hat{\Psi}, \quad (3.16)$$

$$\left[\frac{\partial \hat{\Psi}}{\partial \hat{y}} \right]_{|\hat{y}|=\hat{l}_y} = 0, \quad (3.17)$$

$$\left[\frac{\partial \hat{\Psi}}{\partial \hat{x}} \right]_{|\hat{x}|=\hat{l}_x} = 0, \quad (3.18)$$

$$\left[\frac{\partial \hat{\Psi}}{\partial \hat{n}} \right]_{\hat{r}=\hat{R}} = \hat{v}(\hat{k}, \hat{t}) \sin \theta, \quad (3.19)$$

where $\hat{v}(\hat{k}, \hat{t})$ is the Fourier transform of the impermeability boundary condition:

$$\int_{-\infty}^{\infty} \hat{v}(\hat{k}, \hat{t}) e^{i\hat{k}\hat{z}} d\hat{k} = -(\partial_{\hat{t}} + \partial_{\hat{z}})^2 \hat{w}(\hat{z}, \hat{t}) \quad . \quad (3.20)$$

Thanks to the Fourier formalism, the problem of a cylinder under axial flow in a finite confinement represented in Figure 3.1 can be represented by a 2D parametric problem of a circle in a two dimensional box (which represents the confinement), as represented in Figure 3.3.

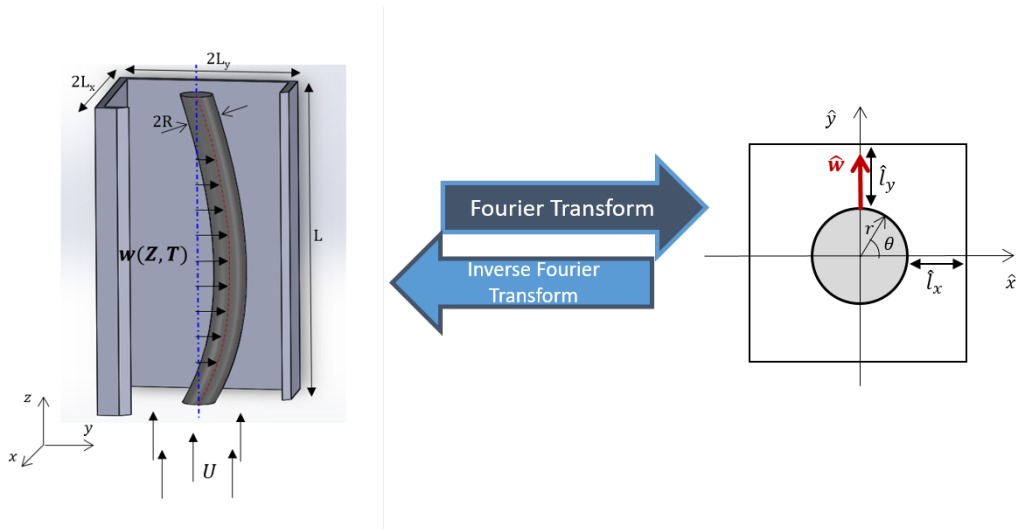


Figure 3.3 – Transformation of the 3D dimensional problem into multiples 2D dimensionless problems

3.2.2 Relation between Interaction Force and Structure Displacement

Fourier transform $\hat{F}^y(\hat{k}, \hat{t})$ of $\hat{f}^y(\hat{z}, \hat{t})$ can be expressed using either $\partial_{\hat{z}}\hat{f}^y$ or the pressure field Fourier transform $\hat{\Psi}$. The first expression is straightforward:

$$\hat{F}^y(\hat{k}, \hat{t}) = \frac{1}{2\pi} \int_{-\infty}^{+\infty} \hat{f}^y(\hat{z}, \hat{t}) e^{-i\hat{k}\hat{z}} d\hat{z} \quad , \quad (3.21)$$

which can also be written using Fourier transform properties:

$$\hat{F}^y(\hat{k}, \hat{t}) = \frac{1}{2\pi} \frac{1}{i\hat{k}} \int_{-\infty}^{+\infty} \frac{\partial \hat{f}^y(\hat{z}, \hat{t})}{\partial \hat{z}} e^{-i\hat{k}\hat{z}} d\hat{z} \quad . \quad (3.22)$$

Then, using dimensionless version of Equation 3.2 and 3.15, one gets:

$$\hat{F}^y(\hat{k}, \hat{t}) = \int_0^{2\pi} \hat{\Psi}(\hat{R}, \theta, \hat{k}, \hat{t}) \sin \theta \hat{R} d\theta \quad . \quad (3.23)$$

Noting that the problem 3.16-3.19 defining $\hat{\Psi}$ is linear and that Equation 3.19 implies that $\hat{\Psi}$ is proportional to $v(\hat{k}, \hat{t})$, Equation 3.23 can be written as follows:

$$\hat{F}^y(\hat{k}, \hat{t}) = -\frac{2}{\hat{k}} \hat{g}(\hat{k}; \hat{R}, \hat{l}_x, \hat{l}_y) \hat{v}(\hat{k}, \hat{t}) \quad . \quad (3.24)$$

The $\hat{g}(\hat{k}; \hat{R}, \hat{l}_x, \hat{l}_y)$ function has \hat{l}_x and \hat{l}_y as parameters as $\hat{\Psi}$ depends on them. Considering that \hat{F}^y and \hat{v} are Fourier transforms of real quantities, the Hermitian symmetry is guaranteed. Thus one gets:

$$\hat{g}(-\hat{k}; \hat{R}, \hat{l}_x, \hat{l}_y) = -\overline{\hat{g}(\hat{k}; \hat{R}, \hat{l}_x, \hat{l}_y)} \quad , \quad (3.25)$$

where \bar{z} denotes the complex conjugate of complex number z .

In order to find further properties of the $\hat{g}(-\hat{k}; \hat{R}, \hat{l}_x, \hat{l}_y)$ function one can consider an elementary Helmholtz problem (Equations 3.19) with a unitary boundary condition ($\hat{v}(\hat{k}, \hat{t}) = 1$). From the theory, the Helmholtz equation admits a real solution if the boundary conditions are real. Thus the equation:

$$\hat{F}^y(\hat{k}, \hat{t})^* = -\frac{2}{\hat{k}} \hat{g}(\hat{k}; \hat{R}, \hat{l}_x, \hat{l}_y) \quad (3.26)$$

represents the elementary solution to the problem with unitary boundary conditions. Since $\hat{F}^y(\hat{k}, \hat{t})^*$ must be real and \hat{k} is real by definition of the Fourier transform, so is the function $\hat{g}(\hat{k}; \hat{R}, \hat{l}_x, \hat{l}_y)$.

It has been thus proved that the function $\hat{g}(\hat{k}; \hat{R}, \hat{l}_x, \hat{l}_y)$ is real and Equation 3.25 becomes:

$$\hat{g}(-\hat{k}; \hat{R}, \hat{l}_x, \hat{l}_y) = -\hat{g}(\hat{k}; \hat{R}, \hat{l}_x, \hat{l}_y) \quad , \quad (3.27)$$

demonstrating that the function $\hat{g}(\hat{k}; \hat{R}, \hat{l}_x, \hat{l}_y)$ is a real odd function.

Equating right-hand-sides of Equations 3.22 and 3.24, an expression for $\hat{v}(\hat{k}, \hat{t})$ is derived:

$$\hat{v}(\hat{k}, \hat{t}) = -\frac{1}{2i} \frac{1}{2\pi} \frac{1}{\hat{g}(\hat{k}; \hat{R}, \hat{l}_x, \hat{l}_y)} \int_{-\infty}^{+\infty} \frac{\partial \hat{f}^y(\hat{\zeta}, \hat{t})}{\partial \hat{\zeta}} e^{-i\hat{k}\hat{\zeta}} d\hat{\zeta} \quad . \quad (3.28)$$

Hence, boundary Equation 3.20 becomes:

$$\frac{1}{2\pi} \int_0^1 \frac{\partial \hat{f}^y(\hat{\zeta}, \hat{t})}{\partial \hat{\zeta}} \int_{-\infty}^{+\infty} \frac{1}{2i} \frac{1}{\hat{g}(\hat{k}; \hat{R}, \hat{l}_x, \hat{l}_y)} e^{i\hat{k}(\hat{z}-\hat{\zeta})} d\hat{k} d\hat{\zeta} = (\partial_{\hat{t}} + \partial_{\hat{z}})^2 \hat{w}(\hat{z}, \hat{t}) \quad , \quad (3.29)$$

where the nullity of $\partial_{\hat{z}} \hat{f}^y$ for \hat{z} outside $[0, 1]$ is taken into account. This equation is rewritten as follows:

$$\frac{1}{2\pi} \int_0^1 \frac{\partial \hat{f}^y(\hat{\zeta}, \hat{t})}{\partial \hat{\zeta}} \hat{G}(\hat{z} - \hat{\zeta}; \hat{R}, \hat{l}_x, \hat{l}_y) d\hat{\zeta} = (\partial_{\hat{t}} + \partial_{\hat{z}})^2 \hat{w}(\hat{z}, \hat{t}) \quad , \quad (3.30)$$

where

$$\hat{G}(\hat{z}; \hat{R}, \hat{l}_x, \hat{l}_y) = \int_{-\infty}^{+\infty} \frac{1}{2i} \frac{1}{\hat{g}(\hat{k}; \hat{R}, \hat{l}_x, \hat{l}_y)} e^{i\hat{k}\hat{z}} d\hat{k} \quad . \quad (3.31)$$

Equation 3.30 represents one of the most important achievements of the application of the potential flow theory. The fluid structure interaction force, in fact, can be written as function of the displacement of the structure itself.

Considering Equation 3.27, \hat{G} can be simplified:

$$\hat{G}(\hat{z}; \hat{R}, \hat{l}_x, \hat{l}_y) = \int_0^{+\infty} \frac{\sin(\hat{k}\hat{z})}{\hat{g}(\hat{k}; \hat{R}, \hat{l}_x, \hat{l}_y)} d\hat{k} \quad . \quad (3.32)$$

Function $\hat{G}(\hat{z}; \hat{R}, \hat{l}_x, \hat{l}_y)$ is a Green's function or a conduction Kernel in Equation 3.30. This function is the real objective of the calculation, because it relates directly the fluid structure interaction force to the displacement of the structure without solving any fluid equation. In Equation 3.29, function $\hat{g}(\hat{k}; \hat{R}, \hat{l}_x, \hat{l}_y)$ is an unknown which could be computed empirically by using numerical calculations. So, the goal of the next mathematical manipulations is to find some relations which can allow us to evaluate $\hat{g}(\hat{k}; \hat{R}, \hat{l}_x, \hat{l}_y)$ by solving the Helmholtz problem for the pressure field $\hat{\Psi}$.

In order to generalize the problem described in Equations 3.16-3.19, we can re-scale all lengths by the dimensionless cylinder radius (\hat{R}), so we obtain the following system:

$$\Delta\tilde{\varphi} = \tilde{k}^2\tilde{\varphi}, \quad (3.33)$$

$$\left[\frac{\partial\tilde{\varphi}}{\partial\tilde{y}}\right]_{|\tilde{y}|=1+\tilde{h}_y} = 0, \quad (3.34)$$

$$\left[\frac{\partial\tilde{\varphi}}{\partial\tilde{x}}\right]_{|\tilde{y}|=1+\tilde{h}_x} = 0, \quad (3.35)$$

$$\left[\frac{\partial\tilde{\varphi}}{\partial\tilde{r}}\right]_{\tilde{r}=1} = \sin\theta, \quad (3.36)$$

where

$$\begin{aligned} \tilde{y} &= \hat{y}/\hat{R}, & \tilde{x} &= \hat{x}/\hat{R}, \\ \tilde{h}_y &= \hat{l}_y/\hat{R} - 1 = (L_y - R)/R, & \tilde{k} &= \hat{R}\hat{k}, \\ \tilde{h}_x &= \hat{l}_x/\hat{R} - 1 = (L_x - R)/R, & \tilde{\varphi}(\tilde{x}, \tilde{y}, \tilde{k}) &= \hat{\Psi}(\hat{x}, \hat{y}, \hat{k}, \hat{t})/(\hat{R}\hat{v}(\hat{k}, \hat{t})), \end{aligned}$$

and

$$\begin{aligned} \tilde{z} &= \hat{z}/\hat{R}, & \tilde{g}(\tilde{k}; \tilde{h}_x, \tilde{h}_y) &= \hat{g}(\hat{k}; \hat{R}, \hat{l}_x, \hat{l}_y)/\hat{R}, \\ \tilde{t} &= \hat{t}/\hat{R}, & \tilde{v}(\tilde{k}, \tilde{t}) &= \hat{v}(\hat{k}, \hat{t})/\hat{R}, \\ \tilde{F}^y(\tilde{k}, \tilde{t}) &= \hat{F}^y(\hat{k}, \hat{t})/\hat{R}, & \tilde{R} &= 1. \end{aligned}$$

Considering Equations 3.23 and 3.24 defining \hat{g} , we can write the unknown function $\tilde{g}(\tilde{k}; \tilde{h}_x, \tilde{h}_y)$ as a function of the re-scaled parameters as follows:

$$\tilde{g}(\tilde{k}; \tilde{h}_x, \tilde{h}_y) = -\frac{\tilde{k}}{2} \int_0^{2\pi} \tilde{\varphi}(\tilde{r} = 1, \theta, \tilde{k}) \sin\theta \, d\theta. \quad (3.37)$$

Since the problem is symmetric respect to the y axis we can affirm that $\int_0^{2\pi} = 2 \int_{-\pi/2}^{\pi/2}$ thus we can write:

$$\tilde{g}(\tilde{k}; \tilde{h}_x, \tilde{h}_y) = -\hat{k} \int_{-\pi/2}^{\pi/2} \tilde{\varphi}(\tilde{r} = 1, \theta, \tilde{k}) \sin\theta \, d\theta. \quad (3.38)$$

By considering the x-symmetry of the problem we can assume that the pressure field in the negative domain ($y < 0$) is specular to that in the positive domain ($y > 0$). Since the integral in Equation 3.38 has a sinus term which is anti symmetrical, Equation 3.38 reduces to:

$$\tilde{g}(\tilde{k}; \tilde{h}_x, \tilde{h}_y) = -2\hat{k} \int_0^{\pi/2} \tilde{\varphi}(\tilde{r} = 1, \theta, \tilde{k}) \sin\theta \, d\theta. \quad (3.39)$$

Such a mathematical manipulation made in the Fourier space could leave the reader confused about the physical sense of these mathematical quantities. In order to better understand the meaning of the previously defined quantities (especially the \tilde{g} function) we will try to make an analogy with a well known example in literature.

In the work of [Lighthill \(1960b\)](#) the formulation for inviscid force term is known in the

form :

$$F_A = C_M \rho \pi R^2 (\partial_t + U \partial_z)^2 w(z, t) \quad , \quad (3.40)$$

which for dimensionless quantities writes:

$$\hat{F}_A = \hat{C}_M (\partial_{\hat{t}} + \partial_{\hat{z}})^2 \hat{w}(\hat{z}, \hat{t}) \quad , \quad (3.41)$$

where the coefficient \hat{C}_M represents the virtual mass coefficient, which is equal to the unity for a cylinder in an unconfined flow.

If we recall Equation 3.24 and we remark that the function $\hat{v}(\hat{k}, \hat{t})$ is the Fourier transform of $-(\partial_{\hat{t}} + \partial_{\hat{z}})^2 \hat{w}(\hat{z}, \hat{t})$ we can directly make the analogy between the \tilde{g} function and the virtual mass coefficient. It follows that, by analogy, we can define a virtual mass coefficient in the Fourier space $\tilde{C}_m(\tilde{k}, \tilde{h}_x, \tilde{h}_y)$ defined as :

$$\tilde{C}_m(\tilde{k}; \tilde{h}_x, \tilde{h}_y) = -\frac{2}{\tilde{k}} \tilde{g}(\tilde{k}; \tilde{h}_x, \tilde{h}_y) \quad . \quad (3.42)$$

Thus, the virtual mass coefficient is directly proportional to the $\tilde{g}(\tilde{k}; \tilde{h}_x, \tilde{h}_y)$ function. For this reason it is interesting to compute this quantity, and to study the effects of different parameters like the confinement size and the wavenumber (this point will be discussed in Chapter 4).

All the calculations, made in Fourier space for computational reasons (from 3D problem to 2D problem), need to be translated in the real space. The transformation from the Fourier space to the real space is described by Equations 3.30 and 3.32. The integral $\tilde{G}(\tilde{z}; \tilde{h}_x, \tilde{h}_y) = \hat{R}^2 \hat{G}(\hat{z}; \hat{R}, \hat{l}_x, \hat{l}_y)$ representing the inverse Fourier transform will be numerically evaluated as the sum of discrete values, taken for different values of the wavenumber, as follows:

$$\tilde{G}(\tilde{z}; \tilde{h}_x, \tilde{h}_y) = \int_0^\infty \frac{\sin(\tilde{k}\tilde{z})}{\tilde{g}(\tilde{k}; \tilde{h}_x, \tilde{h}_y)} d\tilde{k} \approx \sum_{n=1}^N \frac{\sin(\tilde{k}_n \tilde{z})}{\tilde{g}(\tilde{k}_n; \tilde{h}_x, \tilde{h}_y)} \Delta \tilde{k}_n \quad . \quad (3.43)$$

Modal Decomposition

Once an analytical expression for the $\tilde{G}(\tilde{z}; \tilde{h}_x, \tilde{h}_y)$ function is found, one can make a modal decomposition in order to decompose the forcing term into three different terms which can be related to added mass, added damping and added stiffness terms. This operation will allow to directly estimate added mass, added damping and added stiffness coefficients from the calculations. Those parameters are extremely important in the determination of the dynamical behaviour of a structure and they can be easily extrapolated from experimental results for validation comparisons.

The inertial force can be divided into three different terms by operating a modal decomposition on the cylinder displacement \tilde{w} . Considering an external excitation at a given dimensionless frequency $\tilde{\omega}$, the displacement of the cylinder can be written as (see Sec. 1.4.1):

$$\tilde{w}(\tilde{z}, \tilde{t}) = e^{i\tilde{\omega}\tilde{t}} \sum_i \eta_i \tilde{\chi}_i(\tilde{z}) \quad , \quad (3.44)$$

where $\tilde{\chi}_i(\tilde{z}) = \chi_i(z)/R$ are the dimensionless eigenmode shapes of the beam and η_i are modal amplitudes (not depending on the time anymore). Thus, Equation 3.30 can be rewritten as:

$$\frac{1}{2\pi} \int_0^{1/\hat{R}} \frac{\partial \tilde{f}^y(\tilde{\zeta}, \tilde{t})}{\partial \tilde{\zeta}} \tilde{G}(\tilde{z} - \tilde{\zeta}; \tilde{h}_x, \tilde{h}_y) d\tilde{\zeta} = (-\tilde{\omega}^2 + 2i\tilde{\omega}\partial_{\tilde{z}} + \partial_{\tilde{z}}^2) e^{i\tilde{\omega}\tilde{t}} \sum_i \eta_i \tilde{\chi}_i(\tilde{z}) \quad . \quad (3.45)$$

For practical applications, the first bending mode is the one which is predominant in the beam response. Hence, $\tilde{w} \approx e^{i\tilde{\omega}_1\tilde{t}} \tilde{\chi}_1(\tilde{z})\eta_1$ in practical applications. Nevertheless higher modes can be considered for higher accuracy.

Three different terms appears on the right side of Equation 3.45. They refer respectively to the added mass term, added damping term and added stiffness term. Since the model neglects the viscosity, the added damping term is negligible with respect to other terms (the main source of added damping are viscosity forces). The terms resulting from Equation 3.45 will be used in Chapter 4 for comparison between numerical and experimental values.

3.2.3 Main Analytical Results

The analytical model behind the resolution of the equations for calculating fluid structure interaction forces was presented. Fourier formalism was introduced and the relationships between physical quantities in Fourier and real space were established. To ease the reading of the rest of this work, equations which have remarkable importance for the understanding of the next sections are briefly summarised hereafter.

The most important outcome of the mathematical development presented in the previous paragraphs is that the force due to the pressure field around the cylinder can be directly linked to the displacement of the cylinder itself, by the equation:

$$\frac{1}{2\pi} \int_0^{1/\hat{R}} \frac{\partial \tilde{f}^y(\tilde{\zeta}, \tilde{t})}{\partial \tilde{\zeta}} \tilde{G}(\tilde{z} - \tilde{\zeta}; \tilde{h}_x, \tilde{h}_y) d\tilde{\zeta} = (\partial_{\tilde{t}} + \partial_{\tilde{z}})^2 \tilde{w}(\tilde{z}, \tilde{t}) \quad , \quad (3.46)$$

where the function $\tilde{G}(\tilde{z}; \tilde{h}_x, \tilde{h}_y)$ can be directly calculated from the solution of the Helmholtz problem (Equations 3.33 - 3.36) by using the relations:

$$\tilde{G}(\tilde{z}; \tilde{h}_x, \tilde{h}_y) = \int_0^{+\infty} \frac{\sin(\tilde{k}\tilde{z})}{\tilde{g}(\tilde{k}; \tilde{h}_x, \tilde{h}_y)} d\tilde{k} \quad , \quad (3.47)$$

and

$$\tilde{g}(\tilde{k}; \tilde{h}_x, \tilde{h}_y) = -2\hat{k} \int_0^{\frac{\pi}{2}} \tilde{\varphi}(\hat{R} = 1, \theta, \tilde{k}) \sin \theta d\theta \quad . \quad (3.39)$$

The function $\tilde{g}(\tilde{k}; \tilde{h}_x, \tilde{h}_y)$ which can be easily calculated by solving an Helmholtz problem, represents the elementary solution when considering a unitary boundary condition. Given the linearity of the problem, the elementary solution has an extreme importance since all the possible solutions can be written as function of the elementary one by means of the superposition principle.

Another remarkable outcome of the analytical development is the capability to decompose Equation 3.46 in order to decompose the contribution of the interaction force into three different terms as showed in Equation 3.45:

$$\frac{1}{2\pi} \int_0^{1/\hat{R}} \frac{\partial \tilde{f}^y(\tilde{\zeta}, \tilde{t})}{\partial \tilde{\zeta}} \tilde{G}(\tilde{z} - \tilde{\zeta}; \tilde{h}_x, \tilde{h}_y) d\tilde{\zeta} = (-\tilde{\omega}^2 + i\tilde{\omega}\partial_{\tilde{z}} + \partial_{\tilde{z}}^2) e^{i\tilde{\omega}\tilde{t}} \sum_i \eta_i \tilde{\chi}_i(\tilde{z}) \quad , \quad (3.45)$$

3.3 Multi Cylinder Model

In this section it will be discussed how the previous model, established for a single cylinder, will be adapted in order to be used on a multiple cylinder configuration, which represents the fuel assemblies geometry of the ICARE experimental facility and which will be further used in order to validate the model with experimental data.

3.3.1 From one to Multiple Cylinders

The first step in order to extend the single cylinder model to a multiple cylinder model which can be used to simulate a real problem (*i.e.* the ICARE facility), is to gradually increment the complexity of the geometry with 2 cylinders geometry and then with 4 cylinders geometry as shown in Figure 3.4.

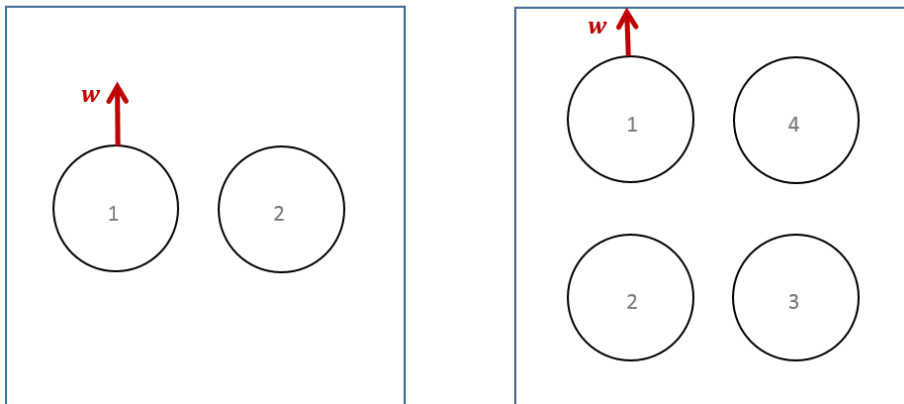


Figure 3.4 – Two and four cylinders configurations

Since the model is linear, only a single cylinder is excited at each time (as shown from the red arrow in Figure 3.4), and in order to model an excitation of multiple cylinders we can take advantage of the superposition principle and sum different calculations with a

single cylinder excitation. The use of the superposition principle is a powerful tool which allows to simplify the modelling process and to really speed up the calculations for complex excitations.

The set of equations which allows to model the single cylinder problem, which was expressed by Equations 3.33 - 3.36 is thus adapted to the multi cylinders problem (assuming that all the cylinders have the same radius) as follows:

$$(\partial_{\tilde{x}}^2 + \partial_{\tilde{y}}^2)\tilde{\varphi} = \tilde{k}^2\tilde{\varphi}, \quad (3.48)$$

$$\left[\frac{\partial\tilde{\varphi}}{\partial\tilde{y}}\right]_{|\tilde{y}|=\tilde{h}_y} = 0, \quad (3.49)$$

$$\left[\frac{\partial\tilde{\varphi}}{\partial\tilde{x}}\right]_{|\tilde{x}|=\tilde{h}_x} = 0, \quad (3.50)$$

$$\left[\frac{\partial\tilde{\varphi}}{\partial\tilde{n}}\right]_{|(\tilde{x}-\tilde{x}_{c_i})^2+(\tilde{y}-\tilde{y}_{c_i})^2|=1} = \sin\theta, \quad (3.51)$$

$$\left[\frac{\partial\tilde{\varphi}}{\partial\tilde{n}}\right]_{|(\tilde{x}-\tilde{x}_{c_j})^2+(\tilde{y}-\tilde{y}_{c_j})^2|=1} = 0 \quad , \quad (3.52)$$

where \tilde{x}_{c_i} and \tilde{y}_{c_i} are respectively x and y dimensionless coordinates of the center of the i^{th} excited cylinder and \tilde{x}_{c_j} and \tilde{y}_{c_j} are x and y dimensionless coordinates of the center of the j^{th} not excited cylinder.

Once the problem is solved, the pressure field of the fluid domain can be used in order to calculate the force acting on every cylinder. In an analogous way to the single cylinder calculations, we can define different \tilde{g}_i functions, each one accounting for the interaction forces on the i^{th} cylinder; it writes as follows:

$$\tilde{g}_i(\tilde{k}; \tilde{h}_x, \tilde{h}_y) = -\frac{\tilde{k}}{2} \int_0^{2\pi} \left[\tilde{\varphi}(\tilde{x}, \tilde{y}, \theta, \tilde{k}) \right]_{|(\tilde{x}-\tilde{x}_{c_i})^2+(\tilde{y}-\tilde{y}_{c_i})^2|=1} \sin\theta d\theta \quad . \quad (3.53)$$

The main difference with single cylinder calculations in this case is that unlike in Equation 3.39 no assumption on the symmetry of the velocity potential field can be made, thus meaning that the integration must be done all along the border of the cylinder and not only on a quarter of it. It follows that in an analogous way the virtual mass coefficient for the i^{th} cylinder can be expressed by:

$$\tilde{C}_{m,i}(\tilde{k}; \tilde{h}_x, \tilde{h}_y) = -\frac{2}{\tilde{k}} \tilde{g}_i(\tilde{k}; \tilde{h}_x, \tilde{h}_y) \quad , \quad (3.54)$$

and the relationship allowing to perform the inverse Fourier transform going back to the real space writes:

$$\frac{1}{2\pi} \int_0^{1/\hat{R}} \frac{\partial \tilde{f}_i^y(\tilde{\zeta}, \tilde{t})}{\partial \tilde{\zeta}} \tilde{G}_i(\tilde{z} - \tilde{\zeta}; \tilde{h}_x, \tilde{h}_y) d\tilde{\zeta} = (\partial_{\tilde{t}} + \partial_{\tilde{z}})^2 \tilde{w}_i(\tilde{z}, \tilde{t}) \quad , \quad (3.55)$$

where:

$$\tilde{G}_i(\tilde{z}; \tilde{h}_x, \tilde{h}_y) = \int_0^\infty \frac{\sin(\tilde{k}\tilde{z})}{\tilde{g}_i(\tilde{k}; \tilde{h}_x, \tilde{h}_y)} d\tilde{k} \quad . \quad (3.56)$$

With such a formalism we are able to analyse the effect of the displacement of a single cylinder over all the other structures present on the computational domain. The equations can be used in order to obtain the response to any combination of excitations of any cylinder on any direction thanks to the superposition principle. The equations and the formalism discussed in this section will be used in the next section for application on a multiple cylinder geometry representing the configuration of the ICARE experimental mock-up.

3.3.2 ICARE Geometry Model

Finally the model will be adapted in order to be able to represent the real geometry of the ICARE experimental facility (presented in Chapter 2). The ICARE structure is made of 4 fuel assemblies (half scale) made of 8×8 fuel rods lattice in a squared section vertical channel under axial flow. Since the geometry is quite complex with over two hundred different elements, the model will be only implemented on the 2D geometries and there will not be any calculations made directly on the 3D geometry. In any case, the 2D model is considered to be consistent with the 3D model since several tests were run on the single cylinder geometry (see Chapter 4) and literature supports this assumption [Doaré et al. \(2011b\)](#).

The geometries, implemented in the FreeFem++ code, are represented in Figure 3.5. Four different geometries are constructed, taking into account the four different configurations used during experimental campaigns (2 and 4 assemblies, small and large confinement).

Some assumptions are made in the modelling of these geometries:

- the spacer grids are neglected;
- all the cylinders inside the same fuel bundle are supposed to move together and in the exact same way;
- only one of the assemblies is excited at a time (the one represented in red in Figure 3.5);
- the presence of four guide tubes in each assembly is neglected;
- boundary conditions are considered to be perfect clamped-clamped boundary conditions;
- the assemblies are numbered in a clockwise direction starting from the excited one (the one represented in red).

Calculation of global interaction forces

Once the pressure field calculations are performed on these multi assemblies geometries, the \tilde{g}_i functions accounting for the interaction forces acting on the cylinders must be calculated.

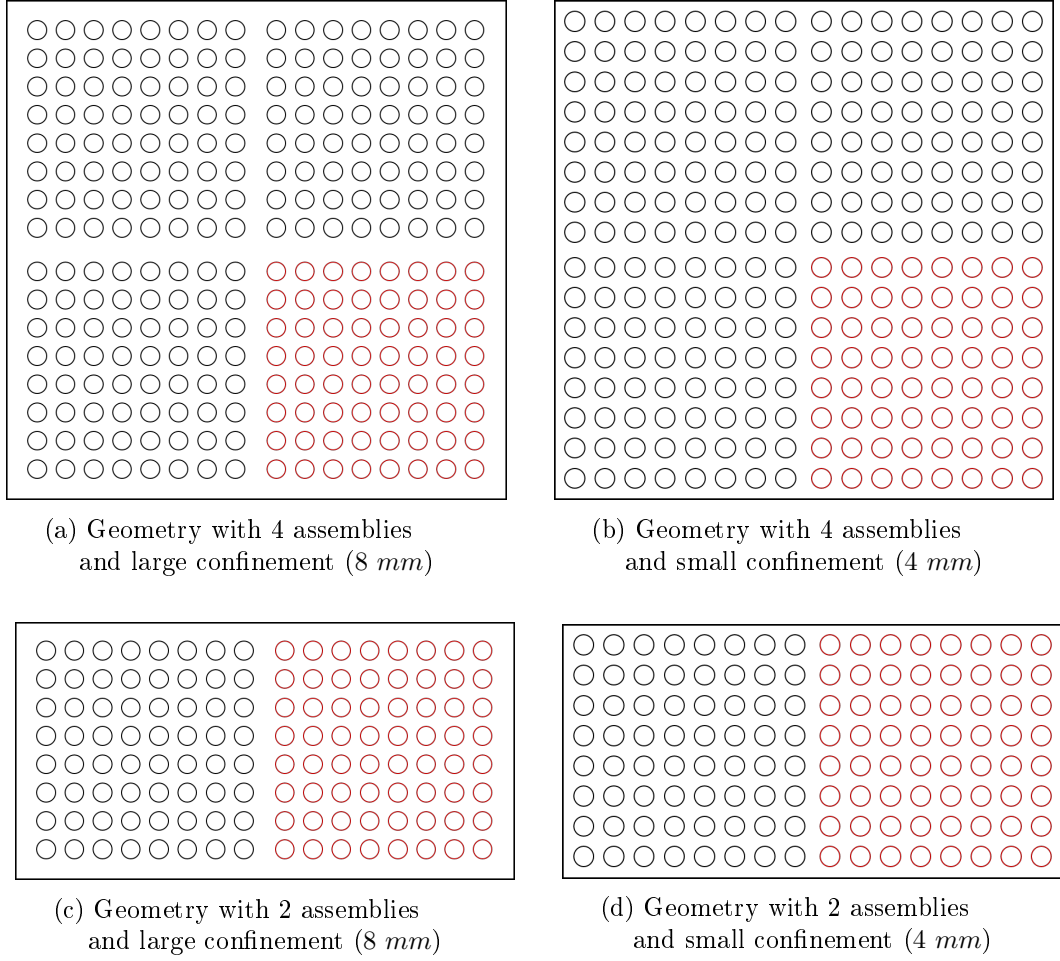


Figure 3.5 – Geometries implemented in the code representing ICARE configurations (red assembly is excited along horizontal direction)

Since one of the main assumption is that all the cylinder of a single assembly move in the same way, it is interesting to calculate the global interaction forces acting on the whole assembly, and not only the force acting on the single cylinders. Even if the excitation on the assembly 1 is given only along one direction (x direction), there will be interaction forces on both directions, which need to be taken into account. For this purpose, Equation 3.53 is used, giving two different equations, one for each direction:

$$\tilde{g}_i^x(\tilde{k}) = -\frac{\tilde{k}}{2} \int_0^{2\pi} \left[\tilde{\varphi}(\tilde{x}, \tilde{y}, \theta, \tilde{k}) \right]_{|(\tilde{x}-\tilde{x}_{c_i})^2+(\tilde{y}-\tilde{y}_{c_i})^2|=1} \cos \theta d\theta \quad (3.57)$$

$$\tilde{g}_i^y(\tilde{k}) = -\frac{\tilde{k}}{2} \int_0^{2\pi} \left[\tilde{\varphi}(\tilde{x}, \tilde{y}, \theta, \tilde{k}) \right]_{|(\tilde{x}-\tilde{x}_{c_i})^2+(\tilde{y}-\tilde{y}_{c_i})^2|=1} \sin \theta d\theta \quad , \quad (3.58)$$

and the global interaction force for the whole assembly is given by:

$$\tilde{\mathcal{G}}_{A_j}^x(\tilde{k}) = \sum_{i=1}^{64} \tilde{g}_i^x(\tilde{k}) \quad (3.59)$$

$$\tilde{\mathcal{G}}_{A_j}^y(\tilde{k}) = \sum_{i=1}^{64} \tilde{g}_i^y(\tilde{k}) \quad , \quad (3.60)$$

where $\tilde{\mathcal{G}}_{A_j}^x$ and $\tilde{\mathcal{G}}_{A_j}^y$ represent the global interaction forces respectively on the x and y directions on the whole j^{th} assembly, with $j = 1, 2, 3, 4$.

With the formalism expressed in this paragraph we are able to calculate the interaction forces on the structure due to a perturbation on the fluid domain. They will be further used in the Chapter 4 for analysis of the numerical simulations and comparison with experimental results.

Chapter 4

Numerical Calculations

In this chapter the numerical calculations performed using the code implemented on FreeFem++ will be presented. The calculations on a single cylinder will be first discussed. Validation of the calculations with works in literature will be discussed and a parametric study on single cylinder geometry will be presented. Finally, calculations with multiple cylinders will be discussed and comparison with experimental results will be carried out.

4.1 FreeFem++

In order to solve the partial differential equations involved in the problem of fluid structure interactions, the software FreeFem++ has been used. A brief presentation of the software is given hereafter. For further details the reader is addressed to [Hecht \(2012a,b\)](#).

4.1.1 Main Characteristics

FreeFem++ is an open source software to numerically solve partial differential equations in two or three dimensions. As its name implies, it is a free software based on the Finite Element Method. It is not a package, it is an integrated product with its own high level programming language; it runs on most UNIX, WINDOWS and MacOS computers. Moreover FreeFem++ is highly adaptive. FreeFem++ can handle arbitrary finite element spaces on arbitrary unstructured and adapted meshes, making it suitable for multi-physics problems.

The characteristics of FreeFem++ are:

- Problem description (real or complex valued) by their variational formulations, with access to the internal vectors and matrices if needed;
- Multi-variables, multi-equations, bi-dimensional and three-dimensional static or time dependent, linear or nonlinear coupled systems;
- Easy geometric input by analytic description of boundaries by pieces;
- Automatic mesh generator, based on the Delaunay–Voronoi algorithm ([George and Hecht, 1999](#));

- Metric-based anisotropic mesh adaptation ([Hecht, 1998](#));
- High level user friendly typed input language with an algebra of analytic or finite element functions;
- Multiple finite element meshes within one application with automatic interpolation of data on different meshes and possible storage of the interpolation matrices;
- A large variety of triangular finite elements: linear, quadratic Lagrangian elements and more, discontinuous P1 and Raviart–Thomas elements, elements of a non-scalar type, the mini-element, etc.;
- Tools to define discontinuous Galerkin finite element formulations P0, P1dc, P2dc
- A large variety of linear direct and iterative solvers, eigenvalue and eigenvector solvers and optimization tools ([Davis, 2003](#))([Amestoy et al., 2006](#))([Lehoucq et al., 1997](#));
- Near optimal execution speed (compared with compiled C++ implementations programmed directly);
- Online graphics, generation of .txt, .eps, .gnu, .mesh files for further manipulations of input and output data;
- A parallel version using MPI available.

4.1.2 Weak Formulation

Due to its design characteristic, FreeFem++ requires that the problem is expressed in the weak, or variational formulation. Weak formulation is an important tool for the analysis of mathematical equations that permit the transfer of concepts of linear algebra to solve problems in other fields such as partial differential equations. In a weak formulation, an equation has weak solutions with respect to certain "test vectors" or "test functions". This is equivalent to formulating the problem to require a solution in the sense of a distribution. Below there is an example of transformation of a simple Poisson problem from the strong to the weak formulation. Consider a Poisson problem on a domain Ω with a partition of the boundary $\partial\Omega$ in Γ_1, Γ_2 such that:

$$-\Delta u = a \quad \text{in } \Omega, \quad u = b \quad \text{on } \Gamma_1, \quad \frac{\partial u}{\partial n} = c \quad \text{on } \Gamma_2 \quad , \quad (4.1)$$

where a, b, c are constants. In order to get the weak formulation, we will make the L^2 scalar between each term of Equation 4.1 and any test function $v \in V_0 = \{H^1(\Omega), v(x) = 0, \forall x \in \Gamma_1\}$, so that:

$$-\int_{\Omega} (\Delta u)v = \int_{\Omega} av \quad . \quad (4.2)$$

Performing an integration by parts using Green's identity and making considerations on boundary conditions, Equation 4.2 becomes:

$$\int_{\Omega} \nabla u \nabla v = \int_{\Omega} av + \int_{\Gamma_2} cv \quad , \quad (4.3)$$

with $u \in V_b = \{H^1(\Omega), u(x) = b, \forall x \in \Gamma_1\}$. Equation 4.3 represents the variational formulation of Poisson problem described by 4.1. All the problems must be expressed in this form in order to be solved by FreeFem++.

4.2 Single Cylinder Calculations

As described in Chapter 3, the first approach for the numerical resolution of the mathematical problem, is to take advantage of the Fourier transformation, and then solve several 2D problems instead of solving a 3D problem. This, in case of complex geometries, can result in much faster calculations.

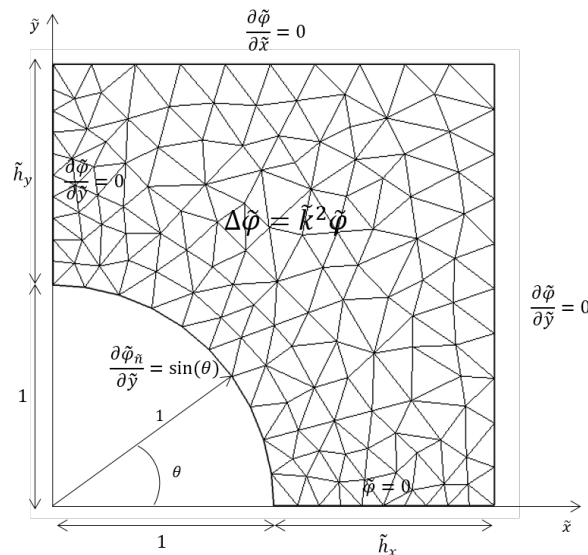


Figure 4.1 – Helmholtz problem represented in the FEM domain

In this section the numerical resolution of the Helmholtz problem described by Equations (3.33-3.36) will be presented. The objective of the calculations is to compute the value of the function $\tilde{g}(\tilde{k}; \tilde{h}_x, \tilde{h}_y)$ for different values of \tilde{k} , \tilde{h}_x and \tilde{h}_y . Thanks to the symmetries of the problem, the equations are solved only on one quarter of the domain, as showed in Figure 4.1, resulting in faster calculations.

Before starting the calculations, some considerations have to be made on the discretization of the domain. A convergence study has been performed in order to find the optimal meshing for different combinations of confinement size and wave number. Typically, the size of the meshes must be decreased if we want to increase the wave number \tilde{k} . In addition, the refinement of meshes will increase as the confinement size decreases. Due to meshing limits, the explored values of \tilde{h}_x , \tilde{h}_y and \tilde{k} belong respectively to $[10^{-4}, 10^2]$, $[10^{-4}, 10^2]$, and $[10^{-3}, 10^3]$.

4.2.1 Slender Body Approximation

First, effort has been put on a validation study of the model and of the calculations performed. In literature (Lighthill, 1960a,b) it is known that in the case of a slender body subjected to an unconfined axial flow, an analytical formulation exists for the interaction force. Thus calculations are performed for some configurations fitting the hypotheses of the model formulated by Lighthill (1960a). The unconfined flow hypothesis is fulfilled by using a confinement size both in x and y directions bigger than 1 diameter of the rod. The hypothesis of slender body is fulfilled using wavenumbers smaller than 1; this means that we only consider low modes oscillations.

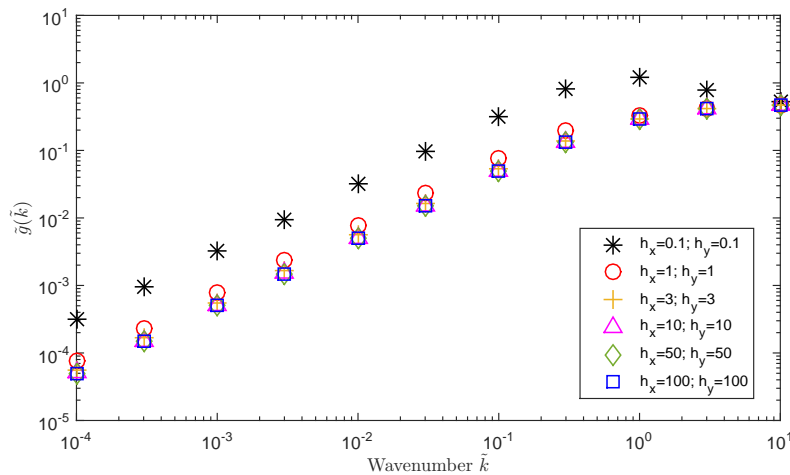


Figure 4.2 – Value of \tilde{g} as function of the wavenumber for several large confinements

Figure 4.2 shows the behaviour of $\tilde{g}(\tilde{k}; \tilde{h}_x, \tilde{h}_y)$ as function of the wavenumber \tilde{k} for different values of the confinement size (squared confinements). As a reminder the $\tilde{g}(\tilde{k}; \tilde{h}_x, \tilde{h}_y)$ function is proportional to the modal added mass coefficient (see Equation 3.42). For large confinement sizes ($\tilde{h}_x, \tilde{h}_y > 1$) and for small wavenumbers ($\tilde{k} < 1$) there is no dependency on the confinement size. This means that, in those situations, confinement does not play any role on the fluid-structure interactions; the cylinder is equivalent to a cylinder in an unconfined flow. One other important remark is that the slope of the curve is constant for small values of \tilde{k} , and, since this is a log-log plot, this means that the modal added mass coefficient curve is directly proportional to the wavenumber. In particular it has been found that:

$$\tilde{g}(\tilde{k}) \approx \frac{1}{4}\tilde{k} \quad \text{for } \tilde{k} \ll 1 \text{ and } \tilde{h}_x, \tilde{h}_y \gg 3 \quad . \quad (4.4)$$

The expression of the \tilde{g} function, in the above specified conditions, is quite simple. Thus, the inverse Fourier transform has been performed in order to go back from the Fourier space to real space by analytically evaluating Equation 3.30.

Equation 3.32 can be simplified using this approximation:

$$\tilde{G}(\tilde{z}, \tilde{h}_x, \tilde{h}_y) = \int_0^\infty 4 \frac{\sin(\tilde{k}\tilde{z})}{\tilde{k}} d\tilde{k} = 2\pi \operatorname{sgn} \tilde{z} \quad (4.5)$$

where $\operatorname{sgn} \tilde{z}$ is the sign function of \tilde{z} . Since \tilde{z} is positive by definition, $\operatorname{sgn}(\tilde{z}) = 1$.

Equation 3.46 can be now analytically solved, and the solution writes as:

$$\tilde{f}^y(\tilde{z}) = (\partial_{\tilde{t}} + \partial_{\tilde{z}})^2 \tilde{w}(\tilde{z}, \tilde{t}) \quad . \quad (4.6)$$

The expression for the interaction force expressed in Equation 4.6 is an expression already found in literature by Lighthill (1960a,b):

$$F_A = \left(\frac{\partial}{\partial t} + U \frac{\partial}{\partial z} \right) \left[M_a \left(\frac{\partial}{\partial t} + U \frac{\partial}{\partial z} \right) \right] w(z, t) \quad , \quad (4.7)$$

where U is the axial flow velocity, $M_a = \rho\pi R^2$ is the virtual mass for a cylinder in an unconfined flow, and $w(z, t)$ is the structure displacement in the y direction.

Equation 4.7 for the fluid-structure interaction force was formulated by Lighthill under the hypotheses of Slender Body Theory. In fact, the physical meaning of a small wavenumber and large confinement correspond to a cylinder in an (almost) unconfined domain, undergoing small amplitude and long period oscillations: those are exactly the same assumptions hidden behind the Slender Body Theory. The agreement between our numerical results and literature works can be considered as a proof that the method implemented to solve the fluid equations is founded and coherent.

4.2.2 Empirical Formulation

Once the model has been proven to be consistent and the calculations coherent with literature works more efforts have been spend on the analysis of the calculations on a wide range of wavenumbers and confinement sizes. Following the idea and the methods used by Doaré et al. (2011b), a first attempt has been done in order to find some analytical formulation (with empirical coefficients) in order to describe the dependencies of the function $\tilde{g}(\tilde{k}; \tilde{h}_x, \tilde{h}_y)$ on three different parameters: the wavenumber and the confinement size both in the x and y directions.

In order to find an empirical formulation for the \tilde{g} function, a first important assumption has been done: each parameter is considered to be independent from the other ones. This assumption can be resumed by the following expression:

$$\tilde{g}(\tilde{k}; \tilde{h}_x, \tilde{h}_y) = f(\tilde{k}) \cdot l(\tilde{h}_x) \cdot s(\tilde{h}_y) \quad , \quad (4.8)$$

where the functions f, l and s represent respectively the dependencies on the wavenumber, on the x -direction confinement and on the y -direction confinement.

Several calculations (more than one thousand) has been performed changing wavenumber and confinement size parameters as summarized by Figure 4.3.

In a first moment, efforts have been spent in order to fit the f function, which represents

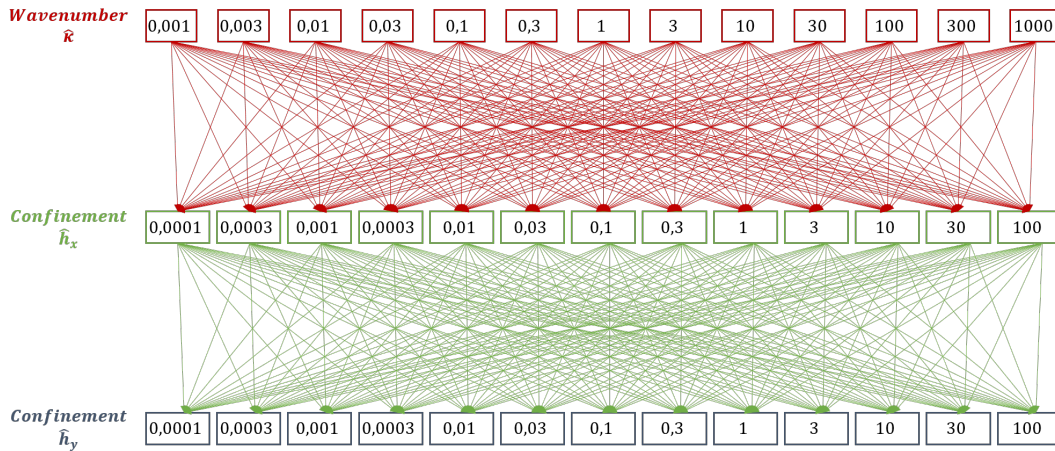


Figure 4.3 – Scheme of the parameters used to perform calculations

the behaviour of \tilde{g} as function of the wavenumber (\tilde{k}). As suggested in the work of [Doaré et al. \(2011b\)](#) we expected to observe very different behaviours for the \tilde{g} function depending on the wavenumber.

As we can see from [Figure 4.4](#) we can outline two different tendencies for big and small wavenumbers. For small wavenumbers ($\tilde{k} < 0.1$) the \tilde{g} function tends to be linear in a semi-logarithmic plot, meaning that a logarithmic relation exists between the \tilde{g} function and the wavenumber ([Figure 4.4a](#)). On the opposite side, [Figure 4.10b](#) shows a completely different behaviour for big wavenumbers ($\tilde{k} > 10$), with the presence of an asymptotic behaviour, which does not depend on confinement parameters.

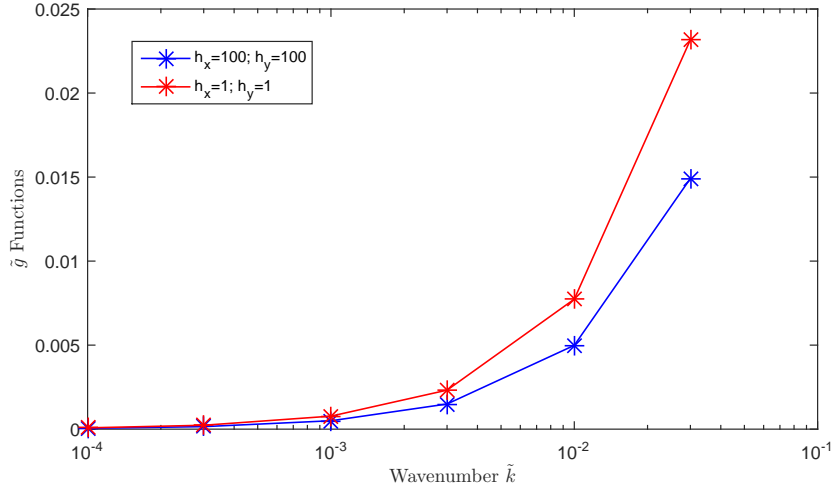
For wavenumbers comprised between these extreme values, the \tilde{g} function has a behaviour which strongly depends on the other parameters.

The two behaviours observed for very small and very big wavenumbers corresponds to very simple models found in literature ([Lighthill \(1960b, 1971, 1960a\)](#)). The theory which corresponds to the behaviour observed for small wavenumber is the Slender Body Theory, while for big wavenumbers, the Large Span Theory fits well the numerical results. Slender body theory is considered to be valid for elongated bodies (length much bigger than span), where the oscillations amplitudes are small compared to the lateral size of the body. The large span theory, instead, is valid for large aspect ratio bodies (length smaller than span). Since all the calculations are applied to cylindrical structures, from now on when the word span is used, it refers to the diameter of the cylinder.

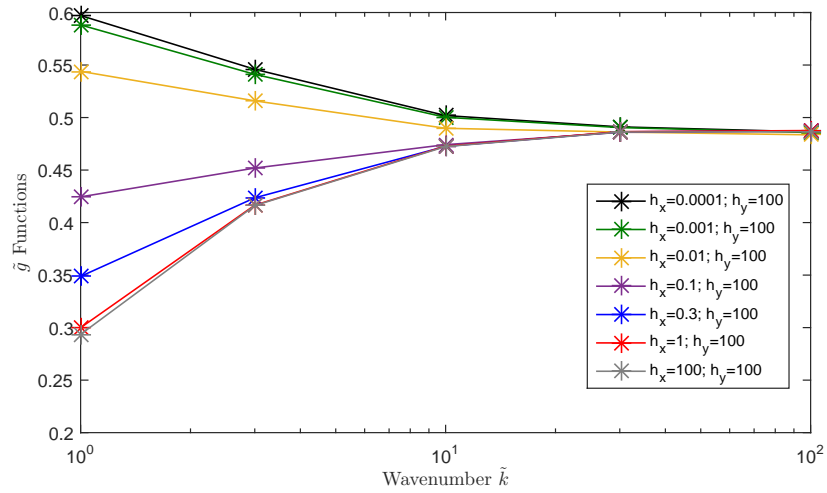
We know that for the practical application we are interested in, the slender body theory assumption are respected; anyway, an empirical formulation which could unify both theories under a single model has been found. The achievement of such a model could bring benefits in the understanding of certain phenomena and could be used for practical applications in other domains.

In order to take into account the two different behaviours that have been outlined from the graphics, the empirical formulation for the \tilde{g} function expressed by [Equation 4.8](#) has

4.2. SINGLE CYLINDER CALCULATIONS



(a) Behaviour of \tilde{g} as function of wavenumber ($\tilde{k} < 0.1$)



(b) Behaviour of \tilde{g} as function of wavenumber ($\tilde{k} > 1$)

Figure 4.4 – Differences in the behaviour of the \tilde{g} function depending on wavenumbers

been divided into two different functions, one accounting for slender body behaviour, and the other one accounting for the large span behaviour (respectively \tilde{g}_{SB} and \tilde{g}_{LS}). So, the two functions are defined as follows:

$$\tilde{g}_{SB}(\tilde{k}; \tilde{h}_x, \tilde{h}_y) = f_{SB}(\tilde{k}) \cdot l_{SB}(\tilde{h}_x) \cdot s_{SB}(\tilde{h}_y) \quad , \quad (4.9)$$

$$\tilde{g}_{LS}(\tilde{k}; \tilde{h}_x, \tilde{h}_y) = f_{LS}(\tilde{k}) \cdot l_{LS}(\tilde{h}_x) \cdot s_{LS}(\tilde{h}_y) \quad , \quad (4.10)$$

where $f_{SB}(\tilde{k})$, $l_{SB}(\tilde{h}_x)$ and $s_{SB}(\tilde{h}_y)$ account for the dependencies on the different parameters in the case of slender body approximation, and $f_{LS}(\tilde{k})$, $l_{LS}(\tilde{h}_x)$ and $s_{LS}(\tilde{h}_y)$ account for the dependencies on the different parameters in the case of large span approximation.

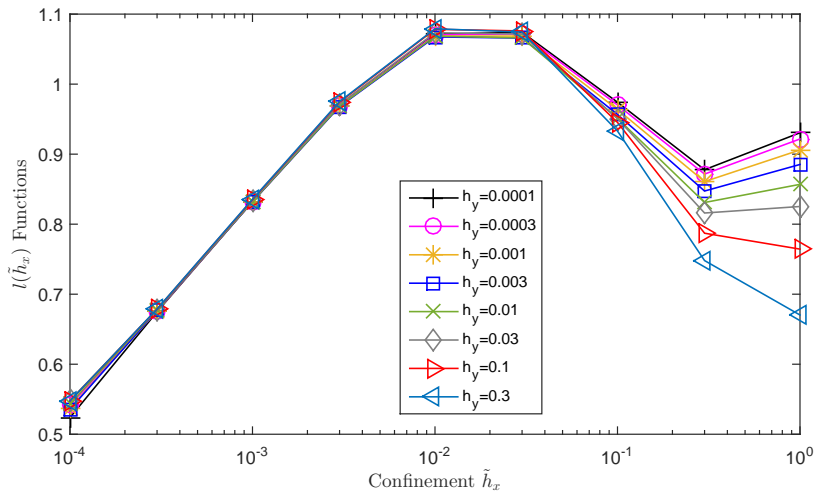
Once the behaviour of the two extreme situations is known, we can assume that for

intermediate values of the wavenumber, the \tilde{g} function can be calculated as a function of the two limit cases, as follows:

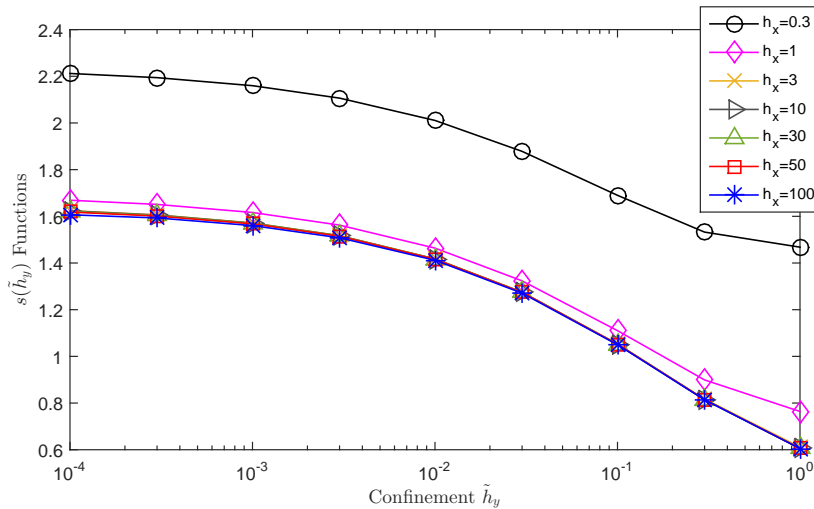
$$\tilde{g}(\tilde{k}; \tilde{h}_x, \tilde{h}_y) = \mathcal{H}(\tilde{g}_{SB}, \tilde{g}_{LS}) \quad . \quad (4.11)$$

Once these observation are made, elementary functions which could fit the numerical data has been identified.

Slender Body Approximation



(a) Behaviour of \tilde{l}_{SB} as function of x confinement size ($\tilde{k} < 0.1$)



(b) Behaviour of \tilde{s}_{SB} as function of y confinement size ($\tilde{k} < 0.1$)

Figure 4.5 – Differences in the behaviour of the \tilde{g} function depending on confinement size

For the slender body limit three different functions has been identified, each one taking into account the dependency from each parameter, with the exception that the two confinement size parameters are not totally independent, thus the function $s_{SB}(\tilde{h}_y)$ still

depends on both \tilde{h}_y and \tilde{h}_x . This means that the hypothesis expressed by Equation 4.9 is no longer valid. Figures 4.4a, 4.5a and 4.5b show the behaviour of each function depending on the different parameters for small wavenumbers.

After performing an analysis with the Matlab Curve Fitting Toolbox, the curves fitting in the best way the numerical data are:

$$f_{SB}(\tilde{k}) = \frac{\pi}{4} \ln(\tilde{k}) \quad , \quad (4.12)$$

$$l_{SB}(\tilde{h}_x) = A(\tilde{h}_x) \cdot B_1(\tilde{h}_x) \cdot B_2(\tilde{h}_x) \cdot B_3(\tilde{h}_x) \quad , \quad (4.13)$$

$$s_{SB}(\tilde{h}_y, \tilde{h}_x) = \ln\left(\frac{C(\tilde{h}_x)}{\tilde{h}_y}\right) \quad , \quad (4.14)$$

where $A(\tilde{h}_x) = a_1 \cdot \tilde{h}_x^{a_2} + a_2 \cdot \tilde{h}_x^{a_4}$, $B_i(\tilde{h}_x) = b_{1i} \cdot (\sin(b_{2i} \cdot \ln(\tilde{h}_x + b_{3i}))$ with $i = (1, 2, 3)$ and $C(\tilde{h}_x) = c_1 \tilde{h}_x^{c_2}$ are analytical functions, and the values of the constants a_1, \dots, c_2 are summarised in Table 4.1.

i	a_i	b_{1i}	b_{2i}	b_{3i}	c_i
1	0.104	1.010	0.098	1.651	0.538
2	0.261	0.162	0.801	-0.733	0.969
3	0.204	0.049	1.196	-1.236	-

Table 4.1 – Fitting parameters for Slender Body Approximation

Thus, the function which fits the numerical behaviour of the function \tilde{g}_{SB} , representing the dependencies of the interaction forces (in the Fourier space) on the problem parameters (wavelength and confinement size), is represented by:

$$g_{\tilde{S}B}(\tilde{k}, \tilde{h}_x, \tilde{h}_y) = \frac{\pi}{4} \ln(\tilde{k}) \cdot A(\tilde{h}_x) \cdot B_1(\tilde{h}_x) \cdot B_2(\tilde{h}_x) \cdot B_3(\tilde{h}_x) \cdot \ln\left(\frac{C(\tilde{h}_x)}{\tilde{h}_y}\right) \quad . \quad (4.15)$$

Large Span Approximation

In a first moment it has been tried to deal with the fitting of data related to large wavenumbers (thus referring to a large span approximation) in the same way of the slender body approximation. Nevertheless, it has been realised that it was not possible to find an analytical formulation that was following the independence hypothesis expressed by Equation 4.10.

A first detail that one can remark from Figure 4.4b is an asymptotic behaviour for wavenumbers larger than 10. One would thus expect this behaviour to be stable for large wavenumbers (in agreement with (Lighthill, 1960a)), but numerical results do not agree with this affirmation. The deviation from the asymptotic behaviour can be explained by analysing the convergence of the calculations. It has been found that the problem does not

CHAPTER 4. NUMERICAL CALCULATIONS

converge with the used mesh resolution. Thus, it has been finally decided not to consider data for wavenumbers bigger than 300 since we were not able to obtain convergence of the calculations with our commercial computers. This will not impact future work, since such calculations do not refer directly to practical problem; this field has been explored mainly for theoretical knowledge.

The analysis of data regarding large span condition brought to write the equation for the $\tilde{g}_{LS}(\tilde{k}, \tilde{h}_x, \tilde{h}_y)$ on the following form:

$$\tilde{g}_{LS}(\tilde{k}, \tilde{h}_x, \tilde{h}_y) = D(\tilde{h}_y) + \frac{E(\tilde{h}_x, \tilde{h}_y)}{\tilde{k}} \quad , \quad (4.16)$$

where $D(\tilde{h}_y)$ and $E(\tilde{h}_x, \tilde{h}_y)$ are empirical functions accounting for the confinement size. They are defined as follows:

$$D(\tilde{h}_y) = d_1 \cdot \tilde{h}_y^{d_2} + d_3 \cdot \tilde{h}_y^{d_4} \quad , \quad (4.17)$$

$$E(\tilde{h}_x, \tilde{h}_y) = \ln \left(\frac{F(\tilde{h}_y)}{\tilde{h}_x + G(\tilde{h}_y)} + H(\tilde{h}_y) \right) \quad , \quad (4.18)$$

where the functions $F(\tilde{h}_y)$, $G(\tilde{h}_y)$ and $H(\tilde{h}_y)$ are defined by:

$$F(\tilde{h}_y) = f_1 \cdot \sin(f_2 \cdot \ln(\tilde{h}_y) + f_3) + f_4 \cdot \sin(f_5 \cdot \ln(\tilde{h}_y) + f_6) \quad , \quad (4.19)$$

$$G(\tilde{h}_y) = \ln \left(\frac{g_1}{\tilde{h}_y + g_2} + g_3 \right) \quad , \quad (4.20)$$

$$H(\tilde{h}_y) = h_1 \cdot \sin(h_2 \cdot \ln(\tilde{h}_y) + h_3) + h_4 \cdot \sin(h_5 \cdot \ln(\tilde{h}_y) + h_6) \quad , \quad (4.21)$$

with the value of the constants f_1, \dots, h_6 listed in the Table 4.2.

i	f_i	g_i	h_i	d_i
1	-0.024	-0.009	1.191	0.1467
2	0.656	0.188	0.134	0.1855
3	1.387	1.064	1.994	0.2031
4	-0.077	-	0.226	-0.288
5	0.164	-	0.671	-
6	-0.634	-	-1.703	-

Table 4.2 – Fitting parameters for Large Span Approximation

Fitting on the whole range of wavenumbers

Finally, in order to have an analytical formulation for the \tilde{g} function over the whole range of wavenumbers an expression for the function $\mathcal{H}(\tilde{g}_{SB}, \tilde{g}_{LS})$ represented by Equation 4.11

needs to be found. The function which allows to combine together the slender body and the large span approximation is defined as follows:

$$\mathcal{H}(\tilde{g}_{SB}, \tilde{g}_{LS}) = \mathcal{R}(\tilde{k}, \tilde{h}_x, \tilde{h}_y) \cdot \tilde{g}_{SB} + (1 - \mathcal{R}(\tilde{k}, \tilde{h}_x, \tilde{h}_y)) \cdot \tilde{g}_{LS} \quad , \quad (4.22)$$

where the function $\mathcal{R}(\tilde{k}; \tilde{h}_x, \tilde{h}_y)$ is defined by:

$$\mathcal{R}(\tilde{k}; \tilde{h}_x, \tilde{h}_y) = \frac{1}{2} - \frac{0.1}{0.2 + \tilde{k}^{-10}} \cdot e^{-I(\tilde{h}_x, \tilde{h}_y)} + \frac{10}{20 + \tilde{k}^{10}} \cdot e^{I(\tilde{h}_x, \tilde{h}_y)} \quad , \quad (4.23)$$

with

$$I(\tilde{h}_x, \tilde{h}_y) = 20 + 2 \cdot \log_{10} \left(\frac{\tilde{h}_y}{10^{-4}} \right) + 5 \cdot \log_{10} \left(\frac{10^{-4}}{\tilde{h}_x} \right) \quad . \quad (4.24)$$

We are now able to have an empirical formulation for the function $\tilde{g}(\tilde{k}; \tilde{h}_x, \tilde{h}_y)$ which represents the dual of the added mass in the Fourier space. Having an analytical formulation for this function could be useful in order to analyse the effect of different parameters, and to be able to perform an inverse Fourier transform in order to come back to the real space.

The empirical formulation discussed above seems to fit the numerical data very closely, as shown in Figure 4.6. It can be noted that only few data are far from the red line (representing the perfect fit between empiric function and numerical data). In any case, the error made with this fitting is always lower than 25%, and in most of the cases is less than 5%, which could be considered a good approximation.

It has been realised that such an empirical formulation is not immediately useful in order to simplify integration calculations. It can be anyway used for further applications on sensitivity analysis on different parameters.

4.2.3 Polynomial Interpolation

Since the fitting with empirical formulation results to be quite complex in order to be used for practical applications, a new method for fitting numerical calculations has been tested. The $\tilde{g}(\tilde{k}; \tilde{h}_x, \tilde{h}_y)$ function is interpolated with a polynomial expression.

The polynomial interpolation provides a more systematic way to fit a data set, which is represented in this situation by the values of the \tilde{g} function. The \tilde{g} function can be thus expressed by the sum of different polynomials, as follows:

$$\tilde{g}^{POL}(\tilde{k}; \tilde{h}_x, \tilde{h}_y) = \sum_i A_i \tilde{k}^\alpha \tilde{h}_x^\beta \tilde{h}_y^\gamma \quad , \quad (4.25)$$

where α, β, γ are respectively the polynomial coefficients for the wavenumber, the x direction confinement size and the y direction confinement size.

Since two different trends are outlined depending on the wavenumber, two different polynomial interpolation are performed for small wavenumbers and for large wavenumbers:

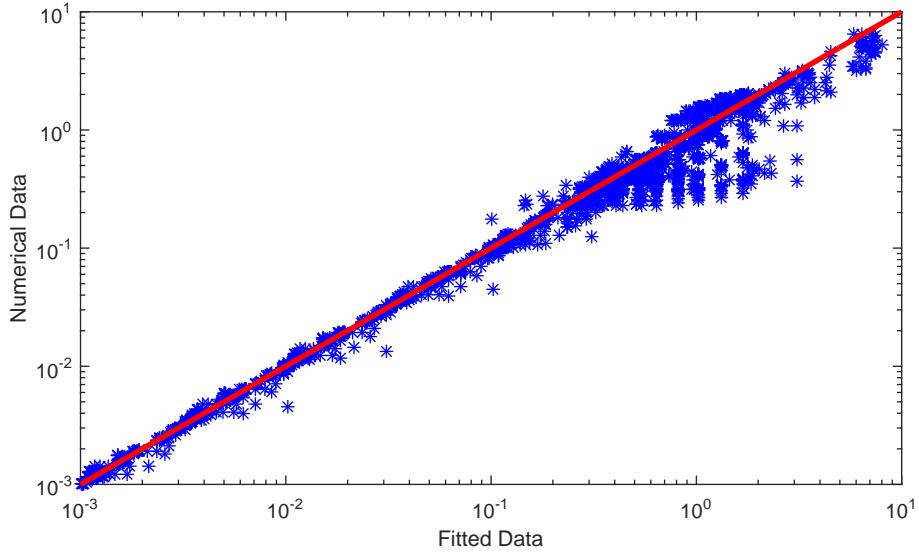
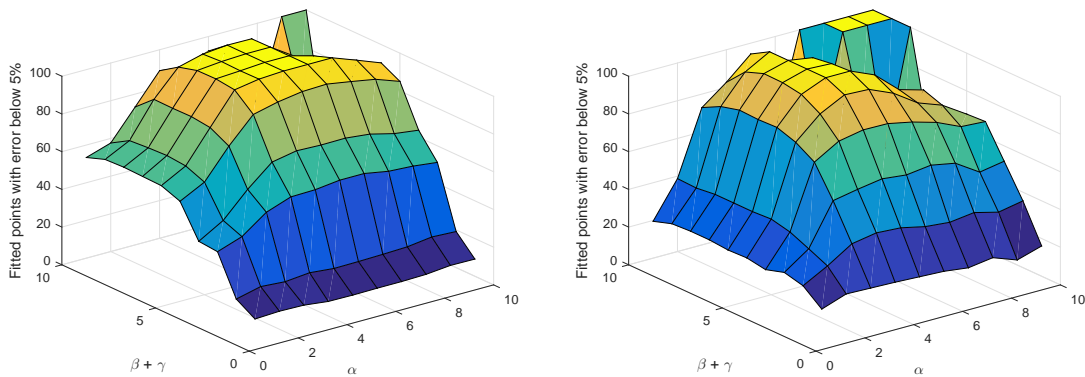


Figure 4.6 – Numerical VS fitted values of the \tilde{g} function

$$\tilde{g}_{SB}^{POL}(\tilde{k}; \tilde{h}_x, \tilde{h}_y) = \sum_i A_{SBi} \tilde{k}^\alpha \tilde{h}_x^\beta \tilde{h}_y^\gamma \quad \text{for } \tilde{k} < 0.3 \quad (4.26)$$

$$\tilde{g}_{LS}^{POL}(\tilde{k}; \tilde{h}_x, \tilde{h}_y) = \sum_i A_{LSi} \tilde{k}^\alpha \tilde{h}_x^\beta \tilde{h}_y^\gamma \quad \text{for } \tilde{k} > 0.3 \quad , \quad (4.27)$$

where \tilde{g}_{SB}^{POL} stays for the slender body polynomial interpolation and \tilde{g}_{LS}^{POL} large span polynomial interpolation.



(a) Low wavenumbers interpolations

(b) Large wavenumbers interpolations

Figure 4.7 – Interpolation error with different polynomial degrees

In order to perform a proper polynomial interpolation, the maximum degree of the polynomial needed must be determined. The degree of the polynomial interpolation determines the number of coefficients needed. Thus, the interpolation degree should be kept

as low as possible. The interpolation error committed with different polynomial interpolations is studied. The acceptable error for the interpolation is assumed to be of the order of 5%. Figure 4.7 shows the percentage of interpolated points which have an error larger than 5% depending on the polynomial degrees. Both the interpolation for small (Figure 4.7a) and large (Figure 4.7a) wavenumbers show the same behaviour respect to the polynomial degrees. It can be seen that in order to have the interpolation error smaller than 5% for all the points, polynomials up to the 5th degree must be used for the wavenumber, while 6th degree polynomials are necessary for the confinement size interpolation. Thus meaning that polynomial up to the 11th degree are needed in order to interpolate the function \tilde{g} with an error smaller than 5%.

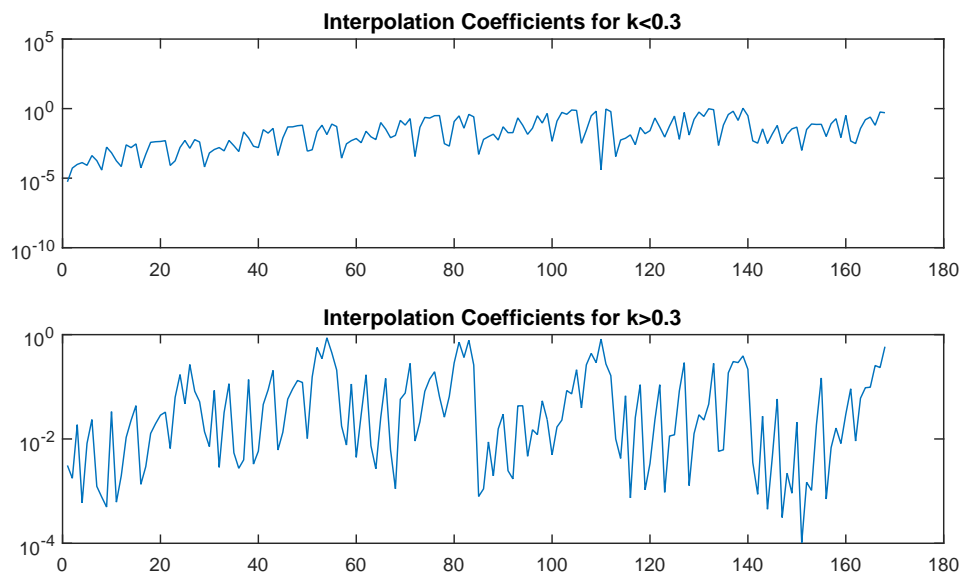


Figure 4.8 – Polynomial fitting coefficients for 11th degree interpolation

The polynomial interpolation is thus carried out using polynomials up to 11th degree. Figure 4.8 shows the behaviour of the fitting coefficient. One can remark that more than 150 coefficients are needed to perform such interpolation. Thus, the polynomial interpolation is not considered useful for practical applications for finding empirical solution to fluid structure interaction forces depending on different parameters.

4.2.4 Confinement Effects

Further numerical calculations have been performed in order to qualitatively evaluate the effects of the confinement size on the function $\tilde{g}(\tilde{k}, \tilde{h}_x, \tilde{h}_y)$, thus on the added mass coefficient. Two extreme cases have been analysed: the first one regarding very low wavenumbers ($\tilde{k} \approx 10^{-2}$) and a second case regarding big wavenumbers ($\tilde{k} \approx 10$).

Figure 4.9a shows in a 3D plot the dependency of the modal added mass coefficient as function of both x and y confinement sizes. From Figure 4.9b, which shows a section of the

CHAPTER 4. NUMERICAL CALCULATIONS

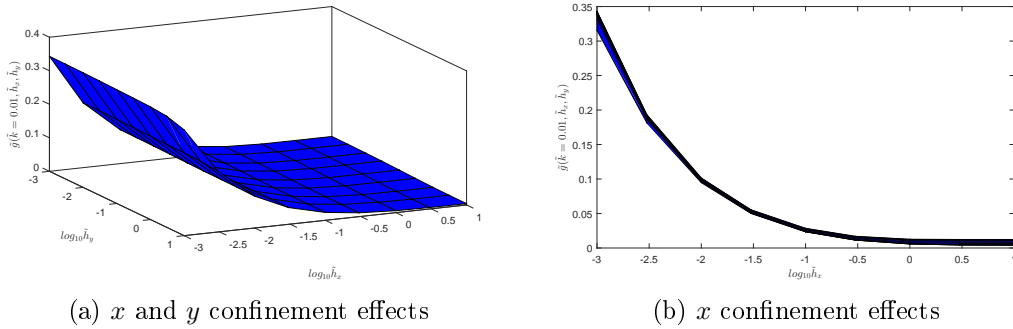


Figure 4.9 – Modal added mass coefficient as function of the confinement size for small wavenumbers

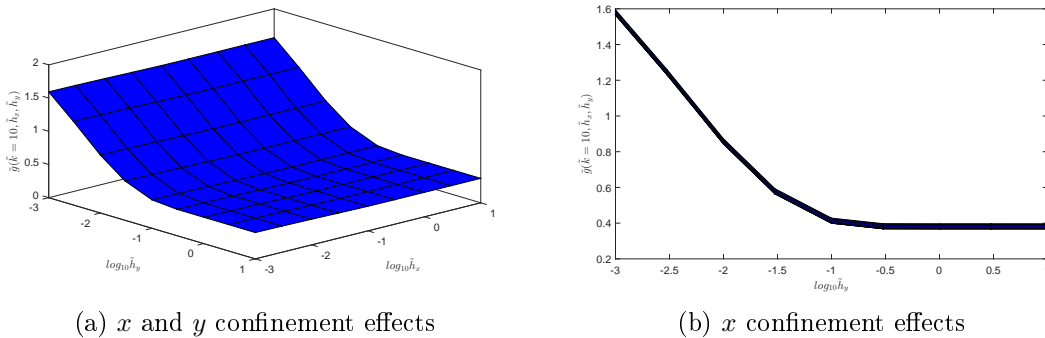


Figure 4.10 – Modal added mass coefficient as function of the confinement size for large wavenumbers

3D plot perpendicular to the $\tilde{g} - \tilde{h}_y$ plane, it is obvious that, for small wavenumbers, only the size of the confinement in the x direction affects the \tilde{g} function (the confinement on the y direction does not play any fundamental role). Observing Figure 4.10b related to big wavenumbers calculations, we reach the opposite conclusion: the added mass strongly depends on the y direction confinement. For wavenumbers in-between the two extreme cases, a different behaviour has been found: \tilde{g} depends on both x and y direction confinements.

Since the cylinder can only move in the y direction, the results for small wavenumbers were first regarded with suspicion. In fact a strong dependency on the y direction confinement (parallel to the structure displacement) was expected, together with a weak dependency on the x direction confinement (perpendicular to the structure displacement). Those results have been thus further investigated and the velocity field in the Fourier space has been plotted. The analysis of the velocity field allowed to understand such a behaviour. For low wavenumbers (corresponding to a cylinder moving with a large wavelength), a strong flow in the y direction (opposite to the cylinder displacement) has been observed along the boundary line $y = 0$ as showed on Figure 4.11a. On the other hand, for large wavenumbers no flow has been observed on the boundary $y = 0$ (Figure 4.11b). Since the confinement in the x direction directly changes the dimension of the boundary $y = 0$, we can now understand the strong dependency of the fluid-structure interaction force on

4.3. MULTIPLE CYLINDERS CALCULATIONS AND COMPARISON WITH EXPERIMENTAL RESULTS

the x direction confinements for low wavenumbers.

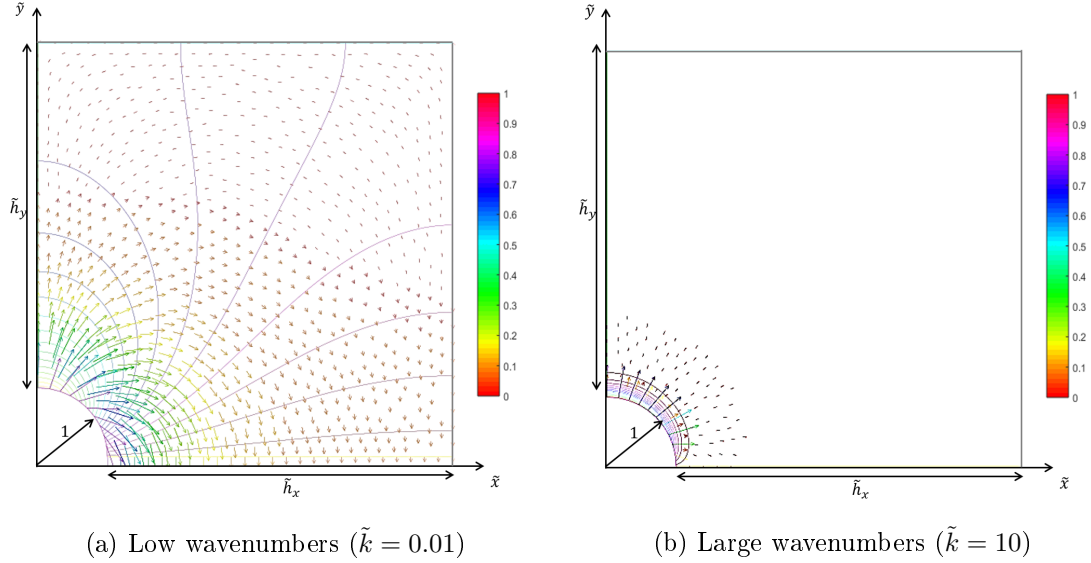


Figure 4.11 – Velocity fields calculations in Fourier space for both small and large wavenumbers

Finally, for any wavenumber that has been considered and for any confinement size, the \tilde{g} function (thus the dual of the added mass coefficient) appears to increase as the confinement size decreases (in both directions). This observation is in agreement with the literature works on channel flows made by [Chen and Wamnganss \(1972\)](#); [Chen \(1985\)](#); [Païdoussis and Pettigrew \(1979\)](#).

4.3 Multiple Cylinders Calculations and Comparison with Experimental Results

In this section the model implemented in the FreeFEM++ software is used for multiple cylinders calculations. First some interesting numerical results with 2 and 4 cylinders configurations are discussed. Then, numerical results regarding the ICARE geometry (2 and 4 8×8 fuel assemblies in small and large confinement) are presented. Finally comparison with some experimental results already presented in [Chapter 2](#) will be carried out.

4.3.1 Two and Four Cylinders Calculations

Numerical calculations for two and four cylinders allow to make some important considerations about the nature of the interaction forces. When more than one cylinder is taken into consideration for the simulations, in fact, it is possible to evaluate the effect of the excitation of one cylinder on the other ones.

Figure [4.12](#) shows calculations for a single configuration of two cylinders for different wavenumbers. The two cylinders are placed on the side along the x direction and the

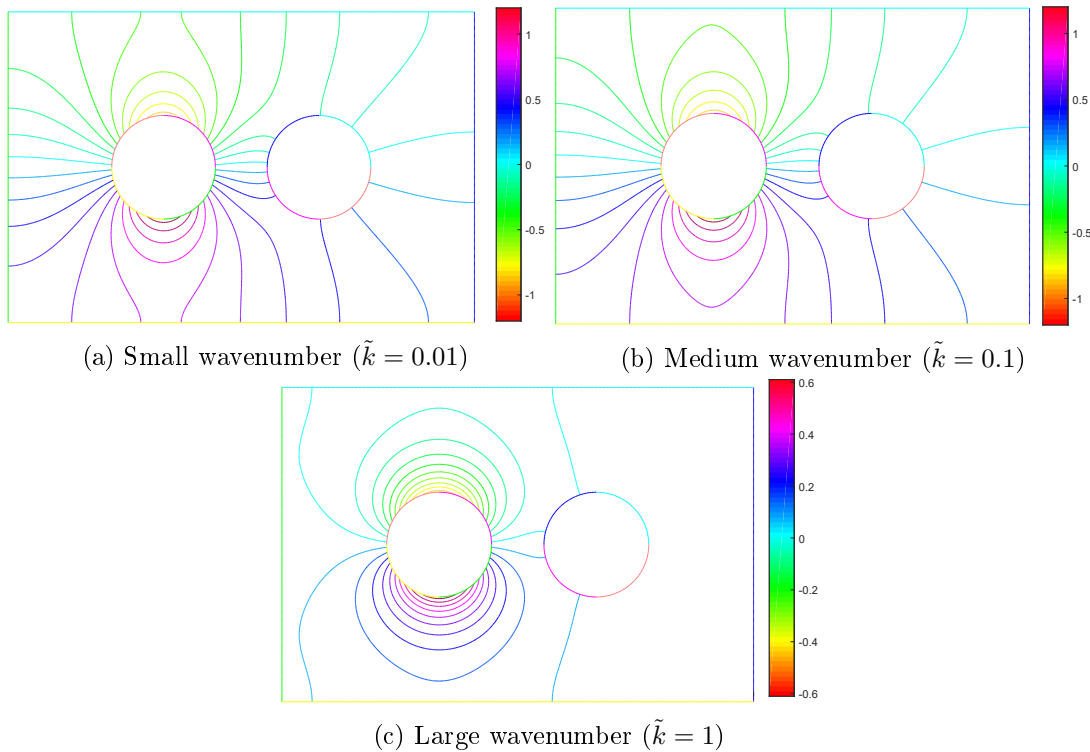


Figure 4.12 – Pressure fields for 2 cylinders configuration with different wavenumbers

cylinder on the left side is excited along the y direction (see Figure 3.4). The curves in the plot represent the isovalues for the pressure field. The perturbation of the pressure field due to the motion of the excited cylinder strongly depends on the wavenumber. This outcome confirms that the calculations are consistent with the physics which they are representing. When the wavenumber becomes smaller, in fact, this means that deformation shape of the cylinder becomes a sinusoidal with large wavelength. Thus, this means that the limit case of the wavenumber going to 0 represents the situation where the cylinder displaces as a rigid body without inflexion.

Another effect that can be studied when two different cylinders are simulated, is the effect of the arrangement of the cylinders. Calculations for three different arrangements are performed. In the first two configurations the centres of the two cylinders lie either on the x direction (Figure 4.12) or on the y direction (Figure 4.13a). In the third configuration (Figure 4.13b) the two cylinders are not arranged following any axial symmetries, but they are arranged along the diagonal line. It can be seen that as long as there exists an axial symmetry between the positions of the two cylinders (Figures 4.12b, 4.13a), the pressure field is symmetrical respect to the y axes of each cylinder, thus meaning that no effort is induced on the direction orthogonal to the excitation direction (as a reminder, cylinder on the left is excited along the y direction). It is evident from Figure 4.13b that when the two cylinders lose the symmetrical positioning, the pressure field induced around the two cylinders loses any kind of symmetries. An orthogonal effort appears on the excited cylinder, and effort in both directions is induced in the second cylinder. More in detail, the

4.3. MULTIPLE CYLINDERS CALCULATIONS AND COMPARISON WITH EXPERIMENTAL RESULTS

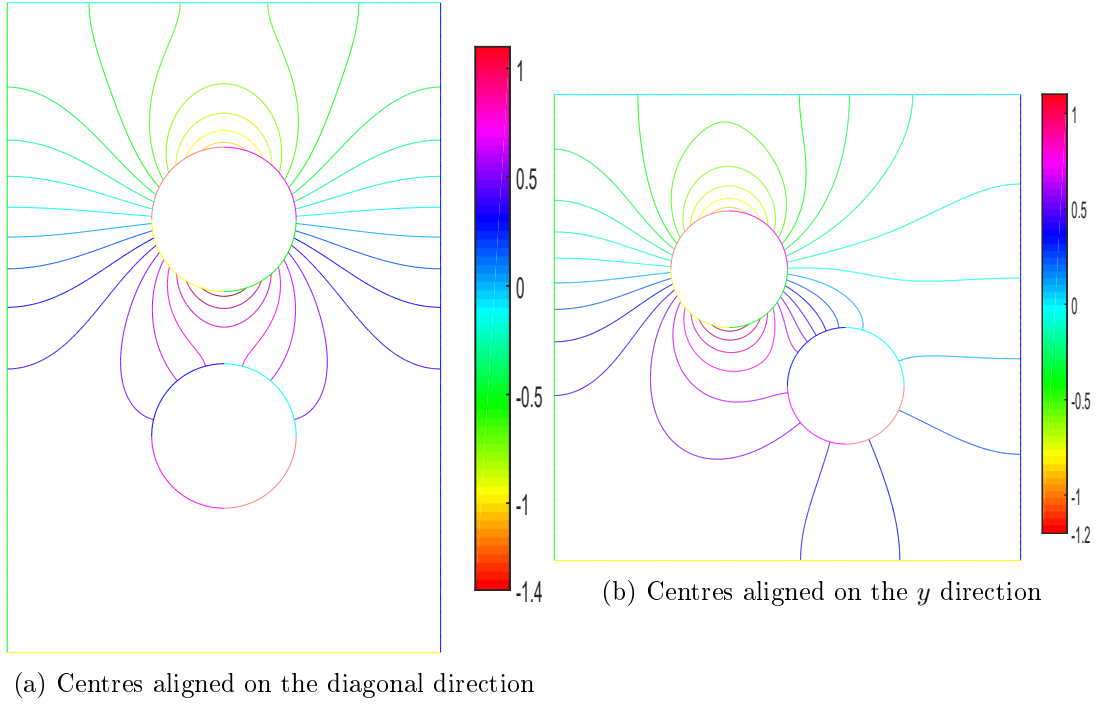


Figure 4.13 – Pressure fields for 2 cylinders configurations with different symmetries for medium wavenumbers ($\tilde{k} = 0.1$)

effort induced on the second cylinder appears to have the same order of magnitude in the two directions. This outcome is important for practical applications, since it means that the perturbation applied on one structure can propagate in all the directions, and not only in the excitation direction. Moreover, the phenomenon above described does not depend neither on the wavenumber nor on the confinement size, it happens for all the situations.

Calculations are also performed for an arrangement of fuel assemblies in a squared lattice. Four fuel assemblies are considered. The calculations are thought, to be a scaled representation of a full calculations for the four fuel assemblies of the ICARE experimental structure. Calculations are performed to have a first hint on what one should expect from full calculations on real ICARE geometry. Thus the geometrical quantities of the rod used in the ICARE set up are considered. The distance between the rods and between the rods and the walls is the same as in small confinement configurations. Thus the parameters used for the computations (dimensionless) are:

$$\tilde{R} = 1, \quad \tilde{L} = 558, \quad \tilde{h}_{\tilde{x}} = \tilde{h}_{\tilde{y}} = 0.9 \quad . \quad (4.28)$$

The calculations are performed for natural mode shapes of a free Euler-Bernoulli beam, which have a sinusoidal natural mode shape function. The dimensionless wavenumber for n^{th} mode is given by:

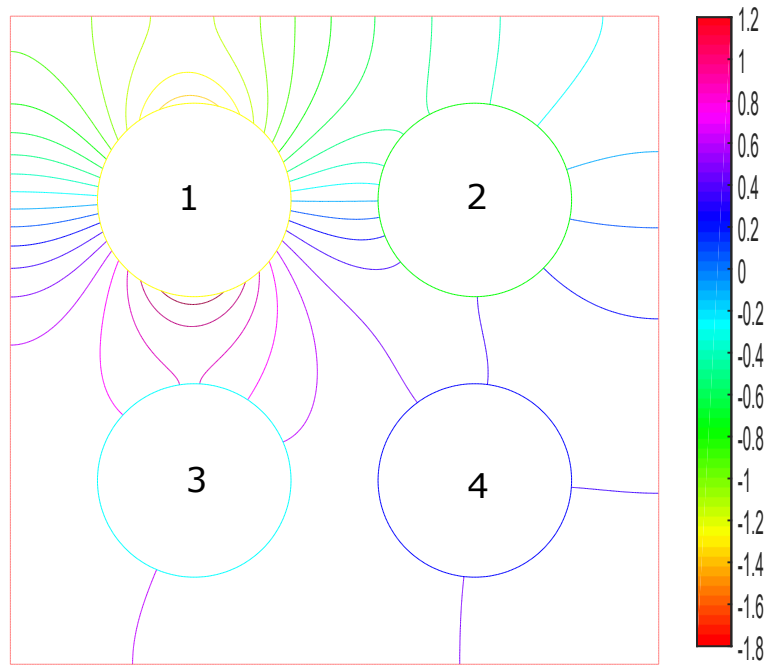


Figure 4.14 – Pressure field calculation for first natural mode ($\tilde{k} = 9 \cdot 10^{-4}$) excitation with four cylinders in 4 mm confinement

$$\tilde{k}_n = n \frac{R}{2L} \quad , \quad (4.29)$$

thus the dimensionless wavenumber for the first natural mode is about $0.9 \cdot 10^{-4}$. The use of sinusoidal mode shapes is not formally correct, since in real conditions the cylinders are not in free conditions and they are more likely to be considered in a clamped clamped condition. Anyway, since the length of the cylinder is much longer than the radius, the effect of boundary conditions is negligible in the central part of the assembly, and this assumption makes the identification of wavenumber much simpler. In Figure 4.14 it is visible that perturbations on the pressure fields propagate on the four cylinders and no symmetries are visible (except on the first cylinder). The excitation of one of the four cylinders induces efforts, thus motion, on all the four cylinders present in the section, in both the excitation direction and in the orthogonal direction. This phenomena were already observed experimentally by [Clement \(2014\)](#) and [Boccaccio \(2014\)](#).

Different calculations are run increasing the wavenumbers for increasing natural modes. The cylinder sizes considered for the calculations have a very high ratio between the length and the diameters, thus causing the first modes having a very low wavenumber. The behaviour of \tilde{g} function, which is related to coupling forces, is analysed. For low natural modes \tilde{g} increases with the increasing of the natural modes, while it starts to decrease when the natural modes overcome a certain threshold. The explication for this behaviour can be found by analysing two different factors: the pressure field and the definition of the \tilde{g} function itself. It can be seen that the perturbation pressure field stays almost constant

4.3. MULTIPLE CYLINDERS CALCULATIONS AND COMPARISON WITH EXPERIMENTAL RESULTS

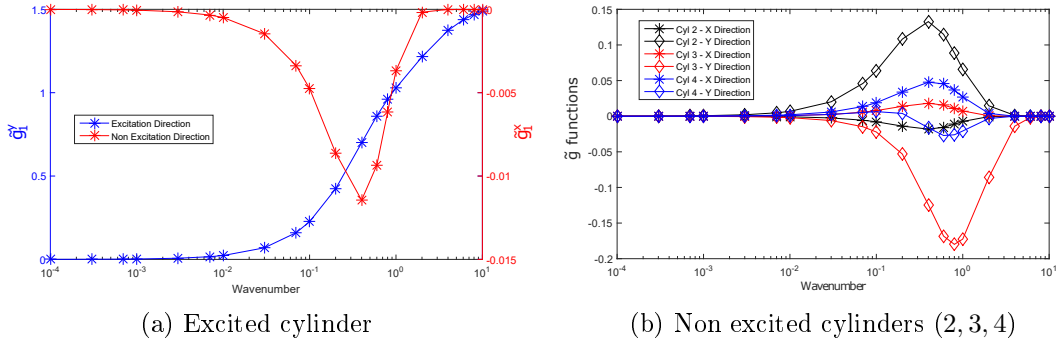


Figure 4.15 – Behaviour of the \tilde{g} functions in both directions as function of wavenumbers for different cylinders and directions with confinement of 4 mm with excitation given on the y direction on cylinder 1

for the first tents of natural modes and it shows an important reduction when natural modes higher than the hundredth ones are considered. On the opposite size, the behaviour of the \tilde{g} function tends to increase with the wavenumber, since it is proportional to the wavenumber \tilde{k} (see Equation 3.53). Thus two competitive trends are present. For low modes, the coupling forces increase, while they start to decrease after a certain threshold which definitely depends on geometrical configuration.

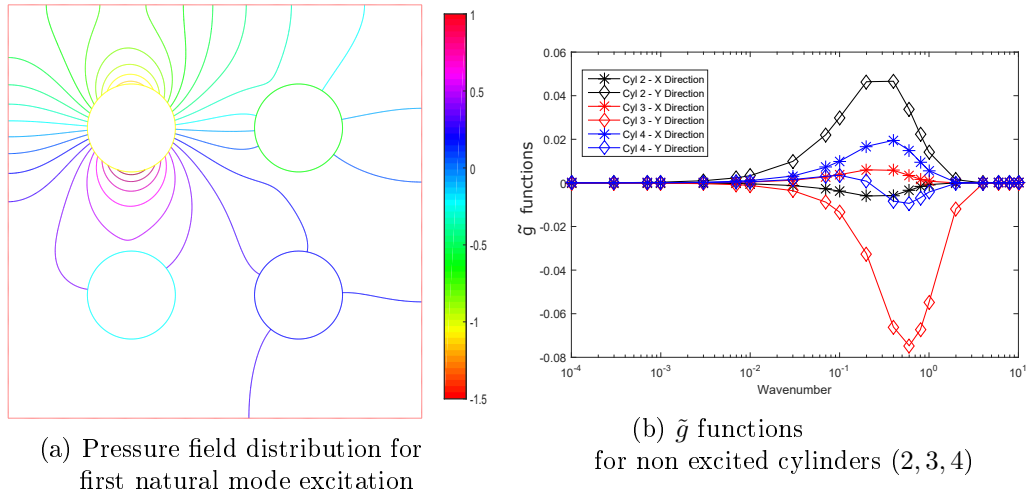


Figure 4.16 – Pressure field distribution and coupling coefficients for large confinement configuration (8 mm)

From a physical point of view two different phenomena are involved. Coupling forces increases due to the increasing mode shapes because the slope of the deformation of the cylinder becomes more important when the higher modes are excited. But, the propagation of the perturbations to other cylinders is more effective for small mode shapes (ideally the most efficient way to make perturbation propagate is to move the rod as a rigid body). Inertial forces are responsible for the increasing perturbation due to the in-

crease of wavenumber, while viscous dissipations are responsible for the efficiency loss in the perturbation propagation for high modes. In Figure 4.15b the described behaviour can be observed. It can be seen that for the excited cylinder (Figure 4.15a) the induced force always have an increasing behaviour. This is reasonable, since there is no propagation of the perturbation. The threshold point where the induced force on non excited cylinder starts to decrease, for the studied configuration is $\tilde{k} \approx 0.8$, representing approximately the thousandth mode of the cylinder. This means that for our practical applications, the coupling forces can be considered to increase with excited natural modes.

The same calculations are repeated increasing the distance between the rods and the confinement size to 8 mm (Figure 4.16). The lack of symmetry in the pressure field distribution, thus inducing interactions forces on both x and y directions can be seen in Figure 4.16a. There are no remarkable effects on the resultant forces exerted on the excited cylinder, while there is a strong decrease (about 50%) of the forces induced on the other rods (see Figure 4.16b). The distance between the assemblies, as expected, plays a fundamental role in the propagation of the pressure perturbation, inducing thus the coupling to reduce when the distance increases. Moreover, the threshold values where the coupling starts to decrease is shifted to smaller wavenumbers. Thus means that the closer two structure are, the more natural modes contributes to the coupling forces.

4.3.2 Calculations for ICARE Geometry and Comparison with Experimental Results

This section is dedicated to the numerical calculations performed using the developed model (based on the potential flow theory) on a multiple cylinders and multiple assemblies geometry.

Calculation Meshing

As already discussed in Chapter 3, these numerical calculations are performed in order to simulate the same geometry of the ICARE experimental set-up. Four different configurations are thus implemented in the code: two and four fuel assemblies in small (4 mm) and big (8 mm) confinement.

All the calculations are performed using dimensionless quantities as a matter of generality. The convergence of the calculations depends on the meshing size. Thus a study on the convergence of calculation depending on the meshing has been conducted. The FreeFem++ has a meshing utility which allows the user to just specify the number of divisions on each border, and then it automatically creates the meshing for the whole domain. It has been found that the convergence is assured when the external border of the domain are divided into 150 sections, and the cylinders border divided in 50 sections. Finally, all the calculations are performed with 200 divisions on external border and 75 divisions on the cylinders borders. This results in about 500000 cells and a computational time of about 60 s. In all the performed calculations, the assembly number one (bottom right)

4.3. MULTIPLE CYLINDERS CALCULATIONS AND COMPARISON WITH EXPERIMENTAL RESULTS

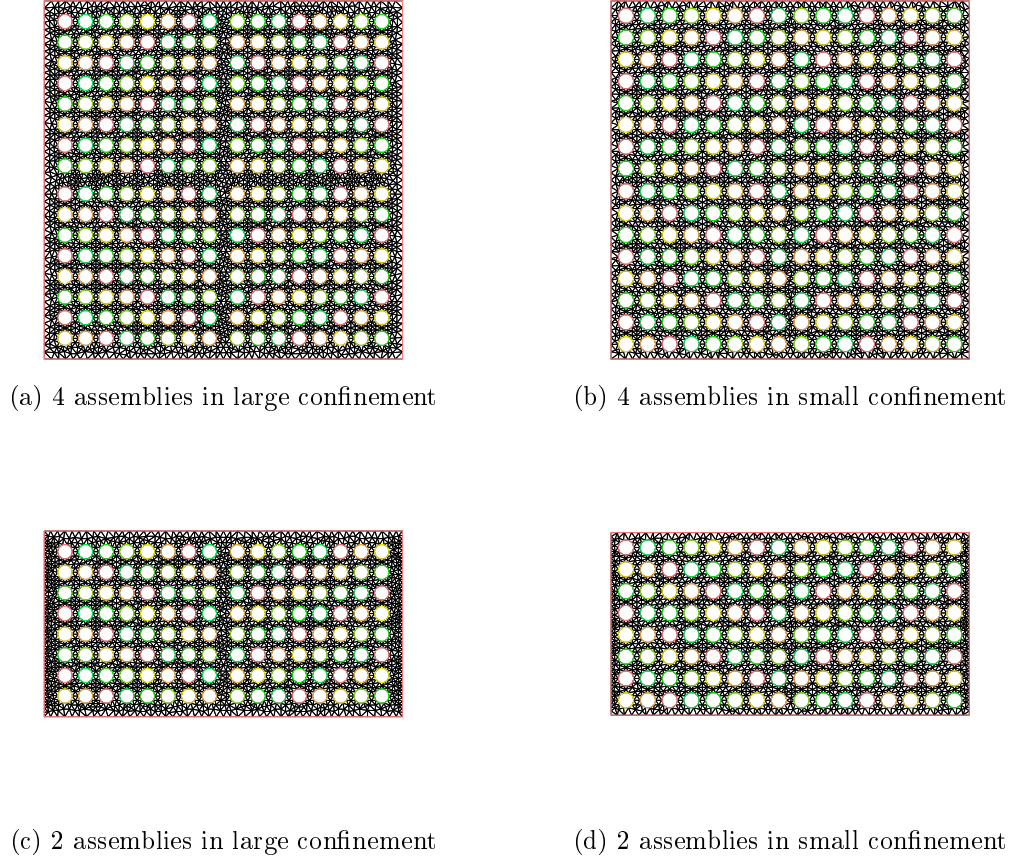


Figure 4.17 – Calculation meshing for the four configurations simulating the ICARE set-up

is excited along the x direction in order to simulate the experimental conditions. As a reminder, all the cylinders of the first assembly are supposed to be excited in the same way. Response functions ($\tilde{\mathcal{G}}$) are calculated as the sum of the response on each cylinder of the same assembly.

Qualitative Analysis

First, some calculations are run for a qualitative analysis and comparison with simple calculations performed on four cylinders geometry (as discussed in the previous Section). Two different calculations, performed with four fuel assemblies in large confinement are compared (see Figure 4.18). The two limit cases of very small wavenumber ($\tilde{k} = 0.001$) and very large wavenumber ($\tilde{k} = 1$) are simulated. Even if such wavenumbers do not correspond to experimental conditions, such simulations can give some information on the theoretical general behaviour of the system. For small wavenumbers (Figure 4.18a) the pressure field perturbation involves the whole calculations domain, while for large wavenumbers (Figure 4.18b) only the excited assembly is affected by pressure perturbation due to its own motion. In agreement with the results obtain with four cylinders calculations, the pressure perturbation reduces in intensity when the wavenumber increases. Furthermore, the effects

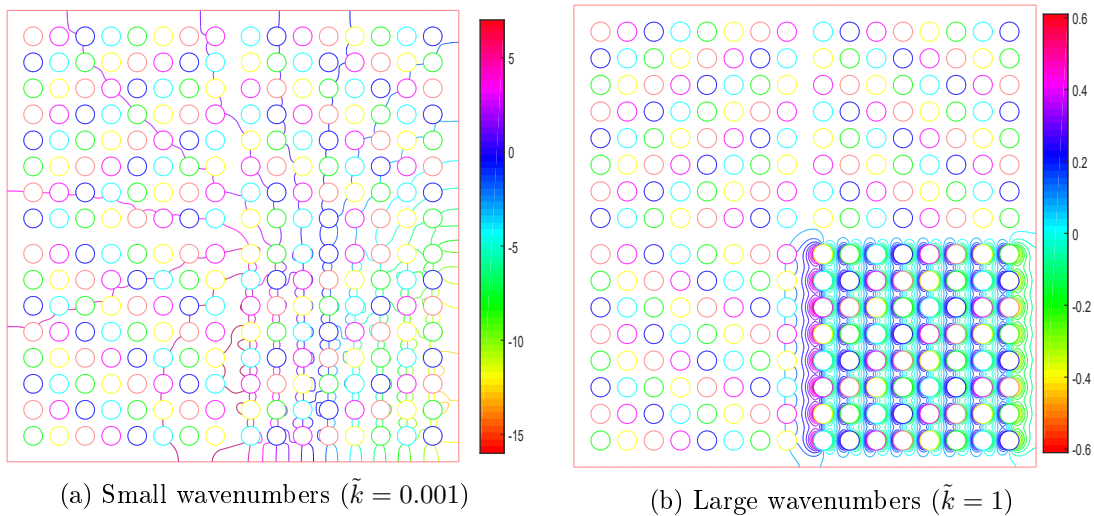


Figure 4.18 – Pressure field calculations for four fuel assemblies in large confinement

of the wall can be remarked observing the pressure field distribution around cylinders of excited assembly close to the wall. The presence of the wall creates an asymmetry in the pressure field. Pressure perturbations are more important close to the wall of the excited assembly, since the water is forced to stay in a smaller space without any possibility of going over the wall.

Analysis on Excited Assembly

After the qualitative analysis, calculations are carried out in order to perform a quantitative analysis and comparison with experimental data. Excitations of the three first natural modes are thus simulated, corresponding to the dimensionless wavenumbers: $\tilde{k} = 0.0009$, $\tilde{k} = 0.0018$ and $\tilde{k} = 0.0027$. Global $\tilde{\mathcal{G}}$ functions are calculated (as defined by Equations 3.59 and 3.60) for each assembly in both x and y direction.

In Figure 4.19 the global force (in the Fourier Space) applied on the excited assembly is represented. As already told before in this document, the global force represented by the $\tilde{\mathcal{G}}$ functions enclose both the added mass, stiffness and damping effect. As expected, since the model is linear, the $\tilde{\mathcal{G}}$ function presents a linear behaviour respect to the excited modes. The linear behaviour depending on the mode can be perfectly retrieved in experimental data for the stiffness (Figure 2.23d) and damping parameters (Figure 2.23c), while the mass parameter (Figure 2.23a) is not linear in experiments.

The effect of the confinement size fits well the experimental data. When the confinement is small, in fact, computed global force increases, meaning that the assembly will be subjected to more resistance in order to displace. This translates in an increasing of the mass and the stiffness of the assembly, as experimentally observed in Figure 2.19. Furthermore the effect of changing configuration from 2 to 4 fuel assembly can be observed both numerically and experimentally: when only two assemblies are present, the interaction

4.3. MULTIPLE CYLINDERS CALCULATIONS AND COMPARISON WITH EXPERIMENTAL RESULTS

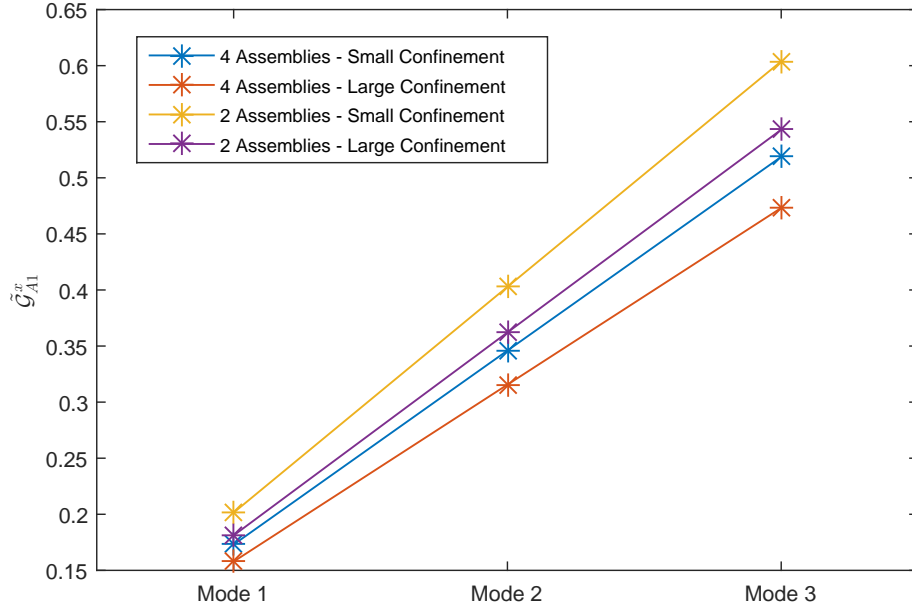


Figure 4.19 – Resultant of global forces (in Fourier Space) for excited assembly in x direction for the four different configurations

forces are more important both for simulations and experiments.

In order to estimate and compare the added mass, damping and stiffness coefficient we need to recall the relationship between the \tilde{g} functions in Fourier space fluid structure interaction force in the real space, which is expressed by:

$$\frac{1}{2\pi} \int_0^{1/\hat{R}} \frac{\partial \tilde{f}^y(\tilde{\zeta}, \tilde{t})}{\partial \tilde{\zeta}} \tilde{G}(\tilde{z} - \tilde{\zeta}) d\tilde{\zeta} = (\partial_{\tilde{t}} + \partial_{\tilde{z}})^2 \tilde{w}(\tilde{z}, \tilde{t}) \quad , \quad (4.30)$$

where:

$$\tilde{G}(\tilde{z}) = \int_0^\infty \frac{\sin(\tilde{k}\tilde{z})}{\tilde{G}_{A1}(\tilde{k})} d\tilde{k} \quad , \quad (4.31)$$

with $\tilde{G}_{A1} = \sum_{i=1}^{64} \tilde{g}_i^x(\tilde{k})$ the global force exerting on the whole assembly.

Considering the excitation of only one natural mode of the structure (the first mode), and considering natural mode shapes for a free Euler Bernoulli beam, the displacement of the structure can be written as:

$$\tilde{w}(\tilde{z}, \tilde{t}) = e^{i\tilde{\omega}_1 \tilde{t}} \sin(2\pi \tilde{k}_1 \tilde{z}) \quad , \quad (4.32)$$

where $\tilde{\omega}_1$ and \tilde{k}_1 are respectively the first natural pulsation and the wavenumber of the first natural mode shape of the structure.

For analogy, the force term $\tilde{f}^y(\tilde{z}, \tilde{t})$ could be expanded in a Fourier series, and the only

term which survives is the sinus term oscillating at the same frequency as the displacement ($\tilde{f}^y(\tilde{z}, \tilde{t}) \approx A_1 e^{i\tilde{\omega}_1 \tilde{t}} \sin(2\pi \tilde{k}_1 \tilde{z})$). Equation 4.30 could be thus rewritten as:

$$\frac{1}{2\pi} \int_0^{1/\hat{R}} e^{i\tilde{\omega}_1 \tilde{t}} A_1 2\pi \tilde{k}_1 \cos(2\pi \tilde{k}_1 \tilde{z}) \frac{\sin(\tilde{k}_1 \tilde{z} - \tilde{k}_1 \tilde{\zeta})}{\tilde{\mathcal{G}}_{A1}(\tilde{k}_1)} d\tilde{\zeta} = (\partial_{\tilde{t}} + \partial_{\tilde{z}})^2 [e^{i\tilde{\omega}_1 \tilde{t}} \sin(2\pi \tilde{k}_1 \tilde{z})] \quad . \quad (4.33)$$

Once the function $\tilde{\mathcal{G}}_{A1}(\tilde{k}_1)$ is calculated by the implemented code, all the quantities of Equation 4.33 are known and the coefficient A_1 can be calculated by a simple integration of the left term.

As it was already achieved in the previous Chapter, the two derivative terms on the right side of Equation 4.33 can be decomposed in three different terms ($-\tilde{\omega}_1^2 + 2i\tilde{\omega}_1 \partial_{\tilde{z}} + \partial_{\tilde{z}}^2$), respectively accounting for added mass, added damping and added stiffness coefficients. The three coefficients can be thus calculated for each considered configuration. Only the coefficients related to the first mode are presented here after.

The relation expressed by Equation 4.33 will allow thus to study the behaviour of the added mass, damping and stiffness coefficient as function of the confinement size, number of assemblies in the test section and excitation mode. Furthermore, there is the dependence from another parameter which is hidden behind the adimensionalization process of the boundary condition. The boundary condition, in fact, with dimensional quantities writes as follows:

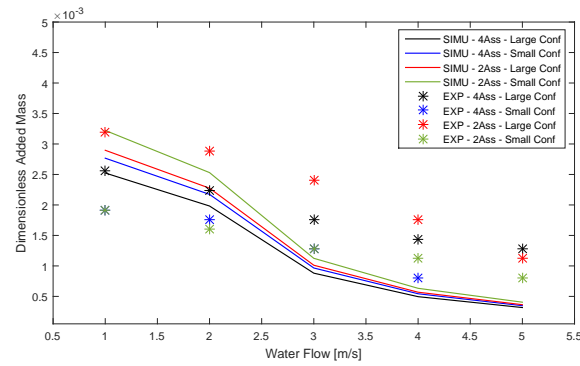
$$\left[\frac{\partial \phi}{\partial n} \right]_{r=R} = (\partial_t + U \partial_z)^2 w(z, t) \sin \theta \quad , \quad (4.34)$$

with the presence of water flow velocity in the derivative terms. Once the dimensionless quantities are used for writing the equation, the flow velocity terms disappears, but it is hidden in the definition of the dimensionless time quantity. For practical application, when the derivative terms are considered for a natural mode excitation ($-\tilde{\omega}_i^2 + 2i\tilde{\omega}_i \partial_{\tilde{z}} + \partial_{\tilde{z}}^2$), the flow velocity parameter is carried by the term $\tilde{\omega}_i$, as expressed below:

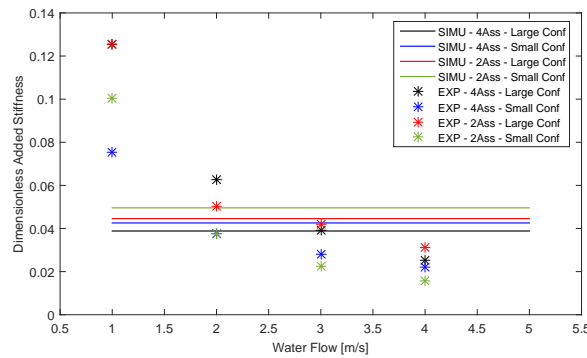
$$\tilde{\omega}_i = \frac{\omega_i}{U} R \quad . \quad (4.35)$$

Thus, the calculation performed with the implemented potential flow model allows to also study the effect of the water flow rate on the dynamic parameters. It can be easily seen that for stagnant water ($U = 0$), even if the dimensionless quantities could not be written, the only term which resists is the added mass term. This phenomenon is clearly remarkable in experimental data, when passing from "In Air" condition to stagnant water the departure of the transfer function does not change (see black and blue curves in Figure 2.18c). The presence of stagnant water, thus, only induces an increase of the apparent mass of the system, thus an added mass effect (with consequent changes in the resonance frequencies). Anyway, calculations for stagnant water are not performed, since it was necessary to use dimensional quantities.

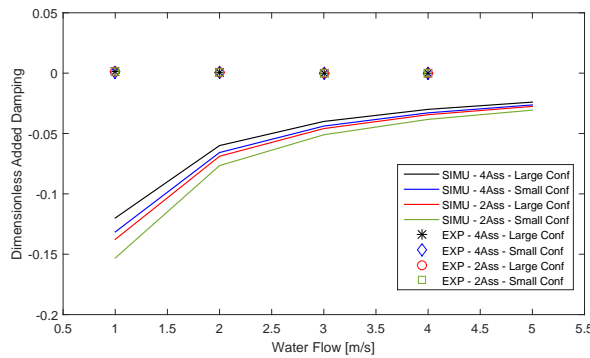
4.3. MULTIPLE CYLINDERS CALCULATIONS AND COMPARISON WITH EXPERIMENTAL RESULTS



(a) Dimensionless added mass



(b) Dimensionless added stiffness



(c) Dimensionless added damping

Figure 4.20 – Added mass, stiffness and damping parameters as function of the water flow rate, simulated VS experimental data

The effect of the water flow on the dynamic parameters of the system (added mass, added damping, added stiffness) is analysed for all the four implemented configurations. The simulated data are compared with experimental ones. The experimental data, which are already presented in Section 2.4.3 need to be transformed in dimensionless quantities in order to be compared with simulated data. Furthermore, in order to estimate the experimental added coefficients, the difference between the measured coefficient and the "In Air" ones needs to be performed.

Figure 4.20a shows the behaviour of the added mass coefficient as function of the

water flow rate. The simulated data for different confinement sizes show a very similar behaviour. The added mass coefficient appears to decrease with the increasing of the water flow. Experimental data and numerical show a similar trend in decreasing respect to the flow rate. Anyway, for large flow rates, the numerical data look to underestimate added mass coefficient. This could be due to some non-linear behaviour of the fuel assembly, but it is also to consider that for large flow rates, the transfer functions become more and more damped, thus the parameter estimation becomes less reliable. The simulated dimensionless added stiffness coefficient, contrariwise, does not show any dependence on the flow rate (see Figure 4.20b). Since the adimensionalization process involves the division by the square of the flow velocity, having a constant dimensionless stiffness means that the stiffness increases proportionally to the square of the flow velocity. Experimental and numerical data have the same order of magnitude, but the model seems to underestimate the added stiffness effect for small flow rates and to over estimate it for large flow rates. The over estimation of the damping coefficient could be due to the negligence of the viscous forces, which cause the added stiffness coefficient to decrease for high flow rates.

Finally, the added damping coefficients are plotted in Figure 4.20c. As expected, the calculations do not fit at all the experimental data. The potential flow theory, in fact, does not account for any viscous forces, which are the main responsible for damping.

The effects of different confinement size on experimental data does not agree with the simulated data. This incoherence is not due to the model, but to some experimental biasing. As already discussed in Chapter 2, in fact, when the confinement size is changed in the experimental set-up, the excitation point is changed, inducing the mechanical response of the assembly to slightly change due to non-linearities. Excitation amplitude and water temperature does not affect calculations in any way, so any considerations on this subject is useless.

Coupling Analysis

The analysis on the coupling between the excited fuel assembly and not excited ones is addressed in this section. By recalling the formalism of Equation 4.33 and considering thus the force displacement relation for two different assemblies, the coupling forces existing between two different assemblies i and j along a direction d at a given frequency \tilde{k} results to be given by:

$$\frac{\tilde{f}_i^d(\tilde{k})}{\tilde{f}_j^d(\tilde{k})} = \frac{\tilde{G}_{A_i}^d}{\tilde{G}_{A_j}^d} . \quad (4.36)$$

It can be seen that for coupling analysis, the effect of the water flow cannot be addressed with such formalism. The derivative terms which hide the water flow rate simplify each other when the ratio of the forces is performed. Anyway, the effects of the confinement size and of the number of assemblies can be analysed. Furthermore, the couplings between different directions and different assemblies can be observed and related to experimental

4.3. MULTIPLE CYLINDERS CALCULATIONS AND COMPARISON WITH EXPERIMENTAL RESULTS

observations.

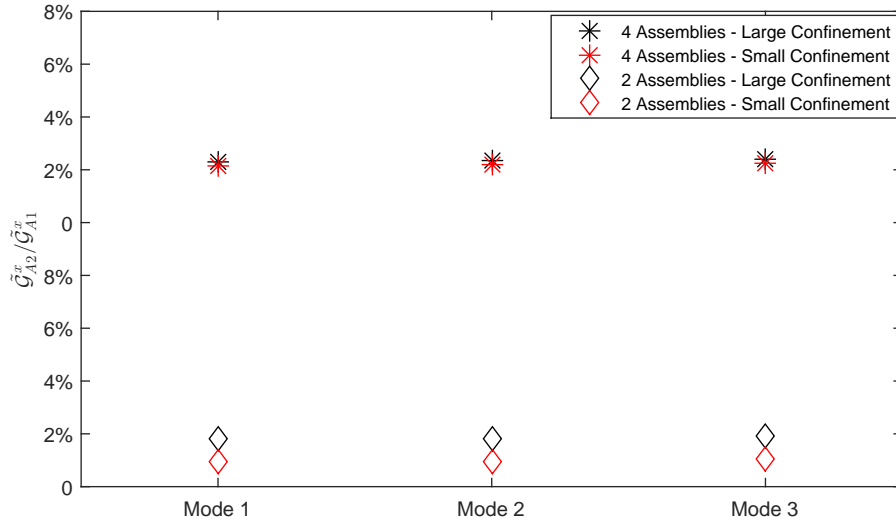


Figure 4.21 – Simulated coupling forces between the assembly 1 (excited) and assembly 2 on the excitation direction (x direction)

The ratios between the force induced on the assembly 2 and the force induced on the assembly 1 are represented in Figure 4.21. The coupling between the two assemblies is on the order of 6% for small confinement and it decreases to about 1% when the confinement size increases. Small differences can be observed between two and four assemblies configurations. These numerical results underestimate in a considerable way the experimental coupling measured between assembly 1 and assembly 2. The experimental values for the coupling are about 20% at the resonance frequencies in small confinement and they are reduced to about 10% when the confinement size is increased (see Figure 2.32). Thus, the model is able to qualitatively predict the effect of the confinement size on the coupling, but is not accurate from a quantitative point of view. Probably the viscous force play a very important role on the coupling along the excited direction, thus it should explain the discrepancies between numerical and experimental results. The coupling on the direction orthogonal to the excitation is also investigated. No couplings are visible between the fuel assemblies 1 and 2 on the y direction. The same observation can be done for experimental results.

Finally the analysis on the coupling between assembly 1 and assembly 4 is carried out. An unexpected outcome is shown by Figure 4.22a. The coupling on the excited direction between the assemblies 1 and 4 (assembly 4 is located in the top right corner) is found to be about 20%. Two important remarks should be done on this observation: first the coupling between the two assemblies which are not oriented following the excitation direction is more important than the coupling of the assemblies 1 and 2; secondly, the numerical value fit perfectly the experimental values for the coupling between assembly 1

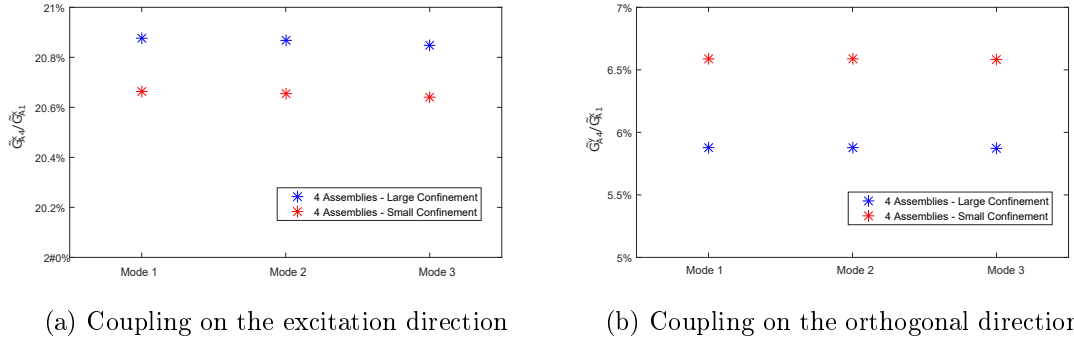


Figure 4.22 – Simulated coupling forces between the assembly 1 (excited) and assembly 4 both on the excited direction and on orthogonal direction

and 4 which are reported in Figure 2.35. Since the linear model implemented and used to perform calculations mainly account for inertial forces, this outcome is a demonstration that inertial forces are more likely to act on assemblies which are side by side and that the coupling existing along the excitation direction may not be due to inertial forces. A smaller, but considerable coupling is also observed between fuel assemblies 1 and 4 on the direction orthogonal to the excitation (about 5%).

4.3.3 Sum-Up on Numerical Calculations

In this Chapter the numerical calculations performed with the potential flow based model have been discussed. First the model for one single cylinder has been validated with reference works in literature. The model for the single cylinder calculations has been used to perform a parametric study on the confinement sizes and wavenumbers. An empirical expression fitting the calculated \tilde{g} function which is a dual of the interaction force acting on the cylinder has been found. Moreover polynomial interpolation has been considered. Both approaches, even if they provided functions which are able to approximate the behaviour of the \tilde{g} function, were not useful from a practical point of view in order to built some empirical model which could have lead to an analytical solution for the interaction forces depending on different parameters.

Once the model for the single cylinder is validated, it has been improved by considering two and four cylinders. Some qualitative analysis has been carried out on the performed calculations. It has been shown that the absence of geometrical symmetries on the arrangement of the cylinders, can induce interaction forces on directions different from the excitation direction. Two competitive phenomena can be observed when the wavenumber changes. With the increasing of the wavenumbers the perturbation of the pressure fields tends to concentrate around the excited cylinder, thus other cylinders are less affected by the perturbation field. On the other hand, the interaction forces, relied to the function \tilde{g} are directly proportional to the wavenumber. A threshold wavenumber can be identified where the \tilde{g} function inverts its behaviour; this threshold value depends on the confinement

4.3. MULTIPLE CYLINDERS CALCULATIONS AND COMPARISON WITH EXPERIMENTAL RESULTS

size.

Finally, calculations with 2 and 4 fuel assemblies geometries are performed. The geometries are made in order to fit the ICARE experimental set-up. Two different confinement sizes are implemented. A first qualitative result, which is in agreement with experimental results, is that the resultant of the global forces on the excited fuel assembly increase with the excitation mode (only first three modes are considered). Furthermore the force is more important when the confinement size is smaller.

Added mass, added stiffness and added damping coefficients are computed from the simulations and are compared with the estimated values from experimental data. Both added mass and added stiffness coefficients agrees qualitatively. Added mass coefficient from simulations decreases with the water flow rate in a similar way to the experimental one, but an important over estimation of the added mass coefficient happens when the flow is 1 m/s . The added stiffness coefficient appears to not to change with the water flow for simulated data. The order of magnitude for added stiffness coefficient is in agreement between numerical and experimental data, but simulations over estimate added stiffness for large flow rates. As a drawback, experimental and simulated the added damping coefficients are not in agreement. This result on the damping coefficient was attended since the model has several simplification as the negligence of viscous forces and the negligence of vorticity effects due to the grids.

Finally the study of the coupling forces from simulation has been addressed. The intensity of the coupling forces between the excited assembly and non excited one is calculated from simulations. The coupling intensity can be also easily obtain from experimental data by the transfer functions which were deeply analysed in Chapter 2. The coupling between excited fuel assembly and fuel assembly 2 are strongly underestimate by the simulation data (simulation coupling is about 5% while experimental one is about 20%). On the opposite side, the model appears to well estimate the couplings between the assembly 1 and assembly 4, for which numerical data well fits experimental ones. Since the model is able to predict in an efficient way the coupling between assemblies which are not located along the excitation direction, and it is fails when the assemblies are located along the excitation direction, this could mean that the forces involved in the coupling along different directions should have a different nature.

In conclusion, the developed simple model, qualitatively predicts the experimental results and for certain quantities (added mass and coupling) it is also able to give accurate predictions. It completely fails, as expected on the damping coefficient.

Chapter 5

GWU Experiments and Physical Analysis

During my PhD I spent two months at the Thermo-Fluids Laboratory (TFL) in George Washington University (GWU). In this chapter the work carried out during these two months of collaboration will be illustrated. An experimental facility was built there which is in some ways similar and complementary to the ICARE experimental facility. It consists of a surrogate fuel bundle (6 by 6) under axial flow put on a shaking table. Once the shaking table is in action, both bundle displacements and fluid flow are measured by PIV (Particle Image Velocimetry) techniques. The main differences with the ICARE facility consists in the presence of the shaking table (which excites the whole structure) and on the use of the flowing fluid, which index matches the fuel bundles, thus giving the possibility to access velocimetry data on the whole fluid domain (even behind and in between the rods). The experimental set-up will be further described in the next section. The work carried out in the framework of this collaboration consists in the analysis of some of the data sets measured during the experimental campaigns in 2015 aiming to attempt to explain some of the phenomena which are outlined using the Potential Flow Model previously developed. The new experimental set-up is implemented in the FreeFem++ code and simulations are performed in order to compare experimental and numerical results.

5.1 Experimental Facility

As discussed in Chapter 1 the nuclear industry needs better understanding of fuel bundle dynamics under earthquakes conditions. During earthquakes, these fuel bundles may be set in oscillation. Understanding the bundle dynamics under such circumstances is important since collisions between bundles or between the bundle and reactor baffle wall may result in damages that can prevent the control rod mechanisms from engaging.

While normal operating conditions involve an axial flow, there are accidental scenarios where there may be a loss of flow. Thus dynamic study of a fuel bundle under earthquake condition in stagnant water is also extremely important.

CHAPTER 5. GWU EXPERIMENTS AND PHYSICAL ANALYSIS

In order to study such phenomena, an experimental facility was realised at the TFL in GWU. The facility consists in a vertical channel that is mounted on a shaking table, and contains a single surrogate nuclear fuel bundle inside. The facility was installed at the Virginia Science and Technology Campus of the George Washington University.

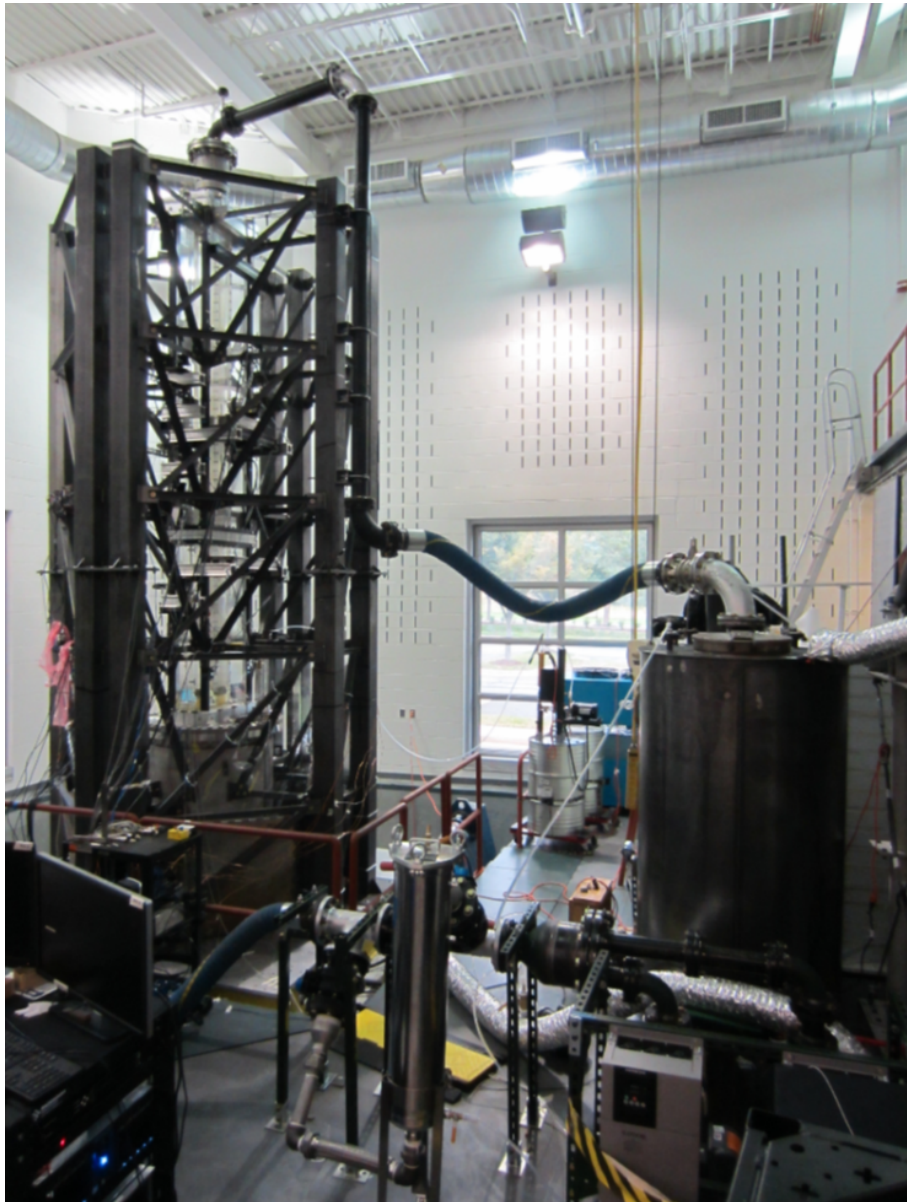


Figure 5.1 – View of the experimental facility ([Weichselbaum, 2015](#))

A brief description of this facility, represented in Figure 5.1 is presented below. Further details are provided in [Weichselbaum \(2015\)](#); [Weichselbaum et al. \(2015\)](#) and [Hussain \(2017\)](#).

5.1.1 Test Section

The test section is made of a vertical channel mounted on a shaking table and attached to a piping system capable to force a fluid flow inside the channel. The channel is composed of a primary section that is centred inside a secondary low pressure boundary that exists as a safeguard against leaks (Figure 5.2). Both sections are made of acrylic to allow optical access. The primary channel has a cross section of $154\text{ mm} \times 124\text{ mm}$, while the secondary one has a $559\text{ mm} \times 216\text{ mm}$ cross section. An aluminium exoskeleton is mounted on the outside of the secondary channel to allow bracing structures to be connected to the channel as well as to facilitate the installation of optical components. The entire facility is around 7 m tall with an overall footprint of around $3\text{ m} \times 3\text{ m}$. The flow loop is driven by two 50 Hp (about 37 kW) centrifugal pumps.

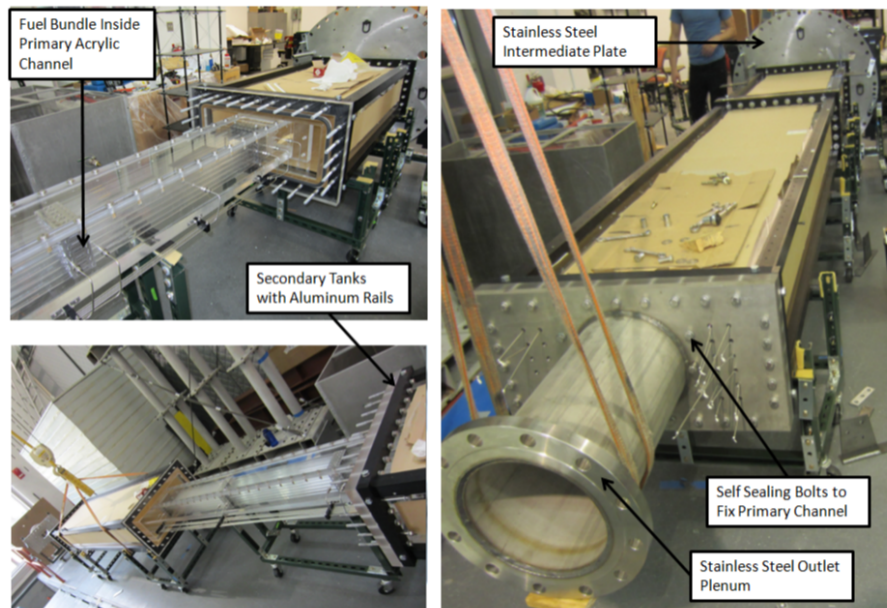


Figure 5.2 – View of primary and secondary tanks (Weichselbaum, 2015)

The single bundle is composed of a 6×6 array of surrogate nuclear fuel rods that are constructed out of solid acrylic with a diameter, $D = 14.25\text{ mm}$, which is 50% larger than prototypical rods, and arranged with a pitch to diameter ratio, $P/D = 1.33$, that is characteristics of PWR bundles. The diameter is chosen to be 50% bigger than real PWR fuel rods in order to fit two important parameters:

- the first resonant frequency of the structure;
- the Reynolds number of the axial flow.

The bundle is 4.00 m tall overall, which is similar to prototypical bundles, but the ratio between the length and the diameter is only $L/D = 280$, which is $2/3$ of the L/D ratio of a prototypical bundle. The ratio between the distance between two spacer grids (L) and the rod diameter (D) is maintained similar to the prototypical one (which is 53.47). Thus,

the spacing between the grids is 750 mm and the rods are held in place by 6 stainless steel spacer grids (SG) that are evenly distributed along the height of the bundle (in prototypical bundles there are 8 grids). These grids are assembled such that the ones on the top and bottom are rigidly fixed to the acrylic channel, while the middle four are free to deflect. The grids contain springs and dimples, which replicate how the rods are held in place in a prototypical bundle.

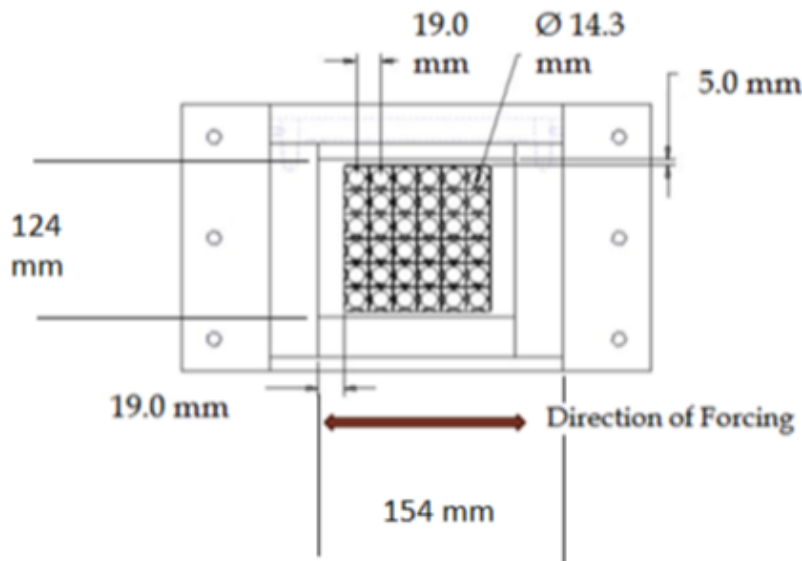


Figure 5.3 – Primary channel profile (Weichselbaum, 2015)

This arrangement results in bypass regions of 19.0 mm in the direction of forcing and 4.5 mm in the out-of-plane direction as shown by Figure 5.3. The entire facility is mounted on a $3\text{ m} \times 3\text{ m}$ shaking table that is capable of motion with 6 degrees of freedom. The table is rated for operation at up to 50 Hz and 1.5 g acceleration. Different experiments are run within a frequency range from 0 Hz to 7 Hz with an amplitude range of $2\div 20\text{ mm}$.

Two different working fluids have been used for testing: water and para-cymene. Para-cymene is nearly index matched to acrylic at room temperature while having a density that is close to water near prototypical conditions. It is also possible to accurately match the refractive index of para-cymene to the acrylic used by either controlling the temperature of the fluid or by adding trace amounts of cinnamaldehyde, as shown by Fort et al. (2015). The use of a fluid which is perfectly index matched with the acrylic (which is the material of the fuel bundle) is extremely important in order to be able to access all the volume filled by the fluid with PIV techniques, since the structure will result transparent for the camera. In this way one can measure the velocity field of the flow even in the space which is hidden behind fuel rods.

5.1.2 Measurement System

In this section the measurement techniques used in this experimental facility are described. LVDT sensor and accelerometers are mounted on the shaking table and all along the structure. Non intrusive techniques for fluid measurements and fuel bundle structural displacement are implemented.

The shaking table is instrumented with 6 built in LVDT (Linear Variable Differential Transformer) sensors. There are two sensors in the direction of forcing (y), one in the out-of-plane (z) direction and three in the vertical (x) direction. Unfortunately we do not have exact information on the locations of the sensors. The sampling rate of the LVDT sensors is 512 Hz . With these sensors we are able to measure and control directly the excitation that is injected in the whole system.

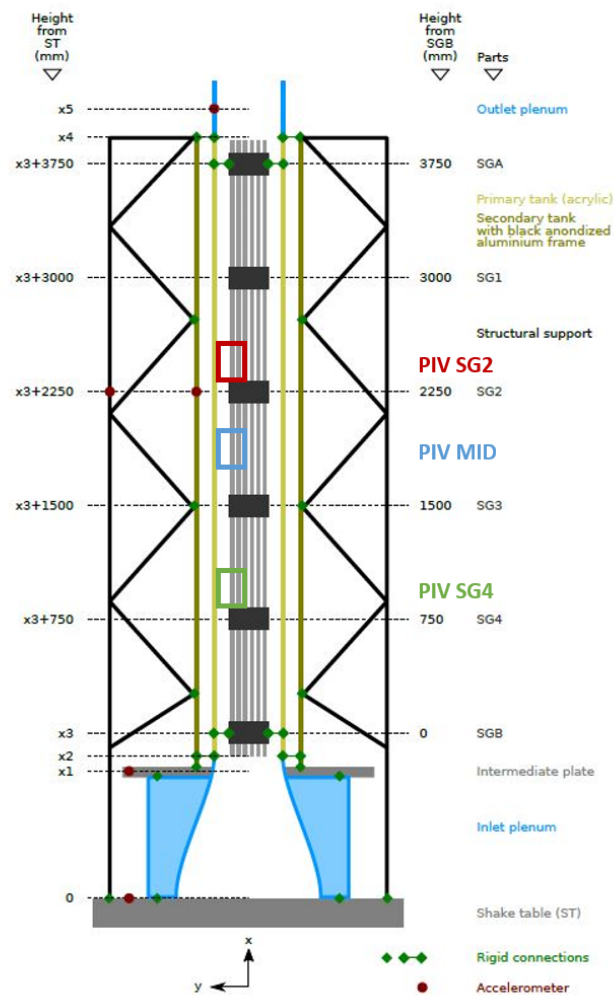


Figure 5.4 – Experimental facility scheme with rigid connections, accelerometers locations and PIV planes location

Five different accelerometers are placed all along the structure. One is placed on the shaking table, one on the inlet plate, two are placed on the same level of the spacer grid

number 2 (on the tank and on the external support structure) and the last accelerometer is placed on the outlet of the structure. The sampling rate of the accelerometers is 2048 Hz . In Figure 5.4 is shown a schematic representation of the positioning of the accelerometers and of the rigid connections between the fuel bundle, the external tank and the supporting structure.

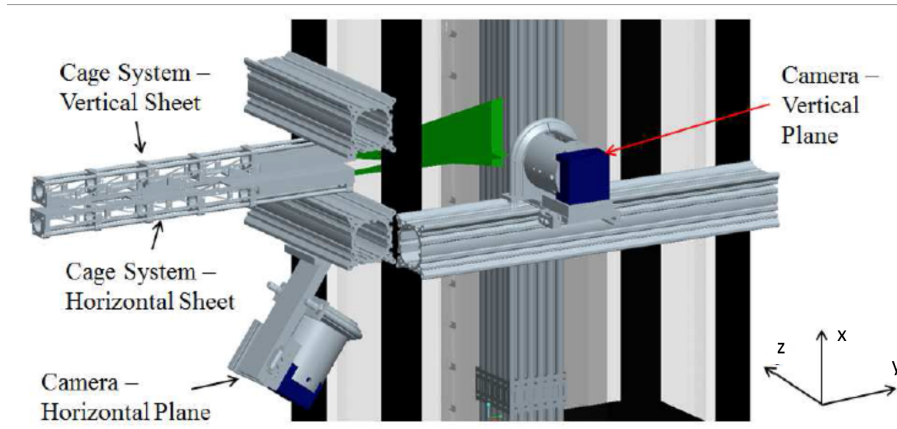


Figure 5.5 – Positioning of cameras in non inertial reference frame for PIV measurements (Weichselbaum, 2015)

A flying PIV (Particle Imaging Velocimetry) has been developed specifically for this experiment for fluid measurements (Weichselbaum et al., 2016). In order to resolve flow features in this confined and shaking environment there is the need to have an high spatial resolution. Given the experimental set-up, the desired resolution is best obtained with the cameras mounted directly on the moving reference frame, as show in Figure 5.5. The camera used are high-speed CMOS cameras which are able to directly record straight to the computer, allowing for high acquisition time. The cameras are fixed to the structure by rigid connections, and efforts has been put in order to minimize the vibrations of internal components. The acquisition rate of the PIV system is 2048 fps .

Finally, in order to monitor the overall vibration of the fuel bundle a DIC (Digital Image Correlation) system made of five high speed cameras has been implemented. Each camera is associated with a dedicated LED lamp to provide adequate light for exposure. Four of the cameras are oriented in order to monitor displacements in the direction of forcing (y displacement), while the fifth camera is oriented to capture out-of-plane displacements of the bundle (z displacement). The four in-plane cameras are aligned height-wise with the four moving spacer grids, which use the laser etched pattern on the outer walls to serve as a target for tracking using DIC. The fifth camera is aligned with the second spacer grid. In order to yield sufficient temporal resolution, an acquisition rate of 256 fps is selected. An error estimation has been done for DIC system: average error is around $4 \mu\text{m}$, which is negligible with respect to the displacement of the structure, which is of the order of the millimetres.

In order to synchronize the various instruments for the fluid and structure measure-

ments, and in order to be able to perform an efficient data reconstruction, a comprehensive timing and synchronization system has been implemented. The only problem is the synchronization of the LVDT data (which are in a closed system in the shaking table) with the other measurements. One way to synchronise these data could be to use the accelerometer mounted on the shaking table, and to compare this signal with a double time derivation of the LVDT data (on the same direction).

5.2 Experimental Data and Repeatability Problem

After some tests on the experimental facility performed in 2014, several campaigns were performed during 2015 with different fluids (water and para-cymene) and with different excitation parameters. A complete list of the experimental campaigns can be found in Weichselbaum (2015). Some preliminary work on the post-treatment of the experimental data are discussed in Weichselbaum (2015); Weichselbaum et al. (2015) and (Hussain, 2017). It has been found that the experimental facility works as expected and all the measurements techniques were coherent, giving useful results for physical interpretations.

Going deeper in the data analysis, the repeatability of the experiments has been investigated. Three different data sets have been analysed; all of them having the same input parameters. The shaking table is excited at 1.3 Hz with an amplitude of 3 mm . The frequency of 1.3 Hz has been chosen because it is supposed to be fairly significant, since it is very close to the first resonance frequency of the structure. We will refer to the three different data sets as "Case 1", "Case 2" and "Case 3"; details of each experiments are summarised in Table 5.1.

Data Set Name	Date	Excitation Amplitude	Excitation Frequency
Case 1	13/08/2015	3 mm	1.3 Hz
Case 2	13/08/2015	3 mm	1.3 Hz
Case 3	18/09/2015	3 mm	1.3 Hz

Table 5.1 – Input parameters for each data set

5.2.1 PIV Data Analysis

First, the velocimetry data on the fluid flow taken with PIV system described above has been analysed. The vertical laser sheet is aligned with the center of the second fuel rod and vertically positioned just below the second spacer grid (about 2.3 m from the bottom of the fuel bundle). Two cameras are aligned with the vertical plane and with an horizontal plate, giving thus the possibility to measure all the three components of the flow velocity. A scheme of the laser sheets arrangement, the cameras positioning and of the FOVs (Field Of Views) for the first camera (orange shape) is sketched in Figure 5.6. Only the data coming from Camera 1 (and FOV 1) are analysed in the following discussion. The data

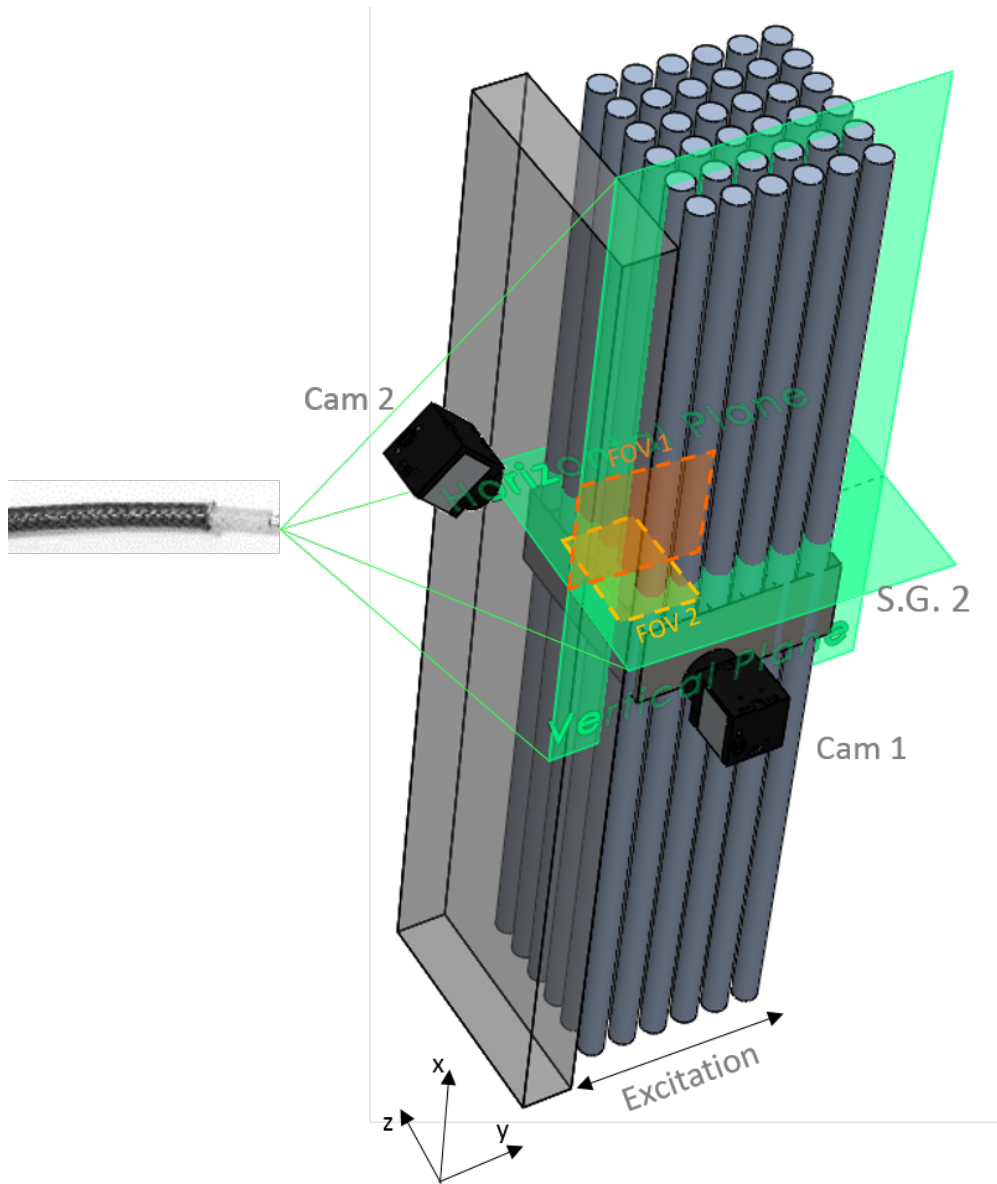


Figure 5.6 – Location of PIV planes, cameras and FOVs for experimental campaigns

related to other cameras, which can give informations on the z velocity profiles are not yet analysed.

From a very first look at the 2D flow charts it has been remarked that the three data sets presents very different behaviours, especially in the axial component of the flow velocity. Specifically, the "Case 1" and "Case 2", which are run during the same day (half an hour difference) look to be the most different ones, while, "Case 1" and "Case 3" seem to be very similar. For a quantitative analysis we can focus on the fluid velocity (axial and transversal) over a single line, so we can easily follow the evolution of the velocity profile with the time. In Figure 5.8 and Figure 5.7 are represented the velocity profiles of respectively the axial and transversal velocities for different phases along a whole excitation period (the excitation frequency is 1.3 Hz thus the excitation period is $T = 0.77 \text{ s}$). From

5.2. EXPERIMENTAL DATA AND REPEATABILITY PROBLEM

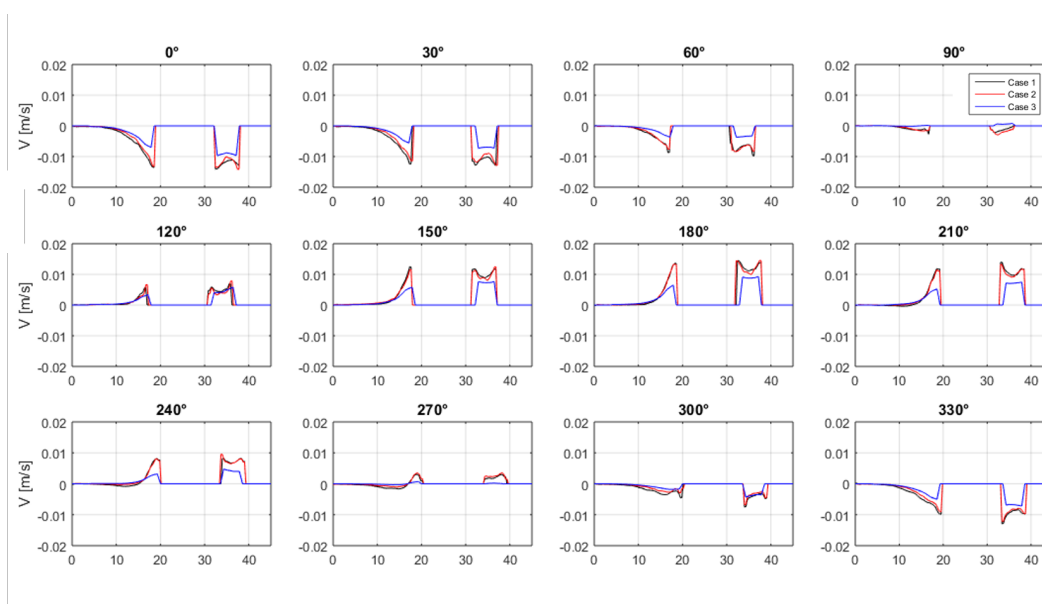


Figure 5.7 – Transversal velocity profiles for three test cases at different phases

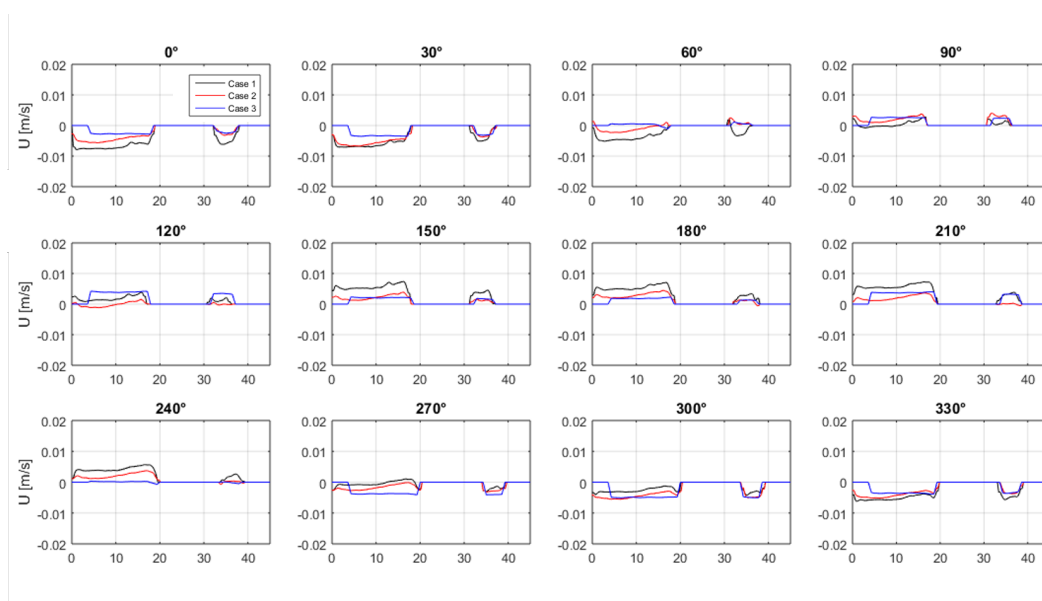


Figure 5.8 – Axial velocity profiles for three test cases at different phases

Figure 5.7 one can observe that the velocity profiles for "Case 1" and "Case 2" are very similar, in fact the red and black lines are almost superposed; the blue line representing "Case 3" is fairly different in amplitude but not in shape. One could think that Figure 5.7 confirms the repeatability of the experiments and that "Case 1" and "Case 2", which are run the same day, are coherent with each other. The behaviour of the axial velocity profiles, represented in Figure 5.8, is investigated next. One can remark the strong presence of an axial flow, even when the fluid was stagnant before the excitation started. This behaviour was attended, since the motion of the fuel assembly will imply some pressure gradient along the bundle, which will force the fluid to flow in the axial direction. Furthermore, the

important results that Figure 5.8 shows, is the non coherence between the axial velocity profile of "Case 1" and "Case 2", even if the transversal velocity profiles are practically the same.

The presence of different behaviours on the axial flow profiles, given by an excitation that has the same input parameters deserves to be further investigated. A check has been done on the measurement systems and the input parameters, and it seems that there are no systematic errors that could explain such observations.

5.2.2 LVDT Data Analysis

A first step for further investigations on the differences on the induced flow starts from the analysis of the excitation itself. The 6 LVDT position sensors which are placed in the shaking table are analysed in the time domain and in the spectral domain. The objective of this analysis is to understand if the seismic excitation which is given to the structure is the same both from an energy point of view and from a frequency point of view. From now on, only the two data sets "Case 1" and "Case 2" are considered since they seem to be the most meaningful ones.

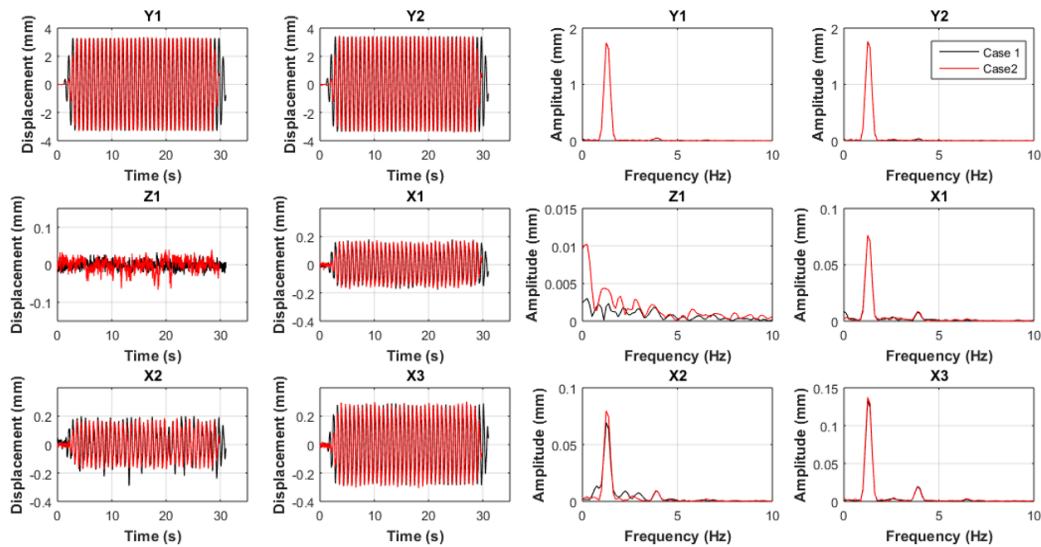


Figure 5.9 – Time plot and FFT plot of the 6 LVDT sensors of the shaking table

From Figure 5.9 one can remark that the shaking table, not only excites the bundle on the y direction, but there is some parasite excitation also on z direction and on the vertical direction, even if they are much smaller than the main excitation ($< 5\%$). From the analysis of the spectral components of the excitation there are no remarkable differences between the two cases on the main component of the excitation (on y direction). Despite, there are some discrepancies on the spectral components of the excitation along the other two axes. Anyway, those discrepancies are very small, and it has been considered that they should not directly affect the flow patterns in such a way to justify the observation that has been discussed in the previous paragraph.

5.3 POD and Projection on Theoretical Modes for GWU Dataset

In order to further investigate the experimental response of the two test cases described before, a better understanding of the surrogate bundle deformation is needed. A very powerful tool for studying the dynamic behaviour of mechanical systems is the Proper Orthogonal Decomposition (POD), which allows to extract the principal modes the system undergoes and to evaluate the energy captured by each mode (Berkooz et al., 1993; Feeny, 1997). In this section a brief description of the POD technique is presented. It is followed by its application to the data sets of interest.

5.3.1 Proper Orthogonal Decomposition

Application of Proper Orthogonal Decomposition (POD) to structures typically requires sensed dynamical quantities at M locations within the system. For our application, these quantities are taken to be displacements of the grids (measured with DIC system) $y_1(t), y_2(t), \dots, y_M(t)$, although in general, other states can be used. For this application $M = 4$ since there are four different grids free to move; top and bottom grids are fixed to the structure, so their relative displacement is zero and it doesn't make any sense to insert them in the matrix. When the displacements are sampled N times, we can form displacement-history arrays (sometimes the means are subtracted to the displacement histories). In performing the proper orthogonal decomposition, these displacements histories are used to form an $N \times M$ ensemble matrix \mathbf{Y} defined as follows:

$$\mathbf{Y} = \begin{bmatrix} y_1(t_1) & y_2(t_1) & \cdots & y_M(t_1) \\ y_1(t_2) & y_2(t_2) & \cdots & y_M(t_2) \\ \vdots & \vdots & \ddots & \vdots \\ y_1(t_N) & y_2(t_N) & \cdots & y_M(t_N) \end{bmatrix}, \quad (5.1)$$

where each row represents a point in the measurement space at a particular instant in time. In order to perform the proper orthogonal decomposition, we need to construct the $M \times M$ correlation matrix \mathbf{R} :

$$\mathbf{R} = \frac{1}{N} \mathbf{Y}^T \mathbf{Y} \quad . \quad (5.2)$$

Since \mathbf{R} is real and symmetric, its eigenvectors are orthogonal. The eigenvalue problem writes as follows:

$$\mathbf{R}\mathbf{v} = \lambda\mathbf{v} \quad , \quad (5.3)$$

where the eigenvectors \mathbf{v} represent the proper orthogonal modes (POMs) and the eigenvalues λ represents the proper orthogonal values (POVs). The POMs represent the principal axes of inertia of the data in the measurement space, and the POVs indicate the mean

squared values of the data in the directions of the corresponding POMs (Feeny, 2002; Feeny and Kappagantu, 1998). POVs can also be seen as the signal power associated with the corresponding POMs.

The dynamics of the system can be decomposed into modal coordinates by using the POMs as basis functions. To this end, we can define a proper orthogonal matrix \mathbf{V} made of the vectors of the proper orthogonal modes:

$$\mathbf{V} = [\mathbf{v}_1, \dots, \mathbf{v}_M] \quad . \quad (5.4)$$

Using the proper orthogonal modes we can now reconstruct the displacements as follows:

$$\mathbf{y}(t) = \sum_{i=1}^M q_i(t) \mathbf{v}_i = \mathbf{q}(t) \mathbf{V}^T \quad , \quad (5.5)$$

where $\mathbf{q}(t)$ represents a modal coordinates (row) vector depending on time. As such, the ensemble matrix \mathbf{Y} can be written as follows:

$$\mathbf{Y} = \mathbf{Q} \mathbf{V}^T \quad , \quad (5.6)$$

where \mathbf{Q} is an ensemble of Proper Orthogonal Coordinates (POCs). For the orthogonality condition we can write (if \mathbf{V} is normalized) that $\mathbf{V}^T \mathbf{V} = \mathbf{I}$. Thus we can extract the POCs histories $q_i(t)$ from the original displacement matrix \mathbf{Y} via:

$$\mathbf{Q} = \mathbf{Y} \mathbf{V} \quad . \quad (5.7)$$

Each modal coordinate represents the dynamics in the axis of a corresponding POM and the mean squared value of this modal coordinate is the associated POV.

The previous equation allows us to calculate the Proper Orthogonal Coordinates of the system given any possible Proper Orthogonal Modes Matrix. In other words this is equivalent to compute the temporal evolution of the system if we imagine that it follows a given spatial evolution, represented by the given POMs.

The technique above discussed above will be used in order to perform a dynamic analysis of the behaviour of the fuel bundle during the two different experiments.

5.3.2 Application of POD Technique to GWU Experimental Data

In this section the application of the POD technique to the datasets previously analysed is discussed. This technique will give us better insight on the dynamics of the fuel bundle and, as consequence, we could be able to understand the nature of the perturbations observed in the fluid flow.

The POD technique is used in order to perform an orthogonal decomposition of the vibration modes of the fuel bundle in the experimental conditions "Case 1" and "Case 2". Figures 5.10, 5.11 represent the Proper orthogonal Modes and Proper Orthogonal Values respectively for "Case 1" and "Case 2". For both cases, the first mode corresponds

5.3. POD AND PROJECTION ON THEORETICAL MODES FOR GWU DATASET

to the first mode of the clamped-clamped Bernoulli beam, while higher modes presents different shapes, which are not directly recognizable as known examples in literature. The POVs values (Figures 5.10b,5.11b) indicate that the first mode contribution is two order of magnitude more important than the second one, while the third and fourth modes are negligible in intensity, compared to the first one.

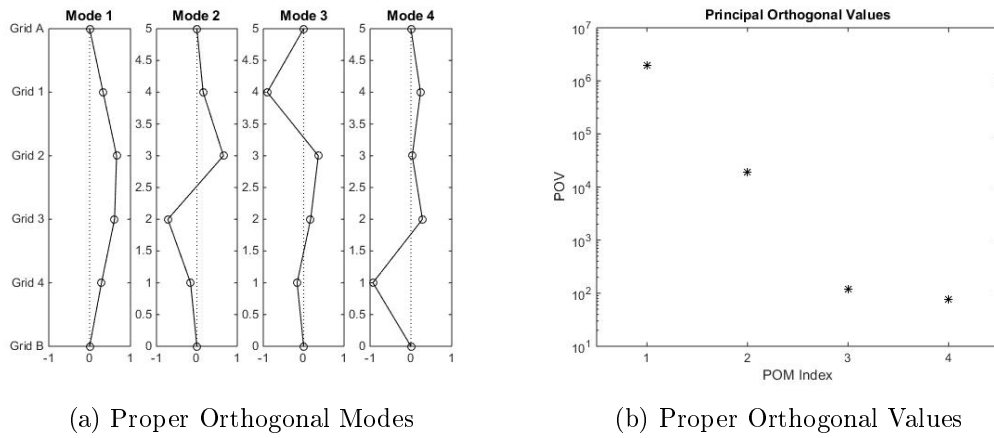


Figure 5.10 – POMs and POVs for dataset "Case 1"

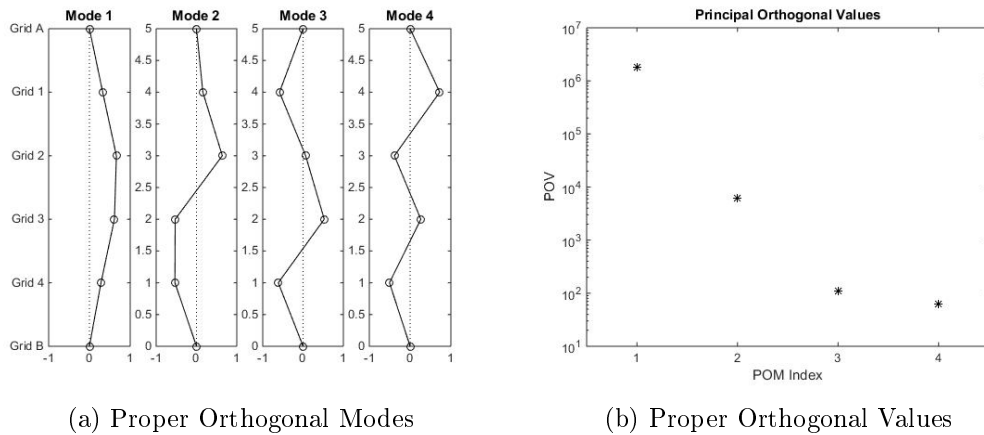


Figure 5.11 – POMs and POVs for dataset "Case 2"

The weight of the different proper orthogonal mode was expected, since the excitation frequency of the structure is 1.3 Hz , which is really close the first resonance frequency of the fuel bundle ($\sim 1.2 \text{ Hz}$). The two data sets, which have the same input parameters should present the same Proper Orthogonal Modes, but the modes higher than the first one are significantly different. It is not easy to explain the reason behind such differences. A first guess could be that the shaking table inserts some different frequencies in the excitation process, but from analyses made in Section 5.2.2 this guess is excluded. A second guess is that the temperature conditions could have changed between the two different experiments, affecting the results of the experimental campaign.

Anyway, the differences remarked on the Proper Orthogonal Modes on the two datasets

are very small on amplitude, since as already said, second, third and fourth modes only affect 1% of the behaviour of the fuel bundle. Thus it is difficult to believe that the flow patterns, which are very different between "Case 1" and "Case 2" (Section 5.2.1) are justified from such a small differences in the fuel bundle dynamics.

In order to verify if such a small perturbation in the high modes of the structure can affect in a very significant way the induced axial flow, the potential flow model, developed during the PhD, and presented in Chapter 3 is used to simulate the experimental structure undergoing different deformation patterns. Since the simulation are performed using a simplified model, the structure should be modelled with simple Euler-Bernoulli boundary conditions. Since the first mode shape of the POD looks symmetric, a first guess has been to use a clamped clamped Bernoulli beam. Thus the calculations are performed using the natural mode shapes, and the temporal evolution of each mode has been calculated with a "projection" on the natural mode shapes.

Natural Mode Shapes

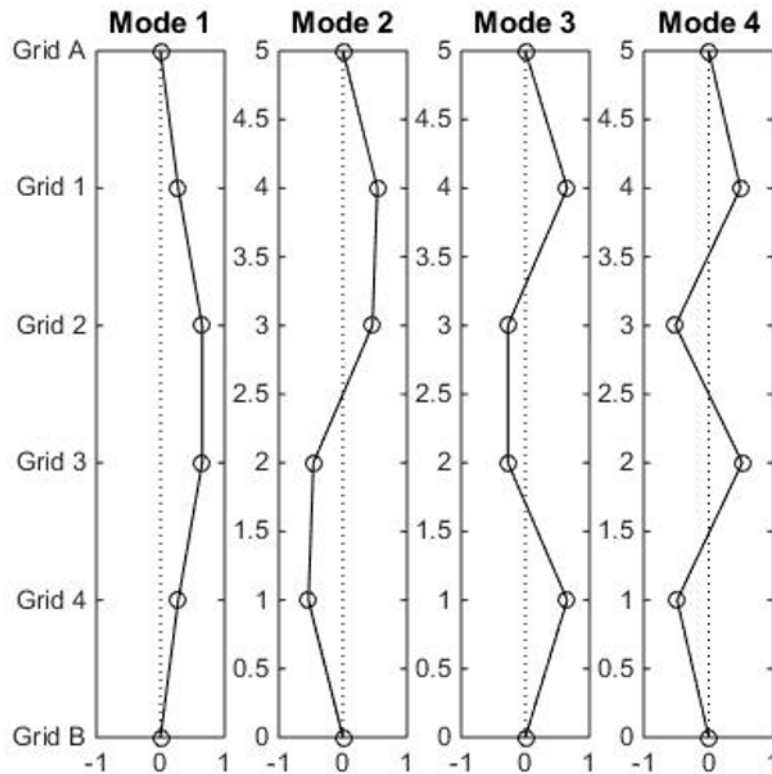


Figure 5.12 – Mode Shapes for Clamped-Clamped Beam

The assumption that the bundle behaves as a Bernoulli beam with clamped-clamped boundary conditions has been made. This assumption will be further discussed at the end of this chapter. Such a system is well known in literature and we can mathematically

5.3. POD AND PROJECTION ON THEORETICAL MODES FOR GWU DATASET

calculate its natural frequencies and mode shapes. The shape function for the n^{th} natural mode is represented by the following equation (Eisley and Waas, 2011):

$$\Phi_n(z) = \cosh(A_n \frac{z}{L}) - \cos(A_n \frac{z}{L}) - \frac{\cos(A_n) - \cosh(A_n)}{\sin(A_n) - \sinh(A_n)} [\sinh(A_n \frac{z}{L}) - \sin(A_n \frac{z}{L})] \quad , \quad (5.8)$$

where L represent the total length of the beam and the values A_n are presented in Table 5.2 for the first four natural modes. The values allowing to sketch the first four normal mode shapes for a clamped-clamped Euler-Bernoulli beam with four measurement point are listed in Table 5.3. The first four normal mode shapes for a clamped-clamped Euler-Bernoulli beam are represented in Figure 5.12.

n	1	2	3	4
A_n	4.73	7.8532	10.9956	14.1372

Table 5.2 – A_n values for Clamped-Clamped beam

Mode	1	2	3	4
Grid A	0	0	0	0
Grid 1	0.277	0.537	0.657	0.486
Grid 2	0.651	0.460	-0.272	-0.513
Grid 3	0.651	-0.460	-0.272	0.513
Grid 4	0.277	-0.539	0.657	-0.486
Grid B	0	0	0	0

Table 5.3 – Natural mode shapes for Clamped Clamped Beam with four measurement points

Using Equation 5.8 we are now able to compute the mode shape matrix \mathbf{V}_{Theo} for a clamped clamped beam:

$$\mathbf{V}_{Theo} = \begin{bmatrix} 0.277 & 0.537 & 0.657 & 0.486 \\ 0.651 & 0.460 & -0.272 & -0.513 \\ 0.651 & -0.460 & -0.272 & 0.513 \\ 0.277 & -0.539 & 0.657 & -0.486 \end{bmatrix} \quad , \quad (5.9)$$

where it has to be noticed that \mathbf{V}_{Theo} matrix does not consider the top and bottom grids which do not move.

Even if the \mathbf{V}_{Theo} matrix does not correspond from a theoretical point of view to the POM matrix (defined in the previous Section), it can be proven the matrix to be almost orthogonal. By definition, if a matrix is orthogonal, it must be $X^T X = X X^T = I$. Once this definition is applied to the mode shapes matrix, one obtains:

$$\mathbf{V}_{Theo}^T \mathbf{V}_{Theo} = \begin{bmatrix} 1.0329 & -0.0007 & 0.0039 & -0.0173 \\ -0.0007 & 0.9726 & -0.0230 & -0.0030 \\ 0.0039 & -0.0230 & -0.9726 & 0.0002 \\ -0.0173 & -0.0030 & 0.0002 & 1.0351 \end{bmatrix} . \quad (5.10)$$

It can be thus assumed (with an error smaller than 3%) the \mathbf{V}_{Theo} matrix to be orthogonal. Now, a projection of the system on the theoretical orthogonal modes of a Bernoulli clamped-clamped beam can be written as:

$$\mathbf{Q}_{Theo} = \mathbf{Y} \mathbf{V}_{Theo} \quad , \quad (5.11)$$

where \mathbf{Y} represents the measurement matrix of the bundle displacements on the 4 different locations, as specified before.

The time histories for the two data sets can be now calculated. Once again one can remark that differences can be outlined on the second, third and fourth mode, which influence less than 5% of the overall behaviour of the fuel bundle (Figure 5.13). The amplitudes of time histories for each mode are listed in Table 5.4 and the phase shift between each mode is listed in Table 5.5. The biggest differences on the dynamic behaviour between the two cases are in the phase shift between the different modes and on the 4th mode shape amplitude.

Amplitude	"Case 1"	"Case 2"
Mode 1	2.6 mm	2.5 mm
Mode 2	0.25 mm	0.18 mm
Mode 3	0.18 mm	0.15 mm
Mode 4	0.15 mm	0.03 mm

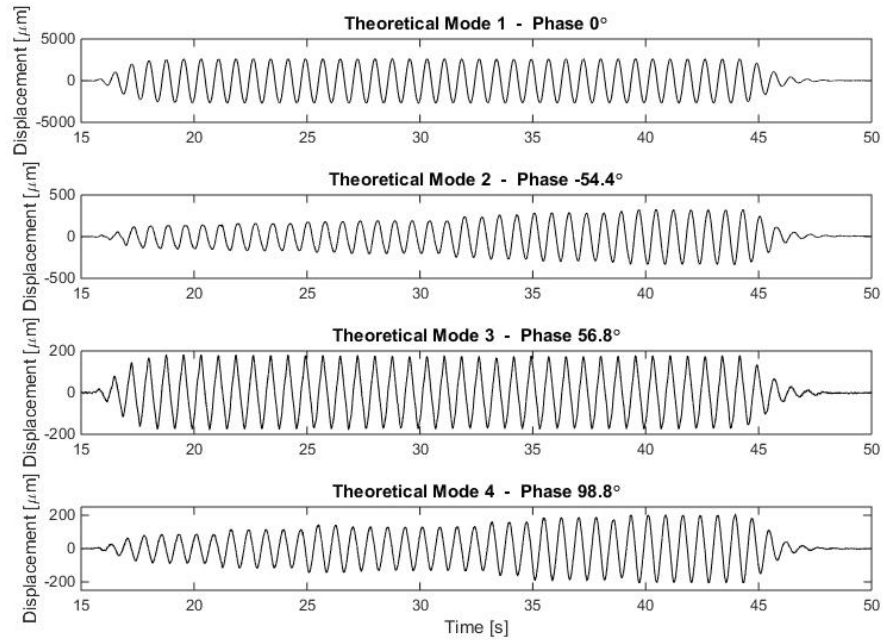
Table 5.4 – Time history amplitudes for two test cases

Phase Shift	"Case 1"	"Case 2"
Mode 1	-	-
Mode 2	-54.4°	-46.3°
Mode 3	56.8°	68.2°
Mode 4	98.8°	-176.8°

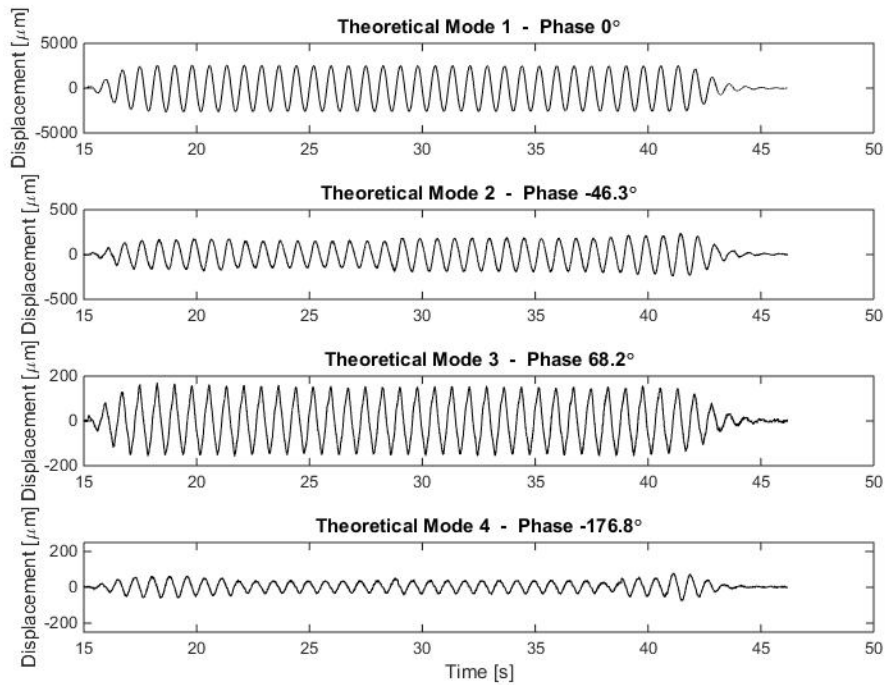
Table 5.5 – Time history phase shift respect to the first mode for two test cases

The calculated temporal evolution will be used in the next section for reconstructing the temporal behaviour of the simulated data using clamped-clamped Bernoulli beam proper modes.

5.3. POD AND PROJECTION ON THEORETICAL MODES FOR GWU DATASET



(a) Time history "Case 1"



(b) Time history "Case 2"

Figure 5.13 – Time history on natural modes projection

5.4 Numerical Simulations

The finite element code implemented in FreeFem++, based on the potential flow model discussed in Chapter 3 is now used in order to simulate the behaviour of the fluid flow around the fuel bundle under the horizontal excitation applied by the shaking table.

5.4.1 Single Cylinder 3D Geometry

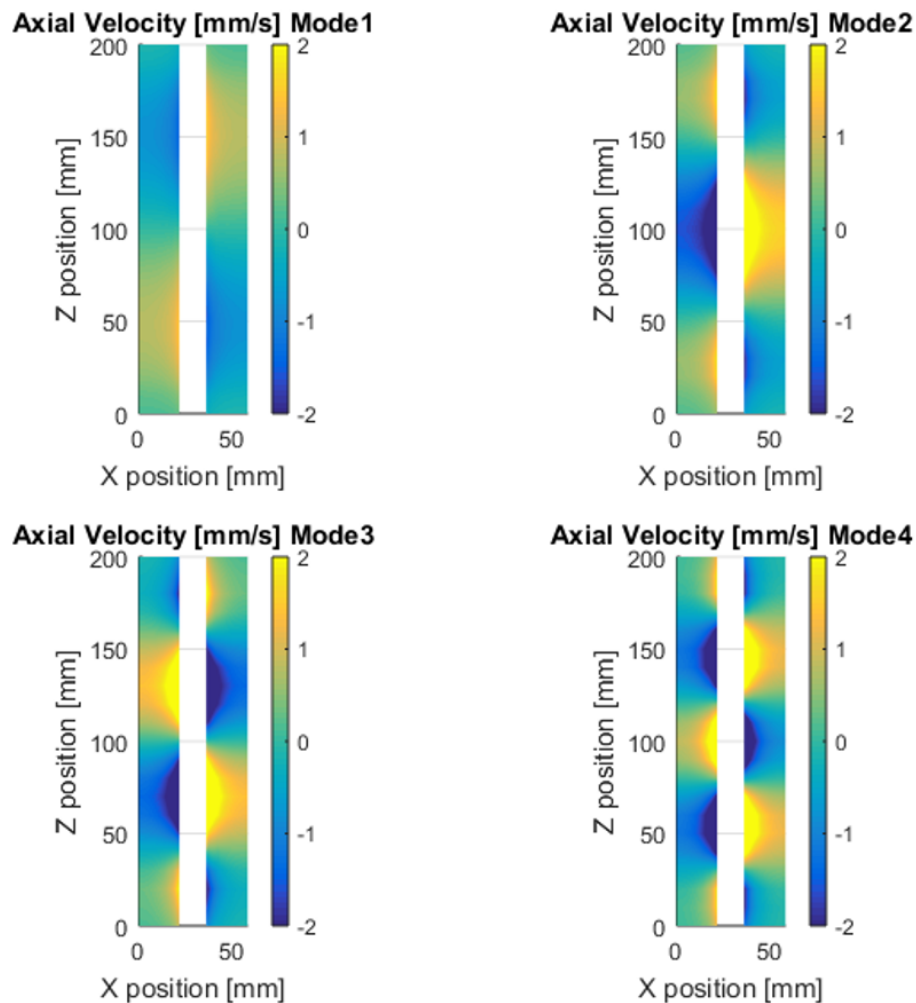


Figure 5.14 – Axial velocity for a single cylinder undergoing 4 different modes displacement ($t = 0$)

Since the implementation of the complete geometry of the GWU facility would have required an important effort, a first exercise has been done in order to understand if the effort was worth it or not. Thus a single cylinder geometry has been implemented and calculations are performed for the simulation of a cylinder deflecting as a clamped clamped Euler Bernoulli beam. The amplitudes of each mode are considered to be the

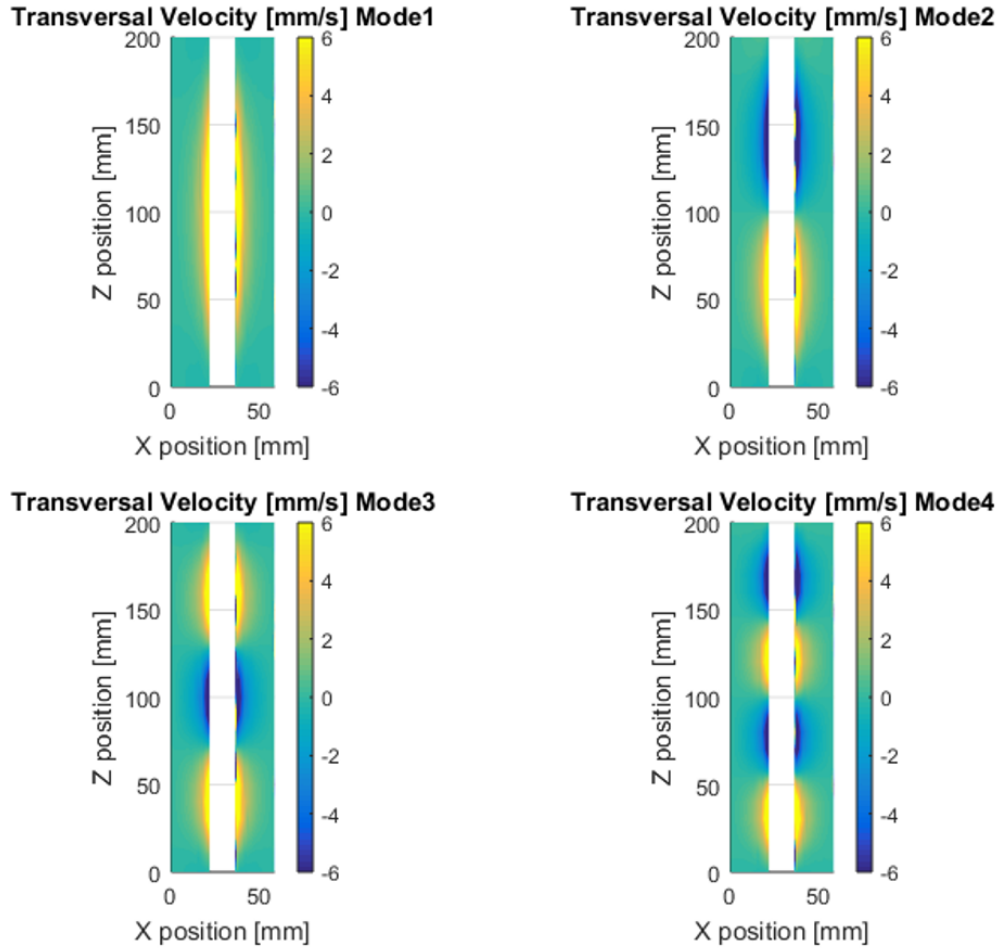


Figure 5.15 – Transversal velocity for a single cylinder undergoing 4 different modes displacement ($t = 0$)

same. These calculations allowed to understand the importance of the deflection shape on the perturbation of the water flow.

The results, represented in Figure 5.14 show that the axial velocity field of the fluid is more important for higher modes than for lower modes (given the same amplitude of deformation). This observation can be explained by the gradients on the surface of the cylinder. In fact, higher modes imply more bending of the structure, and since the amplitude must be the same, it means that the vertical gradient of the structure deflection ($\partial_z w$) is more important for higher modes than for lower ones. The vertical gradient of the deformation drives the perturbation of the fluid domain, as expressed by the impermeability condition (see Equation 3.14).

It can be noted that the calculations give a velocity profile which is not physically meaningful close to walls since the axial velocity profile does not go to zero (adherence condition). This feature was expected since the model neglects viscous effects and the adherence condition is only due to viscous forces.

Figure 5.15 represents the transversal velocity field due to the cylinder displacement. Unlike what happens for the axial velocity, the order of magnitude for the transversal velocity field is the same for all modes. This is expected, since the transversal velocity field is induced by the velocity of the cylinder surface, and not by the gradient of its surface deformation. It can also be remarked that the transversal velocity field is much more important than the axial one (3 times stronger).

These observations lead to the conclusion that deformations having high modes contributions will perturb the axial fluid velocity field in a more important way than deformation with only low modes contributions. Therefore, for the experimental application of GWU dataset, this means that the differences observed for the 3rd and 4th modes (even if they are relatively small) can contribute in a significant way to the pressure perturbation around the bundle. After these consideration we can affirm that it is worth the effort to simulate the behaviour of the whole fuel bundle, in order to understand the reasons why the fluid velocity field in "Case 1" and "Case 2" present important differences even if the bundle appears to move in a quite similar way. Only axial velocity calculations will be treated, since the transversal profiles seem to be similar between "Case 1" and "Case 2" In the next paragraph the results related to the GWU bundle geometry will be illustrated.

5.4.2 Complete 3D Geometry

The 3D geometry of the whole structure of the internal tank is implemented in the code. The spacer grids are also implemented, but their geometry has been strongly simplified: springs and dimple are not considered in the model. The supports holding the top and bottom grids to the tank are neglected as well. These simplifications are considered to be legitimate, since we are only interested in the fluid behaviour, which is mainly influenced by the moving surfaces. The dynamic behaviour of the fuel bundle is considered as an entry parameter for our calculations, and it will be given by the POD analysis of the experimental data discussed in Section 5.3.2.

Since the 3D geometry results to be quite complicated and time consuming in order to be built (~ 0.5 hours), the strategy adopted has been to split in two different parts the geometry construction and the fluid equation resolution. The bundle is supposed to move following the four proper orthogonal modes of a clamped-clamped beam. For each mode, one period of oscillation has been reproduced ($T = 1/1.3 \text{ Hz} = 0.77 \text{ s}$). The period has been divided into 77 different time steps ($\sim 0.01 \text{ s}$ for each time step). Thus meaning for each mode shape, and for each time step the deformed geometry of the fuel bundle has been constructed. Once the library of the whole deformed geometries is constructed, the calculation of the fluid velocity field is performed. One example of a section of the 3D geometry is represented in Figure 5.16. Figure 5.17 represents the meshing; only the fluid domain is meshed for the calculations.

After some analysis on the convergence of the problem, it has been found that the deformation of the fuel bundle geometry (thus of all the surface meshes) does not guarantee

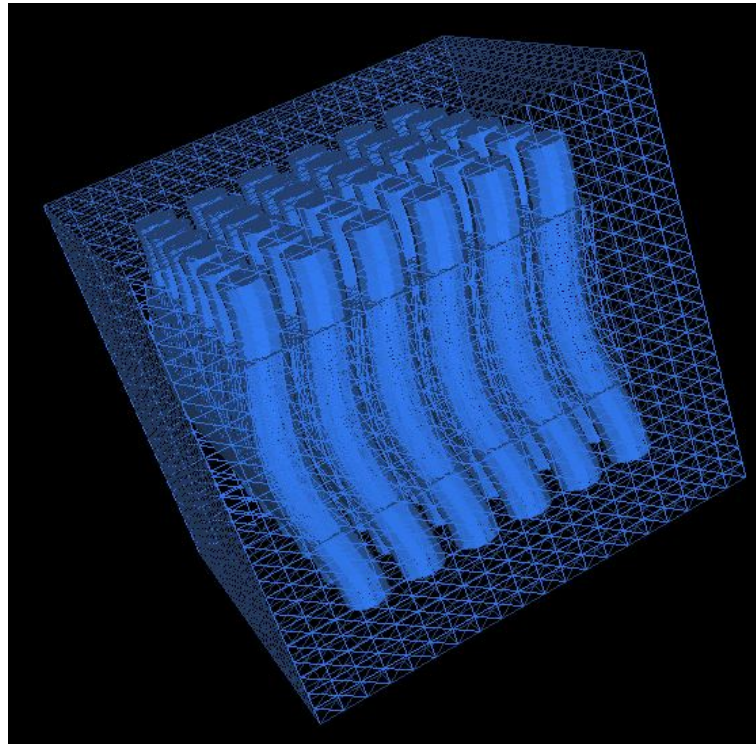


Figure 5.16 – Section of the 3D geometry of the fuel bundle implemented in FreeFEM++

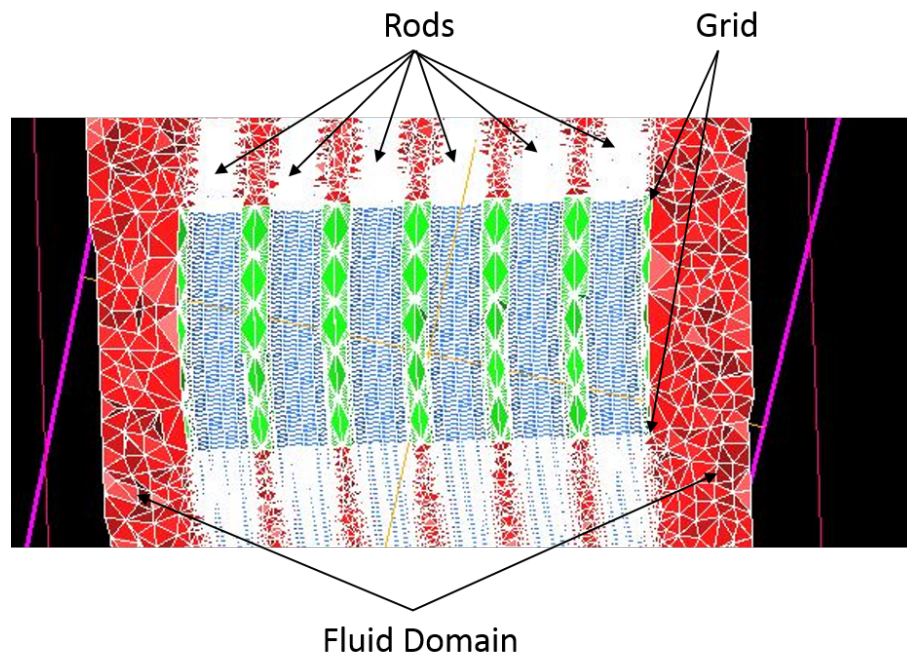


Figure 5.17 – Meshing section of the fuel bundle in FreeFEM++

the convergence of the solution. The problem has Neumann boundary conditions on the walls of the structure, thus the convergence results to be difficult.

In order to avoid this convergence problem, it has been decided to perform the calcula-

tions without the deformation of the geometry of the fuel bundle; the boundary conditions over the cylinders continue to respect the impermeability condition as before (assuming the cylinder surface moves). This approximation is found to introduce a very small error ($< 2\%$) on single cylinder geometry. In addition to that, in order to better control the geometries and the calculation, the geometry has been split into ten different sections on the vertical direction. A convergence study on the meshing size has been carried out, and it was found that the convergence is assured when at least 75000 cells are considered for the computations. With such an approximation, the problem converges in a very fast way (about 2 *min* with about 100000 cells). Anyway, since the whole domain is axially split into 10 sections, for each sections 77 time steps calculations need to be performed for 4 different mode shapes, the total computational time is about one hundred hours for a complete geometry.

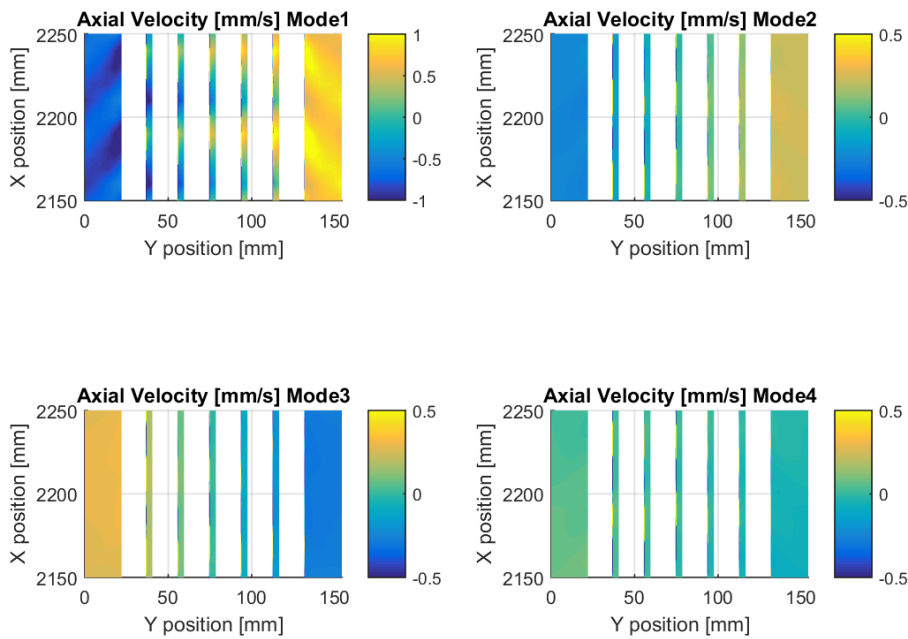


Figure 5.18 – Axial velocity field due to 4 modes on section $z = 33.5 \text{ mm}$, $2150 \text{ mm} < x < 2250 \text{ mm}$ for "Case 1" ($t = 0$)

Figure 5.18 and 5.19 show respectively a section of the axial flow velocity for "Case 1" and "Case 2". The view is a section performed in the middle of the second cylinder (the same level than the laser planes in the experimental facility, $z = 33.5 \text{ mm}$). For practical reasons, only the area around measurement plans is represented (x from 2150 mm to 2250 mm) at time instant $t = 0$. In analogy with the calculation performed for a single cylinder, it is shown that the axial velocity profile given by each mode does not respect the contribution of each mode given to the global dynamic behaviour of the structure.

5.4. NUMERICAL SIMULATIONS

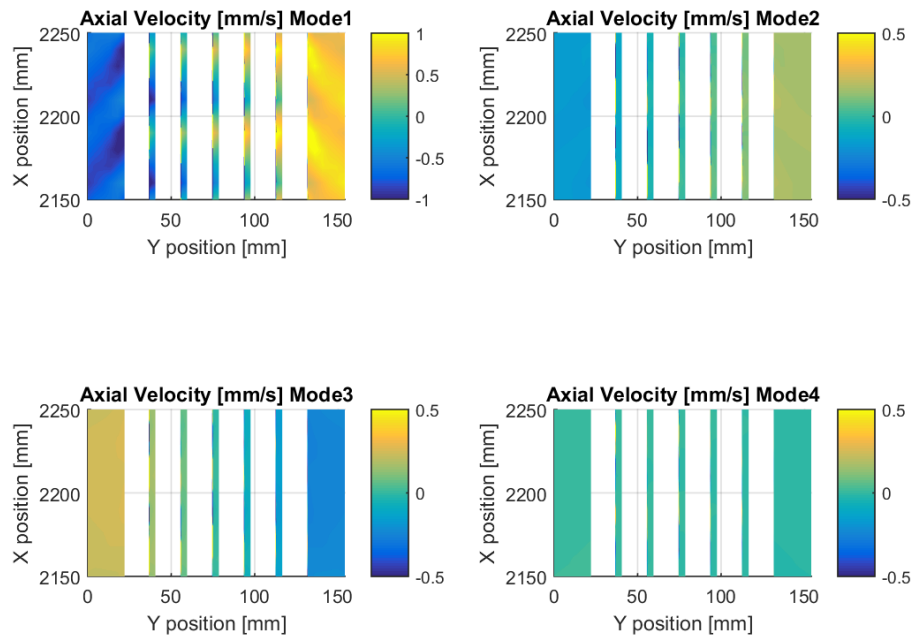


Figure 5.19 – Axial velocity field due to 4 modes on section $z = 33.5 \text{ mm}$, $2150 \text{ mm} < x < 2250 \text{ mm}$ for "Case 2" ($t = 0$)

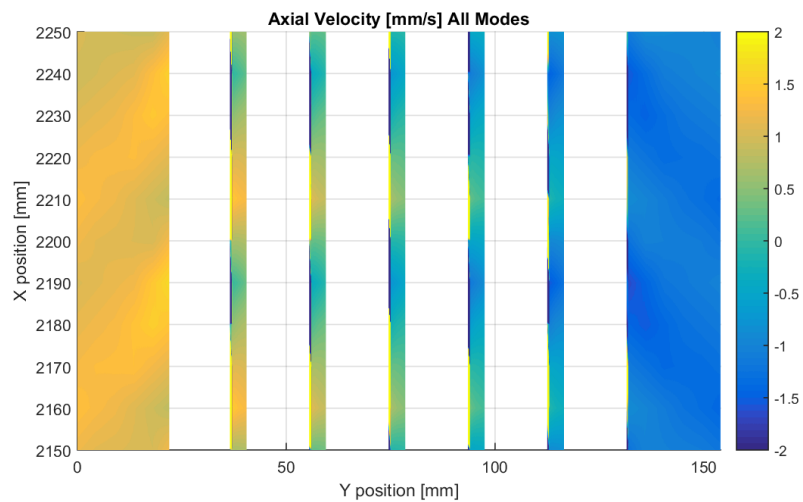


Figure 5.20 – Global axial velocity field on section $z = 33.5 \text{ mm}$, $2150 \text{ mm} < x < 2250 \text{ mm}$ for "Case 1" ($t = 0.45 \text{ s}$)

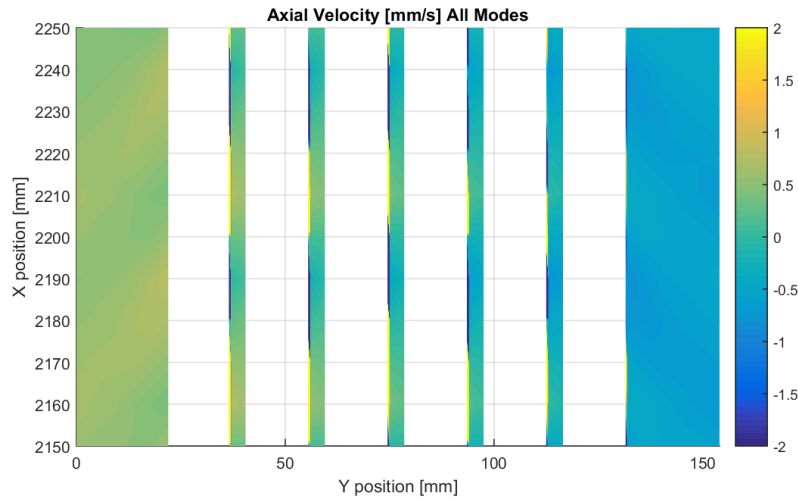


Figure 5.21 – Global axial velocity field on section $z = 33.5 \text{ mm}$, $2150 \text{ mm} < x < 2250 \text{ mm}$ for "Case 2" ($t = 0.45 \text{ s}$)

Table 5.6 and 5.7 contain the ratios between the displacement amplitudes of each mode with respect to the first one, and the ratios between the axial velocity amplitude of each mode with respect to the first one. It can be noted that the axial velocity ratios are strongly different to the displacement one. This confirms once again that the mode shapes strongly affect the axial velocity field. In addition to that, a diagonal pattern on the axial velocity can be remarked (especially on the first mode). This behaviour could be due to the cylindrical shape of the cylinder, which induces flows also on the z direction, giving rise to a kind of diffraction pattern (cylinders are arranged in a squared lattice). Another important remark has to be done on the phase shift of the different proper modes of the structure. For the two experimental data sets, the phase shift are completely different. This will strongly influence the global behaviour of the axial velocity field, which strongly depends on how the different modes are combined together.

Case 1	"Displacement Amplitude"	"Axial Velocity Amplitude"
1 st /2 nd Mode	10.4	~ 4
1 st /3 rd Mode	14.4	~ 2
1 st /4 th Mode	17.3	~ 10

Table 5.6 – Amplitude ratios for displacement and axial velocity - "Case 1"

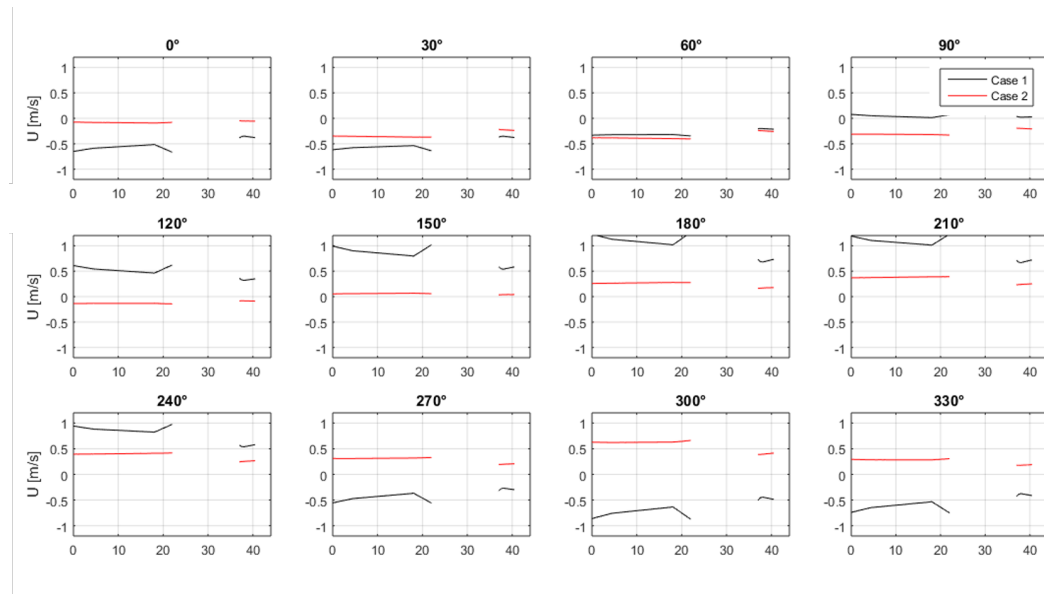
The global axial flow is then reconstructed for the two cases taking into account the values for the amplitudes and phase shift listed in Table 5.4 and 5.5. Global axial flows are reported in Figures 5.20 and 5.21. For each case, the time shot corresponding to the

Case 2	"Displacement Amplitude"	"Axial Velocity Amplitude"
1 st /2 nd Mode	13.8	~ 5
1 st /3 rd Mode	16.6	~ 3
1 st /4 th Mode	83.3	~ 20

Table 5.7 – Amplitude ratios for displacement and axial velocity - "Case 2"

maxim axial velocity amplitude (0.45 s for "Case 1" and 0.65 s for "Case 2) was plotted. It can be noticed that even if the amplitudes of the axial velocity field are quite similar for the two test cases (for the four modes), the global behaviour is strongly different for the two cases. Axial velocity amplitude is about ten times smaller for "Case 2" than for "Case 1". Such a difference cannot be explained by the amplitude difference for each mode; it can only be explained by the cumulated effects of different modes with different phase shifts. In one case ("Case 1") the phase shift of each mode gives raise to a constructive interaction, while in the other case ("Case 2"), it gives raise to a destructive interaction.

This observation is in agreement with the experimental results. In Figure 5.8 it can be remarked that the experimental axial velocity amplitude for "Case 2" is much smaller than that for "Case 1". The ratio of the two experimental velocity profiles is found to be about 8. Numerical results thus match with good approximation the experimental results.

Figure 5.22 – Axial velocity profiles on section $z = 33.5 \text{ mm}$, $x = 2200 \text{ mm}$ for "Case 1" and "Case 2"

In order to have a better comparison with experimental data, the axial flow velocity for a single line ($x = 2200 \text{ mm}$) has been plotted in Figure 5.22 for both "Case 1" and "Case 2". Furthermore the temporal evolution for the axial velocity profiles (both numerical and experimental) for the two cases are represented in Figure 5.23. The ratio between the axial velocity for "Case 1" and "Case 2" is respected, while the magnitude of the axial velocity is different between numerical data and experimental ones.

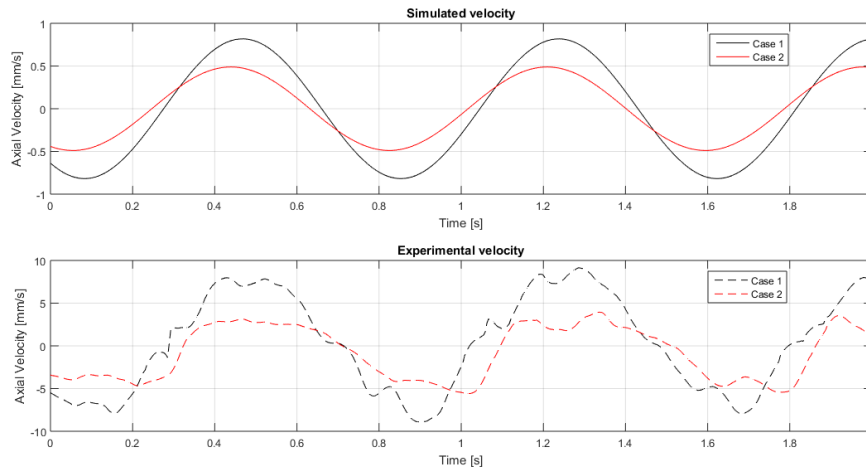


Figure 5.23 – Temporal evolution of axial velocity profiles on point $x = 2200 \text{ mm}$, $y = 10 \text{ mm}$, $z = 33.5 \text{ mm}$ for experimental and numerical "Case 1" and "Case 2"

These calculations seem to find a hint to the difference in the measured axial flow which was not expected. The small differences on the mode shapes induce important differences in the axial velocity field, and the differences on the phase shift induce very different interactions between modal axial flow, which can result to complete different velocity fields.

Further investigation would be needed in order to understand the reasons of such differences on the phase shift. The underestimation of the numerical calculations for the axial velocity should be investigated as well.

5.5 Analysis and Conclusions

In this chapter, an application of the fluid structure interaction model based on the potential flow theory is presented. The model is used to simulate the behaviour of the experimental facility of GWU Thermo Fluid Lab. The experimental campaigns on this experimental mock up gave some unexpected results on the measured axial flow velocity for two different experiments with the same input parameters. The model is thus used in order to try to explain the observed phenomena. A first analysis performed on the POD of the fuel bundle shows a few differences on the 4th mode, which at the beginning were thought to be negligible.

After the calculations were performed with the developed model, the outcomes show how the higher modes are the ones affecting the most the axial flow velocity field. This phenomenon is explained with a consideration on the shape of the different modes; higher modes have more bending, meaning that the gradient of the displacement along the axial direction is more important. Since the displacement gradient induces a pressure perturbation around the structure, it explains why higher modes contribute in a more significant way to the axial velocity field.

It is still to be explained the reason why the fuel bundle moves in different ways between "Case 1" and "Case 2", given that input parameters (shaking table excitation) are the same. One parameter which could have affected the measurements is the temperature. The temperature of the room and of the fluid loop are not controlled (but they are measured). Room temperature for "Case 2" has been measured to be 7 *K* higher than for "Case 1". Since the structure is made of two acrylic cases held by a metal structure, the temperature difference can lead to a prestress on the structure. Using the material properties, the differential elongation between the case and the structure can be found by:

$$\Delta L_{diff} = \Delta L_{acrylic} - \Delta L_{steel} = L\Delta T(\alpha_{acrylic} - \alpha_{steel}) \simeq 0.0015 \text{ m} \quad , \quad (5.12)$$

where $\alpha_{acrylic} \simeq 65 \text{ m/mK}$ and $\alpha_{steel} \simeq 12 \text{ m/mK}$ are the linear thermal expansion coefficients for the acrylic case and for the steel structure respectively and $L = 4 \text{ m}$ is the total length of the structure.

Thus, with a 7 *K* difference the acrylic structure undergoes a compression of about 1.5 *mm*. Such a compression can contribute in a significant way to the reduction of the global stiffness of the structure, thus it will affect the dynamic behaviour of the fuel bundle.

Furthermore, the assumptions made for the modelling of the structure are analysed. In a first approximation the bundle is supposed to behave as a clamped-clamped Euler Bernoulli beam. Some analysis on the whole structure shows that the external structure affect the behaviour of the bundle, and there is a phase lag between the top and the bottom of the external structure. Thus, it would be more adequate to model the bundle

as a clamped-free structure (with an imposed displacement in the top). In addition, the relative displacement between the tank walls and the bundle should be taken into account: even if the relative displacement is small, the walls of tank are solid and they induce the whole fluid to move. This can explain why the model underestimates the axial flow.

Some efforts should be spent in the future in order to take into account previous considerations. Further simulations could provide better insights on the involved phenomena.

Conclusions & Perspectives

This final Chapter is a recapitulation of the work presented in this document. The main outcomes of the PhD are presented and a discussion will be opened on perspectives.

Conclusions

The work presented in this document represents a contribution to the study of vibrational behaviour of a PWR fuel assembly. Two main approaches had been followed during this PhD work. A modelling approach led to the development of a simplified model for fluid structure interactions in PWR assembly. A complementary experimental approach allowed to realise several experimental campaigns on the recently designed experimental facility ICARE. The two approaches are considered complementary since the modelling approach needs the experiments for the validations, and the experimental approach needs good modelling in order to have a solid analysis of the observed phenomena.

Most of the subjects treated in this PhD work were introduced within the bibliographic review, including fluid structure interaction models for general applications. Simplified models were discussed focusing on their advantages of flexibility and reduced computational time. Such simplified models, can be used for parametric simulations allowing to perform a sensitivity analysis on different parameters, which could result in too expensive calculations using complex models.

The ICARE experimental facility for the study of fluid structure interactions on fuel assemblies was presented after a brief review of previous experiences in this domain. ICARE facility allows to host up to four fuel assemblies (half scale) and to excite one of them. The dynamic behaviour of the excited fuel assembly has been investigated and modal parameters (mass, damping, stiffness) were identified. Non linearities have been identified due to the presence of supporting grids. The presence of water flow does affect mainly the mass parameters, while stiffness and damping show smaller, but not negligible, changes. The analysis of coupling between the excited assembly and the other ones confirmed, as expected, that the presence of water flow induces coupling forces between different fuel assemblies. The increase of water flow induces a static coupling and an increase of the coupling forces. Coupling also increases when the confinement size is reduced. Coupling phenomena are observed, with different magnitudes, on all the three non excited assemblies. The analysis of LDV measurements allowed to compare the coupling force with the induced

CONCLUSIONS & PERSPECTIVES

oscillating axial flow. Coupling and oscillating axial flow do not show the same behaviour with respect to the excited frequencies. Experimental data have been later used in order to validate the modelling approach.

Another fundamental aspect of this PhD work is related to the development of a simplified model for fluid structure interactions on fuel assemblies. Potential flow theory was presented putting stress on the advantage that fluid structure interaction forces can be directly written as a function of the displacement of the structure itself. This result is an important achievement since it allows to drastically reduce computational time, avoiding to solve fluid equations. As a drawback it should be considered that the assumption of potential flow lead to the complete negligence of the fuel grids, which introduce vorticity in the flow.

Calculations with potential flow model are performed for single cylinder and multiple cylinders geometries. Confinement size have different effects on interaction forces depending on the considered wavenumber. Coupling forces between the cylinders depends on the wavenumbers and a threshold behaviour has been outlined. The coupling increases with the wavenumber up to a certain threshold, and once the threshold is overcome, coupling force decreases due to inefficient propagation of the pressure perturbations. The importance of symmetries for the presence of out-of-plane coupling have been also identified. When the cylinders are arranged on two dimensional lattice, coupling effects on the non excited directions also appear.

Finally, in order to validate the model, calculations simulating the ICARE geometry are discussed and compared with experimental results. Modal parameters are identified as functions of the flow rates and compared with experimental ones. The model well fits experimental data for the added mass coefficient and qualitatively reproduces the added stiffness effect (which increases with the water flow rate). The added stiffness effect is underestimate for low flow rates, while it is underestimate by the model for large flow rates. Calculations for the added damping coefficient do not agree at all with experimental results. This result was expected since the model does not consider any viscous forces, which are the main source of damping effects. Simulations also allows to estimate the coupling forces between different assemblies. The model underestimates the coupling force between the excited assembly and the one which is in front of it, while it well reproduces out of plane coupling forces.

The comparison between numerical results and experiments allows to define the limits of such a potential flow model: it can reproduce added mass and added stiffness effect and it can only qualitatively predict coupling forces. It also predict qualitatively the effects of confinement size. Furthermore, as expected, the model cannot predict the presence of non-linearities and the effects of water temperature.

Finally, an application of the model to other experimental results is discussed. The model is used in order to simulate experimental data collected in the experimental facility installed at George Washington University. The model is able to reproduce some observed results related to non reproducibility effects. It demonstrated that small differences in high

modes deformations produce important effects on the induced axial flow. This application proved that the model is not only useful for prediction of the dynamical behaviour of the structural part, but it can also predict the water flow perturbations due to the motion of the structure. The model has been proven to be useful for some practical applications and to be flexible thanks to its low computational time.

Perspectives

Many perspectives are opened as a result of this PhD thesis either for modelling, numerical and experimental approaches.

As already discussed in Chapter 4 the model which has been implemented does not account for viscous forces. An improvement that would be of fundamental importance is to introduce with some empirical factor the viscous forces in the model. One possible way in order to introduce viscosity in the model is to consider the axial water flow as the sum of two flows: a potential bulk flow and a viscous flow which has a defined empirical distribution. In this way the viscous forces are taken into account with an empirical formulation, and it would be extremely interesting to assess the effects of such improvements, especially on the added damping coefficient estimation.

Further improvements could be carried out on the numerical implementation of the model. The iterations scheme illustrated in Chapter 3 could be implemented in order to have more accurate solutions. Furthermore, performed simulations only consider natural mode shapes for clamped-clamped Euler-Bernoulli beam. Effort could be spent in order to perform three dimensional calculations taking into account more complex mode shapes and also to consider the effects of the top and bottom ends of the cylinder which are actually neglected.

In relation to the application of the simulations to the GWU experimental facility, some improvements could be carried out in order to take into account a relative deflection between the lateral walls and the fuel assembly. The walls of the confinement tank, which are subjected to the shaking table excitations, also have a deflection which will induce an axial oscillation in the water flow. This displacement could be taken into account in the model and the effects of such improvement could be quantified in order to have a better understanding of the experimental results.

From the experimental point of view, different possibilities remain opened for further exploration. First of all, the huge amount of data which have been collected during the described experimental campaigns could be analysed in a more systematic way, and for instance the identification of parameters could be carried out for all the experiments. Furthermore, the deflection shapes of the fuel assemblies could be studied with application of POD methods.

As already introduced in Chapter 2 a PIV measurements campaign has been carried out on ICARE facility but they are not yet analysed due to time constraints. The analysis of PIV data could provide further understanding of the coupling phenomena. Both axial

CONCLUSIONS & PERSPECTIVES

and horizontal components of the water flow velocity could be compared with the coupling effects which are observed between the different fuel assemblies. Effects of turbulence could also be investigated with PIV measurements.

Moreover, it would be of fundamental interest to spend effort in order to experimentally investigate the effect of viscosity. It has been already discussed that on the ICARE facility some experiments have been performed with different temperatures in order to obtain different viscosities for the water flow. Unfortunately, changing the temperature of the water loop also affects the properties of the assemblies materials. Thus, the effects of viscosity could not be separated from the effects of the temperature on the rigidity of the structural materials. In order to avoid this problem, and to better investigate viscosity effects, some experiments could be designed by using different flowing fluids with similar densities but different viscosities. In this way the temperature would be kept constant, and the only effects of viscosity could be investigated.

Finally, a new experimental facility (EUDORE) has been recently designed. The EUDORE facility, which will replace the ICARE section, will use the same assemblies than used in ICARE. Three assemblies are arranged in a row and pre-deformation could be imposed to the assemblies. The peculiarity of this new facility is that the whole structure can be excited with an hydraulic system. For future projects, the results coming from this new experimental facility could be compared with the data collected on ICARE and the potential flow model could be used to perform calculations on this new geometry, taking into account viscosity effects (as already discussed above) and the motion of walls.

Bibliography

- Ackroyd, J., Axcell, B., and Ruban, A. (2001). Early developments of modern aerodynamics. *Butterworth-Heinemann*.
- Adrian, R. J. (1991). Particle-imaging techniques for experimental fluid mechanics. *Annual Review of Fluid Mechanics*.
- Albrecht, H. E., Damaschke, N., Borys, M., and Tropea, C. (2002). Laser doppler and phase doppler measurement techniques. *Springer Science & Business Media*.
- Amestoy, P., Guermouche, A., L'Excellent, J., and Pralet, S. (2006). Hybrid scheduling for the parallel solution of linear systems. *Parallel Computing*.
- Bauchau, O. and J.I., C. (2009). *Structural Analysis. Solid mechanics and its applications*. Springer.
- Berkooz, G., Holmes, P., and Lumley, J. (1993). The proper orthogonal decomposition in the analysis of turbulent flows. *Annual Review of Fluid Mechanics*.
- Boccaccio, E. (2010). DEDALE 1: Compte rendu de la campagne expérimentale de caractérisation mécanique sous écoulement d'un assemblage AFA3GL. *Rapport interne CEA DEN/CAD/DTN/STRI/LHC/2010/060*.
- Boccaccio, E. (2011). DEDALE 2: Compte rendu de la campagne expérimentale de caractérisation mécanique sous écoulement d'un assemblage AFA3GL - Effet du confinement. *Rapport interne CEA DEN/CAD/DTN/STRI/LHC/2011/027*.
- Boccaccio, E. (2012a). DEDALE 3: Compte rendu de la campagne expérimentale de caractérisation mécanique sous écoulement d'un assemblage AFA3GL - Sollicitations des modes pairs. *Rapport interne CEA DEN/CAD/DTN/STRI/LHC/2012/039*.
- Boccaccio, E. (2012b). DEDALE 4: Compte rendu de la campagne expérimentale de caractérisation mécanique sous écoulement d'un assemblage AFA3GL - Effet de la hauteur cavité coeur. *Rapport interne CEA DEN/CAD/DTN/STRI/LHC/2012/052*.
- Boccaccio, R. (2014). Etude expérimentale du comportement sous seisme de quatre assemblages combustibles a echelle reduite sur ICARE. *Master Thesis*.

BIBLIOGRAPHY

- Boutier, A. (2013). Laser velocimetry in fluid mechanics. *John Wiley & Sons*.
- Brennen, C. (1982). A review of added mass and fluid inertial forces. *Technical Report Naval Civil Engineering Laboratory*.
- Broc, D. (2001). Comportement sismique d'assemblage REP : influence du confinement hydraulique. *Note Technique DM2S/SEMT/EMSI/RT/01-046/A*.
- Broc, D., Queval, J., and Viallet, E. (2003). Seismic behaviour of a PWR reactor core: fluid structure interaction effects. *Transactions of the 17th SMiRT Conference*.
- Brochard, D. (1993). Synthèse et bilan de l'action bi-partite CEA-FRAMATOME sur l'analyse sismique des coeurs REP. *Rapport DMT/93/405*.
- Brochard, D., Ben Jedidia, A., Gantenbein, F., and Gibert, R. J. (1993). Dynamic modelling of PWR fuel assembly for seismic behaviour. *Proceedings of 12th SMiRT Conference*.
- Chen, S. (1985). Flow-induced vibration of circular cylindrical structures. *Hemisphere Pub. Corp.*
- Chen, S. and Wamnganss, M. (1972). Parallel-flow-induced vibration of fuel rods. *Nuclear Engineering and Design*.
- Clasen, P. (1972). Die 'hydrodynamische masse' eines rohres in einem rohrbündel. *Forshung im Ingenieurwesen Nuclear Engineering and Design*.
- Clement, S. (2012a). Réalisation de la boucle ICARE EXPERIMENTAL dans le cadre du projet assemblage. *Note interne CEA DEN/CAD/DTN/STRI/LHC/2012/05*.
- Clement, S. (2012b). Réalisation des maquettes d'assemblages combustibles de la boucle ICARE EXPERIMENTAL. *Note interne CEA DEN/CAD/DTN/STRI/LHC/2012/27*.
- Clement, S. (2014). Mise en oeuvre expérimentale et analyse vibratoire non-linéaire d'un dispositif à quatre maquettes d'assemblage combustibles sous écoulement axial. *PhD Thesis, Aix-Marseille Université*.
- Collard, B. (2000). ECHASSE, analyse des essais d'impact d'un assemblage sur une paroi, recherche d'un effet lame fluide. *Note Technique DEC/SH2C/LHC 2000-16*.
- Davis, T. (2003). UNFPACK version 5.4.0 user guide. *Journal of Computing and Information Science in Engineering*.
- De Lange, O. (1968). Optical heterodyne detection. *IEEE Spectrum*.
- De Langre, E., Paaïdoussis, M., Doaré, O., and Modarres Sadeghi, Y. (2007). Flutter of long flexible cylinders in axial flow. *Journal of Fluid Mechanics*.

- De Ridder, J., Degroote, J., Van Tichelen, K., and Vierendeels, J. (2013). Modal characteristics of a flexible cylinder in turbulent axial flow from numerical simulations. *Journal of Fluids and Structures*.
- De Ridder, J., Degroote, J., Van Tichelen, K., and Vierendeels, J. (2017). Predicting modal characteristics of a cluster of cylinders in axial flow: from potential flow solutions to coupled CFD-CSM calculations. *Journal of Fluids and Structures*.
- De Ridder, J., Doaré, O., Degroote, J., Van Tichelen, K., Schuurmans, J., and Vierendeels, J. (2015). Simulating the fluid forces and fluid-elastic instabilities of a clamped-clamped cylinder in a turbulent flow. *Journal of Fluids and Structures*.
- Divaret, L. (2014). Caractérisation des forces fluides s'exerçant sur un faisceau de cylindres oscillant latéralement en écoulement axial. *PhD Thesis, Ensta Paristech*.
- Divaret, L., Berland, J., Berro, H., Cadot, O., Doaré, O., and Moussou, P. (2013). Quasi-static approach of damping forces exerted upon a long cylinder oscillating in an axial flow. *ASME 2013 Pressure Vessel and Piping Conference*.
- Divaret, L., Cadot, O., Moussou, P., and Doaré, O. (2014). Normal forces exerted upon a long cylinder oscillating in an axial flow. *Journal of Fluid Mechanics*.
- Divaret, L., Moussou, P., Cadot, O., Berland, J., and Doaré, O. (2011). U-RANS simulation of fluid forces exerted upon an oscillating tube array in axial flow at large Keulegan-Carpenter numbers. *Bulletin Ercoftac*.
- Doaré, O., Mano, D., and Bilbao Ludena, J. C. (2011a). Effect of spanwise confinement on flag flutter: experimental measurements. *Physics of Fluids, American Institute of Physics*.
- Doaré, O., Sauzade, M., and Eloy, C. (2011b). Flutter of an elastic plate in a channel flow: confinement and finite-size effects. *Journal of Fluids and Structures*.
- Dong, R. (1978). Effective mass and damping of submerged structures. *US Department of Energy*.
- Drain, L. E. (1980). The laser doppler technique. *John Wiley & Sons*.
- Du Buat, P. (1786). Principes d'hydraulique. *Imprimerie du Monsieur*.
- Duarte, F., Gormaz, R., and Natesan, S. (2004). Arbitrary Lagrangian-Eulerian method for Navier-Stokes equations with moving boundaries. *Computer Methods in Applied Mechanics and Engineering*.
- Durst, F., Melling, A., and Whitelaw, J. H. (1976). Principles and practice of laser doppler anemometry. *Academic Press*.

BIBLIOGRAPHY

- Eisley, J. G. and Waas, M. (2011). *Analysis of Structures: an introduction including numerical methods*. John Wiley and Sons.
- Eloy, C., Doaré, O., Duchemin, L., and L., S. (2010). A unified introduction to fluid mechanics of flying and swimming at high reynolds number. *Experimental Mechanics*.
- Eloy, C., Lagrange, R., Souilliez, C., and Schouveiler, L. (2008). Aeroelastic instability of cantilevered flexible plates in uniform flow. *Journal of Fluid Mechanics*.
- Eloy, C., Souilliez, C., and Schouveiler, L. (2007). Flutter of a rectangular plate. *Journal of Fluids and Structures*.
- Feeny, B. F. (1997). Interpreting proper orthogonal modes in vibrations. *ASME Design Engineering Technical Conferences*.
- Feeny, B. F. (2002). On proper orthogonal co-ordinates as indicators of modal activity. *Journal of Sound and Vibration*.
- Feeny, B. F. and Kappagantu, R. (1998). On the physical interpretation of proper orthogonal modes in vibrations. *Journal of Sound and Vibration*.
- Fontaine, B. Polipopoulos, I. (1999). A non linear model for the PWR fuel assembly seismic analysis. *Nuclear Engineering and Design*.
- Fort, C., Fu, C. D., Weichselbaum, N. A., and Bardet, P. M. (2015). Refractive index and solubility control of para-cymene solutions for index-matched fluid-structure interaction studies. *Experiments in Fluids*.
- Fuhrmann, G. (1911). Theroretische und experimmentelle untersuchungen an ballon-modellen. *Jahrbuch 1911-12 des Motorslufschiff-Studiengesellschaft*.
- George, P. and Hecht, F. (1999). Handbook of grid generation. *CRC Press*.
- Glasston, S. and Sesonske, A. (1994). Nuclear Reactor Engineering. *Chapman and Hall*.
- Gloth, G. and Sinapius, M. (2004). Analysis of swept-sine runs during modal identification. *Mechanical Systems and Signal Processing*.
- Gosselin, F. and De Langre, E. (2011). Drag reduction by reconfiguration of a poroelastic system. *Journal of Fluids and Structures*.
- Guo, C. and Païdoussis, M. P. (2000). Stability of rectangular plates with free side-edges in two-dimensional inviscid channel flow. *Journal of Applied Mechanics*.
- Hecht, F. (1998). BAMG: Bidimensional Anisotropic Mesh Generator. *INRIA*. <http://www.freefem.org/ff++/ftp/freefem++doc.pdf>.
- Hecht, F. (2012a). Freefem++ v.3.19-1. *Universite Pierre et Marie Curie*. <http://www.freefem.org/ff++/ftp/freefem++doc.pdf>.

- Hecht, F. (2012b). New development in FreeFem++. *Journal of Numerical Mathematics*.
- Helen, J. Johansson, A. (1993). Non linear analyses of the buckling load and the eigenvalues in 17x17 PWR fuel assembly. *Proceedings of 12th SMiRT Conference*.
- Hess, J. and Smith, A. (1967). Calculation of potential flow about arbitrary bodies. *Progress in Aeronautical Sciences*.
- Houghton, L., Carpenter, P., Collicott, S., and Valentine, D. (2012). Aerodynamics for engineering students. *Elsevier*.
- Hussain, S. (2017). Analysis of flow induced by an oscillating fuel bundle. *GWU Master Thesis*.
- Imlay, F. (1961). The complete expression for added mass of a rigid body moving in an ideal fluid. *Technical Report, Hydromechanics Laboratory*.
- Jaiman, R., Parmar, M., and Gurugubelli, P. (2014). Added mass and aeroelastic stability of a flexible plate interacting with mean flow in a confined channel. *Journal of Applied Mechanics*.
- Johnson, M. A. (1983). Impacting of fuel assemblies in horizontal seismic analysis of reactor core. *Proceedings of ASME PVP Conference*.
- Kim, J. D. et al. (1981). Comparison of theoretical and experimental examinations on PWR fuel assemblies under external loads. *Proceedings of 6th SMiRT Conference*.
- Konstantinidis, E. (2013). Added mass of a circular cylinder oscillating in a free stream. *Proceeding of the Royal Society*.
- Kornecki, A., Dowell, E., and O' Brien, J. (1976). On the aeroelastic instability of two-dimensional panels in uniform incompressible flow. *Journal of Sound and Vibration*.
- Lamarsh, J. R. Baratta, A. J. (2001). Introduction to Nuclear Engineering. *Prentice-Hall*.
- Lamb, H. (1895). Hydrodynamics. *Cambridge University Press*.
- Lehoucq, R., Sorensen, D., and Yang, C. (1997). Arpack user's guide: solution of large scale eigenvalue problems with implicitly restarted Arnoldi methods. *Society for Industrial and Applied Math*.
- Leroux, J. C. et al. (1983). Structural analysis of PWR fuel assemblies in LOCA and seismic conditions. *Proceedings of 7th SMiRT Conference*.
- Liang, C., Liao, C., Tai, Y., and Lai, W. (2001). The free vibration analysis of submerged cantilever plates. *Ocean Engineering*.
- Lighthill, M. (1960a). Mathematics and Aeronautics. *The Journal of the Royal Aeronautical Society*.

BIBLIOGRAPHY

- Lighthill, M. (1960b). Note on the swimming of slender fish. *Journal of Fluid Mechanics*.
- Lighthill, M. (1971). Large-amplitude elongated-body theory of fish locomotion. *Proceedings of the Royal Society of London*.
- Lucey, A. and Carpenter, P. (1993). The hydroelastic stability of three-dimensional disturbances of a finite compliant wall. *Journal of Sound and Vibration*.
- Martert, R. and Seidler, M. (2001). Analytically based estimation technique for nonlinear dynamic problems. *International Journal of Solids and Structures*.
- Morison, J., Johnson, J., and Schaaf, S. (1950). The force distribution exerted by surface waves on piles. *Journal of Petroleum Technology*.
- Munk, M. (1924). The aerodynamics forces on airship hulls. *National Advisory Committee on Aeronautics*.
- Nakayama, A. and Patel, V. (1978). Calculation of the viscous resistance of bodies of revolution. *AIAA Journal*.
- Nuno, H., Mizuta, M., Kitade, K., and Saruyama, I. (1973). A method of colliding vibration analysis of PWR fuel assemblies under seismic conditions. *Proceedings of 2nd SMiRT Conference*.
- Païdoussis, M. P. (1966a). Dynamics of slender cylinders in axial flow: Part 1 Theory. *Journal of Fluid Mechanics*.
- Païdoussis, M. P. (1966b). Dynamics of slender cylinders in axial flow: Part 2 Experiments. *Journal of Fluid Mechanics*.
- Païdoussis, M. P. (1968). Stability of towed totally submerged flexible cylinders. *Journal of Fluid Mechanics*.
- Païdoussis, M. P. (1970). Dynamics of submerged towed cylinders. *Eighth Symposium of Naval Hydrodynamics: Hydrodynamics in the Ocean Environment*.
- Païdoussis, M. P. (1973). Dynamics of cylindrical structures subjected to axial flow. *Journal of Sound and Vibration*.
- Païdoussis, M. P. (1975). Dynamics of fuel strings in axial flow. *Annals of Nuclear Energy*.
- Païdoussis, M. P. (1979). The dynamics of clusters of flexible cylinders in axial flow: theory and experiments. *Journal of Sound and Vibration*.
- Païdoussis, M. P. (1987). Flow induced instabilities of cylindrical structures. *Applied Mechanics Reviews*.
- Païdoussis, M. P. (1998). *Fluid-structure interactions: slender structures and axial flow*. Elsevier Academic Press.

- Païdoussis, M. P. (2008). *Fluid-structure interactions: slender structures and axial flow*. Elsevier Academic Press.
- Païdoussis, M. P. and Pettigrew, M. (1979). Dynamics of flexible cylinders in axisymmetrically confined axial flow. *Journal of Applied Mechanics*.
- Païdoussis, M. P. and Suss, S. (1977). Stability of a cluster of flexible cylinders in bounded axial flow. *Journal of Applied Mechanics*.
- Païdoussis, M. P., Suss, S., and Pustejovsky, M. (1977). Free vibration of clusters of cylinders in liquid-filled channels. *Journal of Sound and Vibration*.
- Pisapia, S. (2004). étude du comportement vibratoire non-linéaire d'un assemblage combustible de réacteur à eau pressurisée. *PhD Thesis, Université de la méditerranée Aix-Marseille II*.
- Pont, T. (1998). Description du dispositif expérimental ECHASSE. *Note Technique DEC/SECA/LHC 98/028*.
- Preumont, A. et al. (1982). Seismic analysis of PWR-RCC fuel assemblies. *Nucl. Eng. Des.*
- Preumont, A. Van Steenberghe, T. (1981). Dynamic characteristics of PWR fuel assemblies. *Proceedings of 6th SMiRT Conference*.
- Queval, J. C. Brochard, D. (1988). Analysis of impact phenomena between PWR fuel assemblies in earthquake situations. *Proceedings of ASME PVP Conference*.
- Queval, J. (2002). Essais sismiques d'une rangée de 6 assemblage REP échelle 1. *Note Technique DM2S/SEMT/EMSI/RT/02-035/A*.
- Queval, J. C., Gantenbein, F., Brochard, D., and Ben Jedidia, A. (1991). Seismic behaviour of PWR fuel assemblies model and its validation. *Proceedings of 11th SMiRT Conference*.
- Queval, J. C., Porte, J., and Boisliveau, S. (1990a). Essais d'une rangée de 5 assemblages 6×6 en air avec un jeu de 1 mm. *Rapport interne CEA DDMT/90/103*.
- Queval, J. C., Porte, J., Renouvel, M., and Canada, M. (1990b). Essais d'une rangée de 5 assemblages en eau (jeux de 1 mm et 0.5 mm). *Rapport interne CEA DDMT/90/279*.
- Raffel, M., Willert, C. E., Wereley, S., and Kompenhans, J. (2007). Particle image velocimetry: a practical guide. *Springer*.
- Rayleigh, J. (1879). On the instability of jets. *Proceedings of the London Mathematical Society*.
- Ricciardi, G. (2008). Une approche milieu poreux pour la modélisation de l'interaction fluide-structure des assemblages combustibles dans un cœur de réacteur à eau pressurisée: simulation et expérimentation. *PhD Theses, Université Aix-Marseille I*.

BIBLIOGRAPHY

- Ricciardi, G. (2016). Fluid-structure interaction modelling of a PWR fuel assembly subjected to axial flow. *Journal of Fluids and Structures*.
- Ricciardi, G., Bellizzi, S., Collard, B., and B., C. (2009). Modelling Pressurized Water Reactor cores in terms of porous media. *Journal of Fluids and Structures*.
- Sarpkaya, T. (2004). A critical review of the intrinsic nature of vortex-induced vibrations. *Journal of Fluids and Structures*.
- Singh, K., Michelin, S., and De Langre, E. (2012). Energy harvesting from fluid-elastic instabilities of a cylinder. *Journal of Fluids and Structures*.
- Stokes, G. (1851). On the effects of the internal friction of fluids on the motion of pendulum. *Transactions of Cambridge Philosophical Society*.
- Taylor, D. (1894). On ship-shaped stream forms. *Transactions of the Institution of Naval Architects*.
- Taylor, G. (1952). Analysis of the swimming of long and narrow animals. *Proceedings of the Royal Society*.
- Timoshenko, S. (1921). On the correction factor for shear of the differential equation for transverse vibrations of bars of uniform cross-section. *Philosophical Magazine*.
- Timoshenko, S. (1953). History of strength of materials. *McGraw-Hill New York*.
- Triantafyllou, G. and Cheryssostomidis, C. (1985). Stability of a string in axial flow. *ASME Journal of Energy Resources Technology*.
- Vallory, J. (1999). Rapport des essais d'impact d'assemblages sur une paroi. *Note Technique DEC/SH2C/LHC 1999-011*.
- Vallory, J. (2000). Compte rendu des essais d'impact de deux assemblages entre eux et sur la paroi sous écoulement. *Note Technique DEC/SH2C/LHC 2000-017*.
- Van Brummelen, E. (2009). Added mass effects of compressible and incompressible flows in fluid-structure interaction. *Journal of Applied Mechanics*.
- Von Karman, T. (1930). Calculation of pressure distribution on airship hulls. *National Advisory Committee on Aeronautics*.
- Wamsganss, M., Chen, S., and Jendrzeczyk, J. (1974). Added mass and damping of a vibrating rod in viscous fluids. *Technical Report Argonne National Laboratory*.
- Weichselbaum, N. A. (2015). Non-intrusive experimental study on nuclear fuel assembly response to seismic loads. *PhD Thesis*.

- Weichselbaum, N. A., Andre, M. A., Rahimi-Abkenar, M., Manzari, M. T., and Bardet, P. M. (2016). High-resolution flying-PIV with optical fiber laser delivery. *Experiments in Fluids*.
- Weichselbaum, N. A., Rahimi-Abkenar, M., Vanella, M., Manzari, M. T., Balaras, E., and Bardet, P. M. (2015). Validation facility and model development for nuclear fuel assembly response to seismic loading. *ASME Journal of Nuclear and Radiation Science*.
- Wendel, K. (1956). Hydrodynamic masses and hydrodynamic moments of inertia. *TMB Translation*.
- White, F. (1998). Fluid Mechanics: 4th (fourth) edition. *Mc Graw Hill*.
- Wu, T. (2001). Mathematical biofluidynamics and mechanophysiology of fish locomotion. *Mathematical Methods in the Applied Sciences*.
- Yadykin, Y., Tenetov, V., and Levin, D. (2000). The added mass of a flexible plate oscillating in a fluid. *European Congress on Computational Methods in Applied Sciences and Engineering (ECOMAS)*.

BIBLIOGRAPHY

Appendix A

Experimental Campaigns List

In this appendix a comprehensive set of tables of all the experimental campaigns and experimental parameters are provided. Numbering of each experimental test is listed in order for the user to be able to find the data relative to each experiments. Some comments on certain experiments are also included.

ICARE Experimental Campaigns Table

Confinement	# Assemblies	Velocity [m/s]	Temperature [°C]	Excitation Amplitude [mm]							
				0.1	0.3	0.5	0.8	1	1.2	1.7	2
Large (Jack on 4th grid)	4	0	20	0.1	0.3	0.5	0.8	1	1.2	1.7	2
		1	20	0.1	0.3	0.5	-	1	1.2	1.7	2
		2	20	0.1	0.3	0.5	-	1	1.2	1.7	2
		3	-	-	-	-	-	-	-	-	-
		4	-	-	-	-	-	-	-	-	-
		5	-	-	-	-	-	-	-	-	-
		Air	20	0.1	0.3	0.5	0.8	1	1.2	1.7	2
	2	0	15	0.1	0.3	0.5	0.8	-	1.2	1.7	2
			30	0.1	0.3	0.5	0.8	-	1.2	1.7	2
		1	15	0.1	0.3	0.5	0.8	-	1.2	1.7	2
			30	0.1	0.3	0.5	0.8	-	1.2	1.7	2
		2	15	0.1	0.3	0.5	0.8	-	1.2	1.7	2
			30	0.1	0.3	0.5	0.8	-	1.2	1.7	2
		3	15	0.1	0.3	-	0.8	-	1.2	1.7	2
			30	0.1	0.3	0.5	0.8	-	1.2	1.7	-
		4	-	-	-	-	-	-	-	-	-
-	-		-	-	-	-	-	-	-		
5	15	-	-	0.5	-	-	1.2	-	2		
	30	-	-	-	-	-	-	-	-		
Air	15	0.1	0.3	0.5	0.8	-	1.2	1.7	2		
	30	-	0.3	0.5	0.8	-	-	-	-		
Small (Jack on 3rd grid)	4 (*LDV)	0	15	-	-	-	-	-	-	-	
			30	-	-	-	-	-	-	-	
		1	15*	-	0.3	0.5*	0.8	1*	1.2	1.7*	-
			30	-	0.3	0.5	0.8	1*	1.2	1.7	-
		2	15*	-	0.3	0.5*	0.8	1*	1.2	1.7*	-
			30	-	0.3	0.5	0.8	1*	1.2	1.7	-
		3	15*	-	0.3	0.5*	0.8	1*	1.2	1.7*	-
	30		-	0.3	0.5	0.8	1*	1.2	1.7	-	
	4	15*	-	0.3	0.5*	0.8	1*	1.2	1.7*	-	
		30	-	0.3	0.5	0.8	1*	1.2	1.7	-	
	5	-	-	-	-	-	-	-	-	-	
		-	-	-	-	-	-	-	-	-	
	Air	-	-	-	-	-	-	-	-	-	
		-	-	-	-	-	-	-	-	-	
	2 (*also with OLD BELLOWS; ² PIV)	0	15	-	0.3	0.5*	0.8	1	1,2*	1.7	-
			30	-	0.3	0.5	0.8	1	1.2	1.7	-
1		15	-	0.3	0.5* ²	0.8	1	1,2*	1,7 ²	-	
		30	-	0.3	0.5	0.8	1	1.2	1.7	-	
2		15	-	0.3	0.5*	0.8	1	1,2*	1.7	-	
		30	-	0.3	0.5	0.8	1	1.2	1.7	-	
3		15	-	0.3	0.5	0.8	1	1.2	1.7	-	
		30	-	0.3	0.5	0.8	1	1.2	1.7	-	
4		15	-	0.3	0.5	0.8	1	1.2	1.7	-	
		30	-	0.3	0.5	0.8	1	1.2	1.7	-	
5	15	-	0.3	0.5	0.8	1	1.2	1.7	-		
	-	-	-	-	-	-	-	-	-		
Air	15	-	0.3	0.5	0.8	1	1.2	1.7	-		
	30	-	-	-	-	-	-	-	-		

Nomenclature Experiments ICARE

4 Assemblies - Large Confinement						
Configuration	Type	Q [m/s]	x [mm]	T [°C]	Campagne	Test
4 ax - Large	Q-Stat	0	1	15	1	1
4 ax - Large	Q-Stat	0	2	15	1	2
4 ax - Large	Q-Stat	0	3	15	1	3
4 ax - Large	Q-Stat	0	4	15	1	4
4 ax - Large	Q-Stat	1	1	15	2	1
4 ax - Large	Q-Stat	1	2	15	2	2
4 ax - Large	Q-Stat	1	3	15	2	3
4 ax - Large	Q-Stat	1	4	15	2	4
4 ax - Large	Q-Stat	2	1	15	3	1
4 ax - Large	Q-Stat	2	2	15	3	2
4 ax - Large	Q-Stat	2	3	15	3	3
4 ax - Large	Q-Stat	2	4	15	3	4
4 ax - Large	Q-Stat	3	1	15	4	1
4 ax - Large	Q-Stat	3	2	15	4	2
4 ax - Large	Q-Stat	3	3	15	4	3
4 ax - Large	Q-Stat	3	4	15	4	4
4 ax - Large	Q-Stat	5	1	15	5	1
4 ax - Large	Q-Stat	5	2	15	5	2
4 ax - Large	Q-Stat	5	3	15	5	3
4 ax - Large	Q-Stat	5	4	15	5	4
4 ax - Large	Q-Stat	Air	1	15	6	1
4 ax - Large	Q-Stat	Air	2	15	6	2
4 ax - Large	Q-Stat	Air	3	15	6	3
4 ax - Large	Q-Stat	Air	4	15	6	4
4 ax - Large	Q-Stat	Air	3	15	6	5
4 ax - Large	Dyn	Air	0.1	15	7	1
4 ax - Large	Dyn	Air	0.3	15	7	2
4 ax - Large	Dyn	Air	0.5	15	7	3
4 ax - Large	Dyn	Air	0.8	15	7	4
4 ax - Large	Dyn	Air	1.2	15	7	5
4 ax - Large	Dyn	Air	1.7	15	7	6
4 ax - Large	Dyn	Air	2	15	7	7
4 ax - Large	Dyn	0	0.1	15	8	1
4 ax - Large	Dyn	0	0.3	15	8	2
4 ax - Large	Dyn	0	0.5	15	8	3
4 ax - Large	Dyn	0	0.8	15	8	4
4 ax - Large	Dyn	0	1.2	15	8	5
4 ax - Large	Dyn	0	1.7	15	8	6
4 ax - Large	Dyn	0	2	15	8	7
4 ax - Large	Dyn	1	0.1	15	9	1

APPENDIX A. EXPERIMENTAL CAMPAIGNS LIST

Configuration	Type	Q [m/s]	x [mm]	T [°C]	Campagne	Test
4 ax - Large	Dyn	1	0.3	15	9	2
4 ax - Large	Dyn	1	0.5	15	9	3
4 ax - Large	Dyn	1	0.8	15	9	4
4 ax - Large	Dyn	1	1.2	15	9	5
4 ax - Large	Dyn	1	1.7	15	9	6
4 ax - Large	Dyn	1	2	15	9	7
4 ax - Large	Dyn	2	0.1	15	10	1
4 ax - Large	Dyn	2	0.3	15	10	2
4 ax - Large	Dyn	2	0.5	15	10	3
4 ax - Large	Dyn	2	0.8	15	10	4
4 ax - Large	Dyn	2	1.2	15	10	5
4 ax - Large	Dyn	2	1.7	15	10	6
4 ax - Large	Dyn	2	2	15	10	7
4 ax - Large	Dyn	3	0.1	15	11	1
4 ax - Large	Dyn	3	0.3	15	11	2
4 ax - Large	Dyn	3	0.5	15	11	3
4 ax - Large	Dyn	3	0.8	15	11	4
4 ax - Large	Dyn	3	1.2	15	11	5
4 ax - Large	Dyn	3	1.7	15	11	6
4 ax - Large	Dyn	3	2	15	11	7
4 ax - Large	Dyn	5	0.1	15	12	1
4 ax - Large	Dyn	5	0.3	15	12	2
4 ax - Large	Dyn	5	0.5	15	12	3
4 ax - Large	Dyn	5	0.8	15	12	4
4 ax - Large	Dyn	5	1.2	15	12	5
4 ax - Large	Dyn	5	1.7	15	12	6
4 ax - Large	Dyn	5	2	15	12	7
4 ax - Large	Q-Stat	0	1	30	14	1
4 ax - Large	Q-Stat	0	2	30	14	2
4 ax - Large	Q-Stat	0	3	30	14	3
4 ax - Large	Q-Stat	0	4	30	14	4
4 ax - Large	Q-Stat	1	1	30	15	1
4 ax - Large	Q-Stat	1	2	30	15	2
4 ax - Large	Q-Stat	1	3	30	15	3
4 ax - Large	Q-Stat	1	4	30	15	4
4 ax - Large	Q-Stat	2	1	30	16	1
4 ax - Large	Q-Stat	2	2	30	16	2
4 ax - Large	Q-Stat	2	3	30	16	3
4 ax - Large	Q-Stat	2	4	30	16	4
4 ax - Large	Q-Stat	3	1	30	17	1
4 ax - Large	Q-Stat	3	2	30	17	2
4 ax - Large	Q-Stat	3	3	30	17	3
4 ax - Large	Q-Stat	3	4	30	17	4
4 ax - Large	Q-Stat	5	1	30	18	1
4 ax - Large	Q-Stat	5	2	30	18	2
4 ax - Large	Q-Stat	5	3	30	18	3
4 ax - Large	Q-Stat	5	4	30	18	4
4 ax - Large	Q-Stat	Air	1	30	19	1
4 ax - Large	Q-Stat	Air	2	30	19	2

Configuration	Type	Q [m/s]	x [mm]	T [°C]	Campagne	Test
4 ax - Large	Q-Stat	Air	3	30	19	3
4 ax - Large	Q-Stat	Air	4	30	19	4
4 ax - Large	Dyn	Air	0.1	30	20	1
4 ax - Large	Dyn	Air	0.3	30	20	2
4 ax - Large	Dyn	Air	0.5	30	20	3
4 ax - Large	Dyn	Air	0.8	30	20	4
4 ax - Large	Dyn	Air	1.2	30	20	5
4 ax - Large	Dyn	Air	1.7	30	20	6
4 ax - Large	Dyn	Air	2	30	20	7
4 ax - Large	Dyn	0	0.1	30	21	1
4 ax - Large	Dyn	0	0.3	30	21	2
4 ax - Large	Dyn	0	0.5	30	21	3
4 ax - Large	Dyn	0	0.8	30	21	4
4 ax - Large	Dyn	0	1.2	30	21	5
4 ax - Large	Dyn	0	1.7	30	21	6
4 ax - Large	Dyn	0	2	30	21	7
4 ax - Large	Dyn	1	0.1	30	22	1
4 ax - Large	Dyn	1	0.3	30	22	2
4 ax - Large	Dyn	1	0.5	30	22	3
4 ax - Large	Dyn	1	0.8	30	22	4
4 ax - Large	Dyn	1	1.2	30	22	5
4 ax - Large	Dyn	1	1.7	30	22	6
4 ax - Large	Dyn	1	2	30	22	7
4 ax - Large	Dyn	2	0.1	30	23	1
4 ax - Large	Dyn	2	0.3	30	23	2
4 ax - Large	Dyn	2	0.5	30	23	3
4 ax - Large	Dyn	2	0.8	30	23	4
4 ax - Large	Dyn	2	1.2	30	23	5
4 ax - Large	Dyn	2	1.7	30	23	6
4 ax - Large	Dyn	2	2	30	23	7
4 ax - Large	Dyn	3	0.1	30	24	1
4 ax - Large	Dyn	3	0.3	30	24	2
4 ax - Large	Dyn	3	0.5	30	24	3
4 ax - Large	Dyn	3	0.8	30	24	4
4 ax - Large	Dyn	3	1.2	30	24	5
4 ax - Large	Dyn	3	1.7	30	24	6
4 ax - Large	Dyn	3	2	30	24	7
4 ax - Large	Dyn	5	0.1	30	25	1
4 ax - Large	Dyn	5	0.3	30	25	2
4 ax - Large	Dyn	5	0.5	30	25	3
4 ax - Large	Dyn	5	0.8	30	25	4
4 ax - Large	Dyn	5	1.2	30	25	5
4 ax - Large	Dyn	5	1.7	30	25	6
4 ax - Large	Dyn	5	2	30	25	7
4 ax - Large	Q-Stat	0	4	15	26	1
4 ax - Large	Dyn	0	0.3	15	26	2
4 ax - Large	Dyn	0	0.8	15	26	3
4 ax - Large	Dyn	0	1.7	15	26	4

APPENDIX A. EXPERIMENTAL CAMPAIGNS LIST

Configuration	Type	Q [m/s]	x [mm]	T [°C]	Campagne	Test
4 ax - Large	Dyn	0	3	15	26	5
4 ax - Large	Dyn	0	0.8	15	26	6
4 ax - Large	Dyn	0	0.8	15	26	7
4 ax - Large	Dyn	1	0.8	15	26	8
4 ax - Large	Dyn	2	0.8	15	26	9
4 ax - Large	Dyn	3	0.8	15	26	10
4 ax - Large	Dyn	5	0.8	15	26	11
4 ax - Large	Q-Stat	0	1	15	27	1
4 ax - Large	Q-Stat	0	2	15	27	2
4 ax - Large	Q-Stat	0	3	15	27	3
4 ax - Large	Q-Stat	1	1	15	28	1
4 ax - Large	Q-Stat	1	2	15	28	2
4 ax - Large	Q-Stat	1	3	15	28	3
4 ax - Large	Q-Stat	2	1	15	29	1
4 ax - Large	Q-Stat	2	2	15	29	2
4 ax - Large	Q-Stat	2	3	15	29	3
4 ax - Large	Q-Stat	Air	1	15	30	1
4 ax - Large	Q-Stat	Air	2	15	30	2
4 ax - Large	Q-Stat	Air	3	15	30	3
4 ax - Large	Q-Stat	Air	1	15	30	4
4 ax - Large	Q-Stat	Air	2	15	30	5
4 ax - Large	Q-Stat	Air	3	15	30	6
4 ax - Large	Q-Stat	Air	4	15	30	7
4 ax - Large	Dyn	0	0.5	15	31	1
4 ax - Large	Dyn	0	0.8	15	31	2
4 ax - Large	Dyn	0	1.2	15	31	3
4 ax - Large	Dyn	0	1.7	15	31	4
4 ax - Large	Dyn	1	0.5	15	32	1
4 ax - Large	Dyn	1	0.8	15	32	2
4 ax - Large	Dyn	1	1.2	15	32	3
4 ax - Large	Dyn	1	1.7	15	32	4
4 ax - Large	Dyn	2	0.5	15	33	1
4 ax - Large	Dyn	2	0.8	15	33	2
4 ax - Large	Dyn	2	1.2	15	33	3
4 ax - Large	Dyn	2	1.7	15	33	4
4 ax - Large	Dyn	Air	0.5	15	34	1
4 ax - Large	Dyn	Air	0.8	15	34	2
4 ax - Large	Dyn	Air	1.2	15	34	3
4 ax - Large	Dyn	Air	1.7	15	34	4
4 ax - Large	Dyn	Air	0.5	15	34	5
4 ax - Large	Dyn	Air	0.8	15	34	6
4 ax - Large	Dyn	Air	1.2	15	34	7
4 ax - Large	Dyn	Air	1.7	15	34	8
2 Assemblies - Large Confinement						
Configuration	Type	Q [m/s]	x [mm]	T [°C]	Campaign	Test
2 ax -Large	Q-Stat	0	1	15	1	1
2 ax -Large	Q-Stat	0	2	15	1	2

Configuration	Type	Q [m/s]	x [mm]	T [°C]	Campagne	Test
2 ax -Large	Q-Stat	0	3	15	1	3
2 ax -Large	Q-Stat	0	4	15	1	4
2 ax -Large	Q-Stat	1	1	15	2	1
2 ax -Large	Q-Stat	1	2	15	2	2
2 ax -Large	Q-Stat	1	3	15	2	3
2 ax -Large	Q-Stat	1	4	15	2	4
2 ax -Large	Q-Stat	2	1	15	3	1
2 ax -Large	Q-Stat	2	2	15	3	2
2 ax -Large	Q-Stat	2	3	15	3	3
2 ax -Large	Q-Stat	2	4	15	3	4
2 ax -Large	Q-Stat	3	1	15	4	1
2 ax -Large	Q-Stat	3	2	15	4	2
2 ax -Large	Q-Stat	3	3	15	4	3
2 ax -Large	Q-Stat	3	4	15	4	4
2 ax -Large	Q-Stat	5	1	15	5	1
2 ax -Large	Q-Stat	5	2	15	5	2
2 ax -Large	Q-Stat	5	3	15	5	3
2 ax -Large	Q-Stat	5	4	15	5	4
2 ax -Large	Q-Stat	Air	1	15	6	1
2 ax -Large	Q-Stat	Air	2	15	6	2
2 ax -Large	Q-Stat	Air	3	15	6	3
2 ax -Large	Q-Stat	Air	4	15	6	4
2 ax -Large	Q-Stat	Air	3	15	6	5
2 ax -Large	Dyn	Air	0.1	15	7	1
2 ax -Large	Dyn	Air	0.3	15	7	2
2 ax -Large	Dyn	Air	0.5	15	7	3
2 ax -Large	Dyn	Air	0.8	15	7	4
2 ax -Large	Dyn	Air	1.2	15	7	5
2 ax -Large	Dyn	Air	1.7	15	7	6
2 ax -Large	Dyn	Air	2	15	7	7
2 ax -Large	Dyn	0	0.1	15	8	1
2 ax -Large	Dyn	0	0.3	15	8	2
2 ax -Large	Dyn	0	0.5	15	8	3
2 ax -Large	Dyn	0	0.8	15	8	4
2 ax -Large	Dyn	0	1.2	15	8	5
2 ax -Large	Dyn	0	1.7	15	8	6
2 ax -Large	Dyn	0	2	15	8	7
2 ax -Large	Dyn	1	0.1	15	9	1
2 ax -Large	Dyn	1	0.3	15	9	2
2 ax -Large	Dyn	1	0.5	15	9	3
2 ax -Large	Dyn	1	0.8	15	9	4
2 ax -Large	Dyn	1	1.2	15	9	5
2 ax -Large	Dyn	1	1.7	15	9	6
2 ax -Large	Dyn	1	2	15	9	7
2 ax -Large	Dyn	2	0.1	15	10	1
2 ax -Large	Dyn	2	0.3	15	10	2
2 ax -Large	Dyn	2	0.5	15	10	3
2 ax -Large	Dyn	2	0.8	15	10	4
2 ax -Large	Dyn	2	1.2	15	10	5

APPENDIX A. EXPERIMENTAL CAMPAIGNS LIST

Configuration	Type	Q [m/s]	x [mm]	T [°C]	Campagne	Test
2 ax -Large	Dyn	2	1.7	15	10	6
2 ax -Large	Dyn	2	2	15	10	7
2 ax -Large	Dyn	3	0.1	15	11	1
2 ax -Large	Dyn	3	0.3	15	11	2
2 ax -Large	Dyn	3	0.5	15	11	3
2 ax -Large	Dyn	3	0.8	15	11	4
2 ax -Large	Dyn	3	1.2	15	11	5
2 ax -Large	Dyn	3	1.7	15	11	6
2 ax -Large	Dyn	3	2	15	11	7
2 ax -Large	Dyn	5	0.1	15	12	1
2 ax -Large	Dyn	5	0.3	15	12	2
2 ax -Large	Dyn	5	0.5	15	12	3
2 ax -Large	Dyn	5	0.8	15	12	4
2 ax -Large	Dyn	5	1.2	15	12	5
2 ax -Large	Dyn	5	1.7	15	12	6
2 ax -Large	Dyn	5	2	15	12	7
2 ax -Large	Q-Stat	0	3	15	13	1
2 ax -Large	Dyn	0	0.8	19	13	2
2 ax -Large	Dyn	0	0.8	15	13	3
2 ax -Large	Dyn	0	1.2	15	13	4
2 ax -Large	Dyn	0	0.3	15	13	5
2 ax -Large	Dyn	1	0.5	30	13	6
2 ax -Large	Q-Stat	0	1	30	14	1
2 ax -Large	Q-Stat	0	2	30	14	2
2 ax -Large	Q-Stat	0	3	30	14	3
2 ax -Large	Q-Stat	0	4	30	14	4
2 ax -Large	Q-Stat	1	1	30	15	1
2 ax -Large	Q-Stat	1	2	30	15	2
2 ax -Large	Q-Stat	1	3	30	15	3
2 ax -Large	Q-Stat	1	4	30	15	4
2 ax -Large	Q-Stat	2	1	30	16	1
2 ax -Large	Q-Stat	2	2	30	16	2
2 ax -Large	Q-Stat	2	3	30	16	3
2 ax -Large	Q-Stat	2	4	30	16	4
2 ax -Large	Q-Stat	3	1	30	17	1
2 ax -Large	Q-Stat	3	2	30	17	2
2 ax -Large	Q-Stat	3	3	30	17	3
2 ax -Large	Q-Stat	3	4	30	17	4
2 ax -Large	Q-Stat	5	1	30	18	1
2 ax -Large	Q-Stat	5	2	30	18	2
2 ax -Large	Q-Stat	5	3	30	18	3
2 ax -Large	Q-Stat	5	4	30	18	4
2 ax -Large	Q-Stat	Air	1	30	19	1
2 ax -Large	Q-Stat	Air	2	30	19	2
2 ax -Large	Q-Stat	Air	3	30	19	3
2 ax -Large	Q-Stat	Air	4	30	19	4
2 ax -Large	Dyn	Air	0.1	30	20	1
2 ax -Large	Dyn	Air	0.3	30	20	2

Configuration	Type	Q [m/s]	x [mm]	T [°C]	Campagne	Test
2 ax -Large	Dyn	Air	0.5	30	20	3
2 ax -Large	Dyn	Air	0.8	30	20	4
2 ax -Large	Dyn	Air	1.2	30	20	5
2 ax -Large	Dyn	Air	1.7	30	20	6
2 ax -Large	Dyn	Air	2	30	20	7
2 ax -Large	Dyn	0	0.1	30	21	1
2 ax -Large	Dyn	0	0.3	30	21	2
2 ax -Large	Dyn	0	0.5	30	21	3
2 ax -Large	Dyn	0	0.8	30	21	4
2 ax -Large	Dyn	0	1.2	30	21	5
2 ax -Large	Dyn	0	1.7	30	21	6
2 ax -Large	Dyn	0	2	30	21	7
2 ax -Large	Dyn	1	0.1	30	22	1
2 ax -Large	Dyn	1	0.3	30	22	2
2 ax -Large	Dyn	1	0.5	30	22	3
2 ax -Large	Dyn	1	0.8	30	22	4
2 ax -Large	Dyn	1	1.2	30	22	5
2 ax -Large	Dyn	1	1.7	30	22	6
2 ax -Large	Dyn	1	2	30	22	7
2 ax -Large	Dyn	2	0.1	30	23	1
2 ax -Large	Dyn	2	0.3	30	23	2
2 ax -Large	Dyn	2	0.5	30	23	3
2 ax -Large	Dyn	2	0.8	30	23	4
2 ax -Large	Dyn	2	1.2	30	23	5
2 ax -Large	Dyn	2	1.7	30	23	6
2 ax -Large	Dyn	2	2	30	23	7
2 ax -Large	Dyn	3	0.1	30	24	1
2 ax -Large	Dyn	3	0.3	30	24	2
2 ax -Large	Dyn	3	0.5	30	24	3
2 ax -Large	Dyn	3	0.8	30	24	4
2 ax -Large	Dyn	3	1.2	30	24	5
2 ax -Large	Dyn	3	1.7	30	24	6
2 ax -Large	Dyn	3	2	30	24	7
2 ax -Large	Dyn	5	0.1	30	25	1
2 ax -Large	Dyn	5	0.3	30	25	2
2 ax -Large	Dyn	5	0.5	30	25	3
2 ax -Large	Dyn	5	0.8	30	25	4
2 ax -Large	Dyn	5	1.2	30	25	5
2 ax -Large	Dyn	5	1.7	30	25	6
2 ax -Large	Dyn	5	2	30	25	7
2 ax -Large	Q-Stat	0	4	15	26	1
2 ax -Large	Dyn	0	0.3	15	26	2
2 ax -Large	Dyn	0	0.8	15	26	3
2 ax -Large	Dyn	0	1.7	15	26	4
2 ax -Large	Dyn	0	3	15	26	5
2 ax -Large	Dyn	0	0.8	15	26	6
2 ax -Large	Dyn	0	0.8	15	26	7
2 ax -Large	Dyn	1	0.8	15	26	8
2 ax -Large	Dyn	2	0.8	15	26	9

APPENDIX A. EXPERIMENTAL CAMPAIGNS LIST

Configuration	Type	Q [m/s]	x [mm]	T [°C]	Campagne	Test
2 ax -Large	Dyn	3	0.8	15	26	10
2 ax -Large	Dyn	5	0.8	15	26	11
2 ax -Large	Q-Stat	0	1	15	27	1
2 ax -Large	Q-Stat	0	2	15	27	2
2 ax -Large	Q-Stat	0	3	15	27	3
2 ax -Large	Q-Stat	1	1	15	28	1
2 ax -Large	Q-Stat	1	2	15	28	2
2 ax -Large	Q-Stat	1	3	15	28	3
2 ax -Large	Q-Stat	2	1	15	29	1
2 ax -Large	Q-Stat	2	2	15	29	2
2 ax -Large	Q-Stat	2	3	15	29	3
2 ax -Large	Q-Stat	Air	1	15	30	1
2 ax -Large	Q-Stat	Air	2	15	30	2
2 ax -Large	Q-Stat	Air	3	15	30	3
2 ax -Large	Q-Stat	Air	1	15	30	4
2 ax -Large	Q-Stat	Air	2	15	30	5
2 ax -Large	Q-Stat	Air	3	15	30	6
2 ax -Large	Q-Stat	Air	4	15	30	7
2 ax -Large	Dyn	0	0.5	15	31	1
2 ax -Large	Dyn	0	0.8	15	31	2
2 ax -Large	Dyn	0	1.2	15	31	3
2 ax -Large	Dyn	0	1.7	15	31	4
2 ax -Large	Dyn	1	0.5	15	32	1
2 ax -Large	Dyn	1	0.8	15	32	2
2 ax -Large	Dyn	1	1.2	15	32	3
2 ax -Large	Dyn	1	1.7	15	32	4
2 ax -Large	Dyn	2	0.5	15	33	1
2 ax -Large	Dyn	2	0.8	15	33	2
2 ax -Large	Dyn	2	1.2	15	33	3
2 ax -Large	Dyn	2	1.7	15	33	4
2 ax -Large	Dyn	Air	0.5	15	34	1
2 ax -Large	Dyn	Air	0.8	15	34	2
2 ax -Large	Dyn	Air	1.2	15	34	3
2 ax -Large	Dyn	Air	1.7	15	34	4
2 ax -Large	Dyn	Air	0.5	15	34	5
2 ax -Large	Dyn	Air	0.8	15	34	6
2 ax -Large	Dyn	Air	1.2	15	34	7
2 ax -Large	Dyn	Air	1.7	15	34	8
4 Assemblies - Small Confinement						
Configuration	Type	Q [m/s]	x [mm]	T [°C]	Campaign	Test
4 ax - Small	Dyn	1	0.3	15	1	1
4 ax - Small	Dyn	1	0.5	15	2	1
4 ax - Small	Dyn	1	0.8	15	1	2
4 ax - Small	Dyn	1	1	15	2	2
4 ax - Small	Dyn	1	1.2	15	1	3
4 ax - Small	Dyn	1	1.7	15	2	3
4 ax - Small	Dyn	2	0.3	15	1	4

Configuration	Type	Q [m/s]	x [mm]	T [°C]	Campagne	Test
4 ax - Small	Dyn	2	0.5	15	2	49
4 ax - Small	Dyn	2	0.8	15	1	5
4 ax - Small	Dyn	2	1	15	2	50
4 ax - Small	Dyn	2	1.2	15	1	6
4 ax - Small	Dyn	2	1.7	15	2	51
4 ax - Small	Dyn	3	0.3	15	1	7
4 ax - Small	Dyn	3	0.5	15	2	31
4 ax - Small	Dyn	3	0.8	15	1	8
4 ax - Small	Dyn	3	1	15	2	32
4 ax - Small	Dyn	3	1.2	15	1	9
4 ax - Small	Dyn	3	1.7	15	2	33
4 ax - Small	Dyn	4	0.3	15	1	10
4 ax - Small	Dyn	4	0.5	15	1	11
4 ax - Small	Dyn	4	0.8	15	1	12
4 ax - Small	Dyn	4	1	15	1	13
4 ax - Small	Dyn	4	1.2	15	1	14
4 ax - Small	Dyn	4	1.7	15	1	15
4 ax - Small	Dyn	1	0.3	30	1	16
4 ax - Small	Dyn	1	0.5	30	1	17
4 ax - Small	Dyn	1	0.8	30	1	18
4 ax - Small	Dyn	1	1	30	1	19
4 ax - Small	Dyn	1	1.2	30	1	20
4 ax - Small	Dyn	1	1.7	30	1	21
4 ax - Small	Dyn	2	0.3	30	1	22
4 ax - Small	Dyn	2	0.5	30	1	23
4 ax - Small	Dyn	2	0.8	30	1	24
4 ax - Small	Dyn	2	1	30	1	25
4 ax - Small	Dyn	2	1.2	30	1	26
4 ax - Small	Dyn	2	1.7	30	1	27
4 ax - Small	Dyn	3	0.3	30	1	28
4 ax - Small	Dyn	3	0.5	30	1	29
4 ax - Small	Dyn	3	0.8	30	1	30
4 ax - Small	Dyn	3	1	30	1	31
4 ax - Small	Dyn	3	1.2	30	1	32
4 ax - Small	Dyn	3	1.7	30	1	33
4 ax - Small	Dyn	4	0.3	30	1	34
4 ax - Small	Dyn	4	0.5	30	1	35
4 ax - Small	Dyn	4	0.8	30	1	36
4 ax - Small	Dyn	4	1	30	1	37
4 ax - Small	Dyn	4	1.2	30	1	38
4 ax - Small	Dyn	4	1.7	30	1	39
2 Assemblages - Small Confinement						
Configuration	Type	Q [m/s]	x [mm]	T [°C]	Campaign	Test
2 ax - Small	Dyn	1	0.3	15	3	1
2 ax - Small	Dyn	1	0.5	15	3	2
2 ax - Small	Dyn	1	0.8	15	3	3
2 ax - Small	Dyn	1	1	15	3	4

APPENDIX A. EXPERIMENTAL CAMPAIGNS LIST

Configuration	Type	Q [m/s]	x [mm]	T [°C]	Campagne	Test
2 ax - Small	Dyn	1	1.2	15	3	5
2 ax - Small	Dyn	1	1.7	15	3	6
2 ax - Small	Dyn	2	0.3	15	3	7
2 ax - Small	Dyn	2	0.5	15	3	8
2 ax - Small	Dyn	2	0.8	15	3	9
2 ax - Small	Dyn	2	1	15	3	10
2 ax - Small	Dyn	2	1.2	15	3	11
2 ax - Small	Dyn	2	1.7	15	3	12
2 ax - Small	Dyn	3	0.3	15	3	13
2 ax - Small	Dyn	3	0.5	15	3	14
2 ax - Small	Dyn	3	0.8	15	3	15
2 ax - Small	Dyn	3	1	15	3	16
2 ax - Small	Dyn	3	1.2	15	3	17
2 ax - Small	Dyn	3	1.7	15	3	18
2 ax - Small	Dyn	4	0.3	15	3	19
2 ax - Small	Dyn	4	0.5	15	3	20
2 ax - Small	Dyn	4	0.8	15	3	21
2 ax - Small	Dyn	4	1	15	3	22
2 ax - Small	Dyn	4	1.2	15	3	23
2 ax - Small	Dyn	4	1.7	15	3	24
2 ax - Small	Dyn	5	0.3	15	3	25
2 ax - Small	Dyn	5	0.5	15	3	26
2 ax - Small	Dyn	5	0.8	15	3	27
2 ax - Small	Dyn	5	1	15	3	28
2 ax - Small	Dyn	5	1.2	15	3	29
2 ax - Small	Dyn	5	1.7	15	3	30
2 ax - Small	Dyn	0	0.3	15	3	31
2 ax - Small	Dyn	0	0.5	15	3	32
2 ax - Small	Dyn	0	0.8	15	3	33
2 ax - Small	Dyn	0	1	15	3	34
2 ax - Small	Dyn	0	1.2	15	3	35
2 ax - Small	Dyn	0	1.7	15	3	36
2 ax - Small	Dyn	Air	0.3	15	3	37
2 ax - Small	Dyn	Air	0.5	15	3	38
2 ax - Small	Dyn	Air	0.8	15	3	39
2 ax - Small	Dyn	Air	1	15	3	40
2 ax - Small	Dyn	Air	1.2	15	3	41
2 ax - Small	Dyn	Air	1.7	15	3	42
2 ax - Small	Dyn	1	0.3	30	4	1
2 ax - Small	Dyn	1	0.5	30	4	2
2 ax - Small	Dyn	1	0.8	30	4	3
2 ax - Small	Dyn	1	1	30	4	4
2 ax - Small	Dyn	1	1.2	30	4	5
2 ax - Small	Dyn	1	1.7	30	4	6
2 ax - Small	Dyn	2	0.3	30	4	7
2 ax - Small	Dyn	2	0.5	30	4	8
2 ax - Small	Dyn	2	0.8	30	4	9
2 ax - Small	Dyn	2	1	30	4	10
2 ax - Small	Dyn	2	1.2	30	4	11

Configuration	Type	Q [m/s]	x [mm]	T [°C]	Campagne	Test
2 ax - Small	Dyn	2	1.7	30	4	12
2 ax - Small	Dyn	3	0.3	30	4	13
2 ax - Small	Dyn	3	0.5	30	4	14
2 ax - Small	Dyn	3	0.8	30	4	15
2 ax - Small	Dyn	3	1	30	4	16
2 ax - Small	Dyn	3	1.2	30	4	17
2 ax - Small	Dyn	3	1.7	30	4	18
2 ax - Small	Dyn	4	0.3	30	4	19
2 ax - Small	Dyn	4	0.5	30	4	20
2 ax - Small	Dyn	4	0.8	30	4	21
2 ax - Small	Dyn	4	1	30	4	22
2 ax - Small	Dyn	4	1.2	30	4	23
2 ax - Small	Dyn	4	1.7	30	4	24
2 ax - Small	Dyn	0	0.3	30	4	31
2 ax - Small	Dyn	0	0.5	30	4	32
2 ax - Small	Dyn	0	0.8	30	4	33
2 ax - Small	Dyn	0	1	30	4	34
2 ax - Small	Dyn	0	1.2	30	4	35
2 ax - Small	Dyn	0	1.7	30	4	36
2 ax - Small	Q-Stat	0	1.5	15	5	1
2 ax - Small	Q-Stat	1	1.5	15	5	2
2 ax - Small	Q-Stat	2	1.5	15	5	3
2 ax - Small	Q-Stat	3	1.5	15	5	4
2 ax - Small	Q-Stat	4	1.5	15	5	5
2 ax - Small	Q-Stat	5	1.5	15	5	6
2 ax - Small	Q-Stat	0	1.5	30	5	7
2 ax - Small	Q-Stat	1	1.5	30	5	8
2 ax - Small	Q-Stat	2	1.5	30	5	9
2 ax - Small	Q-Stat	3	1.5	30	5	10
2 ax - Small	Q-Stat	4	1.5	30	5	11
2 ax - Small	Q-Stat	Air	1.5	15	5	12

Configuration	Type	Q [m/s]	x [mm]	T [°C]	Campaign	Test
2 ax - Small	Dyn	Air	1.5	15	6	1
2 ax - Small	Dyn	0	1.5	15	6	2
2 ax - Small	Dyn	1	1.5	17	6	3
2 ax - Small	Dyn	2	1.5	16	6	4
2 ax - Small	Dyn	4	1.5	16	6	5

Old Bellow
Old Bellow
Old Bellow
Old Bellow
Old Bellow

Configuration	Type	Q [m/s]	x [mm]	T [°C]	Campaign	Test
2 ax - Small	Dyn	0	0.5	15	7	1
2 ax - Small	Dyn	0	1.2	15	7	2
2 ax - Small	Dyn	1	0.5	15	7	3
2 ax - Small	Dyn	1	1.2	15	7	4
2 ax - Small	Dyn	2	0.5	15	7	5
2 ax - Small	Dyn	2	1.2	15	7	6

Old Bellow
Old Bellow
Old Bellow
Old Bellow
Old Bellow
Old Bellow

APPENDIX A. EXPERIMENTAL CAMPAIGNS LIST

4 Assemblies - Small Confinement - LDV							
Configuration	Type	Q [m/s]	Laser	x [mm]	T [°C]	Campaign	Test
4 ax - Small	Dyn	1	2.A	0.5	15	2	1
4 ax - Small	Dyn	1	2.A	1	15	2	2
4 ax - Small	Dyn	1	2.A	1.7	15	2	3
4 ax - Small	Dyn	1	2.B	0.5	15	2	4
4 ax - Small	Dyn	1	2.B	1	15	2	5
4 ax - Small	Dyn	1	2.B	1.7	15	2	6
4 ax - Small	Dyn	1	2.C	0.5	15	2	7
4 ax - Small	Dyn	1	2.C	1	15	2	8
4 ax - Small	Dyn	1	2.C	1.7	15	2	9
4 ax - Small	Dyn	1	2.D	0.5	15	2	10
4 ax - Small	Dyn	1	2.D	1	15	2	11
4 ax - Small	Dyn	1	2.D	1.7	15	2	12
4 ax - Small	Dyn	1	2.E	0.5	15	2	13
4 ax - Small	Dyn	1	2.E	1	15	2	14
4 ax - Small	Dyn	1	2.E	1.7	15	2	15
4 ax - Small	Dyn	1	1.A	0.5	15	2	16
4 ax - Small	Dyn	1	1.A	1	15	2	17
4 ax - Small	Dyn	1	1.A	1.7	15	2	18
4 ax - Small	Dyn	1	1.B	0.5	15	2	19
4 ax - Small	Dyn	1	1.B	1	15	2	20
4 ax - Small	Dyn	1	1.B	1.7	15	2	21
4 ax - Small	Dyn	1	1.C	0.5	15	2	22
4 ax - Small	Dyn	1	1.C	1	15	2	23
4 ax - Small	Dyn	1	1.C	1.7	15	2	24
4 ax - Small	Dyn	1	1.D	0.5	15	2	25
4 ax - Small	Dyn	1	1.D	1	15	2	26
4 ax - Small	Dyn	1	1.D	1.7	15	2	27
4 ax - Small	Dyn	1	1.E	0.5	15	2	28
4 ax - Small	Dyn	1	1.E	1	15	2	29
4 ax - Small	Dyn	1	1.E	1.7	15	2	30
4 ax - Small	Dyn	3	2.A	0.5	15	2	31
4 ax - Small	Dyn	3	2.A	1	15	2	32
4 ax - Small	Dyn	3	2.A	1.7	15	2	33
4 ax - Small	Dyn	3	2.B	0.5	15	2	34
4 ax - Small	Dyn	3	2.B	1	15	2	35
4 ax - Small	Dyn	3	2.B	1.7	15	2	36
4 ax - Small	Dyn	3	2.C	0.5	15	2	37
4 ax - Small	Dyn	3	2.C	1	15	2	38
4 ax - Small	Dyn	3	2.C	1.7	15	2	39
4 ax - Small	Dyn	3	1.A	0.5	15	2	40
4 ax - Small	Dyn	3	1.A	1	15	2	41
4 ax - Small	Dyn	3	1.A	1.7	15	2	42
4 ax - Small	Dyn	3	1.B	0.5	15	2	43
4 ax - Small	Dyn	3	1.B	1	15	2	44
4 ax - Small	Dyn	3	1.B	1.7	15	2	45

Configuration	Type	Q [m/s]	Laser	x [mm]	T [°C]	Campaign	Test
4 ax - Small	Dyn	3	1.C	0.5	15	2	46
4 ax - Small	Dyn	3	1.C	1	15	2	47
4 ax - Small	Dyn	3	1.C	1.7	15	2	48
4 ax - Small	Dyn	2	1.A	0.5	15	2	49
4 ax - Small	Dyn	2	1.A	1	15	2	50
4 ax - Small	Dyn	2	1.A	1.7	15	2	51
4 ax - Small	Dyn	2	1.B	0.5	15	2	52
4 ax - Small	Dyn	2	1.B	1	15	2	53
4 ax - Small	Dyn	2	1.B	1.7	15	2	54
4 ax - Small	Dyn	2	1.C	0.5	15	2	55
4 ax - Small	Dyn	2	1.C	1	15	2	56
4 ax - Small	Dyn	2	1.C	1.7	15	2	57
4 ax - Small	Dyn	2	1.D	0.5	15	2	58
4 ax - Small	Dyn	2	1.D	1	15	2	59
4 ax - Small	Dyn	2	1.D	1.7	15	2	60
4 ax - Small	Dyn	2	1.E	0.5	15	2	61
4 ax - Small	Dyn	2	1.E	1	15	2	62
4 ax - Small	Dyn	2	1.E	1.7	15	2	63
4 ax - Small	Dyn	2	2.A	0.5	15	2	64
4 ax - Small	Dyn	2	2.A	1	15	2	65
4 ax - Small	Dyn	2	2.A	1.7	15	2	66
4 ax - Small	Dyn	2	2.B	0.5	15	2	67
4 ax - Small	Dyn	2	2.B	1	15	2	68
4 ax - Small	Dyn	2	2.B	1.7	15	2	69
4 ax - Small	Dyn	2	2.C	0.5	15	2	70
4 ax - Small	Dyn	2	2.C	1	15	2	71
4 ax - Small	Dyn	2	2.C	1.7	15	2	72
4 ax - Small	Dyn	2	2.D	0.5	15	2	73
4 ax - Small	Dyn	2	2.D	1	15	2	74
4 ax - Small	Dyn	2	2.D	1.7	15	2	75
4 ax - Small	Dyn	2	2.E	0.5	15	2	76
4 ax - Small	Dyn	2	2.E	1	15	2	77
4 ax - Small	Dyn	2	2.E	1.7	15	2	78
4 ax - Small	Dyn	4	2.A	0.5	15	2	79
4 ax - Small	Dyn	4	2.A	1	15	2	80
4 ax - Small	Dyn	4	2.A	1.7	15	2	81
4 ax - Small	Dyn	4	2.B	0.5	15	2	82
4 ax - Small	Dyn	4	2.B	1	15	2	83
4 ax - Small	Dyn	4	2.B	1.7	15	2	84
4 ax - Small	Dyn	4	2.C	0.5	15	2	85
4 ax - Small	Dyn	4	2.C	1	15	2	86
4 ax - Small	Dyn	4	2.C	1.7	15	2	87
4 ax - Small	Dyn	4	1.A	0.5	15	2	88
4 ax - Small	Dyn	4	1.A	1	15	2	89
4 ax - Small	Dyn	4	1.A	1.7	15	2	90
4 ax - Small	Dyn	4	1.B	0.5	15	2	91
4 ax - Small	Dyn	4	1.B	1	15	2	92
4 ax - Small	Dyn	4	1.B	1.7	15	2	93

APPENDIX A. EXPERIMENTAL CAMPAIGNS LIST

Configuration	Type	Q [m/s]	Laser	x [mm]	T [°C]	Campaign	Test
4 ax - Small	Dyn	4	1.C	0.5	15	2	94
4 ax - Small	Dyn	4	1.C	1	15	2	95
4 ax - Small	Dyn	4	1.C	1.7	15	2	96
4 ax - Small	Dyn	3	2.B	1	30	2	97
4 ax - Small	Dyn	3	2.B	0	30		
4 ax - Small	Dyn	4	2.B	1	30	2	98
4 ax - Small	Dyn	4	2.B	0	30		
4 ax - Small	Dyn	2	2.B	1	30	2	99
4 ax - Small	Dyn	2	2.B	0	30		
4 ax - Small	Dyn	1	2.B	1	30	2	100
4 ax - Small	Dyn	1	2.B	0	30		

Appendix B

FreeFEM++ Script

In this Appendix is reported the script implemented in the FreeFEM++ software used for numerical calculations. Only the script for ICARE geometry simulations in large confinement and four fuel assemblies is reported here. All the other configurations treated in this document and discussed above can be obtained by small modification to the geometrical constructions. The reader is also addressed to ([Hecht, 2012a](#)) which is the main user guide for this software.

APPENDIX B. FREEFEM++ SCRIPT

Problem_4_Assemblies_LargeConfinement.edp

```

load "medit"

int Nx=8; // number of cylinders in x direction
int Ny=8; // number of cylinders in y direction

int NAss=4; // number of assemblies

real Dimr=0.45; // cylinder's radius*100
real Dimk=1; // 100/0.45 wavenumber
real DimPitch=0.35; // distance between cylinders*100
real DimLimit=0.8; // confinement size*100
real DimIntrAss=0.4; // Half distance between assemblies*100

real r=1; // Dimensionless cylinder's radius
real k=1; //Dimensionless wavenumber  $n \cdot \text{Dimk} \cdot R / (2L)$   $L=2.512\text{m}$ 
real pitch=DimPitch/Dimr; //Dimensionless distance cylinders
real limit=DimLimit/Dimr; //Dimensionless confinement size
real intrAss=DimIntrAss/Dimr; //Half dimensionless distance between assemblies

real[int] XX1(Nx*Ny); //x-coordinates of centers 1st Assembly
real[int] YY1(Nx*Ny); //y-coordinates of centers 1st Assembly

real[int] XX2(Nx*Ny); //x-coordinates of centers 2nd Assembly
real[int] YY2(Nx*Ny); //y-coordinates of centers 2nd Assembly

real[int] XX3(Nx*Ny); //x-coordinates of centers 3rd Assembly
real[int] YY3(Nx*Ny); //y-coordinates of centers 3rd Assembly

real[int] XX4(Nx*Ny); //x-coordinates of centers 4th Assembly
real[int] YY4(Nx*Ny); //y-coordinates of centers 4th Assembly

// 1st Assembly
for (int i=0;i<Ny;i++)
{
    for (int j=0;j<Nx;j++)
    {
        XX1[i*Nx+j]=intrAss+r*(j+1)+(r+pitch)*j;
    }
}

for (int i=0;i<Ny;i++)
{
    for (int j=0;j<Nx;j++)
    {
        YY1[i*Nx+j]=-intrAss-r*(i+1)-(r+pitch)*i;
    }
}

```

Problem_4_Assemblies_LargeConfinement.edp

```
// 2nd Assembly (clockward)
if (NAss>1)
{
  for (int i=0;i<Ny*Nx;i++)
  {
    XX2[i]= -XX1[i];
    YY2[i]= YY1[i];
  }
}

// 3rd Assembly (clockward)
if (NAss>1)
{
  for (int i=0;i<Ny*Nx;i++)
  {
    XX3[i]= -XX1[i];
    YY3[i]= -YY1[i];
  }
}

// 4th Assembly (clockward)
if (NAss>3)
{
  for (int i=0;i<Ny*Nx;i++)
  {
    XX4[i]= XX1[i];
    YY4[i]= -YY1[i];
  }
}

real mx=Nx*2*r+(Nx-1)*pitch+limit+intrAss;
real my=Ny*2*r+(Ny-1)*pitch+limit+intrAss;

border Gamma1(t=-mx,mx)      { x=t; y=-my; label=0; }
border Gamma2(t=-my,my)     { x=-mx; y=t; label=0; }
border Gamma3(t=-mx,mx)     { x=t; y=my; label=0; }
border Gamma4(t=-my,my)     { x=mx; y=t; label=0; }

border Cilindres1(t=0,2*pi;i)
```

APPENDIX B. FREEFEM++ SCRIPT

```

                                Problem_4_Assemblies_LargeConfinement.edp
{
    x = XX1[i]+r*cos(t);
    y = YY1[i]+r*sin(t);
    //label = 1;
    label = i+1;
}

border Cilindres2(t=0,2*pi;i)
{
    x = XX2[i]+r*cos(t);
    y = YY2[i]+r*sin(t);
    //label = 2;
    label = Nx*Ny+i+1;
}

border Cilindres3(t=0,2*pi;i)
{
    x = XX3[i]+r*cos(t);
    y = YY3[i]+r*sin(t);
    //label = 3;
    label = 2*(Nx*Ny)+i+1;
}

border Cilindres4(t=0,2*pi;i)
{
    x = XX4[i]+r*cos(t);
    y = YY4[i]+r*sin(t);
    //label = 4;
    label = 3*(Nx*Ny)+i+1;
}

int div1=200,div2=200,cil=75;

// Reference Values: div1=200,div2=200,cil=75;

int[int] sub(Nx*Ny); //subdivision of cylinder border

for (int i=0;i<Nx*Ny;i++)
{ sub[i]=-cil; }

mesh Th;

if (NAss==1)
{
Th=buildmesh(Gamma1(div1)+Gamma2(-div2)+Gamma3(-div1)
              +Gamma4(div2)+Cilindres1(sub));
}

if (NAss==2)

```

```

Problem_4_Assemblies_LargeConfinement.edp
{
Th=buildmesh(Gamma1(div1)+Gamma2(-div2)+Gamma3(-div1)
              +Gamma4(div2)+Cilindres1(sub)+Cilindres2(sub));
}

if (NAss==3)
{
Th=buildmesh(Gamma1(div1)+Gamma2(-div2)+Gamma3(-div1)
              +Gamma4(div2)+Cilindres1(sub)+Cilindres2(sub)+Cilindres3(sub));
}

if (NAss==4)
{
Th=buildmesh(Gamma1(div1)+Gamma2(-div2)+Gamma3(-div1)
              +Gamma4(div2)+Cilindres1(sub)+Cilindres2(sub)+Cilindres3(sub)+Cilindres4(sub));
}

plot(Th,wait=1,ps="Geometry_4Ass_Large.eps");
savemesh(Th,"Multi_Cilindres.meshb");

fespace Vh(Th,P1);
Vh phi, w, kphi;

cout<<"Initial size of mesh="<<phi[].max<<endl;

solve Problem(phi,w)=-int2d(Th)(dx(phi)*dx(w)+dy(phi)*dy(w))
                    -int2d(Th)(k*k*phi*w)
                    -int1d(Th,1)(w*(((x-XX1[0])/r)))
                    -int1d(Th,2)(w*(((x-XX1[1])/r)))
                    -int1d(Th,3)(w*(((x-XX1[2])/r)))
                    -int1d(Th,4)(w*(((x-XX1[3])/r)))
                    -int1d(Th,5)(w*(((x-XX1[4])/r)))
                    -int1d(Th,6)(w*(((x-XX1[5])/r)))
                    -int1d(Th,7)(w*(((x-XX1[6])/r)))
                    -int1d(Th,8)(w*(((x-XX1[7])/r)))
                    -int1d(Th,9)(w*(((x-XX1[8])/r)))
                    -int1d(Th,10)(w*(((x-XX1[9])/r)))
                    -int1d(Th,11)(w*(((x-XX1[10])/r)))
                    -int1d(Th,12)(w*(((x-XX1[11])/r)))
                    -int1d(Th,13)(w*(((x-XX1[12])/r)))
                    -int1d(Th,14)(w*(((x-XX1[13])/r)))
                    -int1d(Th,15)(w*(((x-XX1[14])/r)))
                    -int1d(Th,16)(w*(((x-XX1[15])/r)))
                    -int1d(Th,17)(w*(((x-XX1[16])/r)))
                    -int1d(Th,18)(w*(((x-XX1[17])/r)))
                    -int1d(Th,19)(w*(((x-XX1[18])/r)))
                    -int1d(Th,20)(w*(((x-XX1[19])/r)))
                    -int1d(Th,21)(w*(((x-XX1[20])/r)))

```

APPENDIX B. FREEFEM++ SCRIPT

```

                                Problem_4_Assemblies_LargeConfinement.edp
-int1d(Th,22)(w*(((x-XX1[21])/r)))
-int1d(Th,23)(w*(((x-XX1[22])/r)))
-int1d(Th,24)(w*(((x-XX1[23])/r)))
-int1d(Th,25)(w*(((x-XX1[24])/r)))
-int1d(Th,26)(w*(((x-XX1[25])/r)))
-int1d(Th,27)(w*(((x-XX1[26])/r)))
-int1d(Th,28)(w*(((x-XX1[27])/r)))
-int1d(Th,29)(w*(((x-XX1[28])/r)))
-int1d(Th,30)(w*(((x-XX1[29])/r)))
-int1d(Th,31)(w*(((x-XX1[30])/r)))
-int1d(Th,32)(w*(((x-XX1[31])/r)))
-int1d(Th,33)(w*(((x-XX1[32])/r)))
-int1d(Th,34)(w*(((x-XX1[33])/r)))
-int1d(Th,35)(w*(((x-XX1[34])/r)))
-int1d(Th,36)(w*(((x-XX1[35])/r)))
-int1d(Th,37)(w*(((x-XX1[36])/r)))
-int1d(Th,38)(w*(((x-XX1[37])/r)))
-int1d(Th,39)(w*(((x-XX1[38])/r)))
-int1d(Th,40)(w*(((x-XX1[39])/r)))
-int1d(Th,41)(w*(((x-XX1[40])/r)))
-int1d(Th,42)(w*(((x-XX1[41])/r)))
-int1d(Th,43)(w*(((x-XX1[42])/r)))
-int1d(Th,44)(w*(((x-XX1[43])/r)))
-int1d(Th,45)(w*(((x-XX1[44])/r)))
-int1d(Th,46)(w*(((x-XX1[45])/r)))
-int1d(Th,47)(w*(((x-XX1[46])/r)))
-int1d(Th,48)(w*(((x-XX1[47])/r)))
-int1d(Th,49)(w*(((x-XX1[48])/r)))
-int1d(Th,50)(w*(((x-XX1[49])/r)))
-int1d(Th,51)(w*(((x-XX1[50])/r)))
-int1d(Th,52)(w*(((x-XX1[51])/r)))
-int1d(Th,53)(w*(((x-XX1[52])/r)))
-int1d(Th,54)(w*(((x-XX1[53])/r)))
-int1d(Th,55)(w*(((x-XX1[54])/r)))
-int1d(Th,56)(w*(((x-XX1[55])/r)))
-int1d(Th,57)(w*(((x-XX1[56])/r)))
-int1d(Th,58)(w*(((x-XX1[57])/r)))
-int1d(Th,59)(w*(((x-XX1[58])/r)))
-int1d(Th,60)(w*(((x-XX1[59])/r)))
-int1d(Th,61)(w*(((x-XX1[60])/r)))
-int1d(Th,62)(w*(((x-XX1[61])/r)))
-int1d(Th,63)(w*(((x-XX1[62])/r)))
-int1d(Th,64)(w*(((x-XX1[63])/r)));

real[int] g1y(Nx*Ny),g1x(Nx*Ny);
real[int] g2y(Nx*Ny),g2x(Nx*Ny);
real[int] g3y(Nx*Ny),g3x(Nx*Ny);
real[int] g4y(Nx*Ny),g4x(Nx*Ny);

real g1yTot,g1xTot;
real g2yTot,g2xTot;

```

Problem_4_Assemblies_LargeConfinement.edp

```

real g3yTot,g3xTot;
real g4yTot,g4xTot;

for (int i=0;i<Nx*Ny;i++)
{

    g1y[i]=int1d(Th,i+1)(-k/(2)*(phi/r)*((y-YY1[i])/r))/(r);
    g1x[i]=int1d(Th,i+1)(-k/(2)*(phi/r)*((x-XX1[i])/r))/(r);

        g1yTot=g1yTot+g1y[i];
        g1xTot=g1xTot+g1x[i];

}

for (int i=0;i<Nx*Ny;i++)
{

    g2y[i]=int1d(Th,Nx*Ny+i+1)(-k/(2)*(phi/r)
        *((y-YY2[i])/r))/(r);
    g2x[i]=int1d(Th,Nx*Ny+i+1)(-k/(2)*(phi/r)
        *((x-XX2[i])/r))/(r);

        g2yTot=g2yTot+g2y[i];
        g2xTot=g2xTot+g2x[i];

}

for (int i=0;i<Nx*Ny;i++)
{

    g3y[i]=int1d(Th,2*(Nx*Ny)+i+1)(-k/(2)*(phi/r)
        *((y-YY3[i])/r))/(r);
    g3x[i]=int1d(Th,2*(Nx*Ny)+i+1)(-k/(2)*(phi/r)
        *((x-XX3[i])/r))/(r);

        g3yTot=g3yTot+g3y[i];
        g3xTot=g3xTot+g3x[i];

}

for (int i=0;i<Nx*Ny;i++)
{

    g4y[i]=int1d(Th,3*(Nx*Ny)+i+1)(-k/(2)*(phi/r)
        *((y-YY4[i])/r))/(r);
    g4x[i]=int1d(Th,3*(Nx*Ny)+i+1)(-k/(2)*(phi/r)
        *((x-XX4[i])/r))/(r);

        g4yTot=g4yTot+g4y[i];
        g4xTot=g4xTot+g4x[i];

}

```

APPENDIX B. FREEFEM++ SCRIPT

Problem_4_Assemblies_LargeConfinement.edp

```

cout<< "\n g1y = " ;
for (int i=0;i<Nx*Ny;i++)
{
    cout << " , " << g1y[i] ;
}
cout << "\n\n" ;
cout<< "g1x = " ;
for (int i=0;i<Nx*Ny;i++)
{
    cout << " , " << g1x[i] ;
}
cout << "\n\n" << endl;

```

```

cout<< "g2y = " ;
for (int i=0;i<Nx*Ny;i++)
{
    cout << " , " << g2y[i] ;
}
cout << "\n\n" ;
cout<< "g2x = " ;
for (int i=0;i<Nx*Ny;i++)
{
    cout << " , " << g2x[i] ;
}
cout << "\n\n" << endl;

```

```

cout<< "g3y = " ;
for (int i=0;i<Nx*Ny;i++)
{
    cout << " , " << g3y[i] ;
}
cout << "\n\n" ;
cout<< "g3x = " ;
for (int i=0;i<Nx*Ny;i++)
{
    cout << " , " << g3x[i] ;
}
cout << "\n\n" << endl;

```

```

cout<< "g4y = " ;
for (int i=0;i<Nx*Ny;i++)
{
    cout << " , " << g4y[i] ;
}
cout << "\n\n" ;
cout<< "g4x = " ;

```

```

                                Problem_4_Assemblies_LargeConfinement.edp
for (int i=0;i<Nx*Ny;i++)
{
    cout << " , " << g4x[i] ;
}
cout << "\n\n" << endl;

cout<< "g1yTot = " << g1yTot << "\n" << endl ;
cout<< "g1xTot = " << g1xTot << "\n" << endl ;
cout<< "g2yTot = " << g2yTot << "\n" << endl ;
cout<< "g2xTot = " << g2xTot << "\n" << endl ;
cout<< "g3yTot = " << g3yTot << "\n" << endl ;
cout<< "g3xTot = " << g3xTot << "\n" << endl ;
cout<< "g4yTot = " << g4yTot << "\n" << endl ;
cout<< "g4xTot = " << g4xTot << "\n" << endl ;

string Name="g_Functions_4Assemblies_" + "Large_K" + "_" + k + ".txt";

ofstream file(Name);

file << "Values of g-Functions \n\n"<<endl;

file << "Domain Size:  R=" << r << " hx=" << mx << " hy="
    << my << " \n\n" << endl;

file << "Discretization:  Gamma1-->" << div1 << "\n"
    << " Gamma2-->" << div2 << "\n"
    << " Gamma3-->" << div1 << "\n"
    << " Gamma4-->" << div2 << "\n"
    << " Cilidres-->" << cil << "\n\n"<<endl;

file <<"k \t"<<"Assembly\t"<<"Cyl Number \t"<<"gX(k) \t"<<"gY(k) \n"<<endl;

for (int i=0;i<Nx*Ny;i++)
{
file << k <<"\t"<<"1\t"<< i <<"\t"<<g1x[i]<<"\t"<<g1y[i]<< endl;
}
file <<"\n"<<endl;

for (int i=0;i<Nx*Ny;i++)
{
file << k <<"\t"<<"2\t"<< Nx*Ny+i <<"\t"<<g2x[i]<<"\t"<<g2y[i]<< endl;
}
file <<"\n"<<endl;

for (int i=0;i<Nx*Ny;i++)
{
file << k <<"\t"<<"3\t"<< 2*(Nx*Ny)+i <<"\t"<<g3x[i]<<"\t"<<g3y[i]<< endl;
}
file <<"\n"<<endl;

```


APPENDIX B. FREEFEM++ SCRIPT

```
Problem_4_Assemblies_LargeConfinement.edp

for (int i=0;i<Nx*Ny;i++)
{
file << k <<"\t"<<"4\t"<< 3*(Nx*Ny)+i <<"\t"<<g4x[i]<<"\t"<<g4y[i]<< endl;
}
file <<"\n"<<endl;

file <<"k \t"<<"Assembly \t"<<"gXTot(k) \t"<<"gYTot(k) \n"<<endl;

file << k <<"\t"<<"1\t"<< g1xTot<<"\t"<<g1yTot<< endl;
file << k <<"\t"<<"2\t"<< g2xTot<<"\t"<<g2yTot<< endl;
file << k <<"\t"<<"3\t"<< g3xTot<<"\t"<<g3yTot<< endl;
file << k <<"\t"<<"4\t"<< g4xTot<<"\t"<<g4yTot<< endl;

string SolutionName="Solution_4Assemblies_XDir_K" + k + "_Large.eps";

plot(phi,value=false,wait=1,
      ps=SolutionName);

//savesol("Solution2_4Cilindres_XDir.sol",Th,phi,order=1);
```